# Comprehension and optimisation of the co-evaporation deposition of Cu(In,Ga)Se2 absorber layers for very high efficiency thin film solar cells

Torben Klinkert






**Thèse de Doctorat de l'Université Pierre et Marie Curie**

**Ecole Doctorale 397 - Physique et Chimie des Matériaux**

# Compréhension et optimisation du dépôt de $Cu(In,Ga)Se_2$ par co-évaporation en tant qu'absorbeur pour le développement de cellules solaires en couches minces à très haut rendement

Présentée par **Torben Klinkert**

le 8 janvier 2015 devant le jury composé de:

| | |
|---|---|
| Rapporteurs: | **Dr. Daniel Abou-Ras** |
| | **Dr. Nicolas Barreau** |
| Examinateurs: | **Prof. Dr. Marika Edoff** |
| | **Prof. Dr. Ayodhya N. Tiwari** |
| | **Prof. Dr. Abhay Shukla** |
| Encadrant de thèse (EDF R&D): | **Dr. Marie Jubault** |
| Directeur de thèse: | **Dr. Jean-François Guillemoles** |
| Invité (EDF R&D) | **Dr. Stéphane Andrieux** |

# Acknowledgments

First of all, I would like to express my sincere gratitude to my thesis director Jean-François Guillemoles and my supervisor Marie Jubault. Jean-François has been supporting me continuously during my PhD study and research. He helped me a lot with his motivation, enthusiasm and immense knowledge. His guidance was very important during the time of research and writing of this thesis. Marie has been supporting and guiding me on an every-day basis both in the laboratory as well as in the analysis of the scientific results. I have appreciated very much her profound knowledge, availability and patience and am very happy to have been her first PhD student. I sincerely thank Frédérique Donsanti, who was my superviror for about the first year of my PhD thesis, with who I worked regularly on the co-evaporation reactor and who proof-read all of my articles, conference contributions and finally this manuscript. I appreciated your direct way of communication and advice. You taught me something crucial: how to deal with the review and criticism of my work and not to take it personally.

The excellent laboratory infrastructure, the present experimental methods, the well formed staff and the great working atmosphere have been very important during my work. I thank Daniel Lincot, Matthieu Versavel and Yves Schlumberger for their great work managing IRDEP and EDF R&D, for the exceptional working conditions and the possibility to present and discuss my work on several international conferences.

I acknowledge furthermore the two manuscript rapporteurs Daniel Abou-Ras and Nicolas Barreau for their detailed review and correction of my manuscript. Their remarks were very usefull and constructive to improve my work. I also thank all further members of my defense speech committee for reading the manuscript and their very interesting questions about the $MoSe_2$ layer, Ga and In diffusion in the defect wurtzite (!) precursor layer, the optimal Ga gradient in ultrathin CIGS, the importance (or not) of morphology, the contribution of simulation and so on. Thank you Marika Edoff, Ayodhya Tiwari, Stéphane Andrieux and Abhay Shukla!

I am also grateful to Laurent Lombez for the discussions and review of the device part of my manuscript but also for the Lab-tour when I just arrived at IRDEP (your accent made you easier to understand in the beginning so that was nice!) and the introducion to several experimental characterisation methods (Raman, Photoluminescence, IV, etc.)

My sincere thanks also go to Thibaud Hildebrand and Negar Naghavi for the work accomplished together on the interface Ga composition for Zn(O,S) buffer layers which greately contributes to my manscript and led to two conference contributions

and a paper!

I also thank Dimitri Mercier and Arnaud Etcheberry from the Institut Lavoisier Versailles for the work on chemical etchings of the absorber layer.

Since for a solar cell other layers than the absorber layers are necessary, I also needed other persons to deposit them. Thank you to all of you who made this work possible: Valérie, Alain, Gilles, Laurent, Benoit, Nicolas, Samuel and even Aurélien some time, with a touch of iron in the chemical bath :). And thank you Enrique for all the IV and EQE chracterisation work!

I furthermore thank all the fellow PhD students and all other colleagues I crossed on my way for their general kindness and helpfullness and all the wonderful moments in the laboratory, at conferences or during evenings in Paris! Unforgettable my first IRDEP-PhD-students night organised by Myriam where I got to know most of them, the human pile on top of Pascal (who was about to finish his PhD and leave IRDEP) at 4 am in his bedroom in Chantilly, japanese and french karaoke nights, all the football matches during lunch-breaks and many other pleasant moments. Thank you!

A particular thank goes to Jorge and Cathy for all the 'fruitfull discussions' in our lab and out in Paris. I furthermore thank Amaury, Florian and Jorge for the enriching scientific excursions to Berlin, Barcelona and the presqu'île de Crozon and numerous culinary discoveries (at least for some of us): Empanadas, Haxen, Schnitzel, arepa, galette-saucisse bretonne, stroumpfs, pericos, picon-bière, Aguardiente and many others!

Last but not the least, I would like to thank my family: my parents Ulla and Bernd, my brother Malte and my grandparents Marianne and his sadly deceased Lothar for their continuous support and affection. And I sincerely thank Marion for her love and encouragement every single day during these last three years.

# Contents

**Abstract** **1**

**General introduction** **3**

**1. Technology review of Cu(In,Ga)$Se_2$ solar cells** **9**
1.1. Introduction . . . . . 9
1.2. The classic CIGS solar cell structure . . . . . 10
1.3. Deposition methods for the CIGS absorber layer . . . . . 18
1.4. Conclusion . . . . . 21

**2. Physics of the Cu(In,Ga)$Se_2$ solar cell** **23**
2.1. Light-absorption . . . . . 23
2.2. Separation and extraction of charge carriers . . . . . 26
2.3. Recombination mechanisms . . . . . 28
2.4. Current-voltage characteristic . . . . . 35
2.5. Conclusion . . . . . 39

**3. Experimental Setups and methods** **41**
3.1. The co-evaporation reactor . . . . . 41
3.2. Contact and buffer layer deposition . . . . . 49
3.3. Conclusion . . . . . 50

**4. Comprehension of the 3 - stage process** **51**
4.1. Introduction and addressed questions . . . . . 51
4.2. Optimisation of the Se pre-deposition step . . . . . 53
4.3. The first stage: growth of the $(In,Ga)_2Se_3$ precursor . . . . . 56
4.4. The second stage: recristallisation and the reaction of $(In,Ga)_2Se_3$ with Cu and Se . . . . . 68
4.5. The third stage: influence of the substrate temperature . . . . . 72
4.6. Discussion . . . . . 75
4.7. Conclusion . . . . . 81

**5. Characterisation of in-depth inhomogeneities in the CIGS absorber layer** **83**
5.1. Scanning electron microscopy . . . . . 83
5.2. In-depth composition . . . . . 84
5.3. Raman spectroscopy . . . . . 84
5.4. X-ray diffraction . . . . . 86

5.5. Discussion . . . . . 88
5.6. Conclusion . . . . . 92

**6. Devices** **95**
6.1. Band gap gradient in the absorber layer . . . . . 96
6.2. The front-interface . . . . . 102
6.3. Conclusion . . . . . 120

**General Conclusion and Perspectives** **121**

**Bibliography** **125**

**Appendix** **139**

**A. Material characterisation** **141**
A.1. X-ray fluorescence . . . . . 141
A.2. X-ray diffraction . . . . . 141
A.3. Scanning electron microscopy . . . . . 142
A.4. Raman spectroscopy . . . . . 143
A.5. Glow discharge optical emission spectroscopy, quantified by ICP . . . 143

**B. Solar cell characterisation** **145**
B.1. Current-voltage characterisation . . . . . 145
B.2. As a function of temperature . . . . . 145
B.3. External quantum efficiency . . . . . 145

**C. Material characterization of absorber layers used in the devices studied in chapter 6** **147**

**D. Arrhenius plots for varied Ga surface composition $x_f$ and ZnS buffer layer** **151**

**E. Simulation parameters** **153**

**Nomenclature** **155**

# Abstract

In this thesis the growth of CIGS thin films by co-evaporation has been optimised and studied systematically. The deposition rates and substrate temperature have been identified as key parameters for the control of the local film composition, morphology and crystal orientation. In order to measure the absolute substrate temperature, the value indicated by a thermo-couple close to but not in contact with the substrate has been calibrated with the aid of an infrared camera. The set-up and optimisation of a three-stage process at a new co-evaporation reactor has led to cell efficiencies of up to 16.7 % up to now (without anti-reflection coating). The key for this achievement has been the control of the in-depth Ga gradient. In order to characterise the in-depth inhomogeneities, a novel method based on chemical etching of the absorber layer has been developed which can be applied in principle for any thin film material. In addition to the characterisation of the final absorber layer material, break-off experiments at different points during the 3-stage process unveiled the importance of precursor and intermediate phases on the growth mechanisms, in-depth compositional gradient and film morphology. It has been shown that a Se deposition step prior to the CIGS deposition process itself influences the observed crystal orientation of an interfacial $MoSe_2$ layer and its duration has an influence on the solar cell performance and homogeneity. The absorber/buffer layer interface has been investigated systematically by varying the local surface near Ga composition in the absorber layer for solar cells with both a CdS and a Zn(O,S)-based buffer layer. It has been shown that an adaptation of the CIGS surface composition is beneficial for the replacement of the CdS buffer layer by a Zn(O,S) based buffer layer. Equivalent efficiencies can be achieved with the two different buffer layers if each of them is combined with the absorber layer with the corresponding optimal interface Ga composition. Saturation current activation energies have been extracted from low temperature current-voltage measurements and are compared to values expected from the theory. The results indicate a lower conduction band offset at the CIGS/Zn(O,S) buffer layer as compared to values reported in the literature. For the further optimisation of our CIGS devices towards 20 % and beyond three routes are proposed. They consider essentially the front interface and interface near region and are linked with each other: the optimisation of the absorber layer deposition finalisation, the reduction of detrimental absorption in the buffer layer (large-gap material or thinning of the CdS buffer) and the incorporation of impurity atoms such as potassium which has shown to have a beneficial effect on the photovoltaic properties of CIGS.

# General introduction

Since the beginning of the industrial revolution and the related increase of energy demand, humanity has primarily harnessed fossil energy sources such as coal, oil and gas. Since the 1970s nuclear power has been massively exploited in some countries, leading to a world primary energy consumption as shown in Fig. 0.1. In 2013 the world wide primary energy consumption was 12730.4 Mtoe (million tons oil equivalent). Fossil fuels made up for 86.7 % of this amount while non-conventional renewables (*i.e.* renewables other than hydro-power) represent only 2.2 %.

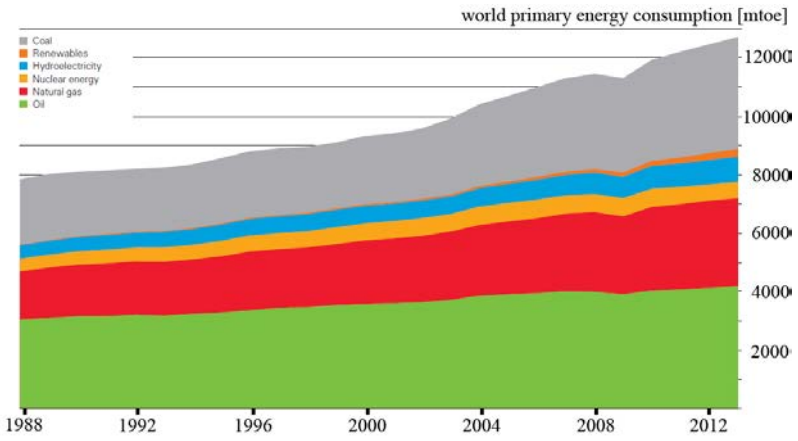


**Figure 0.1.:** World primary energy consumption from 1987 until 2012. Non-conventional renewables energy sources reached a record share of the global primary energy consumption of 2.2 % in 2013 [1].

Regarding only the electricity production (global data for 2013 shown in Fig. 0.2), non-conventional renewable energy plays a more important role with a part of 5.8 %. Photovoltaic (PV) solar energy is responsible for 0.7 % of the worldwide electricity production.

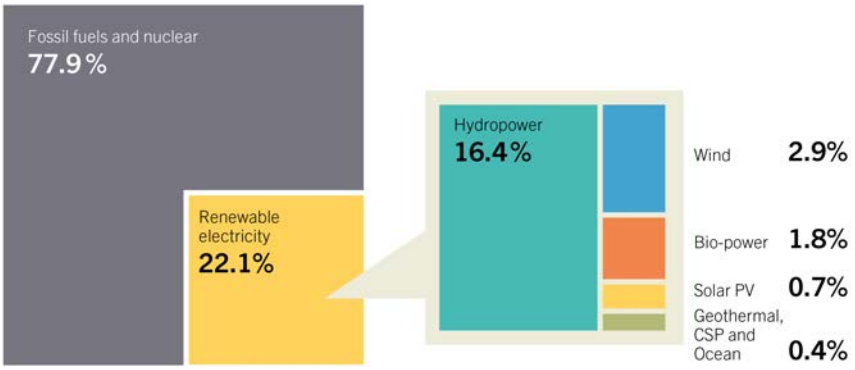


**Figure 0.2.:** Estimated renewable energy share of global electricity production at the end of 2013. Reproduced from [2].

In contrast to fossil and nuclear energy, the production capacities of non-conventional renewable energy sources have been grown and still grow rapidly since the beginning of this century. As can be seen on the left side in Fig. 0.3, the average growth from 2008 to 2013 has been above 50 % per year for solar PV, almost 50 % for concentrating solar thermal power (CSP) and above 20 % for wind power. The global solar PV capacity has grown from only 3.7 GW in 2004 to 139 GW nine years later (Fig. 0.3 right).

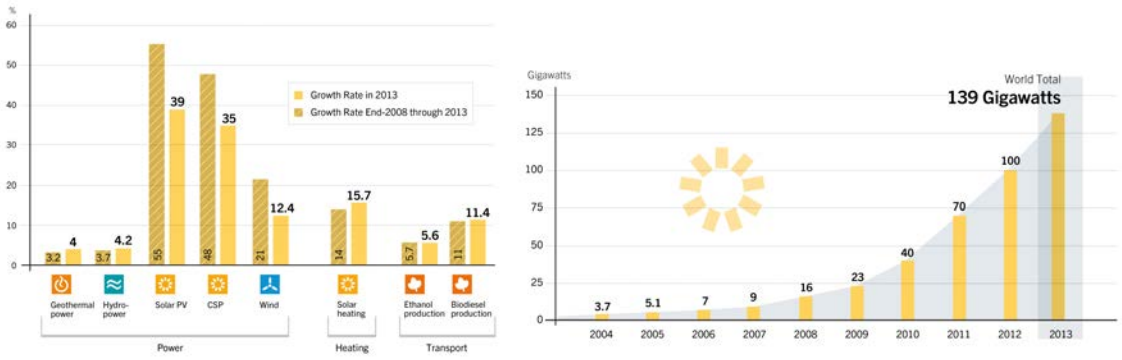


**Figure 0.3.:** Left: Average annual growth rates for different renewable energy capacities. Right: Global solar photovoltaic capacity from 2004 to 2013. Reproduced from [2].

The strong growth of renewable energy sources is not surprising. Our planet contains only limited amounts of fossil and nuclear energy sources. The ratio of proven reserves to their annual consumption, equivalent to the time in years the source would last at a constant level of consumption, is in the order of 100 years (53 years for oil, 55 years for natural gas and 113 years for coal according to [1]). This run-out of today's primary energy ressources and the predicted increase of global energy demand make a transition to alternative, renewable energy sources unevitable on the

mid to long term. But there are two reasons not to wait with this energy transition until the exhaustion of fossil fuels:

1. The climate change due to the exhaustive combustion of fossil fuels. The intergovernmental panel on climate change has identified with high confidence numerous risks and consequences of the climate change [3]. Ironically, these consequences are severe in particular for the least developed and poorest countries in the world which did not contribute, or only to a minor amount, to greenhouse gas emissions and the related climate change.
2. The increasing competitiveness of renewable energy sources. As transistor or flat panel prices, also the PV module price [EUR/kWh] decreases by a constant factor every time the accumulated installation capacity doubles. For PV modules this so-called "learning rate" has been about 20 % since the beginning of PV module production [4]. At the same time fossil energy source prices are increasing since the harnessed ressources get less and less accesible and more expensive to exploit.

Photovoltaics is one of if not the most adapted energy source to meet the increasing world wide energy demand and the transition to renewable energies. It has numerous advantages about conventional and other renewable energy sources. Solar energy is the world's major renewable energy source. The mean incident solar power at the surface of the earth is 184 W/m$^2$or $93.9 \cdot 10^{15}$ W in total [5]. This is about 5000 times the global primary energy consumption of 16.9 TW (corresponding to 12.73 Gtoe /year [1]). Given module efficiencies of 10 % (which is clearly lower then todays achieved module efficiencies) 1/500 or 0.2 % of the earths surface would be sufficient to produce todays energy consumption. Intermittence, distribution and storage of energy from renewable sources are technical issues widely adressed by governments and companies today. Germany, among other countries and regions, has proven that high penetration of renewable energy sources are possible and compatible with net stability and supply security: During the first seven month of 2014, 31 % of the produced electricity came from renewable sources and 7.5 % was solar energy [6]. On the daily basis, renewables have made up to 74 % of the electricity production (sunday, may 11th 2014) [7].

Regarding photovoltaic technologies today commercially available, one can divide into two distinct technologies: Wafer based crystalline silicon (c-Si), often referred to as the $1^{st}$ generation of solar cells and thin films ($2^{nd}$ generation). Solar modules based on c-Si dominate the current market share with 85 % percent [8]. This is due to its good photovoltaïc properties as well as its vast utilization in the micro-electronic industry and its earth abundance. Today's record efficiencies for single-crystalline (sc) and multi-crystalline (mc) Si modules are 22.9 and 18.5 % respectively [9]. Even though c-Si is a mature technology, there is still some room for improvements. Advanced research and devellopment is conducted on back-contact cells, texturing processes, the thickness reduction of the costly high purity Si layer and alternative materials to silver, whose price has increased vastly in the past years, as the front contact.

The second generation of solar cells, thin films, contain a light-absorbing semiconductor with a much higher absorption coefficient than c-Si. For this reason, much thinner layers can be used while still practically 100 % of the incident light is absorbed. The deposition processes that are used can be highly automated and material lifetimes are almost similar to those of c-Si modules today. Use of flexible substrates allows for roll to roll fabrication which lowers the costs further. The efficencies obtained by thin film modules (record for CdTe: 17.5 %, CIGS: 15.7 % [9]) are slightly lower then c-Si module efficiencies which is compensated by potential cost advantages related to the fabrication methods as well as a higher flexibility regarding shape, size and color. Furthermore, light-weight flexible substrates fascilitate the building-integration for thin film solar modules. There are basically three different materials used for thin film solar modules today [10]:

- Cadmium Telluride (CdTe) with a worldwide production of 1.8 $GW_p$ in 2013
- Amourphous silicon (a-Si) with a worldwide production of 0.7 $GW_p$ in 2013
- Copper Indium Gallium Diselenide (CIGS) with a worldwide production of 0.7 $W_p$ in 2013

The market share between CIGS and CdTe can be explained by the domination of two companies (Fig. 0.4): *First Solar* fabricating CdTe modules and *Solar Frontier*, producer of CIGS modules.

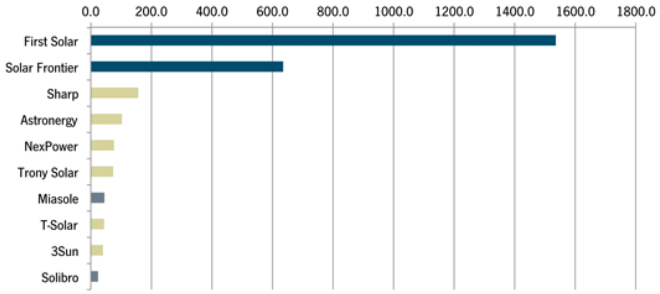


**Figure 0.4.:** Estimated top thin film PV suppliers by Production [MW] in 2012 [11].

The low cost potential translates into reported production costs of 0.55 \$/$W_p$ for CIGS modules fabricated in a production line with an annual capacity of 200 MW or 0.40 \$/$W_p$ from a 1000 MW production line, while crystalline Si manufacturing costs are close to 1 \$/$W_p$ on average [12]. Regarding the experience-curve, thin film and in particular the CIGS technology is at an early stage as compared to c-Si technology and therefore further cost-reduction are probable.

One route which was followed throughout this thesis to cut down costs (in terms of €/$W_p$ or \$/$W_p$) is the increase of the solar cell / solar module conversion efficiency since the conversion efficiency $\eta$ of a module determines by its definition the output

power $P_{\text{out}}$ as described by eq. 0.1.

$$P_{\text{out}} = \eta \cdot P_{\text{in}} \tag{0.1}$$

An overview about the history and state of the art of CIGS based solar cells is given in chapter 1. While solar cells based on CIGS have been subject of research activities for about 40 years, its synthesis by co-evaporation at our laboratory started with my thesis. From the scientific literature numerous information is available about the material itself as well as the co-evaporation process such as the desired chemical phase and the chemical composition allowing for solar cells at a very high conversion efficiency [13, 14, 15, 16]. Therefore I studied in a first attempt (chapter 4) the influence of the various deposition parameters on the CIGS material properties and verified that the grown material meets these requirements. Thereby actual research topics and open questions are addressed which are described in sec. 4.1. Since recent work unveiled a crytical importance of compositional in-depth gradients throughout the absorber layer, a special focus has been put onto diffusion phenomena and the influence of the deposition rates and substrate temperature on the in-depth Ga gradient (sec. 4.5, sec. 4.3.2). In order to characterise in-depth variations of the chemical composition but also of prevalent chemical phases and the preferred crystal orientation, a novel method based on chemical etching of the absorber layer has been developed and the results for a Ga-graded CIGS thin film are shown in chapter 5. In chapter 6, the relation between the obtained CIGS material and the opto-electronic properties of a solar cell based on this material has been studied (chapter 6) with a focus on the in-depth Ga gradient and the properties of the CIGS/buffer layer interface. This gave us at the same time a return for the process optimisation but also resulted in a deeper knowledge of the prevalent recombination mechanisms and their position in the device.

# 1. Technology review of $Cu(In,Ga)Se_2$ solar cells

## 1.1. Introduction

The synthesis of chalcopyrite $CuInSe_2$ has been reported first in 1953 by Hahn *et al.* [17]. The first important work on CIGS solar cells was performed at the Bell laboratories in 1975 where a monocrystalline $CuInSe_2$/CdS solar cell achieved an efficiency of 12 % [18].Thin film $CuInSe_2$ solar cells with efficiencies around 5 % were first fabricated in 1976 at the university of Maine [19] and from then on different companies started to develop CIGS solar cells. An overview about the achieved record efficiencies is given in Fig. 1.1. The most important milestones leading to efficiency improvements, as for example discussed in [20] are explained in the following.

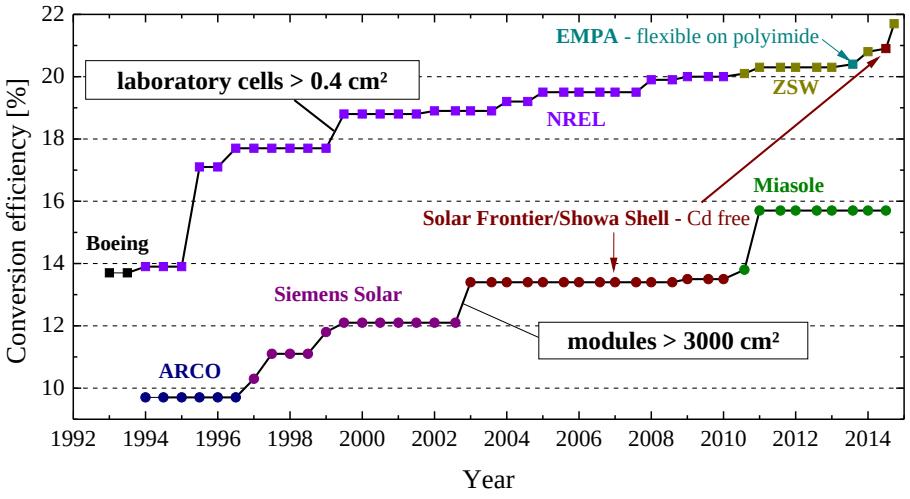


**Figure 1.1.:** CIGS solar cell and module efficiency development. Data is taken from the *Solar cell efficiency tables* [9] published two times a year by Green *et al.* except for the latest record efficiency of 21.7 % [21].

An efficiency of 11 % was first achieved by Boeing in 1984 using a co-evaporation process of Cu, In and Se [22]. In the late 1980s, Arco has reached efficiencies of about 14 % with a two-step process using Cu and In metallic precursors and a reactive annealing in an $H_2S$ atmosphere during which the absorber layer was doped

with Na. The use of soda lime glass substrates for co-evaporation processes around 1993 from which the Na was found to diffuse into the CIGS absorber layer and act as a beneficial dopant has closed the gap to the 2-step process. In the following years, the so-called 3-stage co-evaporation process was invented and developed at NREL and later adopted at ZSW, leading to efficiencies of up to 20.3 % in 2011 [23]. Lately, post-deposition treatments (PDT) with potassium enabled EMPA to fabricate a 20.4 % efficient CIGS solar cell on a flexible polyimide substrate with a low-temperature process well below 500 °C in 2013 [24]. The ZSW (Center for solar and hydrogen research, Stuttgart, Germany) research group has reached a record efficieency of 21.7 % with a K PDT on glass substrate [21] and showed that K PDTs increase the range of possible Ga concentrations in the absorber layer for very high efficiency cells (> 20%) from $GGI \leq 0.35$ to $GGI \leq 0.45$ [25].

In the following sec. 1.2 the role of each of the essential layers in a CIGS solar cell will be explained and current research topics will be presented.

## 1.2. The classic CIGS solar cell structure

The general CIGS solar cell structure is shown in Fig. 1.2. While the glass / Mo / CIGS / CdS / i-ZnO / ZnO:Al structure is the most studied and used structure, various alternative materials, in particular for the substrate and the buffer layer, have been tested and studied and some are even used by today's CIGS fabricating companies. In this chapter, the role in the energy conversion process and relevant materials for each of the functional layers are discussed.

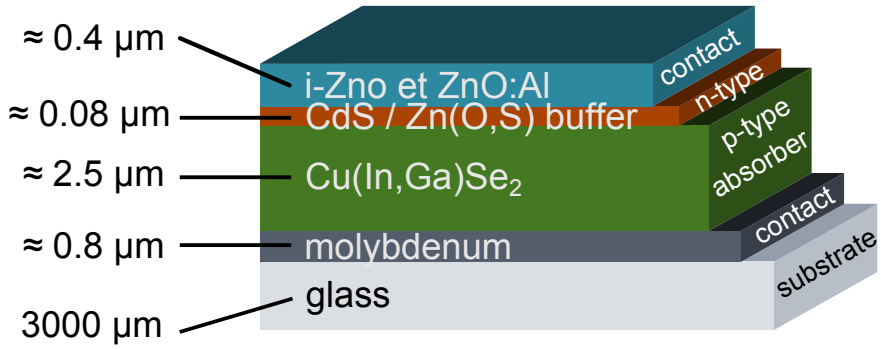


**Figure 1.2.:** The classic CIGS solar cell structure. Depending on the cell size, an additional metallic current collection grid on top of the ZnO:Al layer might be used.

### 1.2.1. The substrate

The substrate is essentially necessary to give the solar cell or module mechanical stability. The historically used ceramic or borosilicate glass substrates have been replaced, initially for cost reasons and good thermal expansion match to CIGS, by soda-lime glass. In the following it became clear that the in-diffusion of sodium from the glass to the CIGS absorber layer had several beneficial effects. CIGS films are found to be more (112) oriented and the solar cell open circuit voltage and efficiency are higher when films are grown on soda-lime glass while it is not clear if the strong orientation is a prerequisite for the good cell performance [26]. Wei *et al.* [27] found theoretically that in small quantities, Na forms defects on Cu ($Na_{Cu}$) and In sites ($Na_{In}$). While $Na_{Cu}$ does not create electric levels in the band gap, $Na_{In}$creates acceptor levels that are shallower than $Cu_{In}$ defects. Since the formation energy of $Na_{In_{Cu}}$ according to Wei *et. al.* is very exothermic, the major effect of Na in Cu-poor $CuInSe_2$ is the elimination of the $In_{Cu}$ defect. This results in an increase of the hole density and decreases the stability of the $(2V_{Cu}^{-} + In_{Cu}^{2+})$ defect complex, also referred to as "ordered vacancy compound" (OVC) in the absorber layer.

More recently, interest has grown in flexible substrates, notably with a record efficiency of 20.4% achieved by EMPA for a CIGS solar cell on a flexible polyimide substrate [24]. Further investigated flexible substrate material are stainless, mild and enameled steel as well as molybdenum, aluminum and titanium. For all these materials, the incorporation of alkaline metals such as sodium and potassium [28, 29, 24, 30, 31] as well as the supression of impurity diffusion from the substrate into the functional layers [31, 32] have shown to be crucial for high solar cell performances and are subject of vast research activities.

### 1.2.2. The back-contact

During solar cell operation, the back-contact serves for current collection of charge carriers generated in the absorber layer and then separated at the p-n junction. In order to avoid an additional series resistance, the lateral conductivity has to be high. An ohmic contact with the CIGS absorber layer without any electrostatic barrier at the interface is desirable. Furthermore a good adhesion of the back-contact to the substrate as well as the CIGS layer to the back-contact are essential.

The most common choice for the back-contact is molybdenum deposited by dc-sputtering. The necessary conductance and thus Mo thickness depends on the cell or module configuration. While the conductance of the Mo film increases for lower Ar pressures, the adherence to the glass substrate is better for higher pressures. Therefore usually an adhesive layer of about 100 nm is deposited at relatively high pressure followed by about 700 nm deposited at low pressure. This results in good adhesion and a resistance of 0.2 $\Omega/\square$, sufficient for small laboratory scale samples of 5x5 $cm^2$ or smaller, as fabricated throughout this thesis.

In the case where sodium is not added during the process, the back-contact needs

to enable the diffusion of sodium from the soda-lime glass substrate into the CIGS absorber layer. The sodium concentration in the final CIGS layer has been found to increase with the plasma pressure during the Mo deposition due to lower density and more porous structure [33]. A decrease of the DC power has been reported to increase the Na and K concentration in the Mo as well as in the CIGS absorber layer [34].

During the Cu(In,Ga)$Se_2$ deposition on molybdenum, a thin $MoSe_2$ layer forms at the interface. This layer is responsible for an ohmic instead of Schottky-contact with the absorber layer [35, 36].

Alternative metals have been tested with limited success. While gold shows good electrical behaviour, only molybdenum is a well working low-cost back-contact [37].

### 1.2.3. The Cu(In,Ga)$Se_2$ absorber layer

Cu($In_{1-x}$,$Ga_x$)$Se_2$ (Copper-Indium-Gallium-Diselenide) is a $I-III-VI_2$ semiconductor. It crystallizes in the chalcopyrite structure that can be described as sphalerite (zincblende) with an ordered replacement of the group II atoms (Zn or Fe in zincblende) by group I (Cu) and group III (In, Ga) atoms. The tetragonal unit cell is shown in Fig. 1.3.

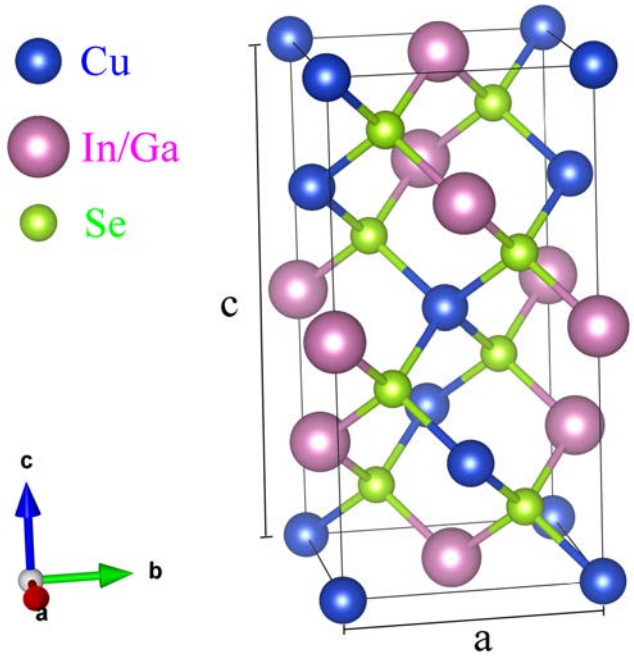


**Figure 1.3.:** Unit cell of chalcopyrite Cu(In,Ga)$Se_2$. Each Se atom is the center of a tetrahedral bond with 2 Cu and 2 group III atoms. Vizualized with [38].

The ratio of the lattice constants is $\frac{c}{a} \approx 2$. The tetragonal distortion (deviation from $\frac{c}{a} = 2$) is the result of different bonding strengths of Cu-Se, In-Se and Ga-Se bonds

and is thus composition-dependend. For the pure ternaries $CuInSe_2$ and $CuGaSe_2$, fabricated by a 3-stage co-evaporation process, the values listed in Tab. 1.1 have been optained by Rietveld refinement of measured x-ray diffraction patterns.

| material | lattice constant $a$ [Å] | lattice constant $c$ [Å] | $c/a$ |
|---|---|---|---|
| $CuInSe_2$ | $5.780 \pm 0.001$ | $11.604 \pm 0.001$ | $2.0075 \pm 0.0002$ |
| $CuGaSe_2$ | $5.607 \pm 0.001$ | $10.983 \pm 0.007$ | $1.9588 \pm 0.0009$ |

**Table 1.1.:** Lattice constants and their fraction of $CuInSe_2$ and $CuGaSe_2$from an identical 3-stage co-evaporation process. Calculated by Rietveld refinement of x-ray diffraction patterns.

Using vegards law this leads to the composition dependences of the lattice constants described by eq. 1.1 and 1.2 where $x$ is the compositional ratio [Ga]/([Ga]+[In]) [39].

#### 1.2.3.1. The chemical composition

One of the reasons why Cu(In,Ga)$Se_2$ is such a successful material for thin film solar cells is its tolerance to deviations from stoichiometry. Very high performances have been demonstrated for devices with [Cu]/([Ga]+[In])ratios from 0.7 to almost unity and [Ga]/([Ga]+[In]) ratios ranging from 0.25 to 0.45 [25]. The influence of the composition on material as well as optical and electronic properties of the cell will be described in the following.

**Cu content** For today's high efficiency CIGS solar cells, the absorber layer is always reported to be Cu-defficient. This is expressed by the atomic concentration ratio [Cu]/([Ga]+[In]) which we will refer to as CGI, which lies between 0.75 and 0.95. The deviation of the CGI from unity is usually interpreted as Cu vacancies $V_{Cu}$ and In on Cu antisite defects $In_{Cu}$ [40]. Even though these defects compensate in $(2V_{Cu}^{-} - In_{Cu}^{2+})$ defect pairs, small deviations from the 1:2 ratio of these defects or others result in a net doping, usually $p$-type for slightly Cu-poor CIGS [40].

**Ga content** Calculations have shown that the formation energy for $Ga_{Cu}$ antisite defects in $CuGaSe_2$ is higher than for $In_{Cu}$ in $CuInSe_2$ [41]. This has several consequences. Firstly, the $(2V_{Cu}^{-} - In_{Cu}^{2+})$ defect cluster, related to the ordered vacancy compound phase, will be supressed. This widens the CIGS phase field [42]. Furthermore, due to the lack of compensating $Ga_{Cu}^{2+}$ donors, no $n$-type doping of CGS has been achieved so far.

Due to the larger atom radius of In compared to Ga atoms, the lattice parameter of CIGS decreases with the ratio [Ga]/([Ga]+[In]) which we will refer to as GGI

throughout this work. From x-ray diffraction measurements of samples with known composition, relations eq. 1.1 and 1.2 have been established [39].

$$a = 5.783\text{Å} - 0.171\text{Å} \cdot x \tag{1.1}$$

$$c = 11.618\text{Å} - 0.586\text{Å} \cdot x \tag{1.2}$$

Also the electronic band structure of CIGS is influenced by its Ga content. Wei and Zunger have calculated in [43] that with increasing GGI, the valence band maximum decreases slightly while the conduction band minimum and the band gap increase: The valence band offset between $CuInSe_2$ ($E_g^{CIS} = 1.04$ eV) and $CuGaSe_2$($E_g^{CGS} = 1.68$ eV) was found to be $\Delta E_\text{v} = -0.04$ eV and the conduction band offset $\Delta E_\text{c} = 0.60$ eV. For semiconductor alloys the band gap typically deviates slightly from a linear-combination of the two constituent band gap energies, expressed by eq. 1.3 with the so-called optical bowing factor $b$.

$$E_\text{g} = E_\text{g}^\text{CIS} + (E_\text{g}^\text{CGS} - E_\text{g}^\text{CIS}) \cdot x + b \cdot x \cdot (1 - x) \tag{1.3}$$

In the literature bowing factors between 0.11 and 0.24 have been reported [16] . In Fig. 1.4 the experimentally obtained efficiency against the Ga content is plotted [44]. It can be seen that by adapting the Ga concentration the CIGS, the tradeoff between $V_\text{oc}$, $J_\text{sc}$ and $FF$ is optimised for a $GGI \approx 0.25$.

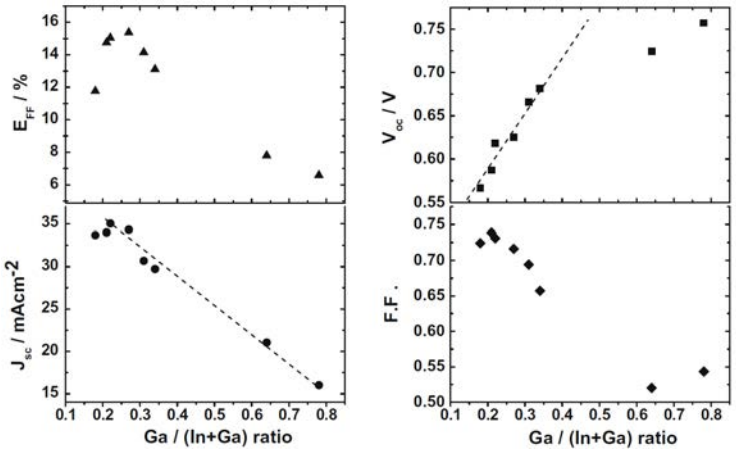


**Figure 1.4.:** Solar cell parameters as a function of the Ga content for CIGS solar cells fabricated by co-evaporation [44].

As we will see later, a gradient of the Ga concentration is prevalent in CIGS fabricated by a 3-stage co-evaporation process. Since this gradient can greatly vary

from one to another sample, it is not quite clear at which position the Ga content is critical for the opto-electronic cell properties. This problem will be adressed in more detail in sec. 6.1.

#### 1.2.3.2. The crystallographic orientation

A wide range of preferred crystallographic orientations is found for CIGS fabricated under different conditions and with different deposition methods. For co-evaporated CIGS, the preferred orientation has been shown to depend on several parameters such as the used substrate, the Se/metal evaporation rate ratio and the substrate temperature. Grown directly on glass, CIGS shows a higher (112) orientation than grown on Mo-coated glass [26]. Schlenker *et al.* showed that on (100) and (111)-oriented monocrystalline molybdenum, thin (up to 1 $\mu$m) CIGS grows purely in the (112) direction, on (110)-oriented Mo the (220/204) orientation dominates and on polycristalline Mo no orientation is clearly preferred [45]. Chaisistak *et al.* have shown in [46] that CIGS films grow more (220)/(204) oriented with an increasing $\tau_{Se}/(\tau_{In} + \tau_{Ga})$ deposition rate ratio during the first stage ($(In,Ga)_2Se_3$ precursor growth) while the (112) orientation becomes more preferred for a decreasing ratio of these deposition rates. They suggest that the deposition parameters in the second stage have few influence on the crystallographic orientation. Mise and Nakada reported in [47]that the deposition temperature of the $(In,Ga)_2Se_3$ precursor layer influences the preferred orientation of the final CIGS layer and temperatures around 400 °C lead to strongly (330) oriented $(In,Ga)_2Se_3$ and (220)/(204) oriented CIGS layers.

No evidence of the CIGS film orientation's influence on the opto-electronic cell properties has been reported in the literature. Furthermore, Powalla *et al.* reported efficiencies $\eta \geq 20\%$ for different intensity ratios $I_{220/204}/I_{112}$ of the (220)/(204) and the (112) XRD peak ranging from 0.3 to 3.9 [48]. For strongly (220)/(204) oriented films ($I_{220/204}/I_{112} > 10$) they found, with for the moment a poor statistical evidence, a decrease of the cell efficiency.

#### 1.2.3.3. Morphology

The relative concentration of the group III elements as well as the substrate temperature during growth are known to change the grain size in CIGS. furthermore influences the morphology of CIGS thin films. Numerous groups have reported a decreasing grain size for an increasing Ga concentration [44, 49], interpreted as a result of a lower diffusion of Ga during the $2^{nd}$ stage of the 3-stage process [44]. The increse of grain size with substrate temperature has been shown for example in references [50, 51, 52, 53]. But it has been shown that very high efficiencies of $\eta \geq 20\%$ can be achieved by CIGS films with only large columnar grains with about 2$\mu$m width as well as by films containing small grains of some 100 nm that do not traverse the whole absorber thickness and even for layers with an accumulation of

very small grains close to the back-interface [48]. This is in agreement with reports on well passivated grain boundaries. Taretto *et al.* reported only low electronic GB activities with recombination velocities $< 10^3$cm/s. Gloeckler *et al.* concluded in [54] that for devices exceeding 20 % efficiency, most likely a significant valence-band downshift or a combination of a valence-band offset and modest hole-repulsive band bending at the grain boundaries minimize their effect on the cell performance.

While its material properties will be explained in detail in sec. 1.3, here the different deposition techniques are explained. The two oldest CIGS deposition methods, briefly introduced in sec. 1.1, are at the same time today's most relevant techniques resulting in the highest cell efficiencies. They will be presented in sec. 1.3.1 and sec. 1.3.2. Atmospheric low-cost approaches of the CIGS absorber deposition are discussed in sec. 1.3.3.

## 1.2.4. The buffer layer

In the classic understanding, the buffer layer is the $n$-type material in the p-n junction formation with the $p$-type CIGS. This hetero-junction nature implies energy band discontinuities at the $p$-$n$ junction. For Cu-poor CIGS (GGI $< 1$), the formation of an $n$-type, so called ordered vacancy compound (OVC) layer in the front region of the CIGS layer has been reported, possibly $Cu(In,Ga)_3Se_5$ or $Cu(In,Ga)_5Se_8$ [55, 56, 57]. This moves the $p$-$n$ junction away from the CIGS/buffer layer interface into the absorber layer and thus decouples the electronic from the structural junction. More recently, the formation of a buried homo-junction due to the diffusion of $n$-dopants from the buffer layer (Cd for CdS [58, 59, 60, 61] and Zn for Zn(S,O) [62]) into the top part of the CIGS absorber layer or OVC have been reported. In all these scenarios, it is clear that the choice of the buffer layer will play a key role in the junction formation mechanism. In the following, the state of the art of the buffer layer materials investigated in this thesis (CdS and ZnS) is given. A comprehensive overview of further buffer layer technologies can be found in [63].

### 1.2.4.1. The CdS buffer layer

The CdS buffer layer is the most widely used buffer layer leading to the best solar cell performance and stability. The deposition method leading to the best efficiencies (up to 21 % [64]) is chemical bath deposition (CBD). A reason that has been proposed is that CBD buffer layers act as protection from the plasma deposition of the i-ZnO/ZnO:Al layers, prevent detrimental shunt paths and permit a conformal absorber coating without pinholes[63]. Precursors usually used are a cadmium salt such as $CdSO_4$, $CdCl_2$, $CdI_2$ or $Cd(CH_3COO)_2$, a complexing agent (usually ammonia) and a sulfur precursor such as $SC(NH_2)_2$ (thiourea) [65].

Despite the very good experience with CdS as the buffer layer up to today, the material has two disadvantages: The toxicity of Cd and its relatively small bandgap

of 2.4 eV which leads to detrimental absorption in the blue spectral range and thus decreases the cells short circuit current.

### 1.2.4.2. The Zn(S,O) buffer layer

First investigated in the early 1990s [66, 67], Zn(O,S) is one of the most studied Cd-free buffer layers for CIGS solar cells. As for CdS, the most common deposition method is CBD and usually thiourea is used as sulfur precursor and ammonia as complexing agent. Typical zinc-complexes are $ZnSO_4$[62], $Zn(SC(NH_2)_2)_n$ and $Zn(NH_3)_n$ [68]. The band gap is generally higher than for CdS and depends on the exact composition $x$ in $ZnO_{1-x}S_x$ as shown in Fig. 1.5.

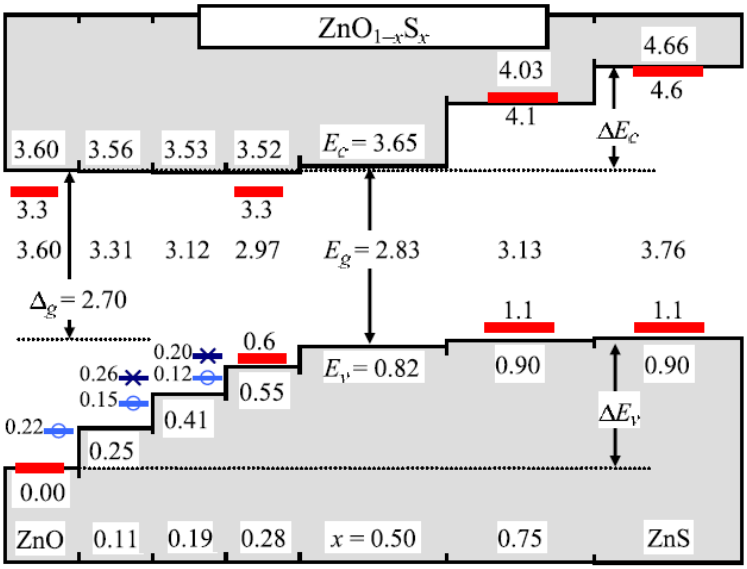


**Figure 1.5.:** Valence band offsets $E_v$, conduction band offsets $E_c$ and band-gap energy $E_g$ in eV, referenced to $E_v$ of ZnO at 0 K. Thick red lines show results from UPS and optical characterization at 300 K. Blue marks depict calculated ionization energies of acceptors. Graph has been taken from ref. [69].

## 1.2.5. The i-ZnO layer and ZnO:Al transparent front contact

Before the deposition of the transparent ZnO:Al front contact, it is common practice to deposit a thin layer of intrinsic high-resistive ZnO, resulting in improved cell efficiencies. Its positive influence on the cell performance has probably several reasons. In the literature, the passivation of pinholes in the CdS layer leading to local CIGS/ZnO junctions [65] has been proposed which agrees with the observation that for thick CdS layers, the i-ZnO layer has no effect [70]. Rau *et al.* suggested locally varying electronic quality of the absorber layer resulting in a locally increased

recombination current [71]. The i-ZnO layer is suggested to reduce the influence of these local high saturation current areas on the total solar cell performance.

The transparent front contact of ZnO:Al is deposited on top of the i-ZnO layer, typically by radio frequency (RF) magnetron sputtering. The thickness has to be adapted to the cell or module geometry. For modules usually no metal current collection grid is used and thus a thicker ZnO:Al layer is needed to keep the resistive losses low. In the case of laboratory cells, thickness about 300-350 $\mu$m are usual to achieve sheet resistances of about 15-25 $\Omega/\square$.

## 1.3. Deposition methods for the CIGS absorber layer

The commonly used deposition methods for the CIGS absorber layer can be divided into three different types and will be described in the following. The first two types, selenization of vacuum-deposited metallic precursors (sec. 1.3.1) and co-evaporation (sec. 1.3.2) are conducted at least partly in a vacuum chamber. This increases the costs but typically results in higher cell efficiencies. The third type (sec. 1.3.3) consists, similarly to the first one, in the deposition of a metallic precursor followed by a selenisation process but in this case the precursor deposition is conducted at atmospheric pressure. This is a cost-advantage but typically results in lower effiicciencies.

### 1.3.1. Two-step process: selenisation of vacucum-deposited metallic precursors

A conversion efficiency of 20.9 % has been demonstrated by Solar Frontier using the two-step process for the absorber layer deposition [72]. This is a world record for Cd-free thin film solar cells since the company used a ZnS-based buffer layer instead of a CdS buffer layer, which is used in other record-level CIGS solar cells.

In this process, the first step consists of the deposition of a metallic CuInGa precursor layer, usually by sputtering. For the second step, the selenization of the metallic precursors, two different approaches exist. Firstly there is an annealing at elevated temperatures of $400 - 500$ °C in a $H_2Se$ atmosphere. While the $H_2Se$ gas is highly toxic, atmospheric pressures during annealing represent a cost-advantage. The second selenization method is rapid thermal processing (RTP) [73]. In this case, a Se layer is evaporated on top of the metallic precursors and in the following the stack is rapidly (in the order of a minute) heated to high temperatures of about 550°C. Halogen lamps are usually used for the very fast sample heating which is necessary to prevent the formation of detrimental binary phases such as $Cu_2Se$ and the dewetting of Se during annealing. The principal advantage of this selenization technique is the absence of the toxic $H_2Se$ gas.

## 1.3.2. Co-evaporation

Co-evaporation of the CIGS absorber layer is the second method achieving very high solar cell efficiencies up to 21 %. In this approach, which is the subject of this thesis, the four constituents of the absorber layer are simultaneously evaporated in a high vacuum chamber from elemental, often knudsen-type, effusion cells. Typical source temperatures are 1300 to 1400 °C for Cu, 950 to 1050 °C for In, 1150 °C to 1250°C for Ga and 250 to 300 °C for Se. The substrate is heated to temperatures in the range of 450-550 °C. While Cu, In and Ga have a sticking coefficient close to unity, Se has a reduced sticking coefficient and a much higher vapor pressure. This is why it needs to be evaporated in excess.

Over time, different evaporation sequences, distinguished by different evaporation rates and substrate temperatures, have been developed by various research groups and companies. The three most prominent ones (one-stage process, Boeing process, three-stage process) will be explained briefly in the following.

### 1.3.2.1. One-stage process

The most simple co-evaporation process is the one-stage process, proposed by Shafarman *et al.* [52]. As illustrated in Fig. 1.6 Cu, In, Ga and Se are deposited at constant rates at a constant substrate temperature throughout the whole process. For the highest cell efficiencies, evaporation rates are set to values that result in a final composition that is slightly Cu-poor ([Cu]/([Ga]+[In]) $\approx$ 0.85) and has a Ga content of [Ga]/([Ga]+[In]) $\approx$ 0.35. CIGS films fabricated by this method have a columnar grain structure with grain widths of some 100 nm and efficiencies up to 15.9 % have been demonstrated [52].

### 1.3.2.2. Boeing process

The Boeing process was first proposed by Mickelsen et al. [74]. It consists of two stages, during the first Cu, In, Ga and Se are evaporated under Cu-rich conditions as shown in Fig. 1.7. At the end of the first stage, the layer is under Cu-rich conditions (CGI $>$ 1). In the following, the Cu deposition rate is decreased while the group 3 deposition rate(s) are increased, leading to a slightly Cu-poor final absorber layer (CGI $\approx$ 0.85).

The Cu-rich growth conditions at the end of the first stage ($t_1$) lead to an increased grain size in the final absorber layer as compared to the 1-stage process. With this process an efficiency of 17.1 % has been demonstrated [75].

### 1.3.2.3. Three-stage process

The 3-stage process has been optimised in the 1990s first an foremost by the National Renewable Energy Laboratory (NREL) and has reached very high cell efficiencies

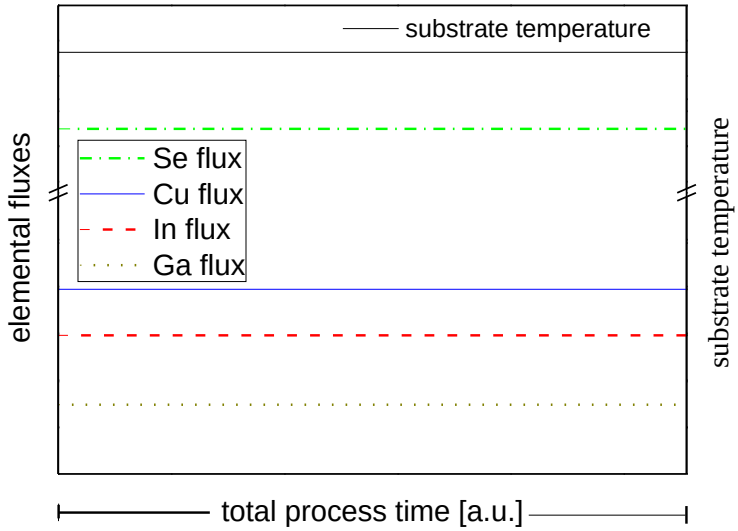


**Figure 1.6.:** Evaporation and temperature profile for the 1-stage process with constant deposition rates for Cu, In, Ga and Se and constant substrate temprature. Typical substrate temperatures are 500 - 550 °C.

exceeding 20 % [76][23][24]. It consists of 3 distinct stages as shown in Fig. 1.8. During the first stage In, Ga and Se are evaporated simultaneously at a substrate temperature of typically 350 - 450 °C forming an $(In,Ga)_2Se_3$ precursor. At the beginning of the second stage, the substrate is heated to an elevated temperature of 500 - 550 °C and Cu and Se are evaporated. At the end of the second stage the sample reaches Cu-rich conditions CGI $> 1$. At this moment, a CuSe phase starts growing at the surface which we will use in order to identify the point of stoichiometry (CGI $= 1$). This method, often referred to as 'end-point-detection', will be described in more detail in sec. 3.1.3. During the third stage the substrate is kept at the same temperature and In, Ga and Se are evaporated in order to reach a final Cu-poor composition of CGI $\approx 0.85$.

Among all CIGS deposition techniques, the three-stage co-evaporation process results in the highest solar cell efficiencies even though its growth mechanisms are not yet completely understood. Open questions and current research topics concerning the comprehension of the 3-stage process will be reviewed in more detail in chapter 4.

### 1.3.3. Atmospheric approaches

Atmospheric deposition methods have a general cost-advantage compared to vacuum methods but the achieved efficiencies ($\lesssim 17$ % [77, 78]) are substantially lower. In general these methods consist of two steps: The material deposition and an annealing step at temperatures similar to the vacuum-process temperatures of 500-550 °C. Explored deposition techniques are electro-deposition [79, 78], spray pyrolosis [80]

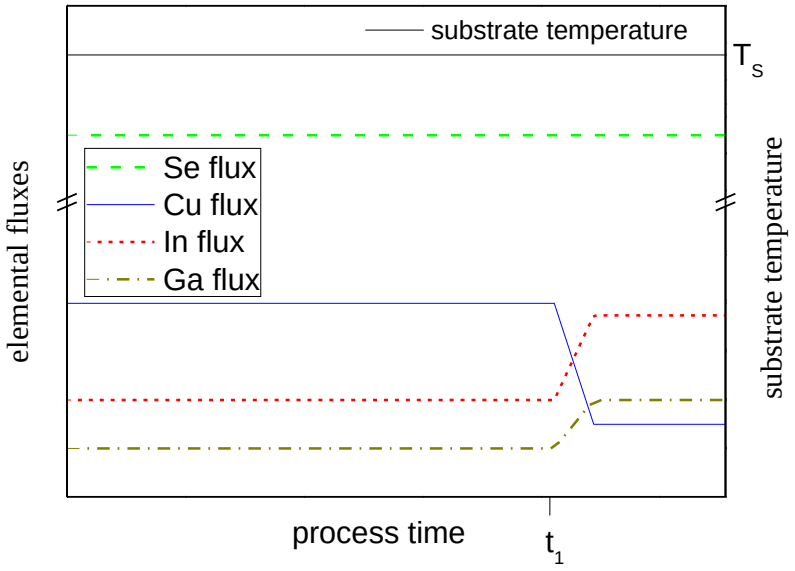


**Figure 1.7.:** Evaporation and temperature profile for the so-called boeing process. At $t_1$ the film is copper rich (GGI $\approx$ 1.2) while at the end of the process Cu-poor conditions of GGI $\approx$ 0.85 are reached. Typical substrate temperatures are 500 - 550 °C.

and spin coating [81] of precursor-consisting solutions, chemical bath deposition [82] and inkjet-printing of CIGS nanoparticles [83, 77].

## 1.4. Conclusion

In this chapter a state of the art of laboratory-scale solar cells based on CIGS has been given. The research milestones on the way from the first CIGS synthesis in 1953 to today's high efficiency devices exceeding 20 % conversion efficiencies have been exemplified with a special focus on the role of each layer in today's CIGS solar cell stack. While the technology of CIGS-based solar cells has been very successful, representing the most efficient thin film solar cells which even exceed the device performance of multi-crystalline silicon solar cells, a lot of its phenomena have not yet been understood and further research is necessary in order to completely unravel the remaining mysteries. It is interesting to note that the conversion efficiency on the cell level (Fig. 1.1) has been increasing stepwise over the years owing to certain technologic novelties: The development of the 2-step process and Na incorporation at the end of 1980's/beginning 1990's, the development of the 3-stage co-evaporation process around 1995 and very recently 2013/2014 the incorporation of potassium in a post-deposition treatment (PDT). The recent discovery of the beneficial effect of K is especially remarkable since not only the K-doping itself increases the material quality. It turned out that K-doped CIGS absorber layers can be grown with a significantly higher Ga concentration and a significantly thinner CdS buffer layer

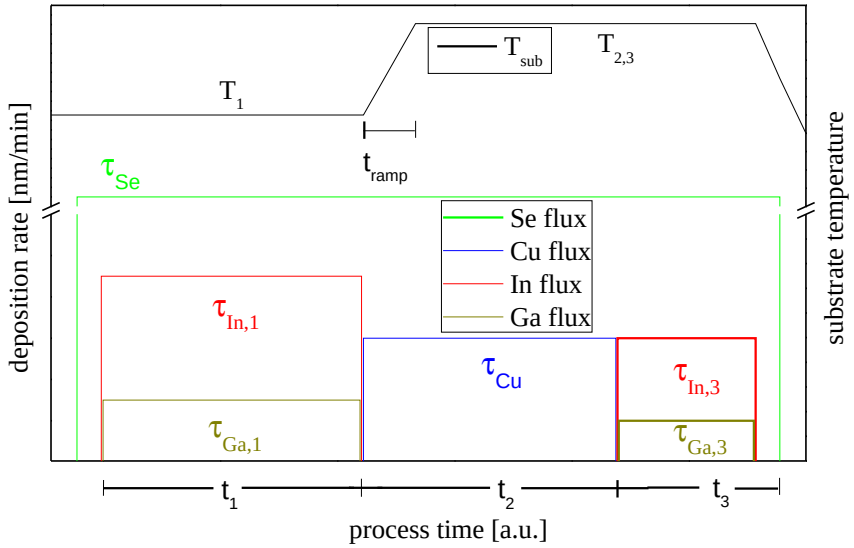


**Figure 1.8.:** Evaporation and temperature profile for the 3-stage process. At $t_2$ the film is copper rich (GGI $> 1$) while at the end of the process Cu-poor conditions of GGI $\approx 0.85$ are reached. Typical substrate temperatures are 350-450 °C during the first and 500 - 550 °C during the second and third stage.

without suffering, as it was the case without a K PDT, a large loss in performance. Due to its novelty the role of K is probably not yet completely understood and might open the door for further large efficiency increases in the near future. Considering also the possible replacement of the CdS buffer layer which reduces the achievable short circuit current density by about 2 mA/cm$^2$ by alternative materials such as Zn(O,S) or $In_2S_3$ a conversion efficiency of 25 % seems to be achievable until the end of the decade.

Naturally the industry includes research results as soon as possible in their production lines and the advancements on the cell level will have an influence few later on large-scale module efficiencies. As can be seen in Fig. 1.1 there is a correlation between cell and module level efficiencies, the module efficiency seems to follow the cell-level performance increases in a few years time lag.

# 2. Physics of the Cu(In,Ga)$Se_2$ solar cell

In this part the basic physical principles occuring during the operation of a CIGS solar cell are explained. These will be necessary in order to understand the opto-electronic device characterisation in chapter 6. The solar cell operation is divided into i) the absorption of light or in other words the transformation of a photon into an electron-hole pair which is explained in sec. 2.1, ii) the separation of the electron and hole and their extraction to two opposite contacts which is illustrated in sec. 2.2. For the second point fundamental semiconductor equations will be explained as well as the energy band structure which is essential to understand the carrier transport. In sec. 2.3 an overview about the most important recombination mechanisms that can occur during carrier transport are explained and finally in sec. 2.4 these carrier generation and transport mechanisms are linked to the solar cells current-voltage characteristic.

## 2.1. Light-absorption

In solar cells only the photons with a sufficient energy $h\nu > E_{\mathrm{g}}$ will contribute to the photocurrent $J_{\mathrm{ph}}$. Assuming no reflection at the back-surface (single-pass) and ideal separation and collection of all created electron-hole pairs, it is given by eq. 2.1 for a standard CIGS solar cell as sketched in Fig. 1.2. Thereby $\Phi_{0,\mathrm{CIGS}}$ refers to the photon flux incident to the CIGS surface and thus corresponds to the sun spectrum $\Phi_{\mathrm{AM1.5G}}$ [$\mathrm{cm^{-2}s^{-1}}$] reduced by the photon flux absorbed or reflected in the CdS and ZnO layers or at their interfaces. The CIGS layer thickness, absorption coefficient and band gap energy are given by $t_{\mathrm{CIGS}}$, $\alpha_{\mathrm{CIGS}}$ and $E_{g,\mathrm{CIGS}}$.

$$J_{\mathrm{ph,\ ideal}} = -q \int_{E_{\mathrm{g,CIGS}}}^{\infty} \Phi_{0,\mathrm{CIGS}}(h\nu) \cdot [1 - exp(- \int_{0}^{t_{\mathrm{CIGS}}} \alpha_{\mathrm{CIGS}}(z, h\nu) dz)] dh\nu \qquad (2.1)$$

While for a position-dependent absorption coefficient $\alpha_{\mathrm{CIGS}}(z, h\nu)$ (as it is the case for CIGS with a Ga gradient) the calculation of $J_{photo}$ becomes complex and can often only be solved numerically, for a homogeneous absorber layer with an ab-

sorption coefficient $\alpha_{\mathrm{CIGS}}(h\nu)$ only dependent on the incident photon energy $h\nu$ the photocurrent is a simple integral over the Beer-Lambert expression (eq. 2.2).

$$J_{\mathrm{ph,\ ideal}} = -q \int_{E_{\mathrm{g,CIGS}}}^{\infty} \Phi_{0,\mathrm{CIGS}}(h\nu) \cdot (1 - e^{-\alpha_{\mathrm{CIGS}}(h\nu)\cdot t_{\mathrm{CIGS}}}) dh\nu \tag{2.2}$$

Experimentally measured absorption coefficient for CIGS with varied Ga contents GGI are shown in Fig. 2.1 [84]. Due to its direct semiconductor nature, high values of up to $10^5 cm^{-1}$ are observed in the relevant spectral range. The shift of the band gap energy to higher energies (and thus smaller wavelengths) with increasing GGI can be well observed.

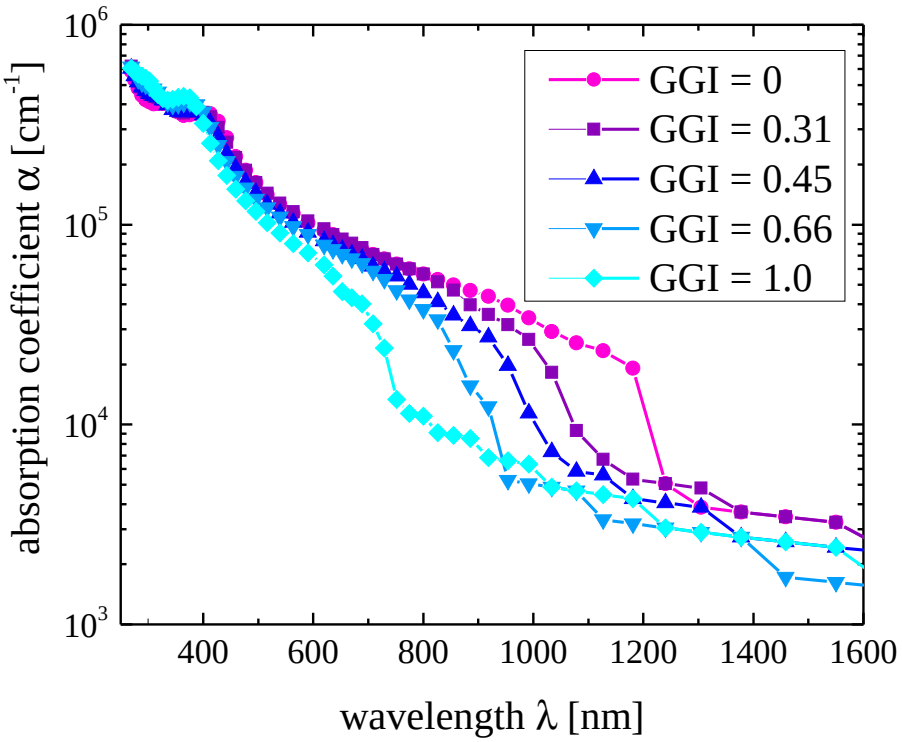


**Figure 2.1.:** Absorption coefficients for CIGS absorber layers with varied GGI ratio [84].

The light absorption can be studied with aid of the external quantum efficiency (EQE) which can be expressed by eq. 2.3 ([85]) as a function of the space charge region (SCR) width $w$ and the minority carrier diffusion length $L_{n,a}$.

$$EQE(h\nu, V) = T\,(h\nu) \left(1 - \frac{exp(-\alpha(h\nu)w}{1 + \alpha(h\nu)L_{n,a}}\right) \tag{2.3}$$

For $\alpha w \ll 1$ and $\alpha L_{n,a} \ll 1$, i.e. for low photon energies, a Taylor expansion of eq. 2.3 until the linear term leads to expression 2.4 which can be used to extract the band gap energy from the low-energy edge of the EQE . The last term follows from the direct band gap nature of CIGS which implies that the absorption coefficient is proportional to $\sqrt{h\nu - E_g}$ with the absorption constant $C$.

$$EQE = T(h\nu)\alpha(h\nu)(L_{n,a} + w) = C \cdot T(h\nu)(L_{n,a} + w)\sqrt{h\nu - E_\mathrm{g}} \tag{2.4}$$

A plot of $EQE^2$ *vs.* $h\nu$ as shown in Fig. 2.2 usually shows a linear behaviour at the low energy edge. The section of a linear fit with the abscissa corresponds to the band gap energy $E_\mathrm{g}$.

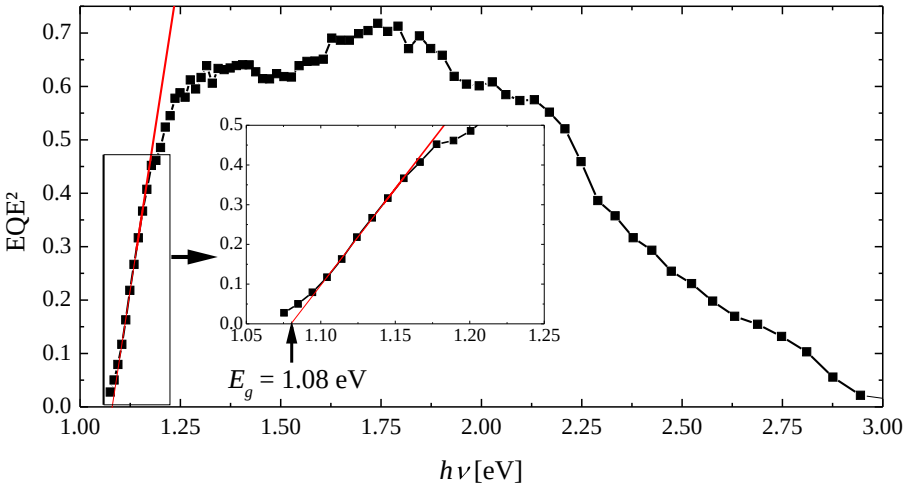


**Figure 2.2.:** External quantum efficiency as a function of incident photon energy and linear fit for the extraction of the band gap energy.

For absorber layers with a gradient of the band gap energy throughout the absorber thickness, it is not directly clear which band gap energy is measured by this method. Throughout the literature it is usually referred to as the minimum band gap in the absorber layer.

In this chapter we considered an ideal collection function $\eta_c = 1$. For real devices the collection function is inferior to 1 and a function of the applied voltage. The general expression for the photocurrent is then given by eq. 2.5 with the electron-hole pair generation rate $G$ and the collection function $\eta_c$ .

$$J_{ph}(V) = -q \int G(z)\eta_\mathrm{c}(z, V)dz \tag{2.5}$$

The loss mechanisms limiting the collection of charge carriers will be subject to the following chapter.

## 2.2. Separation and extraction of charge carriers

Once a photon is absorbed in the CIGS absorber layer, the created electron-hole pair needs to be separated and the electron and hole need to be extracted to the contacts in order to produce energy - the electron to the negative ZnO:Al front contact and the hole to the positive Mo back-contact. In order to explain the carrier extraction, three fundamental equations describing charge carrier transport in semiconductors and the energy band diagram of the Mo/CIGS/CdS/i-ZnO/ZnO:Al heterostructure will be introduced in sec. 2.2.1 and sec. 2.2.2.

### 2.2.1. Fundamental semiconductor equations

In order to understand the carrier transport and current voltage characteristics of a p/n junction, e.g. CIGS/CdS, it is useful to regard three basic semiconductor equations: The Poisson equation, the transport equation and the continuity equation both for electrons and holes as they are described for example in [20]. For simplification, we assume the p and n-type regions to be infinite sheets in the $x$-$y$ plane and regard only the $z$ direction as spatial variable.

The Poisson-equation results from the $1^{st}$ Maxwell equation and relates the local charge density $\rho(z)$ with the resulting electrostatic potential $\varphi(z)$. In case of a spatially constant dielectric function $\epsilon$, for our case the Poisson equation is given by 2.6 with the elementary charge q, hole density $p$, electron density $n$, ionised acceptor density $N_A^-$, ionised donor density $N_D^+$ and electric field component $F$ in $z$-direction. From the solution $\varphi(z)$ of this differential equation, the band diagram discussed in the following sec. 2.2.2 can be derived.

$$\frac{\partial^2\varphi(z)}{\partial z^2} = -\frac{\partial F(z)}{\partial z} = -\frac{\rho(z)}{\epsilon} = -\frac{q}{\epsilon}[p(z) - n(z) - N_{\mathrm{A}}^-(z) + N_{\mathrm{D}}^+(z)] \tag{2.6}$$

The continuity equations result from the principle of charge conversion and rely the temporal alteration of the charge carrier density ($n$ for electrons and $p$ for holes) with the gradient of the charge flux density ($J_n$ for electrons and $J_p$ for holes) . It is given for electrons in eq. 2.7 and for holes in eq. 2.8 with the generation rates $G_n$ of electrons and $G_p$ of holes and the recombination rates $U_n$ of electrons and $U_p$ of holes.

$$\frac{\partial n(z)}{\partial t} = \frac{1}{q}\frac{\partial J_n(z)}{\partial z} + G_n(z) - U_n(z) \tag{2.7}$$

$$\frac{\partial p(z)}{\partial t} = -\frac{1}{q}\frac{\partial J_p(z)}{\partial z} + G_p(z) - U_p(z) \tag{2.8}$$

The transport equation describes the electric current density resulting from a gradient of the quasi Fermi level or in other words from a gradient of the electrochemical potential of a charge carrier type. It is given for electrons in eq. 2.9 and for holes in eq. 2.10.

$$J_n(z) = \mu_n n(z) \frac{dE_{Fn}(z)}{dz} \tag{2.9}$$

$$J_p(z) = \mu_p p(z) \frac{dE_{Fp}(z)}{dz} \tag{2.10}$$

In the following section it is shown how to use the Poisson equation in order to derive the energy band diagram of a heterostructure.

## 2.2.2. Energy band diagram

The energy band structure is essential in order to understand charge carrier transport and recombination. In Fig. 2.3 the possible band diagram formation of a CIGS solar cell is shown.

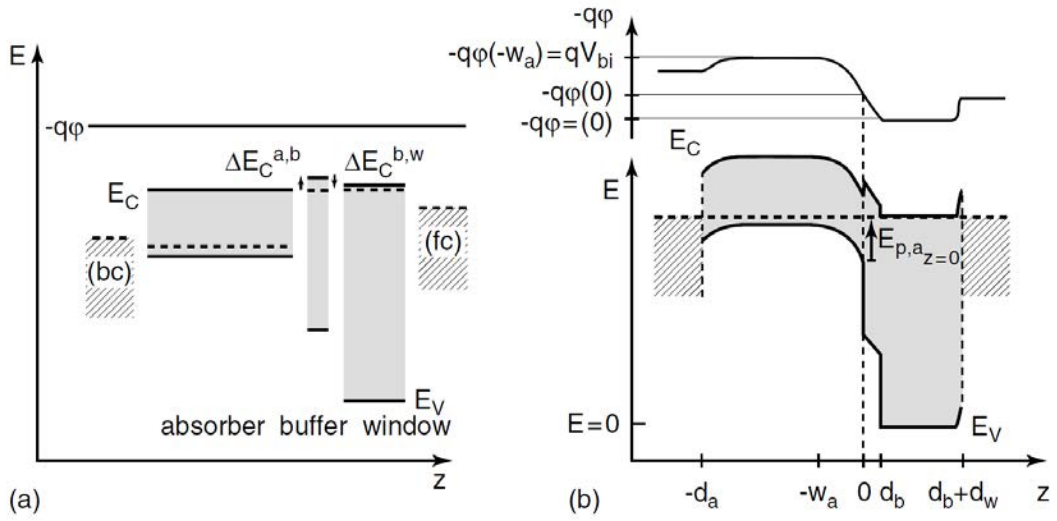


**Figure 2.3.:** Band diagram of a $p$-type absorber/ $n$-type buffer/$n$-type window structure between two metallic contacts after [20].

On the left side in (a) the different materials are shown with no contact between each other. Due to the hetero-structure nature, the layers have different band gaps and electron affinities $\chi(z) = -q\varphi(z) - E_c(z)$. When the different layers are brought to contact, the difference of the chemical potentials will lead to a carrier diffusion in the

interface-near region between absorber and buffer layer. This leads, according to the Poisson equation 2.6 to a gradient of the electric field which corresponds to a bending of the electrostatic potential energy $-q\varphi(z)$ and the conduction and valence band in the interface-near region of the absorber and in the buffer layer (which will be called space charge region or SCR). This electric field leads to a drift of charge carriers and an equilibrium is established when the electro-chemical potential, *i.e.* the fermi energy is constant throughout the whole stack. In Fig. 2.3 no localised charges at the interfaces are assumes so there is no offset in the electrostatic potential $-\varphi(z)$. The quantitative solution of $\varphi(x)$ is obtained by solution of Poisson's equation 2.6. The valence band offset $\Delta E_\mathrm{v}$ at the absorber/buffer ($z = 0$) and at the buffer/window ($z = d_\mathrm{b}$) interface is usually obtained from experiment or calculated from theory. The conduction band discontinuity corresponds to the difference of the electron affinities. For the absorber/buffer interface $\Delta E_\mathrm{c} = \chi - \chi_\mathrm{b}$ with the electron affinity $\chi_\mathrm{a}$ in the absorber and $\chi_b$ in the buffer layer. The bandgap $E_\mathrm{g}$ is often known or can be measured optically and the conduction band offset is then given by eq. 2.11.

$$\Delta E_\mathrm{c} = \Delta E_\mathrm{g} - \Delta E_\mathrm{v} \tag{2.11}$$

## 2.3. Recombination mechanisms

In thin films solar cells different recombination mechanisms exist. The most important ones are illustrated in Fig. 2.4 and will be described in this section. The formalism and the denotations are mainly adopted from [20] and [86]. While there, a theoretical description of the different recombination mechanisms and their deduction from basic semiconductor equations can be found, we will focus on their contribution to the diode current and ways to determine the dominating recombination mechanism from a measured IV curve.

The current contributions of each of the recombination mechanisms can be interpreted as distinct diodes connected in parallel. The current density contribution of each of these recombination mechanisms $i$ can be expressed by eq. 2.12 [87].

$$J_{\mathrm{diode},i}(V) = J_{0,i}[\exp\left(\frac{qV}{A_i kT}\right) - 1] \tag{2.12}$$

For $qV > 3kT$ the exponential function dominates in eq. 2.12 and thus $J_{\mathrm{diode},i}(V) = J_{0,i}\exp\left(\frac{qV}{A_i kT}\right)$. The ideality factor $A_i$ and the saturation current density $J_{0,i}$ depend on the specific recombination mechanism $i$. The latter is given by eq. 2.13.

$$J_{0,i} = J_{00,i}\exp(\frac{-E_{a,i}}{A_i kT}) \tag{2.13}$$

The activation energy $E_{a,i}$ describes the temperature dependence of $J_{0,i}$ and $J_{00,i}$ is a weakly temperature dependent prefactor. From IV chracteristics at different temperatures, the activation energy of the recombination mechanism $i$ can be extracted. Transformation of eq. 2.13 to 2.14 shows that a linear fit of $\ln(J_{0,i})$ *vs.* $\frac{1}{A_i kT}$ leads to the intercept $\ln(J_{00,i})$ and the slope $-E_{a,i}$.

$$\ln(J_{0,i}) = \ln(J_{00,i}) - \frac{E_{a,i}}{A_i kT} \tag{2.14}$$

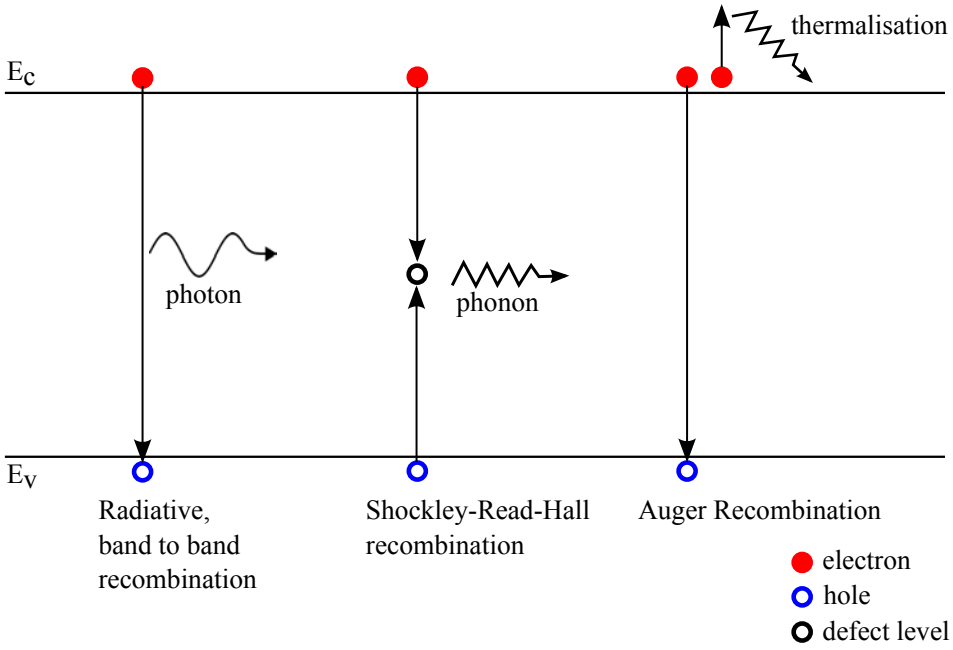


**Figure 2.4.:** Illustration of three fundamental recombination mechanisms in semiconductors. The Auger recombination mechanism is shown as a two-electron process but can also take place as a two-hole process.

### 2.3.1. Radiative band-to-band recombination

Radiative band-to-band recombination is an intrinsic recombination process in semiconductors that can not be avoided and is considered by the Shockley-Queisser limit [88]. It is the inverse process of light absorption: the annihilation of an electron and a hole under creation of a photon. Since a free electron and a free hole are necessary for this process, its rate is proportional both to the electron concentration $n$ and hole concentration $p$. The recombination rate for this process under non-equilibrium conditions given by eq. 2.15 where $B$ is the radiative recombination constant, $n_i$

the intrinsic carrier concentration and $E_{Fn}$ and $E_{Fp}$ are the quasi fermi levels for electrons and holes.

$$R = Bnp = Bn_i^2 \exp\left(\frac{E_{Fn} - E_{Fp}}{kT}\right) \tag{2.15}$$

The principle of detailed balance states that at electrochemical equilibrium, the electron (and hole) recombination rate must equal their generation rate and is thus given by the integral over the black-body emission multiplied by the absorption coefficient as stated by eq. 2.16 [86] whereas $G_n^0$ and $G_p^0$ are the equilibrium generation rates for electrons and holes respectively, $c$ is the speed of light propagation in the medium (CIGS) .

$$R = G_n^0 = G_p^0 = \int_0^\infty \alpha(\hbar\omega) dj_\gamma(\hbar\omega) = \frac{\Omega}{4\pi^3\hbar^3c^2} \int_0^\infty \frac{\alpha(\hbar\omega)(\hbar\omega)^2}{\exp\left(\frac{\hbar\omega}{kT}\right) - 1} d\hbar\omega \tag{2.16}$$

Assuming Fermi energies with some $kT$ distance from the respective band edges, the resulting recombination current density can be expressed by eq. 2.17 [86].

$$dJ_{\text{diode,rad}} = \frac{\Omega}{4\pi^3\hbar^3c^2} a(\hbar\omega) \frac{(\hbar\omega)^2}{\exp\left(\frac{\hbar\omega}{kT_0}\right) - 1} \exp\left(\frac{E_{Fn} - E_{Fp}}{kT}\right) d\hbar\omega \tag{2.17}$$

If the QFL at the contacts are taken into account, their difference corresponds to the applied voltage and a comparison of eq. 2.17 and with eq. 2.12 shows that the diode ideality factor for radiative recombination is $A_{\text{rad}} = 1$.

### 2.3.2. Auger recombination

Auger recombination is a multiple carrier process. In the most simple case, an electron from the conduction band recombines with a hole from the valence band and the released energy is transferred to a third carrier, an electron or a hole. The third carrier then relaxes thermally to the respective energy band edge, as shown for an electron in Fig. 2.4. The general recombination rate for Auger recombination is given by eq. 2.18.

$$R_{\text{Auger}} = C_p(p^2n - p_0^2n_0) + C_n(n^2p - n_0^2p_0) \tag{2.18}$$

In a $p$-type absorber under low injection conditions, *i.e.* $p \approx p_0 \approx N_{\text{A}}$, the small density of minority electrons leads to a negligible Auger excitation probability and

the Auger recombination rate is given by eq. 2.19 and the minority carrier lifetime by eq. 2.20 with $\Delta n = n - n_0$.

$$R_{\text{Auger},p} = C_p N_{\text{A}}^2 \Delta n \tag{2.19}$$

$$\tau_{\text{Aug}} = (C_p N_{\text{A}}^2)^{-1} \tag{2.20}$$

From these equation it can be seen that Auger recombination can not be completely avoided but reduced by keeping the doping density $N_{\text{A}}$ limited. In the literature, no data for the Auger coefficient $C_p$ is available. In order to roughly quantify the influence of Auger recombination, we follow the argumentation in [89] and consider the Auger coefficient $C = 10^{-30}$ cm$^6$s$^{-1}$ that results from an interpolation of values for $III - VI$ semiconductors given in [90]. Assuming an upper limit for the CIGS doping density of $N_{\text{A}} = 1 \cdot 10^{17}$ cm$^{-3}$ (typical values are rather $N_{\text{A}} = 2 \cdot 10^{16}$ cm$^{-3}$) [91] results in a lifetime of $\tau_{\text{Aug}} = 10^{-4}$ s. Since measured lifetimes are in the order of $\tau_{\text{CIGS}} \approx 10^{-9} - 10^{-7}$ s [92, 93], Auger recombination can be considered as negligible mechanism in CIGS solar cells.

### 2.3.3. Defect related recombination

Structural defects in a semiconductor can lead to energy states in between the valence and conduction band. Depending on their energetic position and cross section, they can act as efficient recombination centers. In contrast to band-to-band and Auger recombination, defect states can in principle be avoided. Defects can result in single and multiple defect levels as well as a continuous defect distribution. The case of a single defect level with a well defined energy $E_{\text{d}}$ and density $N_{\text{d}}$ has been investigated in detail by Shockley, Read and Hall and is referred to as SRH (Shockley-Read-Hall) recombination. For this case, Shockley has deduced the recombination rate given by eq. 2.21 from carrier capture and emission rates of a single defect [94].

$$R_{\text{SRH}} = \frac{np - n_i^2}{\gamma_p(n + n_1) + \gamma_n(p + p_1)} \tag{2.21}$$

The auxiliary densities $n_1$ and $p_1$ are the theoretical electron and hole densities if the Fermi level would be located at the defect energy $E_d$ and are given by eq. 2.22 and 2.23.

$$n_1 = N_{\text{C}} \exp\left(-\frac{E_{\text{g}} - E_{\text{d}}}{kT}\right) \tag{2.22}$$

$$p_1 = N_{\mathrm{V}} \exp\left(-\frac{E_{\mathrm{d}}}{kT}\right) \tag{2.23}$$

$\gamma_p$ and $\gamma_n$ are the effective lifetimes of electrons and holes and if tunneling can be excluded they are identic to the minimum lifetimes of electrons and holes $\tau_{n,0}$ and $\tau_{p,0}$.

#### 2.3.3.1. Recombination in the space charge region

The integration of $R_{\mathrm{SRH}}$ over the SCR leads to the diode current density contribution of SRH recombination in the SCR. The voltage dependence of the diode current due to defect-related recombination, expressed by the ideality factor, depends on the energetic position of the defect.

In [20] it is shown that for a single defect at midgap position, this contribution is given by eq. 2.24 where $F_{\mathrm{m}}$ is the electric field at the location of maximum recombination. The index $a$ refers to the absorber layer.

$$J_{\mathrm{diode,SRH,SCR}} = \frac{\pi kT}{2F_{\mathrm{m}}} \left(\frac{N_{c,\mathrm{a}} N_{v,\mathrm{a}}}{\tau_{n0,\mathrm{a}} \tau_{p0,\mathrm{a}}}\right)^{1/2} \exp\left(-\frac{E_{\mathrm{g}}}{2kT}\right) \exp\left(\frac{qV}{2kT}\right) \tag{2.24}$$

Thus it can be seen that for SRH recombination at a midgap state in the SCR the ideality factor is $A_{\mathrm{SRH,SCR,midgap}} = 2$ and the saturation current is $J_{0,\mathrm{SRH,SCR}} = \frac{\pi kT}{2F_{\mathrm{m}}} \left(\frac{N_{c,\mathrm{a}} N_{v,\mathrm{a}}}{\tau_{n0,\mathrm{a}} \tau_{p0,\mathrm{a}}}\right)^{1/2} \exp\left(-\frac{E_{\mathrm{g}}}{2kT}\right)$.

For a defect close to one of the energy band edges, the density $n_1$ becomes dominant ($n_1 \gg n,\ p,\ p_1$). For $qV > 3kT$ and thus $np \gg n_i^2$, eq. 2.21 simplifies to $R_{\mathrm{SCR}} = np/(\tau_{p0,\mathrm{a}} n_1)$ . Inserting eq. 2.22 shows that for SRH recombination at a defect close to one of the band edges in the SCR leads to an ideality factor of $A_{\mathrm{SRH,SCR,edge}} = 1$ and a saturation current activation energy of $E_{\mathrm{a,SRH,SCR}} = E_{\mathrm{g}} - E_{\mathrm{d}}$.

It is furthermore shown in [20] that for a defect between the band edge and midgap in the SCR, the ideality factor will not lie inbetween 1 and 2 but continually change from 1 to 2 for an increasing voltage bias.

#### 2.3.3.2. Recombination in the quasi neutral region

In the QNR in contrast, both deep and shallow defect levels lead to an ideality factor of $A_{\mathrm{SRH,QNR}} = 1$. The physical reason for that is that in the QNR only the QFL $E_{\mathrm{F}n}$ for electrons varies with voltage for low and medium voltages while in the SCR it is both $E_{\mathrm{F}n}$ and $E_{\mathrm{F}p}$.

#### 2.3.3.3. Back-surface recombination

In order to reach the back-surface, injected electrons need to pass the front-interface and diffuse through the whole absorber layer without recombining. Dullweber *et al.* [95] use the effective diffusion length $L_{\text{eff}}$ given by eq. 2.25 [96], which takes into account the back-interface recombination velocity $s$ and describe the saturation current density by expression 2.26 [97].

$$L_{\text{eff}} = L_{n,\text{a}} \frac{1 + (sL_{n,\text{a}}/D)\tanh(d/L_{n,\text{a}})}{(sL_{n,\text{a}}/D) + \tanh(d/L_{n,\text{a}})} \tag{2.25}$$

Thereby $d$ is the absorber layer thickness, $L$ the bulk diffusion length and $D$ the bulk diffusion constant.

$$J_0 \approx q \frac{D N_{\text{c}} N_{\text{v}}}{N_{\text{A}} L_{\text{eff}}} \exp(-E_{\text{g}}/kT) \tag{2.26}$$

Expression 2.26 will be used for the discussion of the back-surface gradient in sec. 6.1.

#### 2.3.3.4. Interface recombination

The recombination rate for SRH recombination at the front interface is given by eq. 2.21. In this case, the unit of R is $\text{cm}^{-2}\text{s}^{-1}$. The diode current for interface recombination is simply given by eq. 2.27.

$$J_{\text{diode,SRH,IF}} = qR_{\text{SRH,IF}} \tag{2.27}$$

The detailed recombination mechanism depends on the nature of the interface: Is the interface a type 1 or type 2 interface? Are the defects present at the interface deep or flat defects? Are one or both fermi levels pinned at the interface? Is the recombination enhanced by tunneling?

Here we will only consider a relatively specific case but which is the case of a CIGS solar cell. It is defined by the following two assumptions:

1. Deep defects dominate recombination at the interface. Therefore the auxiliary carrier densities become negligible: $n_1 \ll n$ and $p_1 \ll p$.
2. The buffer layer is highly $n$-type as compared to the $p$-type absorber layer. The electron density governing the recombination is thus given by $n_{\text{b},z=0} = N_{\text{D},w} \gg p_{\text{a},z=0}$.

The above mentioned assumptions 1 and 2 simplifiy eq. 2.21 to 2.28.

$$R_{\text{SRH,IF}} = \frac{p_{\text{a},z=0}}{\gamma_p} \tag{2.28}$$

It is shown in [20] that the recombination rate and the diode current across the interface depend on the type of the interface: An interface of type 1 is given when both conduction band minimum and valence band maximum at the interface belong to the same material. If this is not the case, the interface is of type 2. At the absorber/buffer layer interface for CIGS solar cells, the valence band offset is usually positive: $\Delta E_\mathrm{v} > 0$. This means that a positive conduction band offset $\Delta E_c > 0$ corresponds to a type 1 interface and a negative conduction band offset $E_\mathrm{c} < 0$ corresponds to a type 2 interface.

**Type 1 interface:** $\Delta E_\mathbf{c} > 0$ As shown by eq. 2.27, the diode current density for interface recombination can easily be calculated from the recombination rate, given by eq. 2.28. Following the argumentation in [20], the effective hole lifetime for interface recombination equals the inverse interface recombination velocity: $\gamma_p = S_{p,0}$ and the hole concentration in the absorber is given by eq. 2.29.

$$p_{\mathrm{a},z=0} = N_{\mathrm{A,a}} \exp\left(\frac{-E_{\mathrm{g,a}} + E_{\mathrm{p,a}} + E_{\mathrm{n,b}} + qV}{kT}\right) \tag{2.29}$$

The replacement $\exp\left(\frac{E_{\mathrm{n,b}}+E_{\mathrm{p,a}}}{kT}\right) = \frac{N_{\mathrm{c,b}}N_{\mathrm{v,a}}}{N_{\mathrm{D,b}}N_{\mathrm{A,a}}}$ leads to expression 2.30 for the diode current density due to SRH recombination at a type 1 interface with the densities of states $N_{c,b}$ in the conduction band of the buffer layer and $N_{\mathrm{v,a}}$ in the valence band of the absorber layer.

$$J_{\mathrm{diode,SRH,IF1}} = qS_{p0}N_{\mathrm{A,a}}\left(\frac{N_{\mathrm{c,b}}N_{\mathrm{v,a}}}{N_{\mathrm{D,b}}N_{\mathrm{A,a}}}\right)^{1/A} \exp\left(-\frac{E_{\mathrm{g,a}}}{kT}\right) \exp\left(\frac{qV}{kT}\right) \tag{2.30}$$

The saturation current density is thus given by eq. 2.31, the activation energy is the absorber band gap energy and the ideality factor is $A_{SRH,IF1} = 1$.

$$J_{0,SRH,IF1} = qS_{p0}N_{\mathrm{A,a}}\left(\frac{N_{\mathrm{c,b}}N_{\mathrm{v,a}}}{N_{\mathrm{D,b}}N_{\mathrm{A,a}}}\right)^{1/A} \exp\left(-\frac{E_{\mathrm{g,a}}}{kT}\right) \tag{2.31}$$

**Type 2 interface:** $\Delta E_\mathbf{c} \leq 0$ At this kind of interface, the activation is smaller than the CIGS bandgap at the interface. The hole density in the absorber layer at the interface is slightly modified as compared to the type 1 interface and given by eq. 2.32.

$$p_{\mathrm{a},z=0} = N_{\mathrm{A,a}} \exp\left(\frac{-E_{\mathrm{g,IF}} + E_{p,\mathrm{a}} + E_{n,\mathrm{b}} + qV}{A_{\mathrm{SRH,IF2}}kT}\right) \tag{2.32}$$

In analogy to the case 1 interface this leads to a diode current density for recombiantion at deep defects of a type 2 interface given by eq. 2.33.

$$J_{\mathrm{diode,SRH,IF2}} = qS_{p0}N_{\mathrm{A,a}}\left(\frac{N_{\mathrm{c,b}}N_{\mathrm{v,a}}}{N_{\mathrm{D,b}}N_{\mathrm{A,a}}}\right)^{1/A_{SRH,IF2}} \exp\left(-\frac{E_{\mathrm{g,IF}}}{A_{\mathrm{SRH,IF2}}kT}\right) \exp\left(\frac{qV}{A_{\mathrm{SRH,IF2}}kT}\right) \quad (2.33)$$

In this case, the saturation current density is thus given by eq. 2.34 and the activation energy is the interface band gap $E_{\mathrm{g,IF}} = E_{\mathrm{g,a}} + \Delta E_{\mathrm{c}}$. Theoretical calculations have shown that the ideality factor $A_{\mathrm{SRH,IF2}}$ for an absorber/buffer/window layer structure depends amongst others on the buffer layer thickness [98] and increase from 1 to about 1.5 for a CdS thickness variation from 0 to 50 nm.

$$J_{0,\mathrm{SRH,IF2}} = qS_{p0}N_{\mathrm{A,a}}\left(\frac{N_{\mathrm{c,b}}N_{\mathrm{v,a}}}{N_{\mathrm{D,b}}N_{\mathrm{A,a}}}\right)^{1/A_{SRH,IF2}} \exp\left(-\frac{E_{\mathrm{g,IF}}}{A_{\mathrm{SRH,IF2}}kT}\right) \quad (2.34)$$

The conduction band discontinuity $\Delta E_{\mathrm{c}} \leq 0$ furthermore is a barrier for the electron transport from the buffer to the absorber layer. Transport over potential barriers can be described by thermionic emission (TE) theory. In [20] the saturation current density for electron transport over a potential barrier $\Delta E_{\mathrm{c}}^{\mathrm{b,a}}$ between buffer and absorber layer is given by eq. 2.35.

$$J_{0,\mathrm{TE}} = \frac{1}{4}qv_{n,p}N_{\mathrm{c,a}}exp\left(-\frac{\Delta E_{\mathrm{c}}^{\mathrm{b,a}}}{kT}\right) \quad (2.35)$$

### 2.3.4. Conclusion

All the recombination mechanisms given in this section are active in CIGS solar cells. Nevertheless in most cases one of these mechanisms will dominate the recombination. For processes with an identical ideality factor, the process with the highest saturation current density $J_0$ dominates the diode current independent of the applied voltage. For mechanisms with different ideality factors, the dominating recombination mechanism can change with the applied voltage. In general, low ideality factors dominate for high voltages while high ideality factors dominate the diode current at low voltages. An overview of the activation energies $E_a$ and diode ideality factors $A$ for different recombination mechanisms is given in Tab. 2.1.

## 2.4. Current-voltage characteristic

The current-voltage characteristic of a solar cell under illumination can be described by eq. 2.36. This sum of the diode-current under illumination $J_{\mathrm{diode}}$ and the voltage-

| Rec. mech. | Loc. | $E_a$ [eV] | A |
|---|---|---|---|
| Band-to-band | SCR | $E_g$ | 1 |
| | QNR | $E_g$ | 1 |
| SRH | SCR midgap | $E_g/2$ | 2 |
| | SCR flat | $E_g - E_d \approx E_g$ | 1 |
| | QNR | | 1 |
| | interface | $E_{g,IF}$ | $\approx 1$ |

**Table 2.1.:** Activation energy $E_a$ and diode ideality factor A for different recombination mechanisms. Assumptions and approximations are explained in the text.

dependent photo-current is called, according to [20], superposition principle. The diode current thereby differs in general in the dark and under illumination.

$$J_{light}(V) = J_{diode}(V) + J_{photo}(V) \tag{2.36}$$

Please note that the superposition principle is different from the shifting approximation in which the current under illumination is the sum of the dark current shifted by the (constant) short circuit current. This approximation is not necessarily valid for CIGS solar cells as we will see in sec. 6.2.3.1 and sec. 6.2.3.2.

The diode current $J_{diode}$ in eq. 2.36 through a p-n diode or a CIGS solar cell more precisely is due to the recombination of injected electrons and holes. Since several recombination mechanisms are active in parallel, it is given by the sum of the diode currents for each recombination process as given in eq. 2.37

$$J_{diode} = \sum_i J_{0,i} \exp\left(\frac{qV}{A_i kT}\right) \tag{2.37}$$

In practice, it is not possible to deduce all the contributing recombination mechanisms from a measured IV curve. It is rather common to fit the IV curve to a model of one or two diodes and extract informations about the dominating recombination mechanism from the diode parameters. In Fig. 2.5, a typical current-voltage characteristic of a standard CIGS solar cell is shown in semi logarithmic scale. For relatively low voltages (zone A), the current is limited by the parallel resistance ($J \approx V/R_p$). For higher voltages (zone B), the injected charge carriers recombine through different recombination mechanisms and the current density increases thus exponentially according to eq. 2.12. With increasing current density, resistive losses described by the series resistance $R_s$ appear and at too high voltages (zone C) dominate the current density.

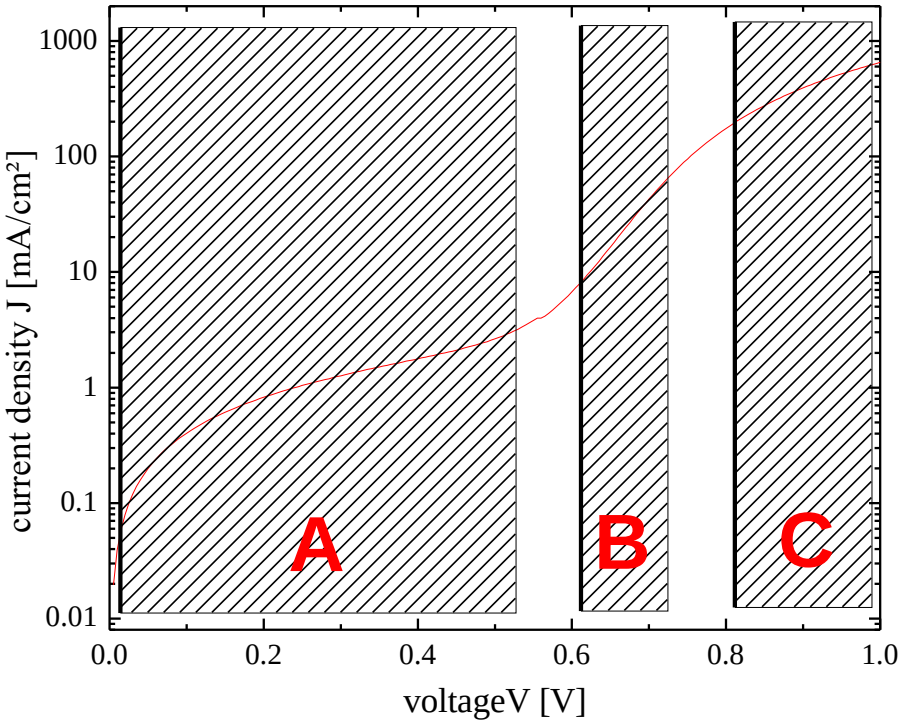


**Figure 2.5.:** Current voltage characteristic in the dark in a semi logarithmic scale of a classic CIGS solar cell. Region A is dominated by the parallel resistance $R_p$, region B by the diode behaviour of the p/n junction and region C by the series resistance $R_s$.

In region B, the current density is dominated by the diode character of the solar cell. Even though theoretically all the prevalent recombination mechanisms with different diode parameters can contribute to the current density in this region of the IV curve, in practice one describes the IV curve by an effective, macroscopic diode. If one mechanism dominates the recombination, the macroscopic diode parameters are identical with those of the specific microscopic recombination mechanism. For thin film solar cells usually one diode or two parallel diodes are chosen to describe the IV curve. Furthermore, the photocurrent in those models is independent of the applied voltage and the diode current is the same under illumination or in the dark, corresponding to the shifting approximation (the IV curve is shifted by the constant photocurrent under illumination).

### 2.4.1. 1-diode model

In the 1-diode model, the ideality factor is variable and represents somehow the mean ideality factor of all recombination processes. The current density under

illumination and voltage bias is given by eq. 2.38

$$J(V,T) = J_0(T) \cdot \left[\exp\left(\frac{q(V - R_s J(V,T))}{AkT}\right) - 1\right] - J_{sc} - \frac{V}{R_p} \tag{2.38}$$

If the current density is dominated by the diode behaviour (as in zone B in Fig. 2.5), the series and parallel resistance can be neglected. For $qV > 3AkT$, this leads to the approximation in eq. 2.39.

$$J(V,T) \approx J_0(T) \cdot \exp\left(\frac{qV}{AkT}\right) - J_{sc} \tag{2.39}$$

The ideality factor $A$ and saturation current density $J_0$ depend, as explained in sec. 2.3 on the dominating recombination mechanism. In order to extract the saturation current density $J_0$, the diode ideality factor $A$ and the series and parallel resistances $R_s$ and $R_p$ from a measured IV curve, the dark IV characteristic can be fitted to eq. 2.38 with $J_{sc} = 0$ using for example a least square fit method. If, as seen in zone B in Fig. 2.5, a region of the IV characteristic is dominated only by the diode behaviour and not by $R_s$ or $R_p$, eq. 2.39 can be transformed to eq. 2.40. For a constant temperature T, a linear fit of $\ln(J)$ *vs.* $V$ yields to $\ln(J_0)$ (intercept) and $\frac{e}{nkT}$ (slope) and $J_0$ and $A$ can be extracted.

$$ln(J(V,T)) = ln(J_0(T)) + \frac{qV}{AkT} \tag{2.40}$$

Eq. 2.41 describes the thermally activated dark saturation current density $J_0$as a function of its activation energy $E_a$and the prefactor $J_{00}$. Reorganisation to eq. 2.42shows that a linear fit of $\ln(J_0)$ *vs.*$1/(AkT)$ yields the intercept $\ln(J_{00})$ and the slope $-E_a$.

$$J_0 = J_{00} \exp\left(-\frac{E_a}{AkT}\right) \tag{2.41}$$

$$\ln(J_0) = \ln(J_{00}) - \frac{E_a}{AkT} \tag{2.42}$$

Under illumination at $V = V_{oc}$ ($J = 0$), eq. 2.39 with 2.41 can be transformed to eq. 2.43. This allows to estimate the activation energy $E_a$ from a $V_{oc}$ *vs.* $T$ plot.

$$qV_{oc} = E_a - AkT \cdot \ln\left(\frac{J_{sc}}{J_{00}}\right) \tag{2.43}$$

### 2.4.2. 2-diode model

The two diodes of this model are set to fix ideality factors of $A_1 = 1$ and $A_2 = 2$ and represent each the recombination mechanisms correlated with the corresponding ideality factor (see Fig. 2.4). The current density is given by eq. 2.44.

$$J(V,T) = J_{0,1}(T) \cdot \left[\exp\left(\frac{q(V - R_\mathrm{s}J(V,T))}{kT}\right) - 1\right] + J_{0,2}(T) \cdot \left[\exp\left(\frac{q(V - R_\mathrm{s}J(V,T))}{2kT}\right) - 1\right] - J_\mathrm{sc} - \frac{V}{R_\mathrm{p}} \quad (2.44)$$

In the diode dominated region (region B in Fig. 2.5) and for $qV > 3kT$, eq. 2.44 can be simplified to eq. 2.45.

$$J(V,T) = J_{0,1}(T) \cdot \exp\left(\frac{qV}{kT}\right) + J_{0,2}(T) \cdot \exp\left(\frac{qV}{2kT}\right) - J_\mathrm{sc} \quad (2.45)$$

Similar to the 1-diode model, the diode parameters can be extracted from a least square fit of the dark IV characteristic with $J_\mathrm{sc} = 0$. In this model, the free parameters (in addition to $R_\mathrm{s}$ and $R_\mathrm{p}$) are the saturation current densities $J_{0,1}$ and $J_{0,2}$ for the recombination currents with ideality factors of 1 and 2. Using their temperature dependence according to eq. 2.41, the activation energies for the respective saturation currents (and the corresponding recombination mechanisms) can be calculated seperately for $A = 1$ and $A = 2$.

In practice ideality factors $A > 2$ can be observed in which case the 2-diode model is not appropriate. In chapter 6 we therefore used both of the models, each for a different set of samples.

## 2.5. Conclusion

The physics of light absorption, charger carrier transport and recombination has been described for a solar cell in general. Then, the recombination mechanisms in the case of a CIGS solar cell have been explained. In order to achieve analytical expressions for the recombination rates and resulting diode currents, several assumptions about the doping densities in the absorber and buffer layers, the Fermi level throughout the junction and the sample thickness compared to the diffusion length have been made. In practice, due to the complex nature of the quaternary absorber layer, these assumptions are often not fullfilled by CIGS solar cells. Compositional gradients and a possibly doping type-inverted CIGS surface further complicate the analysis. Nevertheless, the extracted parameters from fittings of the IV curve to a 1 or 2 diode equivalent circuit model can reveal the loss mechanisms in this type of solar cell and will be used throughout this thesis, in particular in sec. 6.2.

# 3. Experimental Setups and methods

In this part the different experimental methods and setups used for this work are explained and the setup parameters are given. The co-evaporation reactor is handled in sec. 3.1 with a particular focus on the measurement of the correct substrate temperature. Since my work is focused on the fabrication of the absorber layer, the deposition parameters for the contact and buffer layers are given only briefly in sec. 3.2. This part is completed by the experimental setups for material as well as opto-electronic cell characterization in Appendix A and Appendix B.

## 3.1. The co-evaporation reactor

The CIGS films described in this thesis have been fabricated in a commercial co-evaporation system developed by the company *MBE-Komponenten, Erlangen, Germany*, shown in Fig. 3.1.

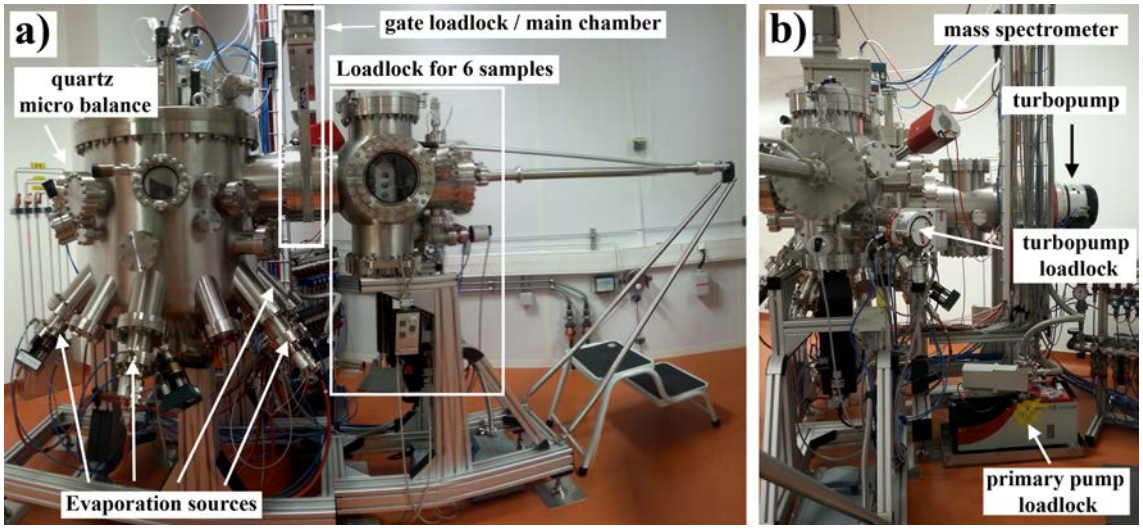


**Figure 3.1.:** Frontview (a) and sideview (b) of the co-evaporation reactor used throughout this thesis.

The film fabrication takes place in a high-vacuum chamber (sketched in Fig. 3.2) at working pressures in the order of $10^{-7}$ mbar which is connected via a valve to a load lock in which up to six 10x10 cm$^2$ substrates can be stored at similar pressures. Both the main chamber and the loadlock are evacuated by turbopumps reinforced

by primary pumps. The high-vacuum chamber contains separate effusion cells for each of the elements. These cells are thermally heated and their temperature is controlled by thermocouples. The deposition rates can be controlled by varying the effusion cell temperature and are calibrated with a quartz micro-balance before each deposition. For qualitative process control a mass spectrometer is installed at the back of the machine. The substrate is mounted face-down (towards the effusion cells) on a heating block in order to heat the sample during CIGS fabrication. The temperature is controlled by a thermocouple in between the heating-block and the sample, which for mechanical reasons (the substrate is turning in-plane for a better lateral homogeneity) cannot touch the sample. This induces a systematic experimental error which has been corrected for by substrate temperature measurements with an infra-red camera, described in sec. 3.1.2.

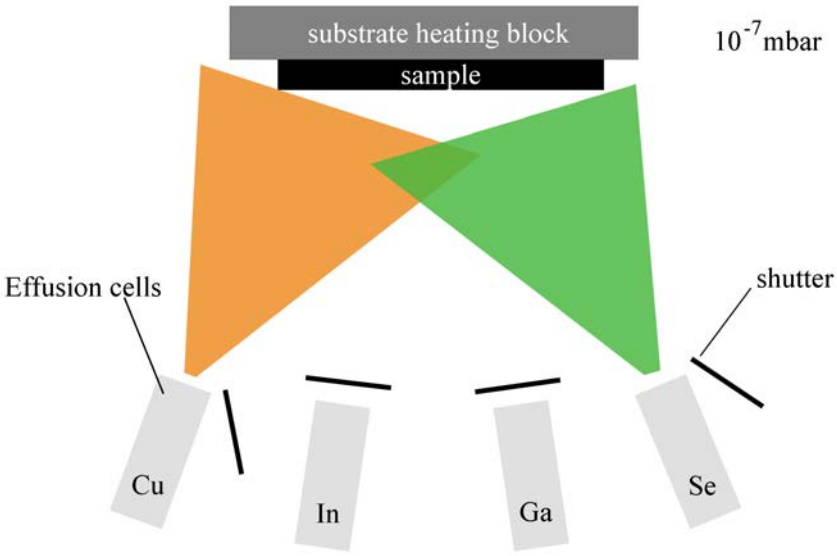


**Figure 3.2.:** Schematic of the co-evaporation system used for CIGS film fabrication.

### 3.1.1. Deposition parameters

Throughout this work we did not change all possible deposition parameters. We focused on the ones we think are important and left constant the ones we think are few important or are already set to an optimum for our evaporation-system. We did not intentionally change the pressure in the deposition-chamber. The pump-frequency was left constant at its maximum value of 630 Hz leading to pressures in the order of about $10^{-6}$ mbar during deposition, slightly changing with substrate temperature and deposition rates. We always used the same type of soda-lime glass substrate. Small differences due to the time of storage before its use can

not be completely excluded and due to the importance of Na-diffusion from the glass into the CIGS, as discussed in sec. 1.2.1, might be one reason for a reduced reproducibility. The deposition parameters we changed are essentially the substrate temperature and the deposition rates of Cu, In, Ga and Se. Since these parameters are continuous functions of time, the parameter-room is theoretically infinite. But throughout this work, if not specified otherwise, we used a so-called 3-stage process. During each of the 3 stages the parameters are kept constant, as can be seen in Fig. 1.8 in sec. 1.3.2.3, ending up with a limited number of parameters. The 3-stage process and the reason we chose to use it for the CIGS deposition are explained in chapter 4.

#### 3.1.1.1. Incertitude

Even though the thermal co-evaporation system allows for high process control, certain sources of uncertitude exist and may potentially reduce the repeatability from one process run to another. While the problem of measuring the correct substrate temperature is adressed in the following chapter, here we will focus on the deposition rates. The Se deposition rate is kept constantly in excess thus it is less critical, the most important deposition rates which will influence the [Cu]/([Ga]+[In]) and [Ga]/([Ga]+[In]) ratios of the absorber layer are the metal deposition rates. Prior to the process, the deposition rates applied throughout the process are assigned to a evaporation source temperature. Throughout the process, this correlation is considered to stay constant. This implies two basic error sources:

1. The consumption of source material leads to a changing charge level of the different sources throughout the process. This results in a changed thermodynamic state and finally changes the deposition rate. We estimate this error to result in a deposition rate uncertainty of $\pm 0.20$ nm/min throughout one process.

2. The radiative heat-exchange between the evaporation sources. While the initial deposition rate calibration takes this into account, the source temperatures are changed throughout the process by several tens of K. The change in emitted heat-radiation absorbed by another source can slightly modify the temperature of the second source. The induced uncertainty in this case is estimated as $\pm 0.15$ nm/min.

The total deposition flux uncertainty is thus estimated to be $\pm 0.35$ nm/min. For typical deposition rates of between 5 and 10 nm/min this corresponds to a relative error between 3.5 and 7 %. This uncertainty for the deposition fluxes is directly correlated to the uncertainty of the final sample composition and needs to be accounted for when interpreting certain results.

## 3.1.2. Substrate temperature calibration

In our CIGS deposition reactor, the substrate temperature is measured by a thermocouple that is located between the heating block and the substrates back-side (see Fig. 3.2). Due to the rotation of the substrate holder, the thermo-couple cannot be fixed to the surface and therefore has no perfect thermal contact to the sample. Furthermore, it is mounted close to the back-surface of the usually 3mm thick glass substrate, whose temperature might be different to the temperature in the CIGS film of some micrometers on the top-surface. This is why we measured the actual front-side CIGS temperature with an infrared (IR) camera.

The basis for the measurement of the surface temperature with an IR camera is the Stefan-Boltzmann law that states that the emitted radiation power from a black-body is proportional to the fourth exponent of its temperature $T$. Since our sample is not a black body we have to account for and measure the sample emissivity $\epsilon$. The results are given in the following.

### 3.1.2.1. Measuring the substrate emissivity

The emissivity has been measured at different temperatures for graphite, 3 mm soda-lime glass, bulk Mo, Mo on glass and CIGS on Mo on glass. The different samples were heated in a furnace and a wavelength-independent value for the emissivity was calculated by user of the commercially available software *ThermaCAM Researcher Professional 2.10* by *FLIR Systems*. For illustration, the IR images at 400°C are shown in Fig. 3.3. It can already be seen that Mo on glass and the glass/Mo/CIGS stack have a much lower emissivity than the graphite, glass and Mo bulk samples. It must be noted though that the Mo bulk and the Mo on glass layers oxidised during the experiment which became optically visible at around 300-400 °C. The emissivity values for the glass/Mo and glass/Mo/CIGS layers serve as input parameters for the substrate temperature measurements afterwards.

The resulting emissivities are shown in Fig. 3.3. In the interesting temperature range of 200 - 500 °C, all emissivities are rather constant except for Mo on glass. We attribute its emissivity at 500°C to surface-oxidation which is visible to the eye due to a change in color to dark brown or black. The slight increase of emissivity for the glass/Mo/CIGS layer (CIGS 160) at 500 °C might as well be due to oxidation, that is why we use the mean value $\epsilon_{CIGS} = 0.138$ between 200 and 400°C for the substrate temperature measurements of CIGS.

The measured values for the emissivity are in the following used in order to estimate the actual substrate temperature with the IR camera.

### 3.1.2.2. Measuring the substrate temperature

A continuous measurement by the infra-red camera during all our deposition processes is not practicable due to the pollution of the window-glass (ZnSe) by Se.

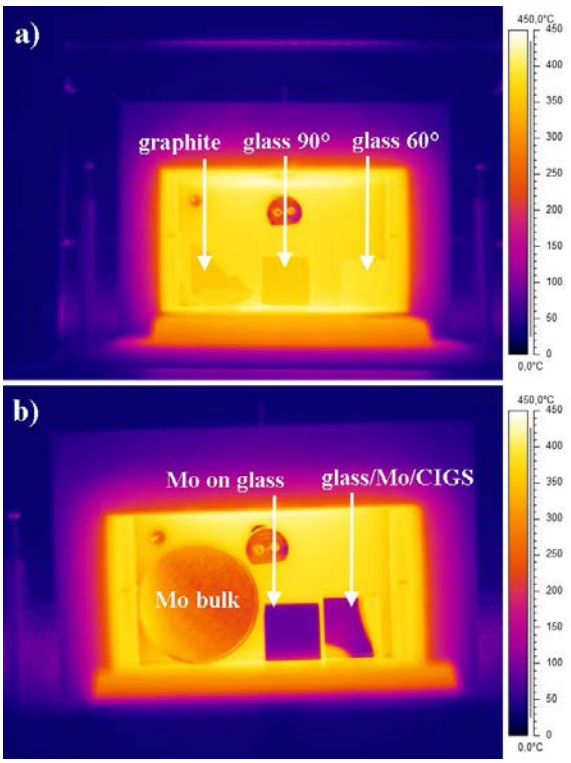


**Figure 3.3.:** Examplatory infrared images with supposed emissivities of 1 of a) graphite and glass substrates at 90° and 60° inclination angles as well as b) bulk Mo, Mo on glass and a glass/Mo/CIGS stack. The furnace was in both cases heated and left stable for about 20 min at 400 °C. The images were aquired immediately (< 1 s) after opening.

Therefore we measured a calibration curve between the imposed temperature $T_1$ of the heating block and the temperature $T_{IR}$ measured by IR as well as the temperature $T_2$ measured by the thermocouple very close to the sample back side and $T_{IR}$. A plot of the differences $T_{IR} - T_2$and $T_{IR} - T_1$ is shown in Fig. 3.5. It can be seen that in the temperature range of $T_1$ between 200 and 425 °C, where we deposit most of our CIGS samples, the difference $T_{IR} - T_2$ is fairly constant at 100 - 107 °C and $T_{IR} - T_1$varies between 75 and 95 °C. For higher substrate temperatures, both differences decline.

The results from this section will be used in this work and the indicated substrate temperatures are the ones corrected by this method.

#### 3.1.2.3. Discussion and conclusion

The accuracy of the temperature measurements with our IR camera is supported by two observations. The first is the observation of the glass deformation at 577°C while the glass melting point is indicated to be 562°C by the producer. Secondly, as described in more detail in sec. 4.4.1, we believe to observe a liquid $Cu_{2-x}$ Se phase

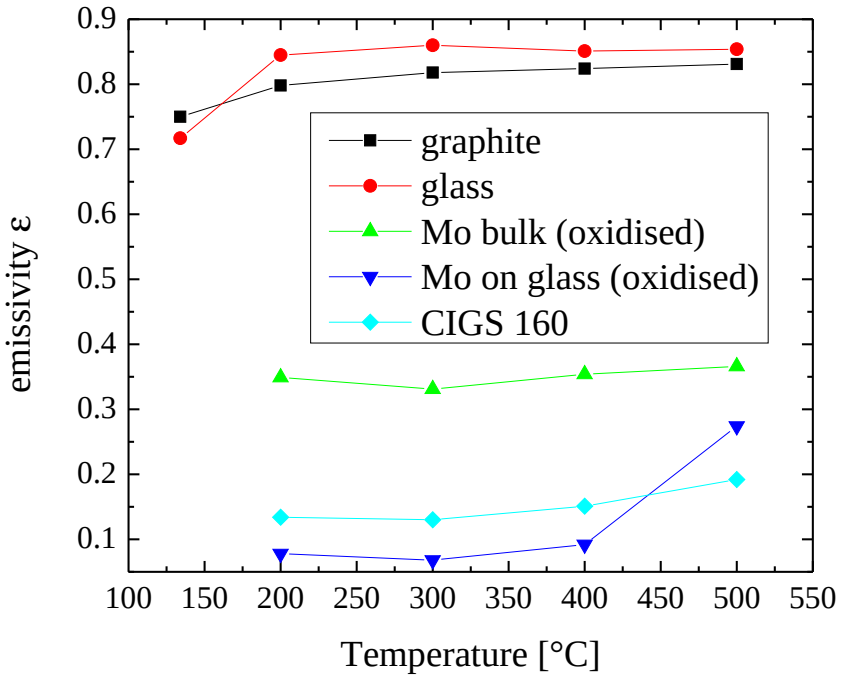


**Figure 3.4.:** Wavelength-independant emissivities for different samples at different temperatures as calculated with *ThermaCAM Researcher Professional 2.10* (*FLIR Systems*) from IR images of heated samples.

at 540°C while for 520°C it is prevalent in a solid state. This corresponds well with a reported melting temperature of 532 °C of $Cu_{2-x}Se$ in the literature [99].

Facing the general problem of measuring the substrate temperature in a reaction chamber in vacuum, IR thermography is a useful and established method. We find a quite large offset of up to 100 °C between the corrected and the nominal substrate temperature measured by a thermocouple. While for process optimisation it is not essential for scientific research, the knowledge of the correct substrate temperature is necessary.

Further in-situ IR measurements during the CIGS deposition might be of interest for example to observe the change of the sample emissivity due to the formation of $Cu_{2-x}Se$ at the end of the second stage. We used the signal from the thermocouple to detect the formation of this phase. This method is referred to as end-point detection and will be explained in the following section.

### 3.1.3. End-point detection

As will be explained in detail in chapter 4, the key-element of the 3-stage process is the transition from Cu-poor to Cu-rich and then back from Cu-rich to Cu-poor stoichiometry. This is achieved by control of the Cu, In and Ga deposition rates. In order to detect the stoichiometric transitions and know when to close the Cu and

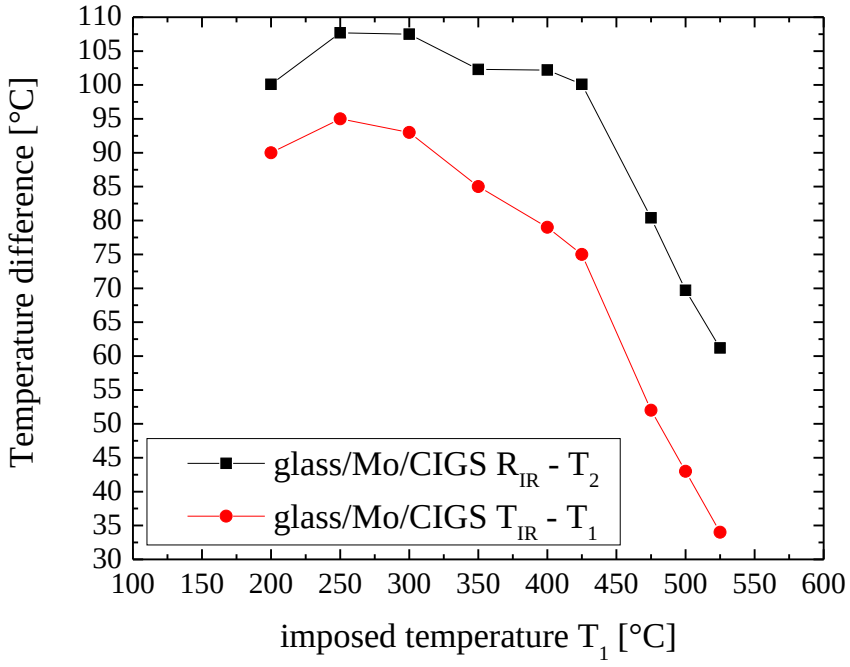


**Figure 3.5.:** Difference between the temperatures detected by the thermocouple ($T_1$ and $T_2$) and the substrate temperature measured by the IR camera.

open the Ga/In evaporation sources and for the transition back to Cu-poor conditions to shut the In/Ga sources and re-open the Cu source, we applied the so-called end-point detection method [100, 101]. This method is based on the measurement of the substrate temperature by a thermocouple and/or the substrate heating power. A typical graph of these two measures throughout the 3-stage process is shown in Fig. 3.6.

We will focus here on the stoichiometric transitions mentioned above. At the beginning of the second stage the sample is Cu-free ($CGI = 0$). During the evaporation of Cu and Se the sample reaches stoichiometry ($CGI = 1$) at a certain moment $t_1$. At this point, a $Cu_{2-x}Se$ surface layer forms (described in more detail in sec. 4.4.1) which changes the thermal behaviour of the sample. It has been shown in several works [102, 103, 104] that the emissivity for samples with a $Cu_{2-x}Se$ surface layer ($CGI > 1$) increases as compared to pure Cu(In,Ga)$Se_2$ ($CGI < 1$) samples. For a recent investigation of the optical properties of CIGS and $Cu_{2-x}Se$ the reader is referred to Schöldström et. al [105]. The increase of the emissivity in particular in the infra-red region leads to an effective cooling of the sample which can be clearly seen at $t_1$ in Fig. 3.6b. Since there is a control loop feedback between the substrate heating power and the sample temperature, the output power is increased quickly after. In the following the temperature decreases further while the output power increases. If one regards in detail the temperature signal it can be seen that after a concave beginning it decreases linearly with time. At a point we refer to as $t_2$ the slope changes and the temperature decreases in a concave form. In order to be

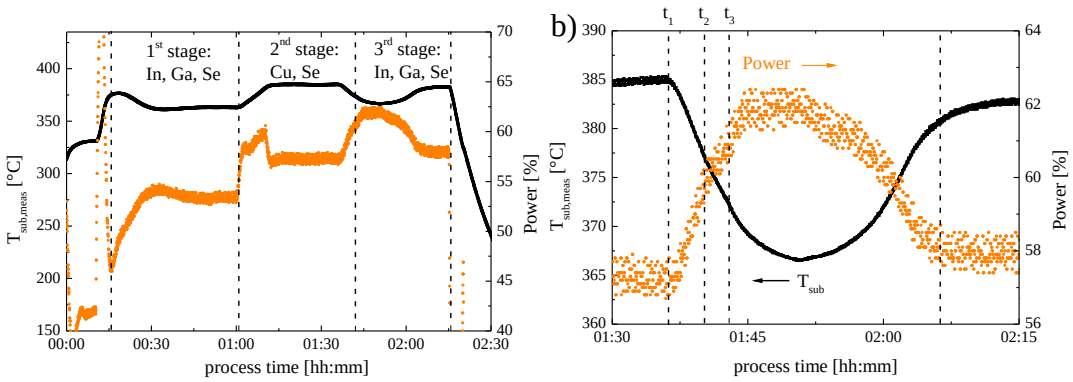


**Figure 3.6.:** Substrate temperature and heating power profiles throughout the 3-stage process.

as reproducible as possible we decide to take this point $t_2$ as a fixpoint and change from stage 2 to stage 3 (close the Cu source, open the In and Ga sources) at a fix distance to this point at $t_3$. In the following, the prevalent $Cu_{2-x}Se$ surface layer is consumed by the reaction with In, Ga and Se to Cu(In,Ga)$Se_2$. During this process the samples emissivity decreases to about its initial value which can be seen at the increase of the substrate temperature and decrease of heating power. Once, the whole $Cu_{2-x}Se$ surface layer is consumed, the values stabilize close to their initial values at $t_4$. This is taken as a second fixpoint for process control. By varying the duration of the 3rd stage (evaporation of In, Ga and Se) from this point on, the final *CGI* composition can be controlled.

## 3.1.4. Conclusion

In this chapter, the co-evaporation reactor and the principal deposition parameters have been explained. In particular the technical challenge of measuring the correct sample temperature was discussed. A thermocouple in permanent touch with the substrate is not imaginable since the surface is turning during the deposition process. The approach of a temperature calibration with the aid of an infrared camera has been followed and an offset between the temperature measured by a thermocouple close to the back-side of the substrate and the IR-measured temperature was found to be up to 100°C. Furthermore the *end-point detection* method was explained which permits the detection of the transition from a Cu-poor to Cu-rich composition and *vice versa* which is essential for the 3-stage process as has been explained in sec. 1.3.2.3.

## 3.2. Contact and buffer layer deposition

The final layer stack necessary for achieving a solar cell has been shown in Fig. 1.2. In addition to the CIGS absorber layer, the deposition of 4 further functional layers is necessary and realised in our laboratory. The applied deposition techniques and most important process parameters will be illustrated in the following.

### Molybdenum back-contact

A molybdenum back-contact of ($800 \pm 50$) nm thickness is deposited by DC magnetron sputtering on a 3 mm thick soda-lime glass substrate using about 5 mbar and 65 W DC power for the i-ZnO layer while the ZnO:Al layer is fabricated at about 0.9 mbar and 90 W DC power. A rectangular Mo target of 99.95 % purity is used. Prior to deposition, an argon plasma treatment is performed to remove contaminations and activate the surface.

### CdS buffer layer

The CdS buffer layer is fabricated by chemical bath deposition (CBD) at 60 °C using a classical solution containing thiourea ($SC(NH_2)_2$) as sulfur precursor, ammonium ($NH_4OH$) as complexing agent and cadmium acetate as Cd donor. The final layer thickness is ($50 \pm 5$ nm ). No post deposition treatments are conducted and all samples with a CdS buffer layer are finished by a i-ZnO/ZnO:Al transparent front contact.

### Zn(S,O) buffer layer

Zn(S,O,OH) films are grown by CBD using thiourea and ammonia as well. In this case, zinc sulfate ($ZnSO_4$) is used as zinc donor. The formulation for the Zn(S,O,OH) bath is $[SC(NH_2)_2]$ = 0.65M, $[ZnSO_4]$ = 0.15M, $[NH_3]$ = 2M with a deposition temperature of 80°C. After Zn(S,O,OH) deposition, the samples are rinsed in a $NH_3$ solution followed by de-ionised water in order to avoid $Zn(OH)_2$ post-precipitation at the surface of the films. All samples with a Zn(S,O) buffer layer are finished by a $Zn_{0.75}Mg_{0.25}O$/ZnO:Al transparent front contact. Post-deposition treatments are conducted only after the front contact deposition as described in the following paragraph.

### i-ZnO/ZnO:Al front contact

Solar cells were finally completed with an i-ZnO/ZnO:Al front contact in the case of a CdS buffer layer and $(Zn_{0.75}Mg_{0.25})O$/ZnO:Al contact layer for a Zn(S,O) buffer layer. Both stacks were fabricated by sputter deposition. In order to reduce metastabilities of the cells with a Zn(S,O) buffer layer, they were annealed in air for 10 min at 200°C and light-soaked for 1 h before current voltage measurements.

## 3.3. Conclusion

In this part the experimental setups for the material deposition have been explained. Since we applied established methods and used mostly commercially available systems for the sample characterisation only a brief explication of the most important measurement parameters are given in Appendix A and Appendix B. A particular focus was put on the measurement of the correct substrate temperature. Even though it is a central parameter and crucial for the nucleation and growth process, the usual way to measure it with a thermocouple close to (but not in touch with) the substrate showed a deviation from the temperature measured by an IR camera (which we consider to be the real substrate temperature) of up to 100 °C. The accuracy of the temperature measurement by the IR camera is supported by the observation of the glass deformation at 577 °C (indicated to be 562 °C by the producer) and an observation we interpret as a liquid $Cu_{2-x}$ Se phase at 540 °C and a solid $Cu_{2-x}$ Se phase at 520 °C while a melting temperature of 532 °C for $Cu_{2-x}$Se has been reported [99].

Throughout the literature, the substrate temperature is usually measured by a thermocouple and the various experimental setups should result in different offsets between the real and the measured substrate temperature. From a scientific point of view the knowledge of the real substrate temperature is very important and crucial to be able to compare different processes throughout the literature.

# 4. Comprehension of the 3 - stage process

Throughout the development of CIGS growth by thermal evaporation since the 1980s, it has become clear that in order to achieve CIGS thin films of high photovoltaic quality, it is important to have a copper-rich growth mechanism during the growth. At the same time, the final CIGS material requires Cu-deficiency. This can be described as CGI $> 1$ (at one moment) during and CGI $< 1$ at the end of the process. One process fullfilling these two conditions is the so-called 3-stage process.

Today, numerous academic research groups and industrial companies work on the 3-stage co-evaporation process. Thereby only a few groups have achieved very high efficiencies of $\eta \gtrsim 20$ % [24, 25, 76]. In order to achieve such high efficiencies and to go even further towards $\eta \approx 25$ % the comprehension of the growth process of CIGS thin films is absolutely necessary.

## 4.1. Introduction and addressed questions

My work consisted in the setup of a 3-stage process at a new co-evaporation reactor. Once a stable process was set up, the goal was to understand the CIGS growth mechanisms during the different stages in order to optimize the deposition parameters and achieve cell efficiencies as close to the state of the art as possible. Thereby I oriented my work on reports from the literature and tried to address questions not yet answered in order to contribute to the comprehension of the growth of CIGS thin films. In spite of

its success, the 3-stage process is not completely understood and questions about its growth mechanisms remain. A review about the present understanding and open questions that are addressed by this work is given in this section. Based on the results in this chapter and on work from the literature [106, 107, 108] a chemical reaction pathway throughout the 3-stage process will be discussed in sec. 4.6 which can as well explain the observed double Ga gradient in CIGS from a 3-stage process.

### 4.1.1. Interfacial $MoSe_2$ layer

It has been shown that a thin $MoSe_2$ layer at the CIGS/Mo interface allows for an ohmic contact instead of a schottky-contact at a pure CIGS/Mo interface [36, 109, 110] and the CIGS/$MoSe_2$ contact is beneficial for the solar cell performance [111].

It has furthermore been shown that such a thin interfacial layer of $MoSe_2$ with a hexagonal unit cell forms during the co-evaporation of CIGS on a Mo back-contact [36]. The role of the $MoSe_2$ orientation is thereby not yet completely clear but might change the contact properties due to its hexagonal structure [112]. Recent work has shown that the $MoSe_2$ orientation with its c-axis parallel to the surface might reduce the secondary barriers for electrical transport at CIGS/Mo back contacts [113]. While the influence of the substrate temperature and the selenisation conditions on the $MoSe_2$ orientation have been investigated [111, 114], it has to the best of our knowledge not yet been investigated which influence a Se deposition step prior to the $1^{st}$ stage and the variation of its duration has on the $MoSe_2$ layer. This question will be addressed in sec. 4.2.

### 4.1.2. Conservation of precursor properties

Numerous studies on the influence of the substrate temperature during the different stages of the 3-stage process on the final absorber layer material have been conducted [51, 53, 115, 116, 117]. The question we address in this work goes further, we try to evaluate what influence the substrate temperature has on the precursor material at the end of the $1^{st}$ stage and to which degree it is conserved or has an influence on the final absorber layer at the end of the $3^{rd}$ stage. Mise and Nakada have addressed this question in [47] with a focus on the crystal orientation and found that highly preferred CIGS films with the (220/204) plane parallel to the surface could be obtained under Cu-rich compositions using $(In,Ga)_2Se_3$ precursor layers with the (300) planes oriented parallel to the surface and deposited at moderate emperatures of 300–400 °C. In addition to the crystal orientation we will analyse the conservation of the morphology and elemental distribution throughout the layer thickness in sec. 4.3.1.

### 4.1.3. Recristallisation under Cu-rich conditions and the $Cu_{2-x}Se$ layer

At the transition from Cu-poor (CGI $<$ 1) to Cu-rich (CGI $>$ 1) CIGS, a so-called recristallisation mechanism occurs, leading to larger and more columnar grains [100, 106]. The preferred crystal orientation has been found to be not affected [100]. It is known that CIGS which underwent this recrystallisation mechanism and a transition back to slightly Cu-poor stoichiometry (CGI $\approx$ 0.8) achieves a significantly increased solar cell efficiency [106]. The recrystallisation mechanism is generally attributed to an observed Cu-Se (most likely $Cu_{2-x}Se$) phase at the sample surface for GGI $>$ 1 with a melting point at about 530 °C [99, 107]. Wada *et al.* described the Cu-rich $CuInSe_2$ growth at a temperature $T \approx 530$ °C as a topotactic reaction of solid $Cu_2Se$ with a liquid Cu-Se phase with soluted In on top of the prevalent CIS phase. Thereby it is not known which influence a solid *vs.* liquid Cu-Se phase has on the surface-near CIGS properties as well as on the

solar cell parameters. Furthermore it was found that the $Cu_{2-x}Se$ phase might not completely cover the surface [107]. These open questions will be addressed in sec. 4.4.

### 4.1.4. Influence of the substrate temperature on the Ga gradient

The formation of the Ga gradient during the 3-stage process has been investigated by numerous groups [118, 119, 120, 121]. Recently, the influence of the substrate temperature on the interdiffusion of Cu, In and Ga and the in-depth Ga profile has been studied as well [53, 122, 123]. Thereby, different temperature ranges are taken into account and in general, a homogenisation of the Ga and In concentration profiles with increasing temperature is found. In this work, we verify the homogenisation for the temperature range of $480 - 540$ °C (sec. 4.5). In contrast to some work in the literature we have corrected the substrate temperature by an infra-red measurement (see sec. 3.1.2) and can thus indicate absolute temperature values. While for CIGS growth temperatures $T \lesssim 500$ °C the cell performance generally increases with T, attributed to a better cristalline quality, for higher temperatures this is not clear. Since in this temperature range, large columnar grains are usually observed and the morphology and crystalline quality do not change drastically, the Ga gradient might play a dominant role for the cell performance.

In the following, the different stages of the 3-stage process are studied in chronologic order while addressing the topics we just discussed.

## 4.2. Optimisation of the Se pre-deposition step

Prior to the first stage in which In, Ga and Se are evaporated, usually Se is evaporated to the substrate. In our case, the substrate temperature was set to the same value as during the first stage, *i.e.* 480 °C for this study. It is interesting to understand the influence of the Se evaporation duration on the material properties. During the deposition of Se onto the Mo substrate, the $MoSe_2$ layer might start to form. Nishiwaki *et al.* [114] have reported that the $MoSe_2$ formation at the Mo/CIGS interface depends on the composition of the deposited film. During the evaporation of Se on a Mo substrate a thin ($\approx 10$ nm) $MoSe_2$ layer forms with its c-axis perpendicular to the Mo surface. In the case of a three-stage process, the $MoSe_2$ layer forms at the beginning of the second stage under Cu-poor conditions at an elevated substrate temperature with the c-axis parallel to the surface. Due to the hexagonal structure of $MoSe_2$ with van-der-Waals gaps inbetween the Se-Mo-Se sheats, $MoSe_2$ with its c-axis parallel to the surface should show much higher adhesion and possibly a better electric contact. The electric contact might also be influenced by the $MoSe_2$ thickness.

Due to these results it is expected that the nature of the $MoSe_2$ layer (thickness, preferred orientation) is influenced by the duration of the 'Se-only' stage prior to the metal deposition.

In order to analyse the interfacial $MoSe_2$ layer, the CIGS absorber layer has been mechanically lifted off from the Mo substrate. It has been shown [124] that the $MoSe_2$ layer remains on the side of the Mo substrate and is not found on the CIGS side. Raman spectra of the Mo/$MoSe_2$ layers are shown in

Fig. 4.1. The observed peaks can be attributed to $MoSe_2$ vibrational modes as reported e.g. in [125]. While the intensity of the $E_{1g}$ mode at 168.8 $cm^{-1}$ is slighly more pronounced for $t_{Se,pre} = 10$ and and $t_{Se,pre} = 15$ min, the peaks for the other vibration modes superpose well. Thus the existence of a $MoSe_2$ surface layer is confirmed for all samples but no difference between the samples can be observed in Raman measurements.

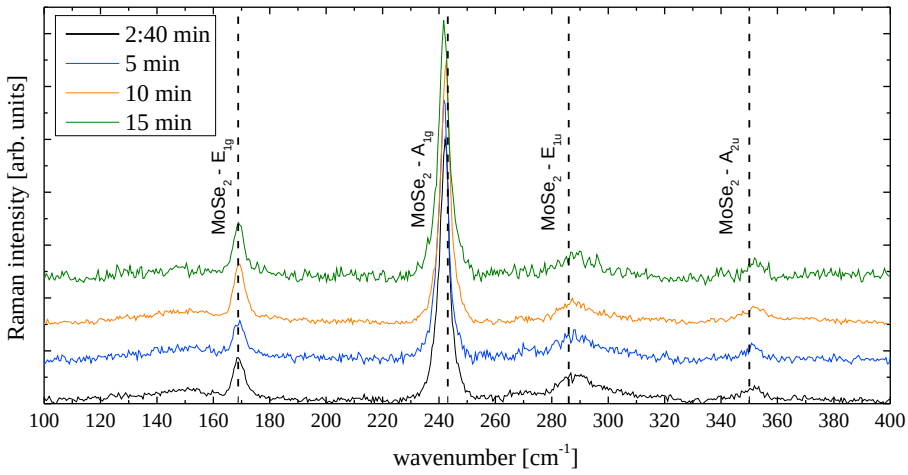


**Figure 4.1.:** Raman spectra measured at Mo substrates after mechanical lift-off of the CIGS absorber layers fabricated with different evaporation durations $t_{Se,pre}$ of Se prior to the $1^{st}$ stage. Curves are shifted for better visibility.

In order to study the crystal orientation of the hexagonal $MoSe_2$ phase, X-ray diffraction measurements have been performed at the Mo/$MoSe_2$ samples after the mechanical lift-off of the CIGS absorber layer. The results are shown in Fig. 4.2 and unveil a change in orientation. For $t_{Se,pre} = 2{:}40$ min no diffraction peak of the (002) planes is observed while the (100) and (110) peaks are clearly visible. This means that the c-axis of the hexagonal $MoSe_2$ lattice is oriented parallel to the surface. For $t_{Se,pre} = 5$ min the (002) peak appears and its intensity increases with $t_{Se,pre}$. At the same time, the (100) and (110) peaks stay at about constant intensity independant of $t_{Se,pre}$. These results can be explained by in increasing thickness of the $MoSe_2$ layer with increasing $t_{Se,pre}$. The hexagonal $MoSe_2$ layer is supposed to cover the Mo grains with its c-axis normal to the grain surface. Due to the small width of the Mo grains and their rather round shape, there is no part where the (002) planes are parallel to the substrate plane if the $MoSe_2$ layer is very thin ($t_{Se,pre} = 2{:}40$ min). When increasing the $MoSe_2$ film thickness for higher $t_{Se,pre}$, the $MoSe_2$ layer will be partly oriented with the (220) planes parallel to the surface inbetween the Mo grains. A further confirmation by transmission electron microscopy images of the

Mo/$MoSe_2$ cross-section would be usefull. It is important to note that the $MoSe_2$ formation can depend on the temperature. In [114] it has been shown that at a Mo/$(In,Ga)_2Se_3$ interface, a $MoSe_2$ interfacial layer does not form if the substrate temperature during the first stage of the 3-stage process is 350 °C but when heating to 550°C after the $(In,Ga)_2Se_3$ deposition, a $MoSe_2$ layer forms. This means that if $T_1$ is below the $MoSe_2$ formation temperature, the interfacial layer forms only at the beginning of the second stage when the substrate temperature exceeds the $MoSe_2$ formation temperature.

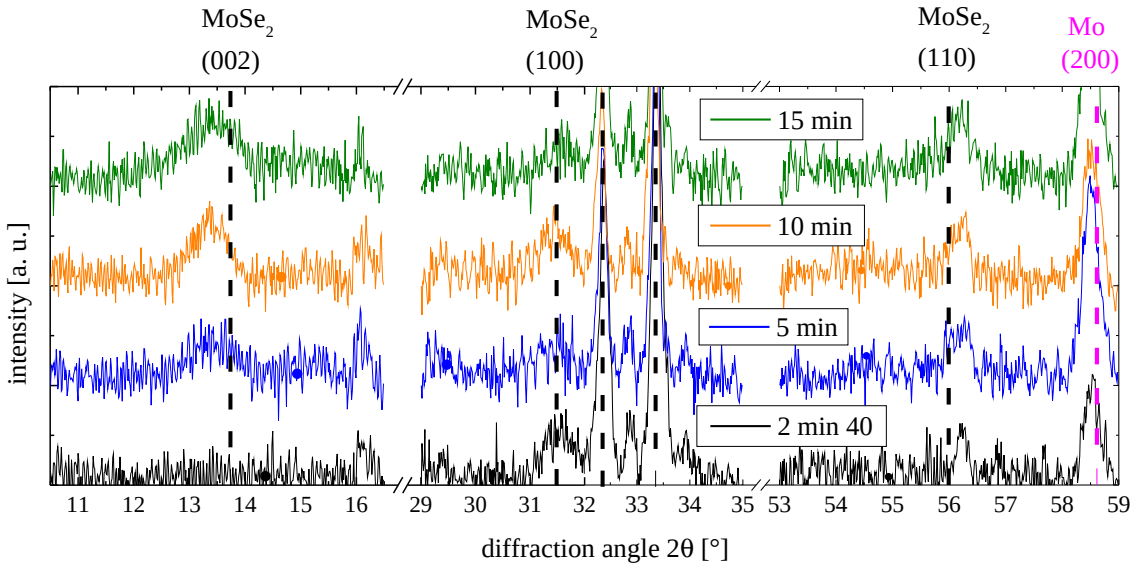


**Figure 4.2.:** X-ray diffraction diagrams at Mo substrates after mechanical lift-off of the CIGS absorber layers fabricated with different evaporation durations $t_{Se,pre}$ of Se prior to the first stage. Curves are shifted for better visibility.

The analysis of final CIGS solar cells with these absorber layers show that the duration $t_{Se,pre}$ of the pre-evaporation phase changes the opto-electronic cell properties as shown in Fig. 4.3. While for a short duration of 2:40 min the sample is very inhomogeneous (indicated by the error bar in Fig. 4.3b which corresponds to the standard deviation of the 36 cells for each sample, see sec. B.1 for more details), the homogeneity is increased for durations $t_{Se,pre} \geq 5$ min. All solar cell parameters plotted in Fig. 4.3b increase clearly for $t_{Se,pre} = 2:40$ min $\rightarrow t_{Se,pre} = 5$ min. In Fig. 4.3a typical IV curves for each absorber layer are shown. It can be seen that for $t_{Se,pre} = 2:40$ min the series resistance is clearly higher then for $t_{Se,pre} \geq 5$ min. For $t_{Se,pre} \geq 5$ min the fill factor increases successively with increasing $t_{Se,pre}$ but only by about 1 %. absolute. The open circuit voltage and short circuit current density show only minor variations with the evaporation duration in the $t_{Se,pre} \geq 5$ min region and their is no clear tendency with $t_{Se,pre}$. Therefore $t_{Se,pre}$ has a neglegible influence (0.1 % absolute) on the efficiency as long as $t_{Se,pre} \geq 5$ min. Throughout

my work, $t_{\mathrm{Se,pre}}$ will be fixed to 5 min.

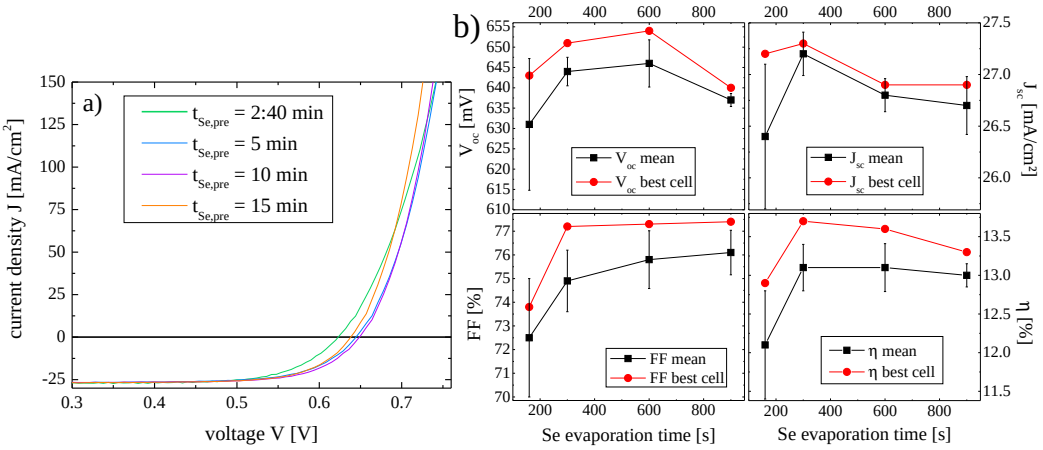


**Figure 4.3.:** Current-voltage characteristics of approximately 30 cells for each of the four durations $t_{\mathrm{Se,pre}}$ of Se evaporation prior to the first stage of a 3-stage co-evaporation process.

So in conclusion it can be said that for a low series resistance and thus an increased fill factor and better homogenity, a certain minimum thickness of the $MoSe_2$ layer is necesary. The increased thickness for $t_{\mathrm{Se,pre}} \geq 5$ min leads to the observation of the x-ray diffraction peak corresponding the (002) planes parallel to the surface in addition to the (110) and (100) peaks which are also observed for $t_{\mathrm{Se,pre}} = 2:40$ min. A further increase of $t_{\mathrm{Se,pre}}$ has a negligible influence on the $MoSe_2$ layer and on the solar cell parameters.

## 4.3. The first stage: growth of the $(In,Ga)_2Se_3$ precursor

During the first stage of the 3-stage co-evaporation process, In, Ga and Se are deposited simultaneously to form a $(In,Ga)_2Se_3$ precursor.

### 4.3.1. Influence of the substrate temperature

In the literature the substrate temperature during the first stage is usually lower than during the third stage [106, 126]. In order to understand the influence of the substrate temperature during the first stage on the material properties both of the precursor at the end of the first stage as well as the final CIGS absorber layer at the end of the third stage, we performed break-off experiments. We stopped our process at the end of the first stage in order to analyse the $(In,Ga)_2Se_3$ precursor as well as at the end of the third stage to obtain final absorber layers. In both cases

we varied the substrate temperature only during the first stage between 270 and 480 °C. Material characterization was performed by scanning electron microscopy, XRD, Raman spectroscopy and GD-OES.

#### 4.3.1.1. Precursor: morphology

The morphology of the precursor, shown in Fig. 4.4, varies with the substrate temperature $T_1$. With increasing temperature, the mean grain size increases clearly. At the same time, an increase of the surface roughness can be observed. For $T_1 = 400$ °C, the grain size is superior to the layer thickness resulting to large grains in the $\mu$m-range extending over the whole sample cross-section. It is clear that $T_1$ has a large influence on the $(In,Ga)_2Se_3$ precursor morphology.

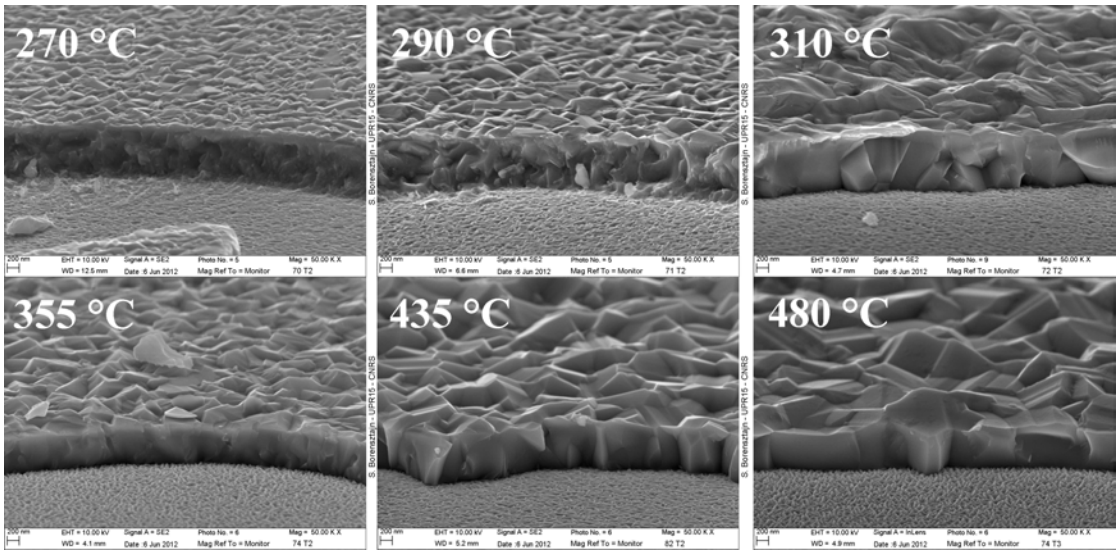


**Figure 4.4.:** SEM images of the $(In,Ga)_2Se_3$ precursor at the end of the first stage for different substrate temperatures.

#### 4.3.1.2. Precursor: crystal structure

In Fig. 4.5, x-ray diffractograms of the precursor layer at the end of stage 1 for different $T_1$ are shown.

For all three substrate temperatures, peaks are observed at the same diffraction angles. With the exception of the Cu and Ni peaks indicated by the orange lines in Fig. 4.5, all peaks can be attributed either to the Mo substrate or to $(In,Ga)_2Se_3$. The intensities of the $(In,Ga)_2Se_3$ vary slightly between the temperatures. For the very low temperature of 250°C, the film is more (110) oriented while for the higher temperatures, higher intensities are observed for the (116) and (306) peaks. This difference in preferential orientation can not be attributed unambiguously to the substrate temperature since we do not have a sufficient statistical evidence.

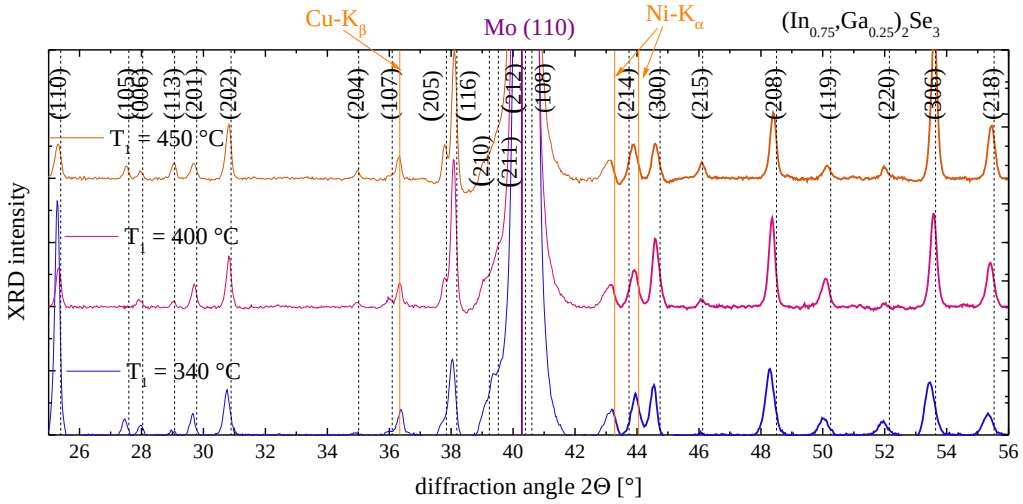


**Figure 4.5.:** X-ray diffractogram of the precursor at the end of the first stage for three different substrate temperatures during the first stage. The dashed lines indicate peak positions reported in the literature. Mo: ICDD 00-001-1207 [127], $(In,Ga)_2Se_3$: ICSD 634424 [128] . All peaks can be attributed to either Mo or $(In,Ga)_2Se_3$.

#### 4.3.1.3. Precursor: elemental composition profiling

Elemental composition profiles measured by GD-OES of precursor layers fabricated at 180, 240, 350 and 400 °C are shown in Fig. 4.6.

It can be seen that at low deposition temperatures of 270 and 330 °C the In, Ga and Se concentrations are fairly homogeneous throughout the sample thickness and the ratio corresponds well to the $(In,Ga)_2Se_3$ phase. At the back-interface, the Se signal decreases while the In signal increases to about the stoichiometry of (In,Ga)Se. For $T_1 = 435$ °C, the front half of the precursor layer with a slightly more Se-rich composition than $(In,Ga)_2Se_3$. Towards the back-interface, the Se signal decreases and the In signal increases so that the $(In,Ga)_2Se_3$ stoichiometry is reached. For the very high temperature of $T_1 = 485$ °C, the composition throughout the samples is fairly constant and close to the (In,Ga)Se stoichiometry. At the surface, a Se enrichment and In deficiency are observed while at the back-interface the composition approaches a slightly In-rich (In,Ga)Se stoichiometry. The Na concentration in the Mo-back contact is observed to increase with $T_1$. The signal is well correlated with the Mo signal and the concentration in the bulk of the In-Ga-Se layer does not vary significantly with the substrate temperature. A surface enrichment of Na is observed for $T_1 = 435$ °C and even stronger for $T_1 = 480$ °C but not for $T_1 = 270$ °C and $T_1 = 330$ °C.

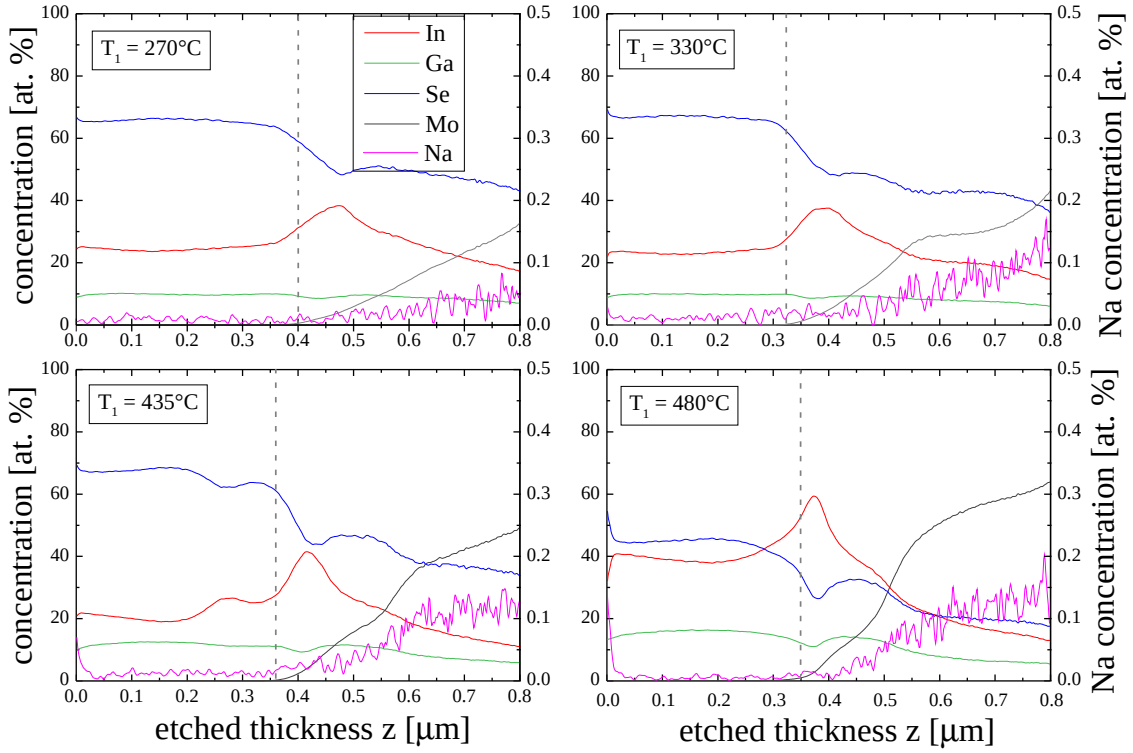


**Figure 4.6.:** Elemental concentrations measured by GD-OES for precursor layers at the end of the first stage fabricated at different substrate temperatures $T_1$. As a guide for the eye, the dotted grey line marks the beginning of Mo sputtering.

#### 4.3.1.4. Precursor: summary and discussion

XRD measurements show that independent of the substrate temperature, at least between 250 and 370 °C, during the $1^{st}$ stage of our 3-stage process, the $\gamma$ phase of $(In,Ga)_2Se_3$ is formed. The elemental composition profiles measured by GD-OES confirm that. The deviation from the $(In,Ga)_2Se_3$ stoichiometry for $T_1 = 400$ °C might result from a surface migration and following evaporation of Se once the evaporation of In, Ga and Se is finished and the sample is still at elevated temperature. This is supported by the Se surface enrichment observed in Fig. 4.6 and is not a contradiction to the formation of $(In,Ga)_2Se_3$. From SEM images it is evident that the precursor grain size increases with increasing substrate temperature $T_1$. The Na incorporation into the precursor bulk is low ($< 0.025$ %) and no temperature-dependence is observed. In the Mo layer, the Na content is found to increase steadily with temperature. A Na surface enrichment is observed for high temperatures ($T_1 \geq 350$ °C) and increases with temperature.

#### 4.3.1.5. Final absorber: morphology

SEM images of the final absorber layers with varied $T_1$ and identical second and third stages are shown in Fig. 4.7. It can be seen that $T_1$ only has a minor influence on the final absorber layer's morphology. The surface roughness is about the same and the grain size in the $\mu$m range for all layers. For 280, 350 and 400 °C there seems to be a slightly increased grain size and more grains extending the whole layer thickness, but to confirm we would need a higher statistic. Nevertheless it is clear that the substrate temperature in the first stage plays only a minor role for the final absorber layer's morphology. During the reaction with Cu and Se throughout our process, the $(In,Ga)_2Se_3$ layers reorganise completely and for the low temperatures (180 and 200°C), the final absorber layer has a much higher grain size than the precursor layers. Thus a morphological reorganisation takes place in the second or third stage, probably the re-crystallisation mechanism under Cu-rich conditions at the end of the second stage which is observed by other groups as well [99, 107].

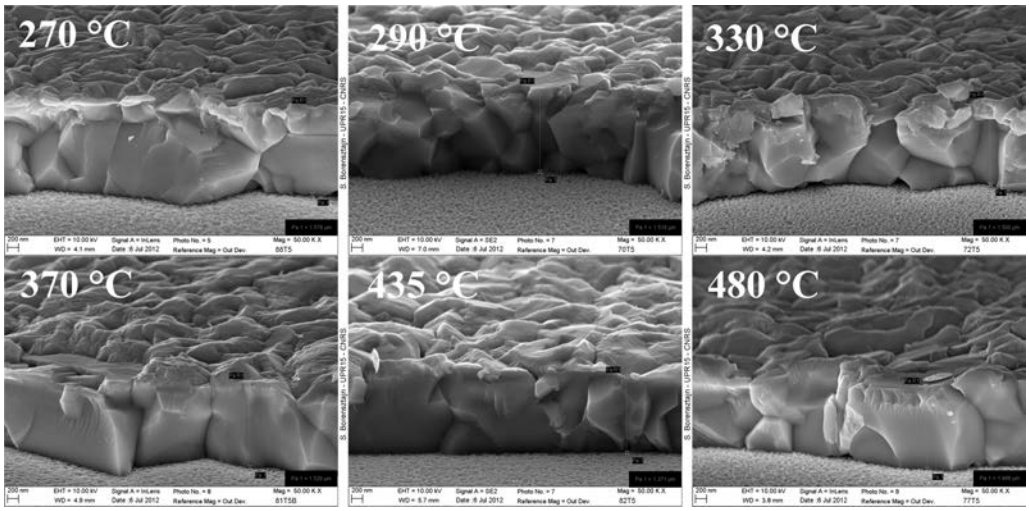


**Figure 4.7.:** SEM images of the final absorber layer fabricated at different substrate temperatures during the first stage.

#### 4.3.1.6. Final absorber: crystal structure

X-ray diffractograms of the final absorber layers fabricated at different $T_1$ between 180 and 400 °C are shown in Fig. 4.8.

Independent of $T_1$, all observed peaks can be attributed to the chalcopyrite CIGS phase or the Mo substrate. The peak position and shape are independent on $T_1$. From these measurements it seems that the substrate temperature during the first stage has no influence on the crystal structure of the final absorber layer.

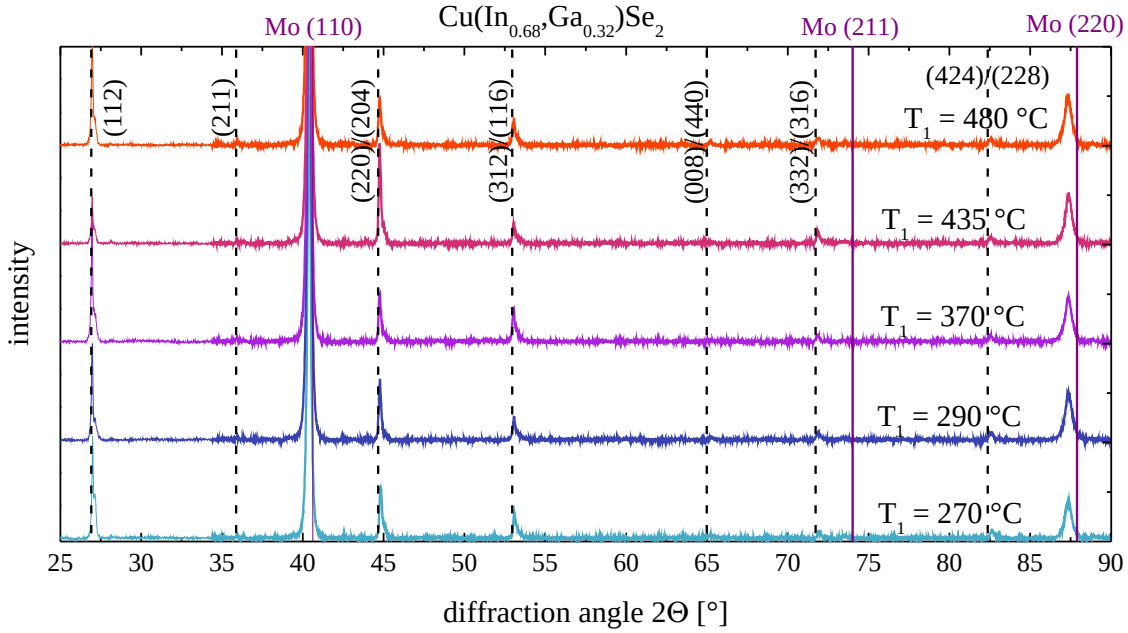


**Figure 4.8.:** X-ray diffractogram of the final absorber layer at the and of the third stage for different substrate temperatures during the first stage. The dashed lines indicate peak positions reported in the literature: Mo: ICDD 00-001-1207 [127], $Cu(In,Ga)Se_2$: ICDD 00-035-1102 [128]. All peaks can be attributed to either Mo or $Cu(In,Ga)Se_2$.

#### 4.3.1.7. Final absorber: elemental composition profiling

The in-depth composition profiles measured by GD-OES are shown in Fig. 4.9. While for Cu, In, Ga and Se no significant differences with $T_1$ are observed, the Na concentration is about a factor 2 higher for the low temperature samples (180 and 240 °C) compared to the high temperature (350 and 400 °C) samples. The increase is particularly significant towards the surface. This observation is quite surprising since the diffusion from the glass substrate to the CIGS layer is a thermally activated process and in the precursor layers, we observed an increase of the Na concentration in the Mo back-contact layer with increasing $T_1$. A possible explanation might be a desorption of the Na from the surface while the sample is still at high temperatures after the CIGS deposition but we have no further evidence of this hypothesis.

#### 4.3.1.8. Evolution of the crystal orientation

In order to describe the crystal orientation of the $(In,Ga)_2Se_3$ precursor layer at the end of the first stage and the $Cu(In,Ga)Se_2$ layer at the end of the third stage, the main XRD peaks were numerically fitted. The area of each peak has then been normalised to the total area of all of the considered peaks resulting in the relative

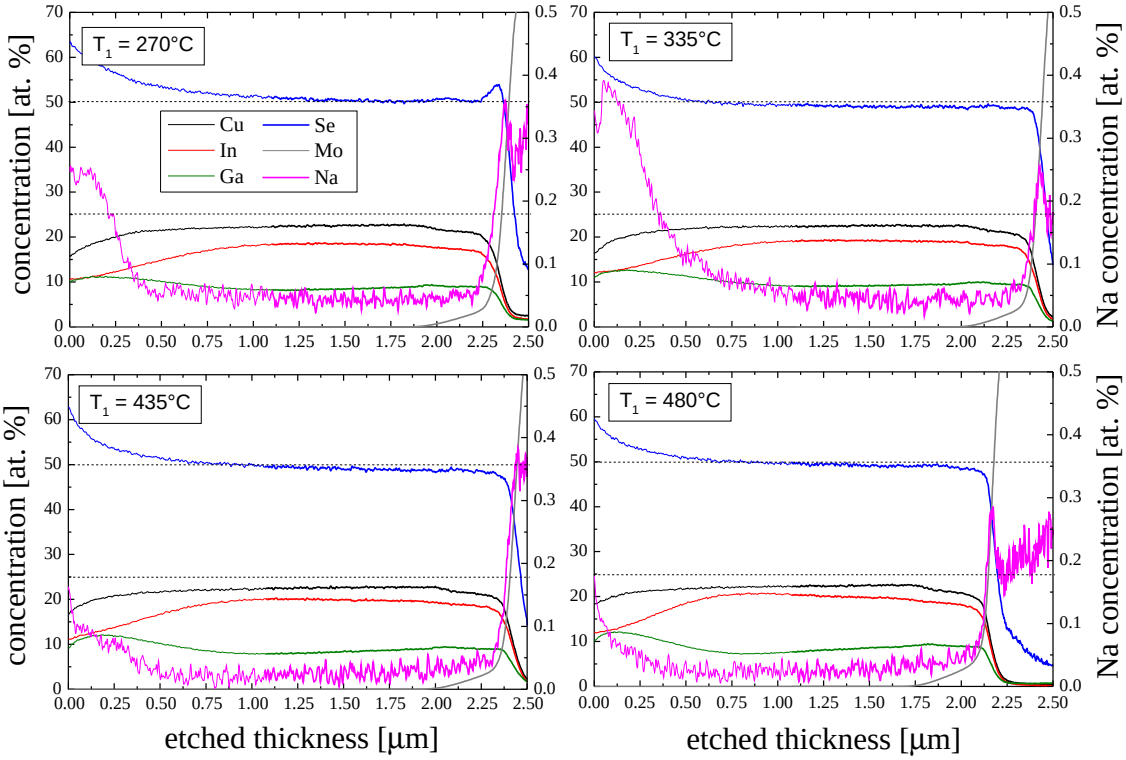


**Figure 4.9.:** Elemental concentrations measured by GD-OES for final absorber layers at the end of the third stage fabricated at different substrate temperatures $T_1$ only during the 1st stage. As a guide for the eye, the dotted lines mark atomic concentrations of 50 and 25 % respectively.

peak area. The results for the precursor and final absorber layers fabricated at varied process temperature $T_1$ during the first stage are shown in Fig. 4.10.

It can be seen that for the precursor layer (top graph in Fig. 4.10) deposited at a relatively low temperature $T_1 < 350$ °C the (110) plane is oriented preferentially parallel to the surface while for increasing temperature $T_1 \geq 400$ °C this orientation is less pronounced and the film is oriented rather with the (306) plane parallel to the surface. A crystalline orientation witht the (300) plane parallel to the surface is pronounced strongly for moderate temperatures around $T_1 \approx 400$ °C.

This evolution of the crystal orientation partly confirm results of Mise and Nakada [47] who reported that at moderate temperatures $T_1$ the $(In,Ga)_2Se_3$ precursor was oriented preferentially with the (300) plane parallel to the surface with led to a $Cu(In,Ga)Se_2$ orientation with the (220)/(204) planes parallel to the surface. The difference of the reported temperatures (300-400 °C in [47]) might be explained by different measurement techniques of the temperature. Our reported values of $400 - 450$ °C (corrected by an infrared measurement, see sec. 3.1.2) correspond to uncorrected values (measured by a thermo-couple close to the substrate) of $\approx 310 - 370$ °C. While we observe in accordance with [47] a reduction of the orientation

with the (220)/(204) planes parallel to the surface for an increasing temperature $T_1 \approx 475$ °C, in our case this is not correlated to a dominant $(In,Ga)_2Se_3$ orientation with the (110) planes parallel to the surface, as observed by Mise, but rather with the (306) planes parallel to the surface.

#### 4.3.1.9. Discussion and Conclusion

The influence of the substrate temperature on the formation of the $(In,Ga)_2Se_3$ precursor formation has been investigated. The morphology and Na-incorporation have been found to change with $T_1$. The average grain size and surface roughness increase gradually with $T_1$.

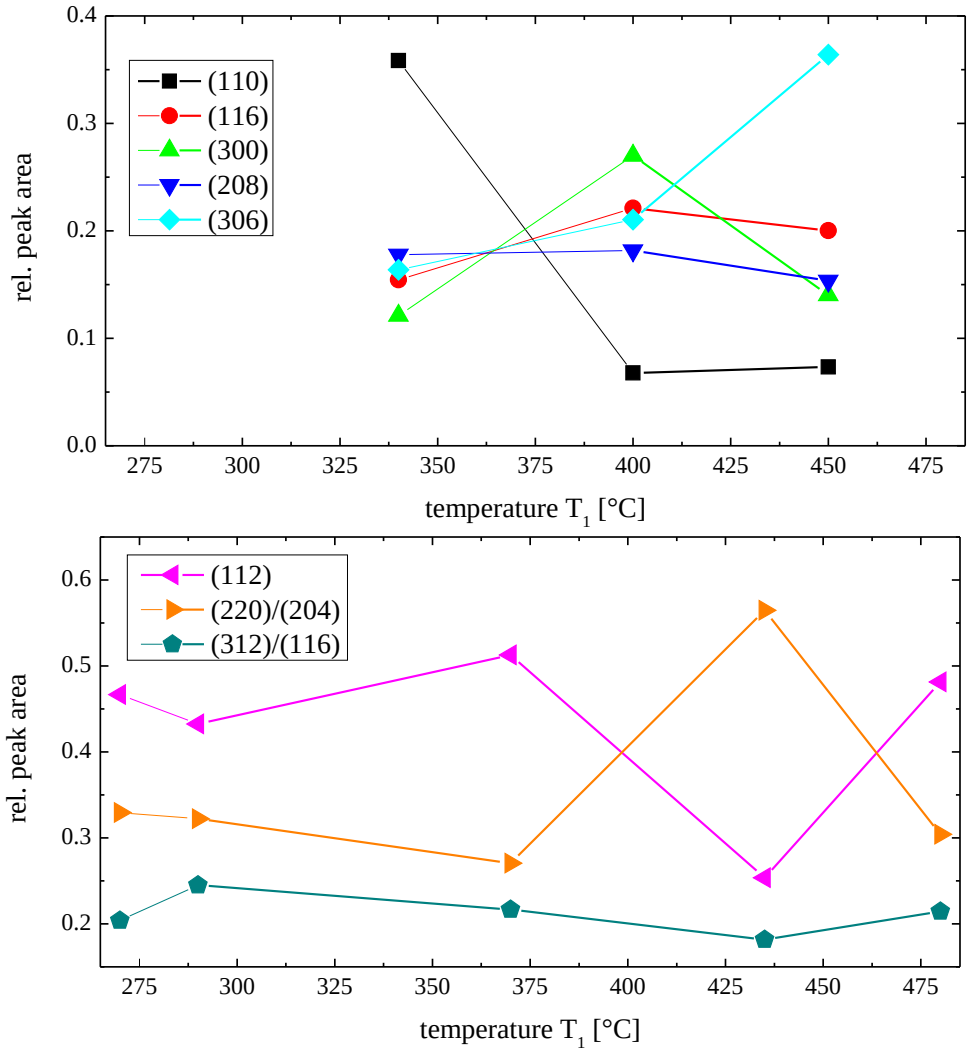


**Figure 4.10.:** Relative XRD peak areas for the main peaks of the $(In,Ga)_2Se_3$ precursor at the end of the first stage (top) and of the $Cu(In,Ga)Se_2$ layer at the end of the third stage (bottom) as a function of the deposition temperature $T_1$ during the first stage.

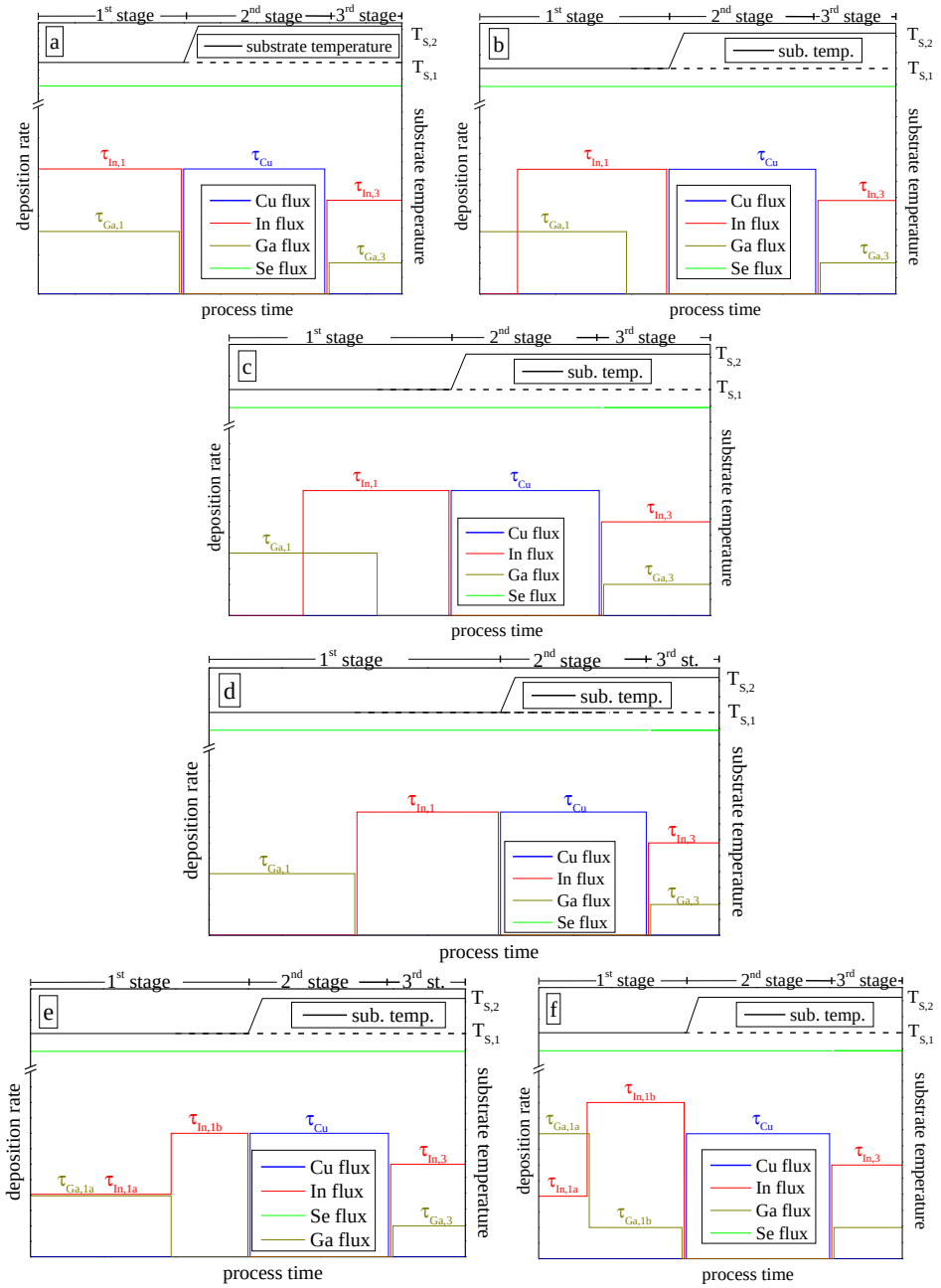


**Figure 4.11.:** Deposition rate profiles for a) the standard 3-stage process and b) to f) a modified first stage of the 3-stage co-evaporation process in order to extrinsically increase the notch-deepness of the double Ga gradient.

This can be explained by the increased lateral adatom mobility at the beginning of the 3-dimensional crystal growth and in return the formation of larger clusters which are then transformed to growth islands. The observed increase of the Na concentration in the Mo back-contact with $T_1$ is a consequence of the thermally activated diffusion of Na from the soda-lime glass substrate. The independence of

the Na concentration in the precursor layer indicates a saturation of the Na impurity levels in the $(In,Ga)_2Se_3$ precursor layer while with increasing temperature the Na surface migration still increases.

The analysis of final absorber layers allowed to study if the precursor material properties are conserved throughout the second and third stage and play a role for the final absorber material as it is used in a solar cell. From SEM and GD-OES measurements, no clear influence of the substrate temperature in the first stage on the material properties of the final absorber layer could have been identified. This indicates a recrystallisation of the precursor layer throughout the second and third stage.

The evolution of the crystal orientation described in sec. 4.3.1.8 confirmed that a $(In,Ga)_2Se_3$ precursor oriented preferentially with the (300) plane parallel to the surface grows at moderate temperatures on a Mo-coated glass substrate and leads to a $Cu(In,Ga)Se_2$ orientation with the (220)/(204) planes parallel to the surface as reported in [47].

## 4.3.2. Influence of the In and Ga deposition rates

The Ga gradient in CIGS is known to be crucial for the device optimisation. In this section we will evaluate how we can manipulate this gradient with the goal to lower the Ga concentration at the minimum of the GGI profile. This is known to decrease the optical band gap and permitd to shift the absorption edge to higher wavelengths and eventually increase the short circuit current. The challenge hereby is to keep the open-circuit voltage at about the same level in order to increase the cell efficiency. Therefore we deposited the same total quantities of In and Ga and only shifted their deposition profiles against each other, as seen in Fig. 4.11. Thereby we expect for all process variations (Fig. 4.12b-f) a steeper Ga gradient and a lower Ga concentration at the Ga-profile minimum as well as an increased Ga concentration towards the back interface CIGS/Mo as compared to the standard process (Fig. 4.11a). The elemental in-depth composition was measured by glow discharge optical emission spectroscopy (GD-OES) quantified by inductively coupled plasma mass spectroscopy (ICP-MS).

### 4.3.2.1. In-depth composition

The Ga gradients for the different samples are shown in Fig. 4.12. It can be seen that for all variations, the Ga concentration at the notch position is reduced while it is increased near the back-interface as compared to the standard sample a. While sample d has a very high Ga concentration GGI $\approx 0.75$ at the back interface, samples b, c, e and f have an equal amount of GGI $\approx 0.60$ at the back-interface. The GGI depth profiles of samples c, e and f superpose very well throughout the whole absorber thickness. As seen in Tab. 4.1 the integral compositions varied only slightly which was the goal of this study since we investigate the influence of the Ga gradient and not of the global composition.

| sample | a | b | c | d | e | f |
|---|---|---|---|---|---|---|
| GGI | 0.30 | 0.29 | 0.28 | 0.30 | 0.26 | 0.29 |
| CGI | 0.81 | 0.79 | 0.76 | 0.79 | 0.73 | 0.79 |
| $E_{g,opt}$[eV] | 1.11 | 1.08 | 1.07 | 1.04 | 1.07 | 1.06 |

**Table 4.1.:** Integral atomic concentration ratios GGI and CGI measured by x-ray fluorescence and optical band gap conducted from linear fits of the square of the external quantum efficiency vs. energy.

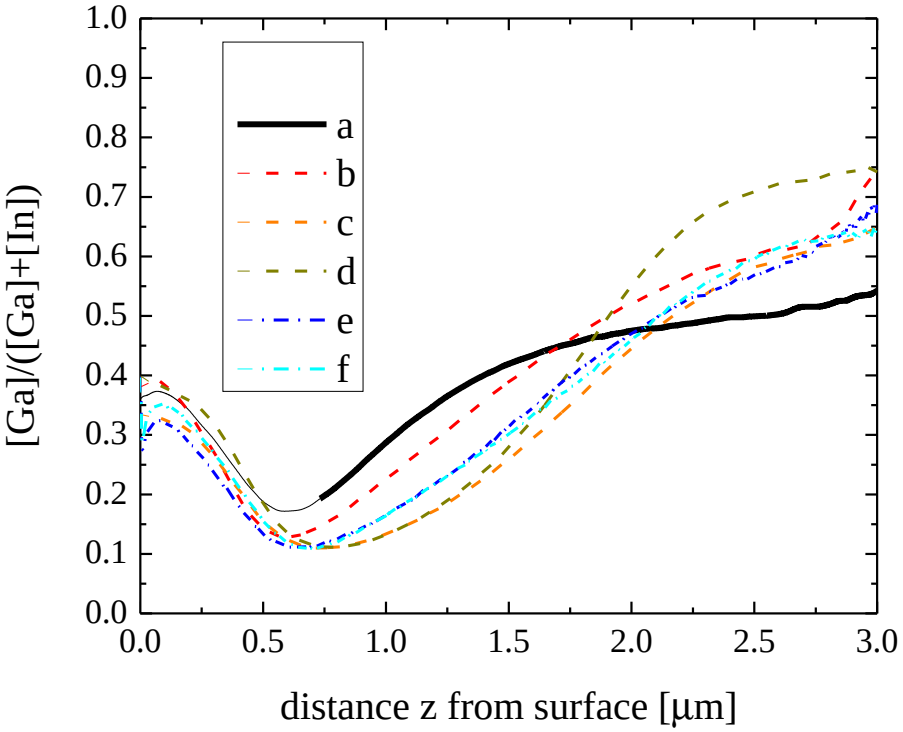


**Figure 4.12.:** Atomic concentration rates and Mo at.% for the 4 CIGS absorber layers with varied notch deepness. Evaporation profiles are shown in Fig. 4.11.

#### 4.3.2.2. Morphology

Scanning electron microscopy images of the absorber layers cross sections are shown in Fig. 4.13. It can be seen that the morphology is different for the six absorber layers. For samples a and e, relatively high grains with diameters in the µm order are prevalent throughout the whole absorber thickness. For samples b-d, very small grains with diameters inferior to 100 nm are present close to the back-interface. Interestingly, these small grains do not form for sample e which has the same Ga concentration at the back-interface as samples b-d but has been fabricated, in contrast to b-d, without a 'Ga-only' deposition step at the process beginning.

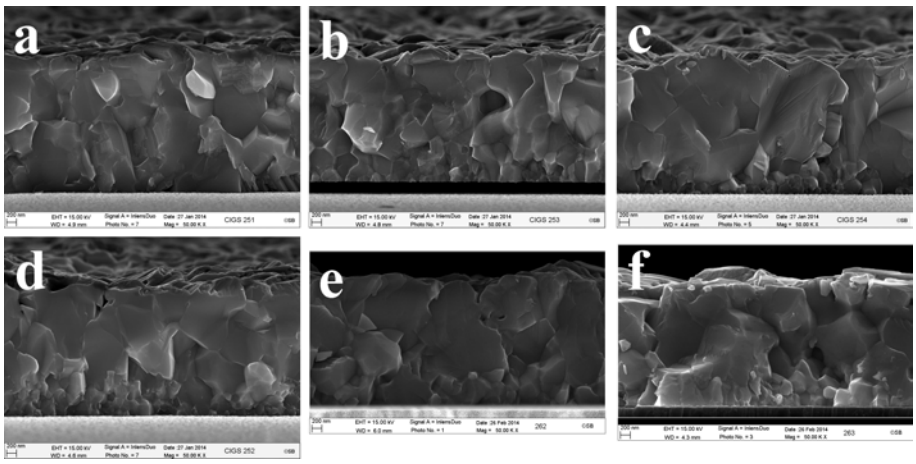


**Figure 4.13.:** Scanning electron microscopy images of the absorber layer cross-sections fabricated with the processes illustrated in fig. Fig. 4.11.

#### 4.3.2.3. Discussion and conclusion

Work in the literature [129] suggests that the decrease of the grain-size with increasing Ga content is related to a deviation of the lattice parameter ratio $\frac{c}{a}$ from 2. Since recombination at the grain boundaries can decrease the device performance, these small grains at the back-interface need to be avoided. We thus have to find a trade-off between the grain size and the deepening of the Ga gradient which is considered to be beneficial for the solar cell. A simple shift of the Ga and In profiles (samples b, c and d) is not desirable due to the small grains at the back-interface. The probably best solution is a reduction of the In deposition rate in the first part of the first stage followed by the solely deposition of In in the second part of the first stage (sample e), which results in both a deepened Ga gradient and a morphology similar to the morphology of the reference sample a.

It is furthermore interesting to note that in this case the morphology of the final absorber layer is influenced by a deposition parameter (the Ga deposition rate) during the first stage. We have seen in sec. 4.3.1 that the temperature during the first stage has no influence on the final absorber layer morphology. The morphology of the final CIGS absorber layer is thus independent of the precursor morphology but depends on its In and Ga composition.

## 4.4. The second stage: recristallisation and the reaction of $(In,Ga)_2Se_3$ with Cu and Se

During the 2nd stage, Cu and Se are evaporated and react with the prevalent $(In,Ga)_2Se_3$. The substrate temperature is typically increased at the beginning of the second stage to a level we will refer to as $T_2$. X-ray diffractograms performed at

samples at the end of stage 2 are shown in Fig. 4.14 for two different substrate temperatures $T_1$ during the first stage. The peak positions and intensities are close to identic, confirming a complete reorganisation of the $(In,Ga)_2Se_3$ layer independent of $T_1$ already at this point. All peaks can be attributed to either the Mo substrate or the $\alpha$-Cu(In,Ga)$Se_2$ phase.

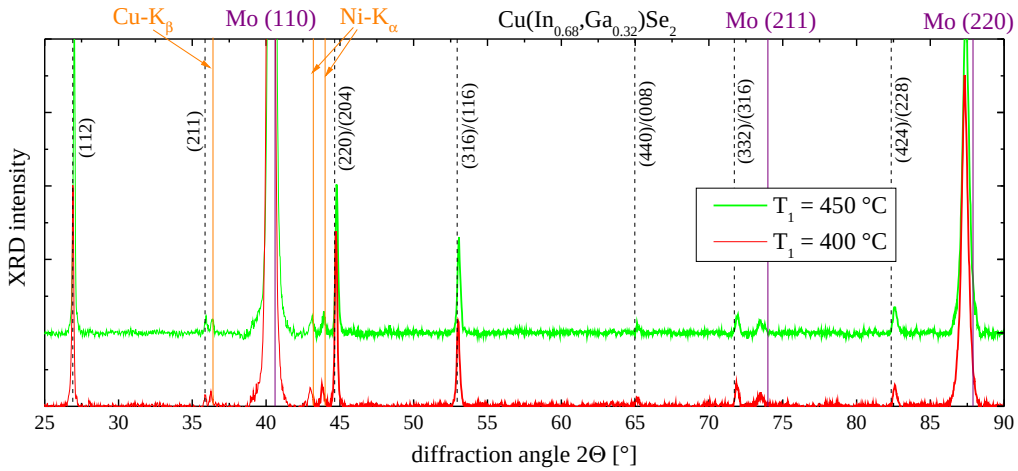


**Figure 4.14.:** X-ray diffractogram of the sample at the end of the second stage for three different substrate temperatures during the first stage. The dashed lines indicate peak positions reported in the literature: Mo: ICDD 00-001-1207 [127], Cu(In,Ga)$Se_2$: ICDD 00-035-1102 [39] . All peaks except for peaks 36, 43 and 44 can be attributed to either Mo or Cu(In,Ga)$Se_2$.

### 4.4.1. The $Cu_{2-x}Se$ layer

The GD-OES profiles of the break-off samples fabricated at $T_2$ = 480 and 540 °C are shown in Fig. 4.15a and several elemental fractions in Fig. 4.15b. As can be well observed in Fig. 4.15b, already at the end of the second stage, the Ga gradient is less pronounced with increasing temperature. Towards the surface, for both samples, the measured Cu concentration increases while the Se concentration decreases. This might indicate a thin layer of $Cu_{2-x}Se$ or CuSe at the surface. The Cu over-stoichiometry measured by ICP is slightly higher for the sample fabricated at 540 °C ($[Cu]/([III])$ = 1.18) than for the sample fabricated at 480 °C ([Cu]/([III]) = 1.13). For the sample fabricated at 540 °C, the surface composition (Fig. 4.15 right) deviates from the quasi-binary tie line between $(In,Ga)_2Se_3$ and $Cu_2Se$ (2[Se]/([Cu]+3[In]+3[Ga])>1). This might indicate the presence of a liquid CuSe phase as it has been reported in co-existence with a solid $Cu_{2-x}Se$ phase for temperatures of about 530 °C by Wada *et al.* [130] . There should not be any presence of condensed Se at the surface since the substrate cools down from 400 °C was realized without Se evaporation for both samples.

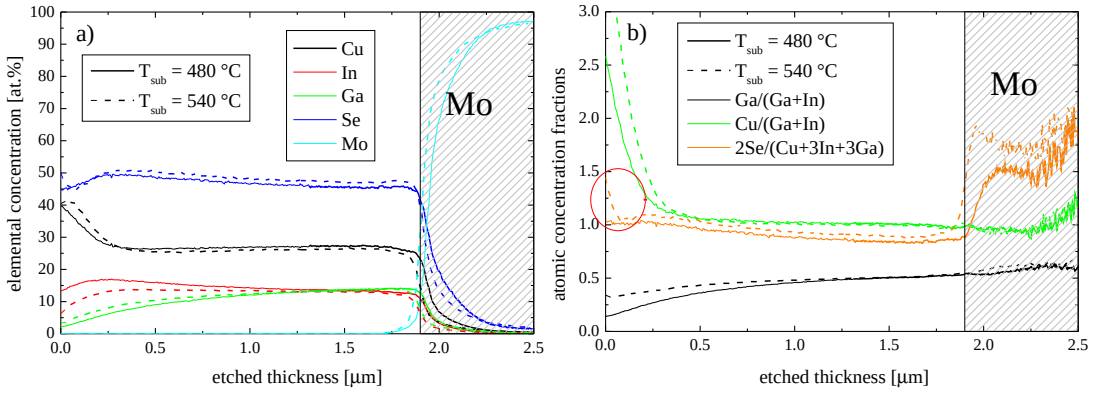


**Figure 4.15.:** a) Atomic concentration and b) their ratios measured by GDOES of two samples from a process that was interrupted at the end of stage 2 (Cu-rich) for different substrate temperatures of 480 and 540 °C.

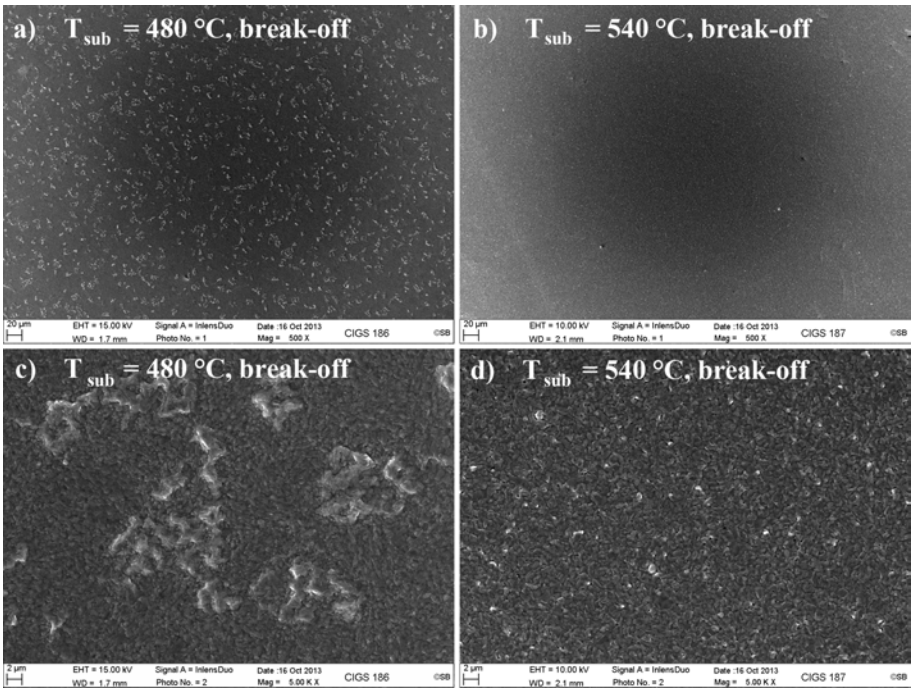


**Figure 4.16.:** SEM top views of two samples from a process that was interrupted at the end of stage 2 (Cu-rich) for different substrate temperatures of 480 and 540 °C. At 540 °C (b and d) a layer of $Cu_{2-x}Se$ covers the surface completely, as confirmed by the Raman measurements in Fig. 4.18 while for 480 °C (a and c) there are holes with a diameter of several micrometer prevalent in that layer.

Furthermore there is no reason why for $T_{2,3}$ = 540 °C Se should condensate at the surface and not for $T_{2,3}$ = 480 °C. SEM top views of the break-off samples are shown in Fig. 4.16. It can be seen that for the sample fabricated at 480 °C, randomly

distributed valleys of sizes between 2 and 10 $\mu$m are present all over the surface. These valleys are not present for the sample fabricated at 540 °C. The analysis of the chemical composition by energy-dispersive x-ray spectroscopy (Fig. 4.17) and phase analysis by Raman spectroscopy (Fig. 4.18) of these valleys reveal that they are holes in the $Cu_{2-x}Se$ layer that covers the $Cu(In,Ga)Se_2$.

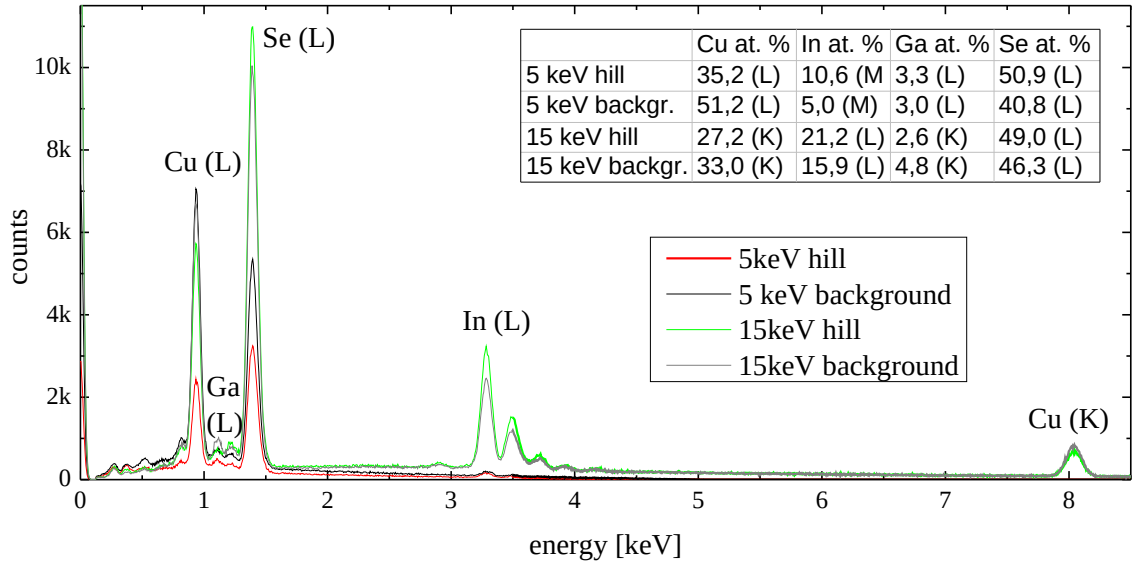


| | Cu at. % | In at. % | Ga at. % | Se at. % |
|---|---|---|---|---|
| 5 keV hill | 35,2 (L) | 10,6 (M | 3,3 (L) | 50,9 (L) |
| 5 keV backgr. | 51,2 (L) | 5,0 (M) | 3,0 (L) | 40,8 (L) |
| 15 keV hill | 27,2 (K) | 21,2 (L) | 2,6 (K) | 49,0 (L) |
| 15 keV backgr. | 33,0 (K) | 15,9 (L) | 4,8 (K) | 46,3 (L) |

**Figure 4.17.:** Energy-dispersive x-ray spectroscopy () measurements performed on background as well as valley regions of the sample fabricated at 480 °C shown in Fig. 4.16.

The results of the EDX measurements were performed at incident electron beam energies of to 15 keV and 5 keV. It is important to notice that the signal is generated in a certain volume of approximately a few hundred nanometers and thus the top layer of $Cu_{2-x}Se$ is measured as well as the underlying CIGS. By decreasing the excitation energy, this volume becomes smaller and the method becomes thus more surface-sensitive. Regarding the 5 keV signal in the table in Fig. 4.17 it can be seen that the valleys have a composition closer to the $Cu(In,Ga)Se_2$ stoichiometry with a slightly increased Cu and decreased In concentration. The 5 keV background signal might correspond to the $Cu_{2-x}Se$ stoichiometry with slightly decreased Cu and increased In, Ga and Se signals in accordance with the $Cu_{2-x}Se$ detection by Raman spectroscopy (Fig. 4.18).

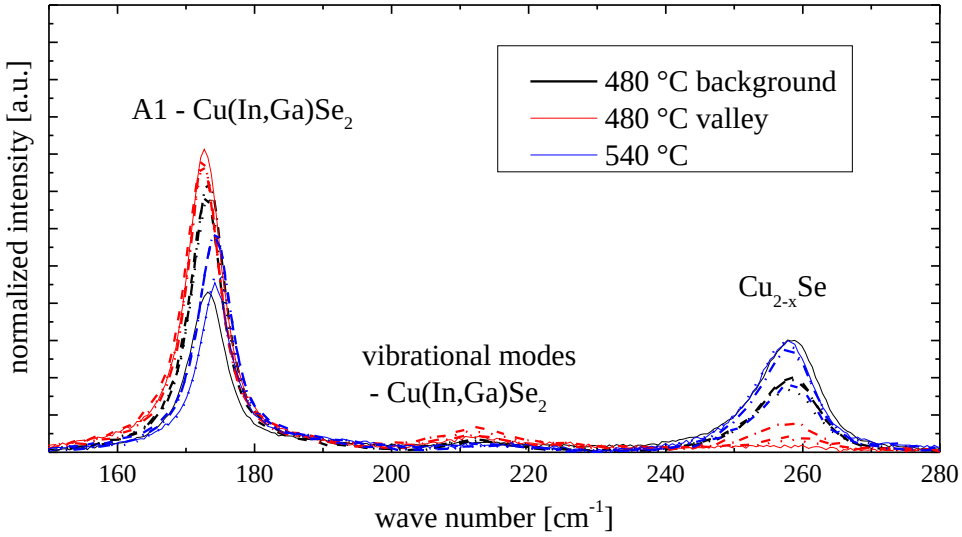


**Figure 4.18.:** Raman spectroscopy measurements performed on background as well as valley regions of the sample fabricated at 480 °C and 540 °C shown in Fig. 4.16.

## 4.5. The third stage: influence of the substrate temperature

In this section, the influence of the substrate temperature during the second and third stage on material and device properties is investigated. The given values for the substrate temperature have been corrected, as described in sec. 3.1.2, using a calibration curve that was measured with an IR camera. The ratios of the evaporation rates for In and Ga as well as the substrate temperature during the 3 stages are listed in Tab. 4.2. The Se evaporation rate was in all stages about 3 times higher than the sum of the respective metal evaporation rates (Cu in the second and In and Ga in the first and third stage). In the classic 3-stage process, the substrate temperature is at a relatively low level in the first stage during the evaporation of In, Ga and Se and is then increased at the beginning of the second stage and held at a constant level during stage 2 and 3. We kept the temperature at the same level during the second and third stage but varied this level between 480 and 540 °C, as shown in Fig. 4.19. In order to obtain samples of the same thickness, the duration of the first stage was set to 45 min for all 4 samples. The duration of the second stage is predetermined by the moment of Cu-stoichiometry and varies only very few between 52 and 56 min (see Tab. 4.2).

| $1^{st}$ stage: | |
|---|---|
| $\tau_{Ga,1}/(\tau_{Ga,1}+\tau_{In,1})$ | 0.37 |
| substrate temperature $T_1$ | 480 °C |
| duration | 45 min |
| $2^{nd}$ stage: | |
| substrate temperature $T_{2,3}$ | varied between 480 and 540 °C |
| duration | between 52 and 56 min |
| $3^{rd}$ stage: | |
| $\tau_{Ga,3}/(\tau_{Ga,3}+\tau_{In,3})$ | 0.28 |
| substrate temperature $T_{2,3}$ | varied between 480 and 540 °C |
| duration | between 16 and 20 min |

**Table 4.2.:** Deposition parameters for the deposition of 4 different CIGS absorber layers at different substrate temperatures during the second and third stage of a 3-stage co-evaporation process. Substrate temperature values have been corrected by IR camera measurements, as described in sec. 3.1.2.

The duration of the 3rd stage is predetermined by the time needed to consume the excess Cu, which is prevalent at the end of stage 2, as shown in sec. 4.4.1. This duration varies only slightly between 16 and 20 min for the 4 samples.

The integral composition and the composition ratios GGI and CGI of the 4 absorber layers deposited at different substrate temperatures are listed in Tab. 4.3.

| Final absorber | 480 °C | 500 °C | 520 °C | 540 °C |
|---|---|---|---|---|
| thickness [$\mu$m] | 2.18 | 2.28 | 2.37 | 2.34 |
| [Cu] (at. %) | 24.2 | 23.9 | 23.6 | 23.6 |
| [In] (at. %) | 17.1 | 16.7 | 16.4 | 16.0 |
| [Ga] (at. %) | 10.7 | 10.7 | 10.9 | 10.7 |
| [Se] (at. %) | 48.0 | 48.8 | 49.2 | 49.7 |
| [Cu]/([In]+[Ga]) | 0.87 | 0.88 | 0.87 | 0.88 |
| [Ga]/([Ga]+[In]) | 0.38 | 0.35 | 0.35 | 0.40 |
| duration $2^{nd}$ stage | 42 min | 43 min | 46 min | 42 min |
| duration $3^{rd}$ stage | 16 min | 17 min | 20 min | 18 min |

**Table 4.3.:** Thickness, elemental composition and duration of the second and third process stages for the samples fabricated at different substrate temperatures $T_{2,3}$ during the second and third stage.

It can be seen that the values are rather constant for the different samples and they are as desired slightly Cu-poor ([Cu]/([III])<1) and have about the same integral Ga concentration (0.35≤GGI≤0.4). The small variations are attributed to minor uncontrolled and nonsystematic variations of the deposition rates during the process. SEM images of the absorber layer cross sections are shown in Fig. 4.20. The grain

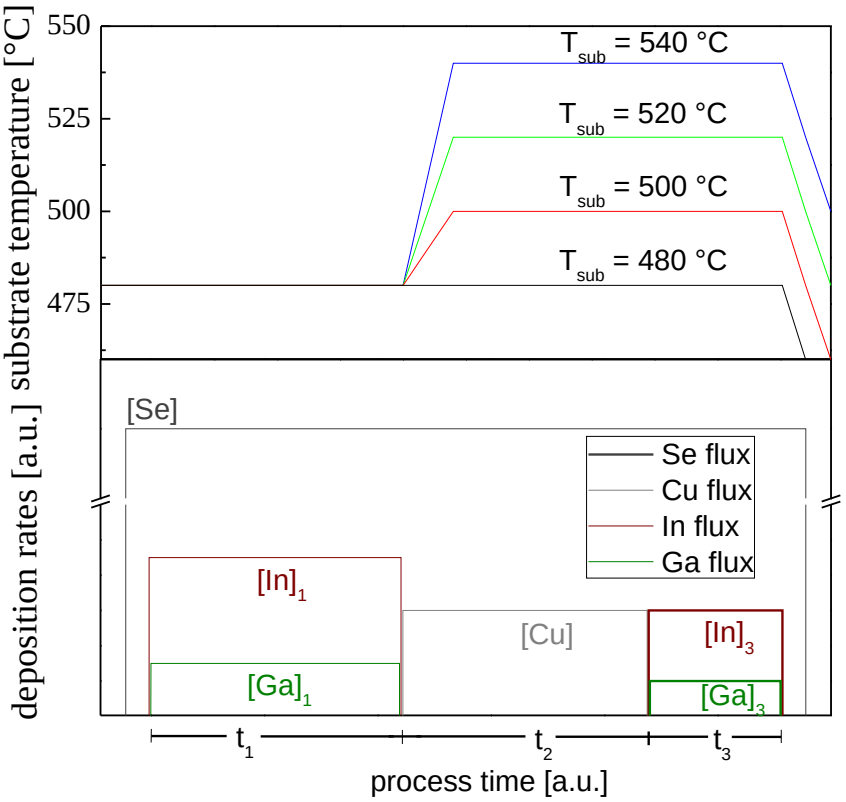


**Figure 4.19.:** Deposition rates and substrate temperature profiles for 4 samples deposited at different substrate temperatures.

size increases and the columnar grain structure becomes more pronounced with increasing substrate temperature. This is in accordance with work in the literature, e.g. [131]. For the lowest substrate temperature of 480 °C, there is an accumulation of small grains close to the Mo back contact. While for $T_{2,3}$ = 520 °C there are still a lot of small grains visible towards the surface, for $T_{2,3}$ = 540 °C large columnar grains are observed, extending from the bottom over the whole layer thickness to the surface.

The in-depth Ga grading is found to be the deepest for the very low temperature of $T_{2,3}$ = 480 °C and becomes less pronounced with increased substrate temperature. This can be observed directly in the GDOES profile as shown in Fig. 4.21a or indirectly by XRD diffraction measurements, e.g., of the orientation of (112) planes parallel to the surface as shown in Fig. 4.21b. Since the GGI ratio between the atomic concentrations of Ga and of all group III elements changes the lattice constant and thus the diffraction angle $2\Theta$, the peak width can be regarded as a measure of the Ga profile-depth. The decrease of the XRD peak width thus confirms the homogenization of the GGI profile with increasing temperature. While the Ga profile becomes less pronounced with substrate temperature, the Ga composition at the surface stays constant at GGI = 0.38 except for the very high temperature of

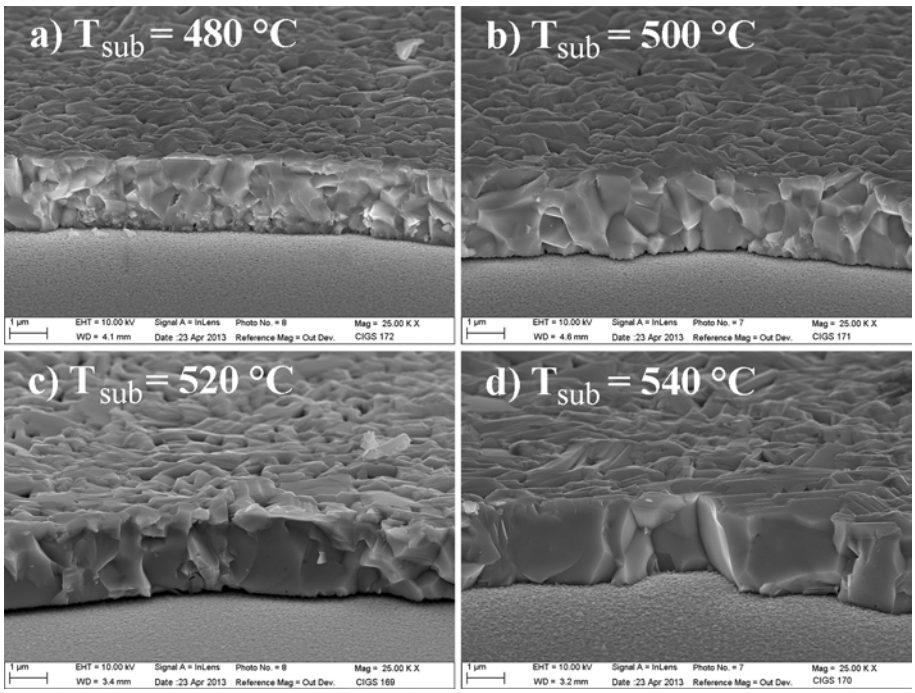


**Figure 4.20.:** Scanning electron microscopy (SEM) images of samples with varied substrate temperatures in stage 2 and 3 of the 3-stage co-evaporation process, as shown in Fig. 4.19.

540 °C. This value is higher than the ratio of the evaporation fluxes $\tau_{\mathrm{Ga}}/(\tau_{\mathrm{Ga}} + \tau_{\mathrm{In}})$ = 0.28 in the 3rd stage, which is due to a faster in-diffusion of In during the third stage. The distance of the GGI notch from the absorber surface is very similar for all samples and the slight variations can be explained by the slightly different durations of the third stage (see Tab. 4.2). These differences were necessary in order to achieve similar [Cu]/([III]) ratios (also shown in Tab. 4.2). For $T_{2,3}$ = 540 °C, the gradients shape towards the front surface differs from the shape for the three lower temperatures. This homogenization of the Ga gradient towards the surface at the corrected substrate temperature of 540 °C might be due to the existence of a solid $Cu_{2-x}Se$ phase at the end of stage 2 while for the lower substrate temperatures this phase is believed to be solid. We have shown in sec. 4.4.1 that at 540 °C this phase is probably liquid which is in agreement to the reported solid/liquid transition of $Cu_{2-x}Se$ at 532 °C [99].

## 4.6. Discussion

In break-off experiments the presence of $(In,Ga)_2Se_3$ at the end of the first stage, the co-existence of $Cu(In,Ga)Se_2$ and $Cu_{2-x}Se$ at the end of the second stage (Cu-rich conditions) and $Cu(In,Ga)Se_2$ as well as an ordered defect compound (ODC) phase such as $Cu(In,Ga)_3Se_5$ in the final absorber layer have been confirmed. The observed

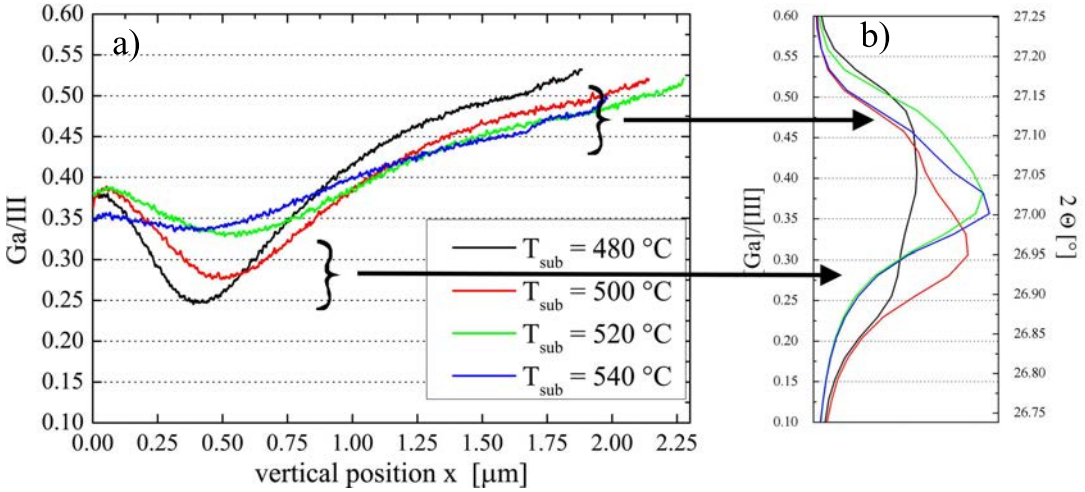


**Figure 4.21.:** a) In-depth profiles of GGI concentration fractions measured by GDOES and (b) x-ray diffraction intensity as a function of the diffraction angle $2\theta$ or the GGI for samples fabricated at different substrate temperatures during the second and third stage of the 3-stage co-evaporation process, as shown in Fig. 4.19. The Ga gradients signature is observed in the x-ray diffractogram: the regions of GGI = 0.3 and GGI = 0.45, to which a relatively large quantity (in terms of thickness) of CIGS material corresponds, result each in an x-ray peak or shoulder.

phases are in accordance to the literature [106, 107, 108] and can be explained by phase transitions following the quasi-binary tie line between $(In,Ga)_2Se_3$ and $Cu_2Se$ as indicated by the dashed line in the ternary phase diagram shown in Fig. 4.22.
In the following possible partial reactions during the 3-stage process as proposed in [132, 133] will be explained and analysed with regard to elemental diffusion in order to explain the development of the in-depth Ga gradient.

### Stage 1

The simple reaction of the deposited educts is given by the following reaction:

$$2(In,Ga) + 3Se \rightarrow (In,Ga)_2Se_3. \tag{4.1}$$

The $(In,Ga)_2Se_3$ precursor at the end of the first stage has been detected by XRD (sec. 4.3.1.2). In-depth analysis by GD-OES showed that the In and Ga concentrations are fairly constant throughout the absorber (sec. 4.3.1.3).

### Beginning of stage 2

During the second stage, Cu and Se react with the prevalent material leading to the succesive formation of the ODC phases as marked in Fig. 4.22, $Cu(In,Ga)_2Se_3$

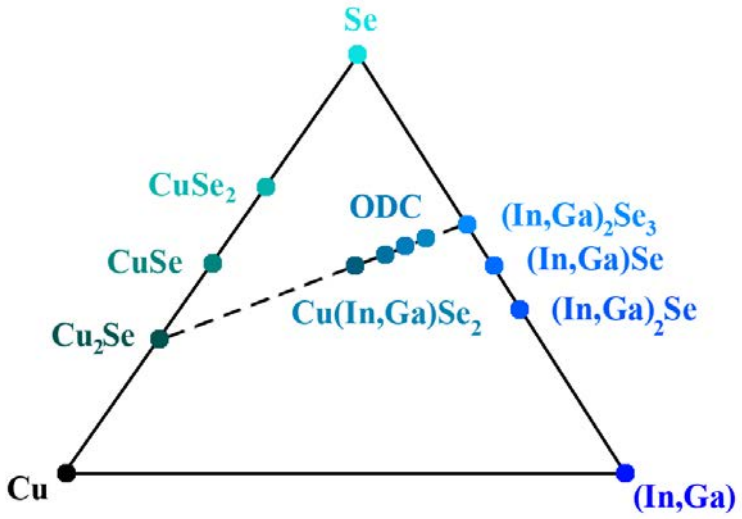


**Figure 4.22.:** Ternary phase diagram of the Cu-(In,Ga)-Se system. The dashed line indicates the pseudobinary tie line between $Cu_2Se$ and $(In,Ga)_2Se_3$. Reproduced from [65].

and $Cu_2Se$. For simplicity we will only consider the ODC phase $Cu(In,Ga)_3Se_5$, also referred to as ordered vacancy compound (OVC). The equivalent reaction path including the ODC phase $Cu(In,Ga)_5Se_8$ can be found in [133]. The following reactions have been proposed:

| | |
|---|---|
| surface: | $Cu + 3(In,Ga) + 5Se \rightarrow Cu(In,Ga)_3Se_5$ |
| bulk: | $3Cu + 5(In,Ga)_2Se_3 \rightarrow 3Cu(In,Ga)_3Se_5 + (In,Ga)$ |
| total: | $3Cu + 5(In,Ga)_2Se_3 \rightarrow 3Cu(In,Ga)_3Se_5 + (In,Ga)$ |

**Table 4.4.:** Possible surface and bulk reactions at the beginning of the $2^{nd}$ stage of the 3-stage process.

The bulk reaction implies that for each 3 Cu atoms diffusing into the bulk, one (In,Ga) atom migrates to the surface and there reacts with the arriving Cu and Se atoms to form the OVC compound (surface reaction). This is an exchange between 3 atoms with +1 valence versus 1 atom with +3 valence guaranteeing the transition from one neutral to another neutral crystal structure [132].

### Mid of stage 2

Here we consider the reaction between the OVC phase with deposited Cu and Se. The following reaction path has been proposed:

| | |
|---|---|
| surface: | $Cu + (In, Ga) + 2Se \rightarrow Cu(In, Ga)Se_2$ |
| bulk: | $3Cu + 2Cu(In, Ga)_3Se_5 \rightarrow 5Cu(In, Ga)Se_2 + (In, Ga)$ |
| total: | $4Cu + 2Cu(In, Ga)_3Se_5 + 2Se \rightarrow 6Cu(In, Ga)Se_2$ |

**Table 4.5.:** Possible surface and bulk reactions in the middle of the second stage of the 3-stage process.

In this case the prevalent precursor material is $Cu(In,Ga)_3Se_5$ and as before for 3 Cu atoms diffusing into the bulk one (In,Ga) atom diffuses to the surface. This diffusion reaction will continue until the hole sample consists of the $Cu(In,Ga)Se_2$ phase. From the beginning of the second stage until this point, an atom exchange of one Cu atom diffusing into the bulk *vs.* 3 (In,Ga) atoms migrating to the surface takes place. It is the medium of diffusion which changes throughout the second stage from $(In,Ga)_2Se_3$ to successively Cu-richer ODCs (here we treated for simplicity only $Cu(In,Ga)_3Se_5$). The preferential surface migration of In over Ga atoms is the reason for the GGI gradient we observe at the end of the second stage (Fig. 4.23). The difference of the surface migration velocity might be due to either a faster surface reaction if the group III atom in the reactions in Tab. 4.4 is In or simply a higher In mobility in the $Cu(In,Ga)_3Se_5$ lattice. Simultaneously a direct interdiffusion of In and Ga will take place and counteract the formation of the Ga gradient. In [133] an increasing Ga diffusivity in the ODC phases as well as in Cu-poor and Cu-rich CIGS with increasing temperature has been reported which explains the increasing homogenity with substrate temperature at the end of stage 2 (Fig. 4.23).

### End of stage 2

The existence of the $Cu_2Se$ layer at the end of stage 2 has been shown in sec. 4.4.1. Its formation can be explained by the simple reaction of Cu and Se at the surface as described by 4.2.

$$2Cu + Se \rightarrow Cu_2Se \tag{4.2}$$

### Beginning of stage 3

A possible reaction describing the consommation of the $Cu_2Se$ layer by adsorbed (In,Ga) and Se is the following:

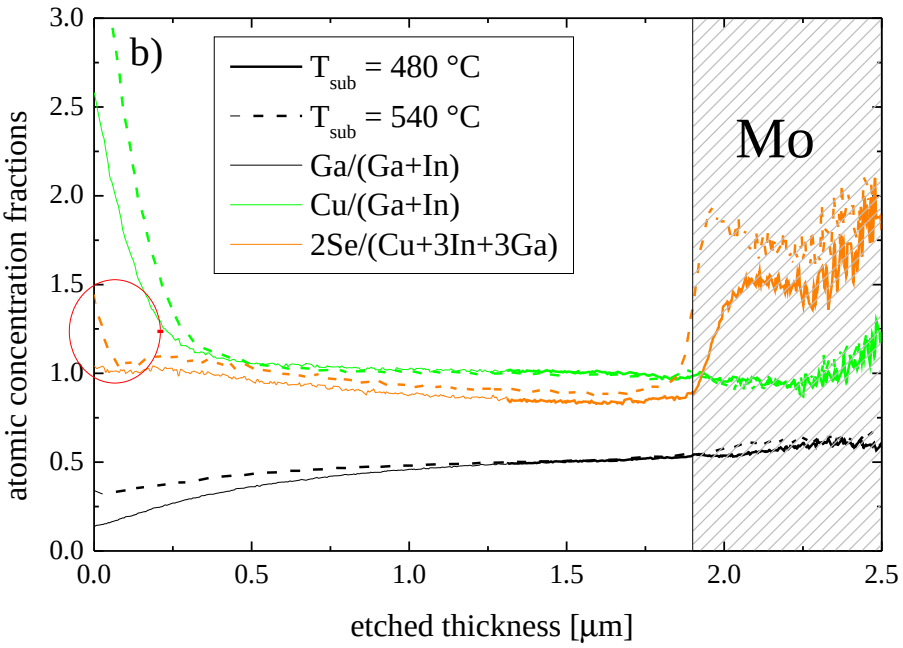


**Figure 4.23.:** Atomic concentration fraction profiles measured by GD-OES at the end of the second stage for 2 different substrate temperatures during the second stage.

$$Cu_2Se + 2(In, Ga) + 3Se \rightarrow 2Cu(In, Ga)Se_2. \tag{4.3}$$

It has been shown in the literature that CIGS grown under Cu-rich conditions has superiour photovoltaic properties such as an increased grain size leading to higher conversion efficiencies [52, 106]. Klenk *et al.* [134] and Gabor *et al.* [135] proposed a vapor-liquid-solid growth mechanism due to a liquid Cu-Se surface phase with increased atom mobilities as a reason. Wada *et al.* [130] proposed a co-existence of the solid $Cu_{2-x}Se$ phase with a liquid CuSe phase for temperatures at about 530 °C and a reaction was proposed in which (In,Ga) atoms in the CuSe solution react directly with the solid $Cu_{2-x}Se$ to form $Cu(In,Ga)Se_2$. Due to the similar crystal structure of $Cu_{2-x}Se$ and $Cu(In,Ga)Se_2$ this reaction can be of topotactic nature where the Se sublattice unchanged and one part of the Cu atoms is dissolved in the liquid CuSe phase and another part is replaced by In atoms. Our observation of no grain boundaries at about 400 nm into the absorber layer for 540 °C and grains extending over the hole layer thickness can be explained by the hypothesis of a topotactic reaction. To go further and definitely confirm the proposed growth mechanism it could be usefull to perform in-situ measurements, for example XRD or Raman spectroscopy.

### End of stage 3

At the end of the third stage the enrichment with the Cu-poor OVC phase by deposition of (In,Ga) and Se can be explained by the following reaction pathway which is the inverse pathway to the proposed reactions for the mid part of stage 2 (Tab. 4.5):

| | |
|---|---|
| surface 1: | $Cu + (In, Ga) + 2Se \rightarrow Cu(In, Ga)Se_2$ |
| surface 2: | $Cu + 3(In, Ga) + 5Se \rightarrow Cu(In, Ga)_3Se_5$ |
| bulk: | $(In, Ga) + 5Cu(In, Ga)Se_2 \rightarrow 2Cu(In, Ga)_3Se_5 + 3Cu$ |
| total: | $4Cu + 2Cu(In, Ga)_3Se_5 + 2Se \rightarrow 6Cu(In, Ga)Se_2$ |

**Table 4.6.:** Possible surface and bulk reactions at the end of the third stage of the 3-stage process.

In analogy to the growth process in stage 2, there is a counterdiffusion of 3 Cu vs. 1 (In, Ga) atom but this time in the opposite direction: The Cu atom migrates to the surface were it can react with adsorbed (In,Ga) and Se atoms to form either $Cu(In,Ga)Se_2$ (surface reaction 1 in Tab. 4.6) or the OVC $Cu(In,Ga)_3Se_5$ (surface reaction 2 in Tab. 4.6). In analogy to the diffusion mechanism in the second stage the In atom is the preferential group III atom participating in the bulk reaction given in Tab. 4.6. This leads to a Ga enrichment at the surface near reagion and explains the front part of the V-shape Ga gradient.

It can be seen in Fig. 4.24 that the substrate temperature during the second and third stage has an influence on the slope of the GGI towards the surface but not on the GGI value itself at the surface, except for 540 °C which will be addressed later. The variation of the slope is rather attributed to a deeper notch at lower $T_{\mathrm{sub}}$ already at the end of the second stage, as seen in Fig. 4.23. Furthermore the surface GGI is superior to the ratio of the deposition fluxes $\frac{\tau_{\mathrm{Ga}}}{\tau_{\mathrm{Ga}}+\tau_{\mathrm{In}}} = 0.28$ in the third stage. This leads to the conclusion that the reaction-driven interdiffusion of Cu *vs.* (In,Ga), more precisely the preference of In compared to Ga to participate in this diffusion-reaction mechanism is rather temperature independent (both in the second (Tab. 4.4 and Tab. 4.5) and third (Tab. 4.6) stage). It is the direct interdiffusion within the group-3 elements which is increased with $T_{\mathrm{sub}}$. Since the material towards the back-contact is exposed during almost the whole deposition process to the direct interdiffusion mechanism, the composition at the back-interface decreases over time and stronger at increased temperature. Directly after the deposition of the material close to the front contact, the sample is cooled down to 200 °C and the temperature-activated interdiffusion of In and Ga is stopped almost immediately after the deposition. Therefore the surface Ga composition is not influenced by $T_{\mathrm{sub}}$.

It would be of interest to perform in-situ measurements of the in-depth Ga composition. This would allow to access the diffusion-reaction mechanisms directly without the overlay of the In,Ga intersiffusion during the rest of the process. While with

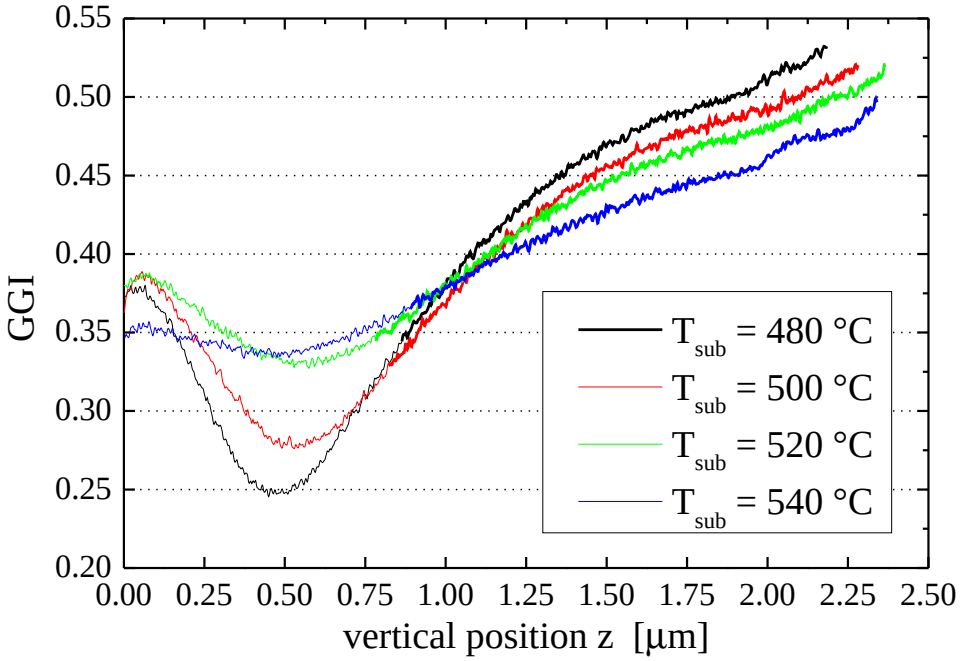


**Figure 4.24.:** GGI in-depth profiles for CIGS absorber layers fabricated by a 3-stage co-evaporation process with varied substrate temperature in the $2^{nd}$ and $3^{rd}$ stage.

GD-OES this is technically not possible, XRD measurements could be used to extract the composition dependent lattice constant as has been shon in chapter 5. The use of different incident angles in the grazing-incidence setup would even allow for in-depth information.

## 4.7. Conclusion

Each stage of the 3-stage process as well as a pre-deposition step have been explained and the influence of several deposition parameters during the different stages has been studied. The substrate temperature $T_1$ during the first stage was found to modify the $(In,Ga)_2Se_3$ precursor morphology. A preferential $(In,Ga)_2Se_3$ precursor orientation with the (330) plane parallel to the surface at a moderate temperature $T_1 \approx 400$ °C leading to a preferential $Cu(In,Ga)Se_2$ orientation with the (220)/(204) planes parallel to the surface, as observed by Mise and Nakada [47], could be confirmed . Besides the crystal orientation, the material seems completely reorganised independent of $T_1$. The In and Ga deposition rates were found to influence the in-depth Ga gradient in the bulk and towards the back interface but to leave to surface-near region unchanged. For high Ga concentrations (samples b-d and f in sec. 4.3.2), an accumulation of small grains with diameters in the order of 100 nm are observed. The resulting increase of the effective grain boundary surface was

interpreted as source of an increased recombination.

The substrate temperature $T_{2,3}$ in the second and third stage is found to be crucial for the material properties of the absorber layer. Break-off experiments at the end of the second stage confirmed a co-existence of the chalcopyrite Cu(In,Ga)$Se_2$ phase with a $Cu_{2-x}Se$ surface layer. At $T_{2,3} = 540$ °C, a deviation of the surface composition from $Cu_2Se$, a more homogeneous surface morphology without holes in the surface-layer as well as a distinct difference of the front Ga gradings of finished absorber layers was interpreted as the existence of a liquid CuSe surface phase on top of the solid $Cu_{2-x}Se$ phase at this temperature. For lower temperatures $T_{2,3} \leq 520$ °C only the $Cu_{2-x}Se$ phase is observed.

The mean grain size increases with increasing $T_{2,3}$ while the in-depth Ga profile becomes more homogeneous. Based on work of Schleussner *et al.* [132] and Rodriguez-Alvarez *et al.* [120] possible reaction paths during the different stages were proposed for bulk and surface. These imply a diffusion of 3 Cu atoms into the bulk for each (In,Ga) atom migrating to the surface during the second stage. In the third stage the inverse process is proposed: For each (In,Ga) atom diffusing into the bulk, one Cu atom migrates to the surface [132]. The observed double Ga gradient was explained by the preferred participation of In over Ga in this diffusion-reaction mechanism.

In order to deepen the understanding of prevalent diffusion mechanisms during the 3-stage process, the development of a detailed numerical model on the basis of the diffusion coefficients of the different elements via certain lattice cites or vacancy defects would be useful. Therefore, the reaction pathways presented here and in [120] and [132] shown in sec. 4.6 can be used as starting point.

We have seen that in CIGS from a 3-stage process, a double Ga gradient is prevalent with an increased Ga concentration towards the front and back surfaces. This brings up the question if there are other material properties which vary as a function of the vertical position in the CIGS layer. To address this question, an innovative approach for the in-depth material characterisation is proposed in the following chapter.

# 5. Characterisation of in-depth inhomogeneities in the CIGS absorber layer

As explained in sec. 4.6, compositional in-depth variations in the CIGS absorber layer are important to achieve high performance photovoltaic devices. Furthermore the in-depth dependence of the preferential orientation in $\alpha$-CIGS as well as the locations of ordered vacancy compound (OVC) phases such as $Cu(In,Ga)_3Se_5$ and $Cu(In, Ga)_5Se_8$ in Cu-poor CIGS are not clear [136], [137]. In this section an alternative approach to perform in-depth characterisation of the absorber layer is proposed. While often the co-evaporation process is interrupted at different points and the intermediate material is analysed, as has been done in this thesis as well (sec. 4.3, sec. 4.4) we have also perform in-depth analysis on the finished absorber layer as it will be used in the solar cell. A co-evaporated CIGS layer was therefore cut to several samples, which then were chemically etched to different thicknesses. The etchings were performed in a $HBr/Br_2$ solution. Its effect on $CuInSe_2$ was first described by Birkmire and McCandless [138] and adapted to improve devices made on $Cu(In,Ga)Se_2$ by Canava et al. [139]. By varying the etching duration, we obtained 5 samples of different thicknesses.Compared to sputtering ablation techniques, this avoids the selective abrasion of atoms with different binding energies. The samples were analysed by Raman spectroscopy and x-ray diffraction. In-depth information is obtained by differentiating the signals of samples with different thicknesses after etching and a first order correction for absorption losses was executed.

## 5.1. Scanning electron microscopy

Fig. 5.1 shows a SEM image of the un-etched absorber layer E0. Some of the CIGS grains extend to the whole absorber layer thickness (A), others only over a certain fraction (B). By combining x-ray fluorescence spectroscopy measurements with selective area diffraction, Li *et al.* showed in [140] that compositional gradients within single grains occur in CIGS from multi-stage coevaporation processes. This is supported by the fact that even in CIGS with columnar grains ranging over the whole absorber thickness, the typical double Ga grading is observed. We focus on the question, if there is a systematic appearance of grains of certain phases and/or orientations at different vertical positions: Are more grains close to the back con-

tact crystallized in a certain direction than near the surface? Do OVC phases like $Cu(In,Ga)_3Se_5$ and $Cu(In,Ga)_5Se_8$ appear preferentially close to the surface, the backcontact or the centre of the CIGS absorber layer?

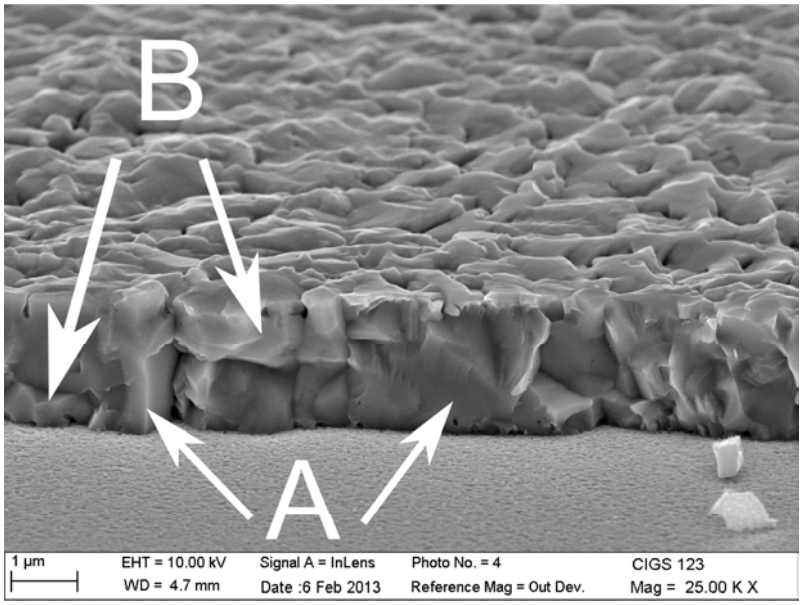


**Figure 5.1.:** SEM image of the complete CIGS absorber layer on top of the molybdenum backcontact.

## 5.2. In-depth composition

The in-depth composition profile was measured by GD-OES (Fig. 5.2). The typical double Ga gradient is observed. While the Ga signal increases towards the front and back surfaces, the In signal shows opposite behaviour. Cu is distributed quite homogeneously while the Se signal increases slightly in direction to the front surface.

Due to the sample roughness, Mo abrasion does not start simultaneously at the whole sputtering area. This leads to an initially smooth increase of the Mo signal at a sputter-depth of 2 $\mu$m and a small artefact in the signal. Due to its low value, the Na concentration is measured with a limited accuracy. Nevertheless, a slight increase of the Na concentration towards the surface ($\approx$ 600 nm) and an accumulation at the back-surface, well correlated to the Mo signal are observed.

## 5.3. Raman spectroscopy

The Raman spectra for the 5 samples, each one normalized to its area (integrated signal from 120 to 300 $cm^{-1}$) are shown in Fig. 5.3. The measured intensities are

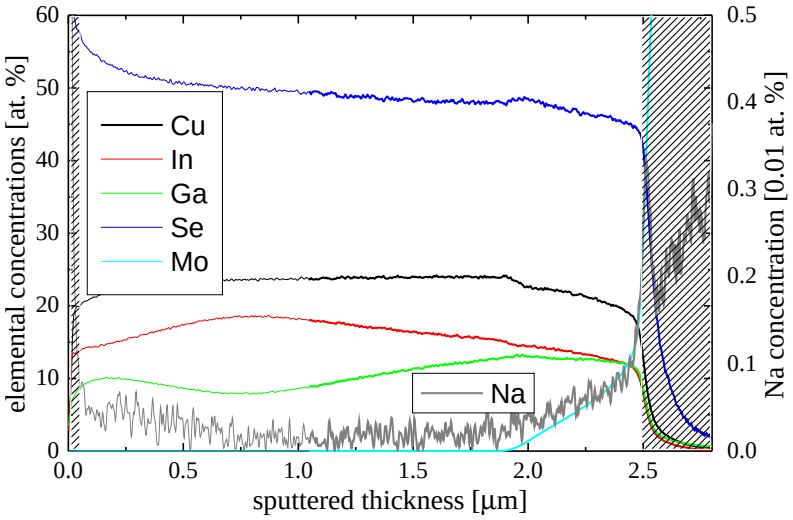


**Figure 5.2.:** Compositional in-depth profile obtained by GD-OES. Left side shaded area is attributed to a sputtering artefact; right shaded area marks the Mo back contact.

considered to be generated close to the surface. It is shown in sec. A.4 that 90 % of the measured Raman signal for an excitation at a wavelength $\lambda = 532$ nm is scattered in the top 85 nm. For all samples, the dominant A1 mode of the $\alpha$-$Cu(In_{1-x},Ga_x)Se_2$ phase is found between 176.5 and 178.2 $cm^{-1}$ while mixed B2/E modes of CIGS appear at approximately 225 and 260 $cm^{-1}$. Furthermore a shoulder like shape is apparent at 150–170 $cm^{-1}$, which is usually attributed to an OVC phase like $Cu(In,Ga)_3Se_5$ or $Cu(In,Ga)_5Se_8$. This is consistent with documented Raman lines (e.g. [137], [141], [106]). There are no intermediate phases visible, such as $Cu_{2-x}Se$ or $(In,Ga)_2Se_3$ which would result in peaks at 260 and 153 $cm^{-1}$ according to [142] and [143]. In [144], Calvo-Barrio *et al.* have conducted in depth Auger microscopy and Raman spectroscopy at $CuInS_2$ samples. While they conducted information about structural quality and residual stress from the in-depth evolution of the A1 mode peak's full width at half maximum, we focus on its shift due to a varying local composition.

As seen in Fig. 5.3, the position of the A1 peak varies between the samples according to their varying Ga content. Between E0 and E1 (from the front surface towards the space charge region), the peak shifts to lower wavenumbers, indicating a decrease of the Ga concentration. From E1 towards the back-surface (E2 to E4), the A1 mode shifts successively to higher wavenumbers, indicating an increase of the Ga concentration towards the back-surface, in agreement to the GDOES measurements. Furthermore, the shoulder at 170 $cm^{-1}$ has the same intensity for samples E0 to E4. Thus a confinement of ordered vacancy compound phases to the surface near region is not confirmed but rather its homogeneous distribution across the absorber thickness is suggested.

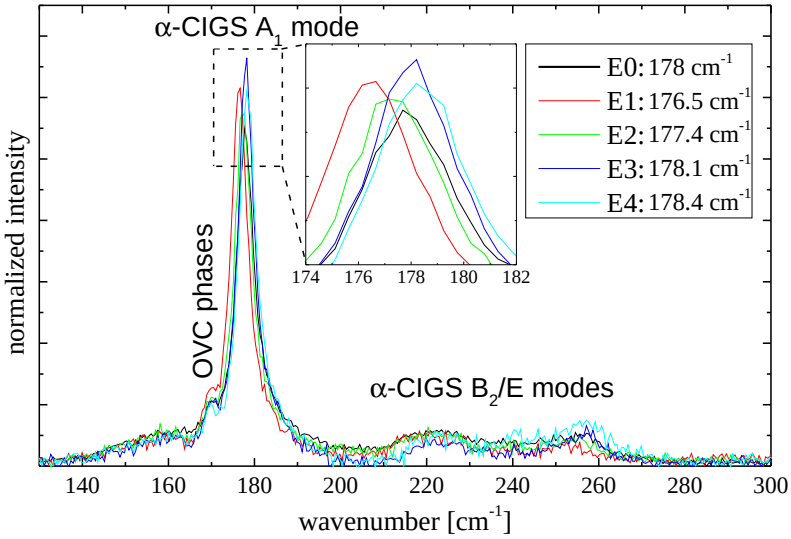


**Figure 5.3.:** Normalized Raman spectra of the samples etched to different thicknesses. The inset is an amplification of the principal peak ($A_1$ mode) and the indicated wavenumber values are the peak positions as extracted from fits to Gaussian curves (not shown here).

## 5.4. X-ray diffraction

Fig. 5.4 shows an overview of the XRD diffractograms of all 5 samples. For the samples E0–E3, we identified the CIGS diffraction peaks corresponding to the (112), (220)/(204), (312)/(116), (400)/(008), (332)/(316), (424)/ (228) and (400)/(008) lattice planes. For sample E4, only the CIGS lattice planes (112), (211), (220)/(204) and (312)/(116) parallel to the surface could clearly be identified. Other intensities were too low to identify further orientations, probably due to the highly reduced sample thickness. The CIGS peaks are shifted to slightly higher angles compared to the values from the ICDD definition file 00-035-1102. This is attributed to a higher global Ga concentration for our sample (mean GGI = 0.4) as compared to the sample in the reference file (GGI = 0.3).

A systematic variation of the peak shape between the different samples is observed, shown for the (112) peak in Fig. 5.5. The deeper the sample was etched (E0→E4), the thinner the XRD peak becomes. Furthermore, the position of maximal intensity shifts to larger angles $2\Theta$. By subtracting the XRD intensities of samples with different etching durations, we gain information about the removed material. The fact that deeper in the sample, the incident X-ray intensity is reduced by diffraction and absorption on atom layers above (closer to the surface) has been corrected by multiplying the subtracted term with an angular dependent correction factor $k_i(2\Theta)$. This results in a corrected intensity difference $\Delta I_{i,i+1}$ between samples $E_i$ and $E_{i+1}$

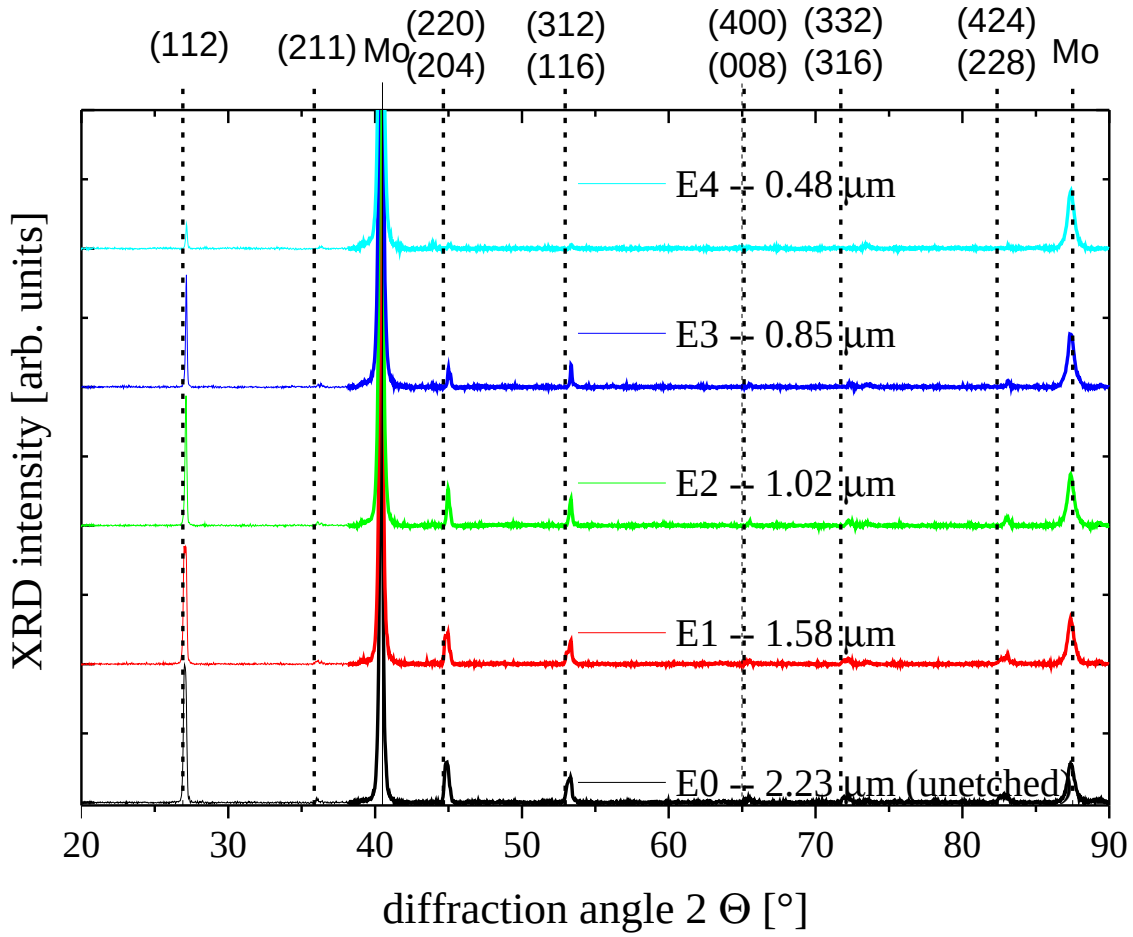


**Figure 5.4.:** X-ray diffractograms performed on etched CIGS samples with indication of thickness of remaining layer. Dashed vertical lines represent $Cu(In_{0.7}Ga_{0.3})Se_2$ peak positions from ICDD definition file 00-035-1102 [39].

given by 5.1 with the diffraction intensity $I_i$ of sample $E_i$ for $x_i = 0, 1, 2, 3$.

$$\Delta I_{i,i+1} = I_i - I_{i+1}/k_i^2(\Theta) \tag{5.1}$$

The correction factor $k_i(2\Theta)$ is based on an exponential decline of the signal intensity with path length. Its angular dependence is given by $k_i(\Theta) = k_i(90°)^{1/sin(\Theta)}$. Since the Mo back contact was the same for all samples, as well as the sample size and diffraction optics, its diffraction peak was used to calculate the correction factors: $k_i(20.2°)$ has been set to the value that resulted in equal diffraction intensities for the Mo diffraction peak at $2\theta = 40.4°$ for the samples $E_i$ and $E_{i+1}$. Afterwards the correction factor was interpolated for all diffraction angles using 5.1.

In Fig. 5.9, the corrected intensity differences between samples E0 and E1 (black line), E1 and E2 (red), E2 and E3 (green) and E3 and E4 (blue) are shown. These

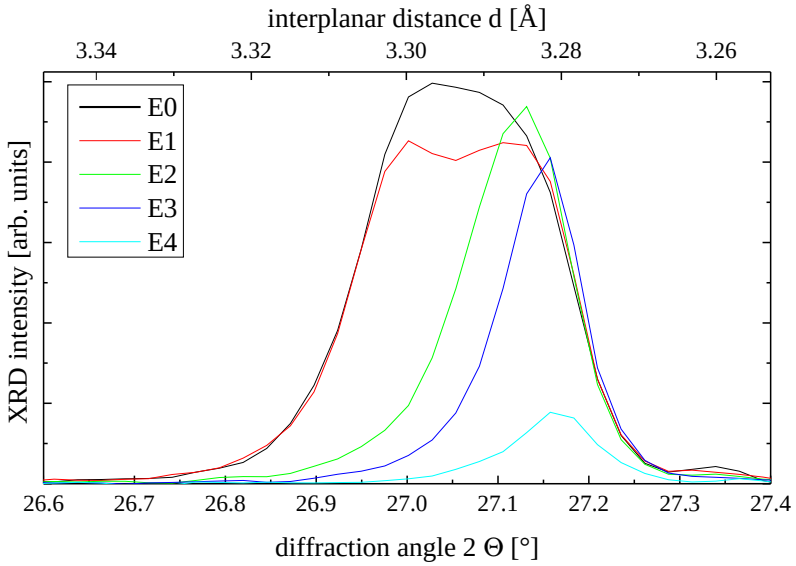


**Figure 5.5.:** (112) peaks of differences of diffractograms performed at CIGS layers E0–E4 as a function of diffraction angle and interplanar distance.

differences of diffractograms can be interpreted as diffractograms of the removed material between two samples. The preference of the (112), (220), (204), (312) and (116) planes to be oriented parallel to the surface is calculated for different vertical positions by normalizing the difference between the corresponding peak intensity and the corresponding peak intensity of powder CIGS to the powder intensity: $(I_{hkl} - I_{\text{powder}})/I_{\text{powder}}$. The XRD data for CIGS powder was taken from the literature [145]. The results are shown for all 4 difference diffractograms in Fig. 5.6.

At all 4 vertical positions, the CIGS is preferentially oriented with the (112) and (220) planes parallel to the surface, while the intensities for the (204), (312) and (116) planes are suppressed compared to the powder intensities, the intensity of refraction at the (204) plane to a quite large extent. Towards the Mo back contact, more grains are oriented with the (312) planes parallel to the surface while less grains are oriented with the (220) and (116) planes parallel to the surface.

## 5.5. Discussion

As we have seen the initial growth of grains with the (312) planes in plane with the surface close to the Mo back contact is supressed throughout the growth by grains with the (116) and (220) planes parallel to the surface towards the surface. While columnar grains do not contribute to this change in preferential orientation, the rather small grains which do not traverse the whole sample thickness, change their preferred orientation throughout the deposition process as described above. The orientation of the different lattice planes in the tetragonal $Cu(In,Ga)Se_2$ unit cell is shown in Fig. 5.7.

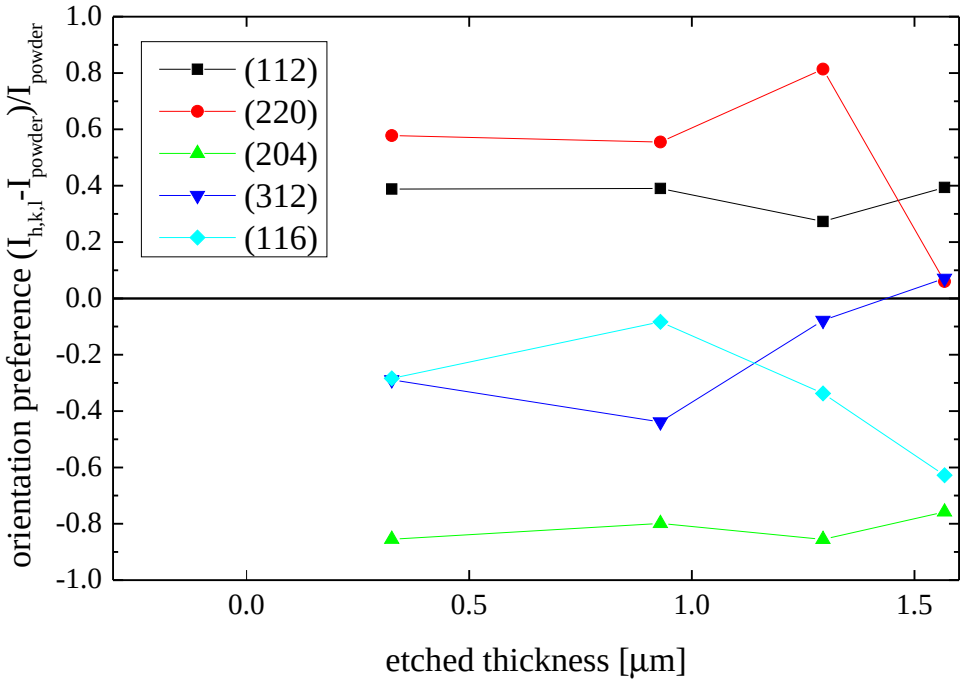


**Figure 5.6.:** Relative variation between measured XRD intensities and powder diffraction intensities for diffraction at the most important lattice planes (112), (220), (204), (312) and (116). Powder data was taken from [145].

The planes (220) and (204) as well as (312) and (116) are very similar to each other, in the corresponding cubic zinc blende lattice they would be identical. 2D views of the different planes are shown in Fig. 5.8.

The (220) and (204) planes are non-polar, all the indicated Cu, group III and Se atoms lie in one identical plane. For the polar (112), (312) and (116) planes, the indicated Se atoms lie slightly underneath the plane of Cu and group III atoms shown in Fig. 5.8 (at a distance of $d/8$ with the space diagonal $d = (2a^2+c^2)^{1/2}$ of the CIGS unit cell). For (112) in the surface plane, one of the 4 tetrahedral bonds between Se and one of the metal atoms is parallel to the growth direction. For (220) and (204) in plane, two of these tetrahedral bonds lie in plane thus perpendicular to the growth direction. Regarding Fig. 5.8 it can be seen that grain boundaries between (220)/(204) as well as (312)/ (116) planes can be formed by an ordered arrangement of $Cu_{III}$ and $III_{Cu}$ antisite defects at the interface or alternatively they can share an identical Se plane (the Se sublattice is identical for (220) and (204) as well as for (312) and (116) planes as seen in Fig. 5.8). For other types of grain boundaries between the 5 main orientations discussed here, i.e. (112)/(220 or 204 or 312 or 116), (220)/(312 or 116) and (204)/(312 or 116), a reorganisation of the crystal structure at the grain boundary would be necessary and this type of grain boundary should be energetically less favourable. This explains well our observation from Fig. 5.6 that CIGS grains with the (116) plane parallel to the surface tend to grow on top

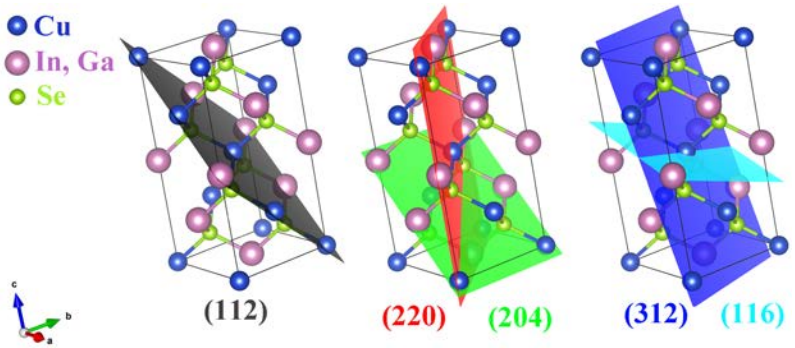


**Figure 5.7.:** Orientation of the most prevalent lattice planes in the chalcopyrite Cu(In,Ga)Se2 unit cell. Visualized with VESTA [38].

of grains with (312) planes parallel to the surface. The Ga content of the removed CIGS material can be estimated from the peak position of the difference curves, e.g. from the (112) peak shown in Fig. 5.9. The two top layers (black and red curves) are notably broader than the $3^{rd}$ and $4^{th}$ layers (green and blue curves), indicating a larger compositional gradient and possibly the existence of different phases in the 2nd layer (red). From each peak position $2\theta$, the inter-planar distance d can be determined using the Bragg diffraction equation with the wavelength $\lambda = 1.5406$ Å of the incident Cu-$K_\alpha$ radiation. The lattice constants $a$ and $c$ can then be calculated using at least two diffraction peaks with different miller indices h, k, l simultaneously (Rietveld refinement). This has been done using a least square fit method for each of the difference spectra with commercial software.

From x-ray diffraction measurements on $CuInSe_2$ and $CuGaSe_2$ samples fabricated by a similar co-evaporation process and in the same reactor as samples E0–E4, we deduced the relation in 5.2 and 5.3 between the lattice parameters $a$ and $c$ and the Ga content $x$ (= GGI) in CIGS. These relations are very close to relations reported in the literature, e.g. $a = 5.783\ \text{Å} - 0.171\ \text{Å} \cdot x$ and $c = 11.618\ \text{Å} - 0.586\ \text{Å} \cdot x$ [144] and were used to estimate the lattice parameters a and c of the tetragonal CIGS lattice

$$a = 5.780\ \text{Å} - 0.173\ \text{Å} \cdot x \tag{5.2}$$

$$c = 11.604\ \text{Å} - 0.614\ \text{Å} \cdot x \tag{5.3}$$

The lattice parameters and resulting GGI ratios $x$ for the different samples are listed in Tab. 5.1. By atomic absorption spectroscopy of each $HBr/Br_2$ solution after etching, the quantity of the removed material and the etched thickness was calculated. For each curve in Fig. 5.9 we took the mean etched thickness of the 2 included samples (E0 and E1 for the black curve, E1 and E2 for the red curve etc.)

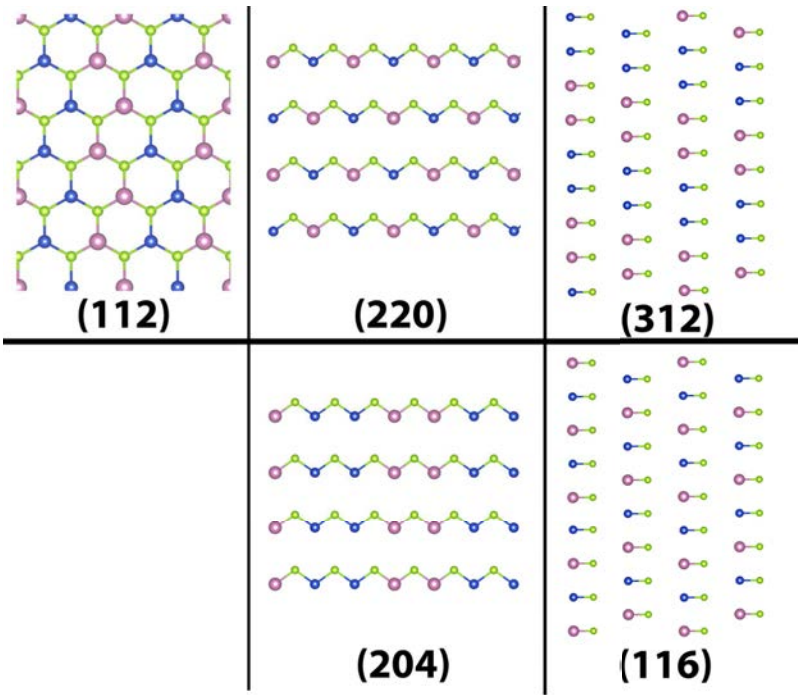


**Figure 5.8.:** 2D projections of the most prevalent lattice planes in Cu(In,Ga)$Se_2$. Cu atoms are indicated in blue, group III elements in magenta and Se atoms in green. For the polar (112), (312) and (116) planes, the indicated Se atoms lie slightly underneath the plane of Cu and group III atoms (at a distance of $d/8$ with the space diagonal $d = (2a^2 + c^2)^{1/2}$ of the CIGS unit cell). Visualized with VESTA [38].

as the corresponding vertical position. The same procedure was applied to the x-ray diffractogram of E4. This results in a GGI profile consisting of 4 points, shown together with the GGI GDOES profile in Fig. 5.10.

The Ga content calculated by XRD from $a$ and $c$ qualitatively matches the GGI gradient measured by GDOES, indicating an increased Ga content towards the front and back contacts. This indicates a homogeneous degree of crystallinity. The curve calculated from lattice parameter c matches even quantitatively quite well with the GDOES results.

| | $a$[Å] | $c$[Å] | $x$ from $a$ | $x$ from $c$ |
|---|---|---|---|---|
| E1-E0 | 5.709 | 11.350 | 0.410 | 0.414 |
| E2-E1 | 5.720 | 11.382 | 0.347 | 0.362 |
| E3-E2 | 5.699 | 11.349 | 0.468 | 0.415 |
| E4-E3 | 5.695 | 11.317 | 0.491 | 0.467 |

**Table 5.1.:** Mean lattice parameters and resulting Ga ratios for the differentiated diffractograms of the samples E0–E4.

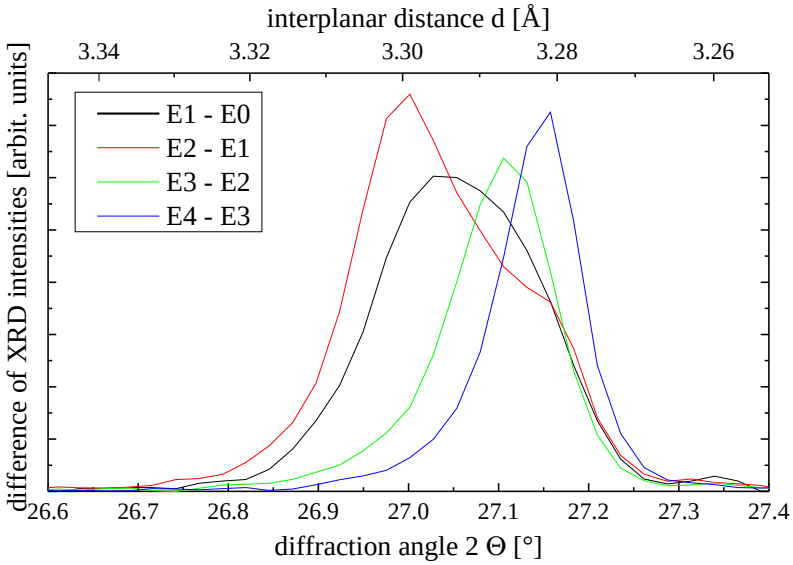


**Figure 5.9.:** Differences of (112) peak intensities for diffractograms of CIGS layers E0–E4 as a function of diffraction angle (bottom axis) and interplanar distance (top axis).

## 5.6. Conclusion

By chemical etching of CIGS absorber layers in a $HBr/Br_2$ solution we obtained layers of successively decreasing thickness. The differential intensity signals provided a clear view on in-depth material properties such as apparent chemical phases, preferential crystal orientation, local lattice parameter and Ga concentration. Raman measurements showed no intermediate phases such as $Cu_{2-x}Se$ or $(In,Ga)_2Se_3$. A varying Ga content is observed and confirmed by GD-OES. The OVC peak is not confined to the surface near region but observed across the whole sample thickness. The preferential orientation with the (112) plane parallel to the surface and the minor orientation of (204) planes parallel to the surface do not change with vertical position. Towards the Mo back contact, orientation with (312) in plane increases and the orientation of (220) planes parallel to the surface decreases both to about the powder value while no grains are oriented with the (116) planes parallel to the surface. This suggests a preferential growth of grains with (116) planes parallel to the surface on top of grains with (312) planes parallel to the surface during the evaporation process. This can be explained by the fact that the boundary between (312) and (116) planes can be formed by an ordered arrangement of $Cu_{III}$ and $III_{Cu}$ antisite defects at the interface or alternatively the (312) and (116) planes can share an identical Se plane (the Se sublattice is identical for (312) and (116) planes as seen in Fig. 5.8) and thus the boundary between (312) and (116) planes should have a relatively low formation energy. The GGI atomic concentration ratio has been calculated at 4 different vertical positions using Vegard's law. The results confirm a double Ga gradient. The Ga concentrations calculated from the lattice parameter

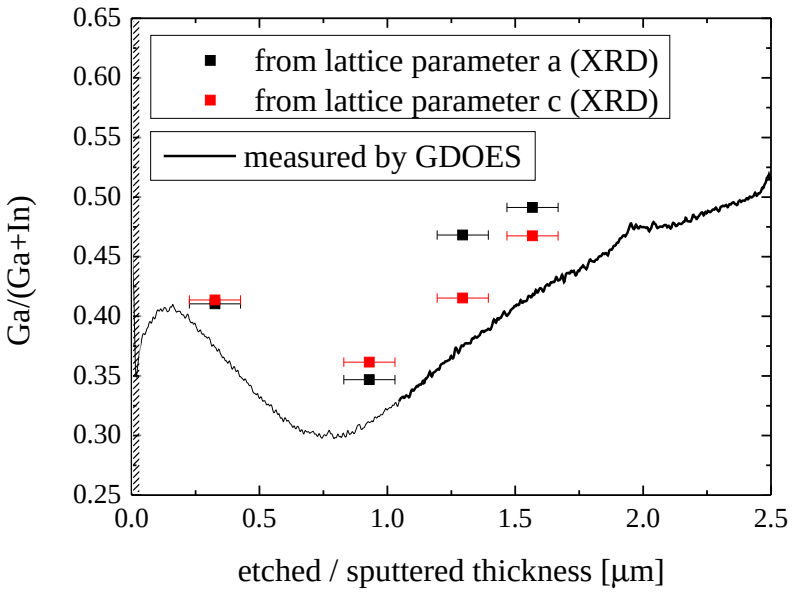


**Figure 5.10.:** GGI profile calculated from XRD measurements at etched samples as described in the text and from GDOES. The error bars are estimated from the sample roughness as observed in the SEM image in Fig. 5.1.

c result even qualitatively in a profile consistent with the GDOES results.

After the detailed study of the deposition process and its influence on the absorber layer properties in this part, the link between the absorber layer and the opto-electronic properties of a finished solar cell will be established in the following chapter.

# 6. Devices

In this chapter we study the opto-electronic properties of complete devices in the typical Mo/CIGS/buffer/i-ZnO/ZnO:Al structure. The goal is to understand which physical mechanisms dominate the carrier recombination in devices with a graded band gap energy throughout the absorber thickness and which influence particular band gap profiles have on light absorption and carrier transport. We will furthermore adress the question of the influence of the conduction band offset at the absorber/buffer layer interface on the carrier transport and recombination. Therefore two sets of absorber layers were fabricated:

1. A set of 4 absorber layers for which a varied substrate temperature during the second and third stage led to different depths of the V-shape Ga-gradient in the bulk of the absorber layer.
2. A set of 7 absorber layers for which only the In and Ga deposition rates in the second stage of the 3-stage process were varied in order to change the surface-near Ga content and thus essentially the conduction band position. By finishing these layers with CdS as well as Zn(O,S) buffer layers, also the energy band structure in the buffer layer has been varied.

For each of the sample sets all further deposition parameters were kept constant in order to change as few material properties as possible except for the local Ga and In composition. In order to investigate if other material properties have changed we conducted X-ray fluorescence, X-ray diffraction and scanning electron miscroscopy measurements on these absorber layers. For the first set of samples, the material characterization results have been presented in sec. 4.5. The integral composition varied only marginally. We have observed that the X-ray diffraction peaks were influenced by the varying lattice constant due to the different Ga gradients throughout the absorber layer. Furthermore the mean grain size increases for increasing substrate temperature / more flat Ga-gradient. With the applied measurement techniques no further particular difference was observed. The material characterisation results for the second set of samples can be found in Appendix C. SEM images show no distinctive difference between the grain size and grain structure of the different absorber layers. The preferred orientation does not vary significantly as can be seen in the XRD diagram. A detailed peak analysis of the (112) peak showed that the peak-width and position correlates with the variation of the lattice parameter due to the Ga gradient.

The strongest observed difference of the investigated absorber layers is the in-depth Ga gradient. Nevertheless, the differences in grain size needs to be taken into account for the interpretation of the opto-electronic cell properties. Even though in CIGS

they are commonly believed to be passivated by the prevalent Na [146] they might still represent a location of increased carrier recombination compared to the bulk.

## 6.1. Band gap gradient in the absorber layer

During the 3-stage co-evaporation process a so-called double Ga gradient or V-shape gradient (*i.e.* an increased Ga concentration towards the front and the back surface and a relative minimum inbetween) is obtained intrinsically [121, 118, 48, 147] which means without changing the In and Ga deposition rates throughout the first or third stage to actively control the gradient. Device simulations have shown that the active optimisation of the Ga gradient can improve the device efficiency [13, 14, 148, 149]. In general an increased Ga content towards the front (space-charge region) and the back interfaces are considered to be beneficial due to a reduced recombination in the SCR and at the interfaces while a relatively low bandgap inbetween increases light absorption and the short circuit current density [14]. The exact quantitative band gap gradient leading to an optimal device performance is not known. It will depend on the prevalent recombination mechanisms and thus can change for different deposition conditions.

In order to optimise the Ga gradient for our process, various different in-depth Ga gradients have been obtained in the context of my thesis. Therefore various deposition parameters have been varied. In this chapter, we will focus on the variation of the Ga-gradient in the absorber layer due to the variation of the substrate temperature and its influence on the solar cell properties. The deposition process and the characterisation of the absorber layer material has been presented in sec. 4.5. As we have seen there, the substrate temperature during the second and third stage has a significant influence on the in-depth Ga gradient of the final CIGS absorber layer. On the basis of these absorber layers solar cells have been fabricated by the deposition of a CdS buffer and i-ZnO/ZnO:Al transparent front contact. The CdS buffer as well as the i-ZnO/ZnO:Al layer were each deposited in one single run, guaranteeing that observed variations can be attributed to the absorber layer. Each sample was mechanically scribed into 36 cells of 0.1 $cm^2$ surface each.

### 6.1.1. Solar cell characteristics

External quantum efficiency measurements are shown in Fig. 6.1. It can be seen that the long-wavelength absorption edge is shifted to higher wavelengths $\lambda$ for a deeper Ga gradient (the Ga gradient becomes deeper with lower $T_{sub}$) indicating a variation of the optical band gap energy. Furthermore, a higher quantum efficiency at $\lambda \approx 900$ nm is observed for the two relatively flat Ga profiles of the samples fabricated at 520 and 540 °C. For $\lambda < 850$ nm, the EQE for all four samples superpose very well.

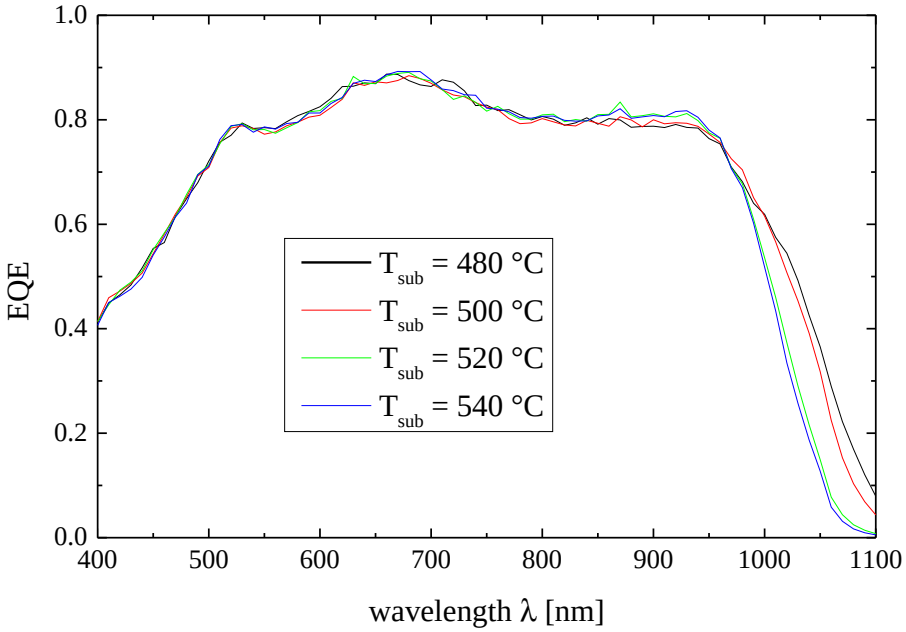


**Figure 6.1.:** External quantum efficiency of the solar cells with the 4 CIGS absorber layers with varied deepness of the Ga gradient as shown in Fig. 6.4a.

The solar cell parameters of each cell were extracted from current-voltage measurements under standard test conditions. The values for the best cell of each sample are shown in Fig. 6.2. The best cell values are shown in order to be able to better compare with the EQE curves which were measured for the best cell of each sample as well. Anyway the homogeneity is very high (standard deviations $< 2$ % of the best cell values for $J_{sc}$, $V_{oc}$ and FF) and the tendencies of best cell and mean value are the same for each sample.

The open circuit voltage as well as the short circuit current density decrease with increasing process temperature / more flat Ga profile. The variation of the fill factor is very small (1.6 % relative while $\eta$ varies by 5 % relative) and does not vary systematically with the substrate temperature. The efficiency in result decreases as well with increasing $T_{sub}$.

### 6.1.2. Discussion and conclusion

We focus on the principal parameters that change with the grading depth: the $V_{oc}$ and the $J_{sc}$. In the following we will try to illustrate the reasons for their increase with increasing band gap gradient depth.

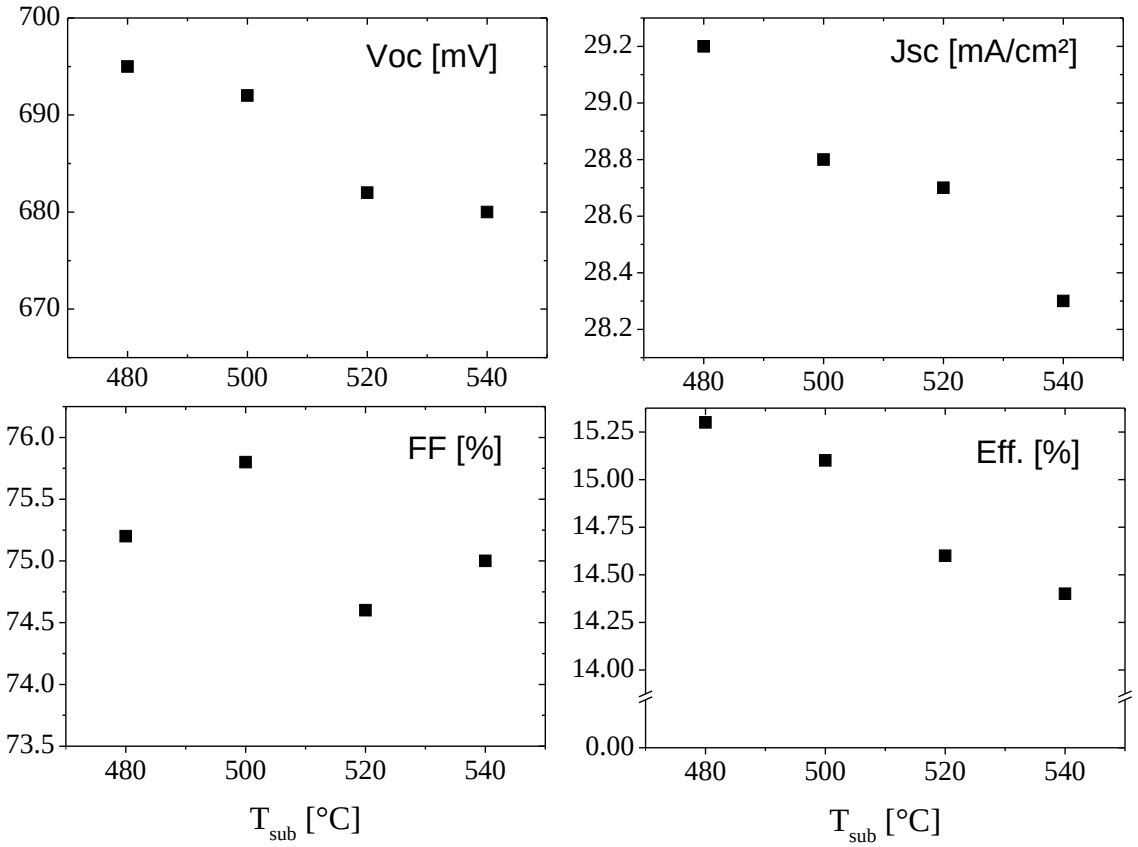


**Figure 6.2.:** Solar cell parameters of the solar cells fabricated with the 4 CIGS absorber layers with varied deepness of the Ga gradient as shown in Fig. 6.4a.

#### 6.1.2.1. Light absorption in graded absorber layers

The short circuit current density $J_{sc}$ is dominated by the decreasing optical band gap with substrate temperature. The difference between the $J_{sc}$ values for 500 and 520 °C is relatively low because the band gap effect is partly compensated by an increased quantum efficiency at $\lambda = 900$ nm for $T_{sub} = 520$ °C. In order to understand the influence of a double grading on the short circuit current density, the absorption of the AM1.5g spectrum has been calculated in the case of a material with and without a double band gap gradient. As usual approach for direct band gap materials such as CIGS, an absorption coefficient in the form of $\alpha = A \cdot \sqrt{E - E_g}$ is assumed. It is reported in the literature that an absorption constant $A = 5 \cdot 10^4 \mathrm{cm}^{-1}\mathrm{eV}^{-1/2}$ leads to the typically measured absorption coefficients for CIGS [150]. The absorption constant for the CdS layer has been extracted from fits of experimental absorption measurements of CdS on glass: $A = 10^5 \mathrm{cm}^{-1}\mathrm{eV}^{-1/2}$.

In Fig. 6.3 two materials with identical mean band gaps of 1.23 eV, a typical value for CIGS, are compared. On the left side, a constant band gap is assumed while on the right side, a double Ga gradient with two different band gaps close to the

interfaces (1.31 eV) and in the center (1.15 eV) as seen in Fig. 6.3 (d) has been assumed. In Fig. 6.3 (b) and (e), which show the photon flux [$\mathrm{cm}^{-2}s^{-1}\mathrm{eV}^{-1}$] as a function of penetration depth (first 0.05 $\mu$m are CdS, following 2 $\mu$m are CIGS) and photon energy, the absorption of the low band gap material for the graded material in (e) can be seen at $z \approx 0.8\mu$m (red arrow). In (c) and (f) the total absorption of the initial spectrum in the CIGS and the CdS layers are shown for both gradings. As can be seen for the graded absorber layer (f), the absorption edge is less steep but starts already at 1.15 eV (red arrow) instead of 1.31 eV for the ungraded case. The result is an increase of the ideal short circuit current density from 34.71 mA/cm² for the ungraded layer to 36.06 cm² for the graded layer.

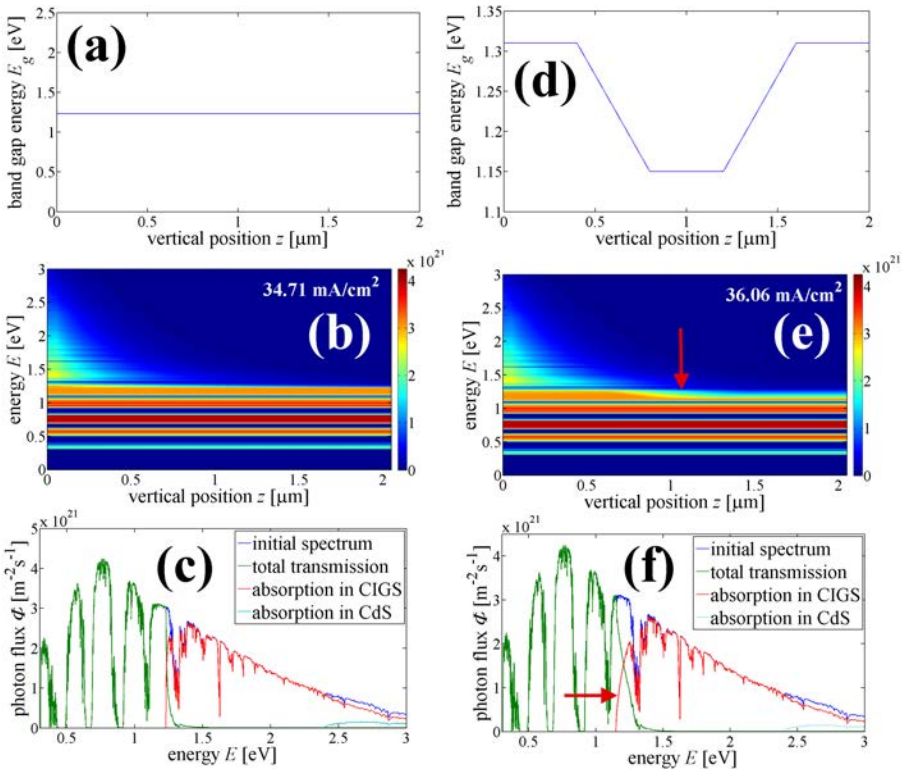


**Figure 6.3.:** Calculated absorption of the AM1.5g spectrum by a material (in our case CIGS) with a constant band-gap (a) and a double-graded band gap material (d). (b) and (e) show the photon flux [$\mathrm{cm}^{-2}s^{-1}\mathrm{eV}^{-1}$] as a function of penetration depth (first 0.05 $\mu$m are CdS, following 2 $\mu$m are CIGS) and photon energy for the non-graded and graded material respectively. The spectrum at $z = 0$ is the AM1.5g spectrum. The increased absorption in the CIGS layer is visible at $z \approx 0.8\mu$m (red arrow) where the band gap decreases from 1.31 to 1.15 eV. In (c) and (f) the total absorption of the initial spectrum in the CIGS and the CdS layers are shown. For the graded absorber layer (f), the absorption edge is less steep but starts already at 1.15 eV (red arrow) instead of 1.31 eV for the ungraded case.

These results show the beneficial effect of a double band gap grading: With the same mean band gap energy, corresponding in first order to the mean Ga composition, the $J_{sc}$ could be improved by 1.35 mA/cm². This gain will be further improved by a deeper band gap in the central part of the absorber layer and this explains the increase of $J_{sc}$ we observe with increasing band gap depth (lower deposition temperature $T_{sub}$). Since the thickness of the low-gap material is relatively low (in this case 400 nm), photons just above the low bandgap are not completely absorbed. This leads to a less steep absorption edge, as marked by the red arrow in Fig. 6.3 (f). A broader band gap minimum would steepen the absorption edge and thus increase as well the $J_{sc}$.

The local decrease of the band-gap energy is a potential source of charge carrier recombinations and for the cell optimisation the critical question is if the absorption gain can dominate the increase in carrier recombination. Therefore we will now adress the carrier recombination in the graded absorber layer.

#### 6.1.2.2. Carrier recombination in graded absorber layers

The decrease of the open circuit voltage with increasing $T_{sub}$ indicates an increase of at least one of the prevalent recombination mechanisms. We have seen in sec. 2.3 that the recombination rate in a semiconductor is generally related to its band gap energy. The only position where $E_g$ decreases with increasing $T_{sub}$ is towards the back-surface. Therefore we attribute the $V_{oc}$ losses to an increased recombination velocity at the back-interface due to a decreased $\Delta E_g^{back}$. Indeed in Fig. 6.4a we see that the open circuit voltage increases with $\Delta E_g^{back}$. The increase of $V_{oc}$ by only 15 meV for an increase of $\Delta E_g^{back}$ by 80 meV indicates that a second recombination mechanism exists and the back-interface recombination is not the dominating recombination mechanism. The homogenization of the GGI profiles with temperature as seen in Fig. 6.4a leads to a decrease of the conduction band diffusion barrier $\Delta E_g^{back}$ (difference between minimum band gap energy and band gap energy at the back-interface, as indicated in Fig. 6.4) towards the back surface.

If we take into account expression 2.26 for the saturation current density for back-interface recombination we can discuss the influence of the back-interface recombination for the two extreme cases:

1. If the absorber layer thickness $d$ is much higher than the electron diffusion length $L_{n,a}$ in the CIGS bulk material ($d \gg L$ ), the effective diffusion length (2.25) becomes $L_{eff} = L_{n,a}$.
2. For the contrary ($L_{n,a} \gg d$), the effective diffusion length becomes $L_{eff} = D/s$.

In the first case, the minority charge carriers recombine before arriving at the back-interface and thus the saturation current density is independent of the back-interface recombination velocity $s$ and given by

$$J_0^{d \gg L} = q \frac{D N_c N_v}{N_A L_{n,a}} \exp(-E_g/kT) \tag{6.1}$$

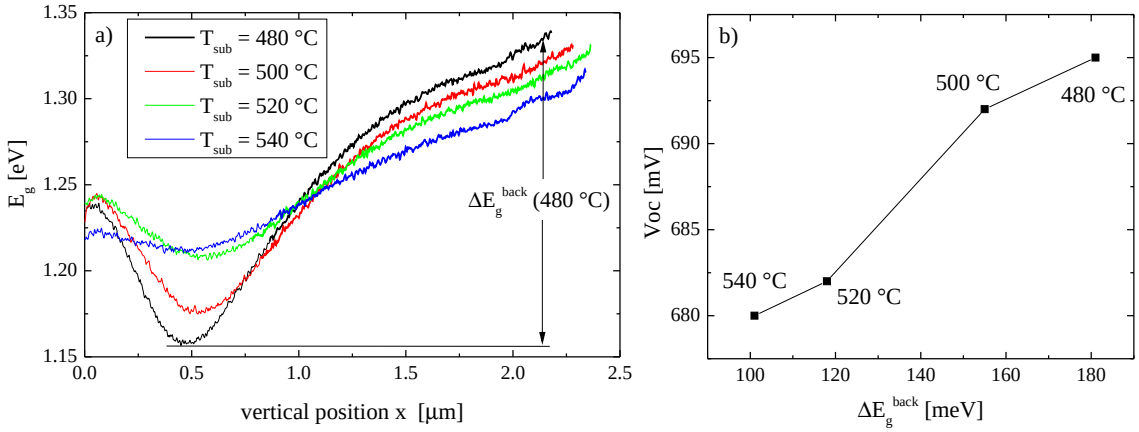


**Figure 6.4.:** (a) Band-gap profiles and (b) open circuit voltage vs. electron barrier towards the back interface.

In the second case, the quasi-fermi level splitting $\Delta\mu$ is constant over the absorber layer thickness [151]. The minority electrons do not recombine before arriving at the back-interface and thus $J_0$ is dependent on $s$. If we make the assumption of a thermally activated back-interface recombination rate $s = s_0 \exp\left(-\frac{\Delta E_{\mathrm{g}}^{\mathrm{back}}}{kT}\right)$ with the back-interface barrier as activation energy [95], expression 6.2 is obtained for $J_0$. Recombination in the bulk is considered to be dominant at the position of the minimum band gap energy. Therefore $E_{\mathrm{g}} + \Delta E_{\mathrm{g}} = E_{\mathrm{g}}^{\mathrm{back}}$ can be used.

$$J_0^{L\gg d} = q\frac{DN_{\mathrm{c}}N_{\mathrm{v}}}{N_A D} \cdot s \cdot \exp(-E_g/kT) = q\frac{N_{\mathrm{c}}N_{\mathrm{v}}s_0}{N_A} \cdot \exp(-E_{\mathrm{g}}^{\mathrm{back}}/kT) \tag{6.2}$$

We define the prefactor in eq. 6.2 as $J_{00}^{L\gg d} = q\frac{N_{\mathrm{c}}N_{\mathrm{v}}s_0}{N_A}$. According to eq. 2.43 in the extreme case of $L \gg d$ a plot of $V_{oc}$ vs. $E_{\mathrm{g}}^{back}$ should lead to a straight line with a slope of unity and an intercept of $-kT \cdot \ln(J_{sc}/J_{00}^{L\gg d})$. The experimental values and a linear fit with fix slope of unity are shown in Fig. 6.5.

It can be seen that the measured values for $V_{\mathrm{oc}}$ roughly follow the fit with a slope $m = 1$. This indicates that the increase of $V_{\mathrm{oc}}$ can be explained by a reduction of the back-interface recombination velocite $s$ with increasing back-side Ga gradient. Since the assumption $L_{n,\mathrm{a}} \gg d$ is not necessarily true for CIGS, the influence of $L_{n,\mathrm{a}}$ and $D/s$ in expression 2.25 on the effective diffusion length $L_{n,\mathrm{a}}$ are studied. In Fig. 6.6 the effective diffusion length is plotted against the electron bulk diffusion length $L_{n,\mathrm{a}}$. It is interesting to note that for high values of $L_{n,\mathrm{a}}$, $L_{\mathrm{eff}}$ converges only for $D/s \geq 0.001$ to $D/s$. For lower values of $D/s$, $L_{\mathrm{eff}}$ does not decrease futher than $L_{\mathrm{eff}} \approx 2 \cdot 10^{-4}$ cm $= 2$ $\mu$m. This is due to the fact that under the assumptions of $L_{n,\mathrm{a}} \gg d$ and $sL_{n,\mathrm{a}}/D \gg 1$, equation 2.25 results in 6.3. In these limits, $\tanh(d/L_{n,\mathrm{a}})$

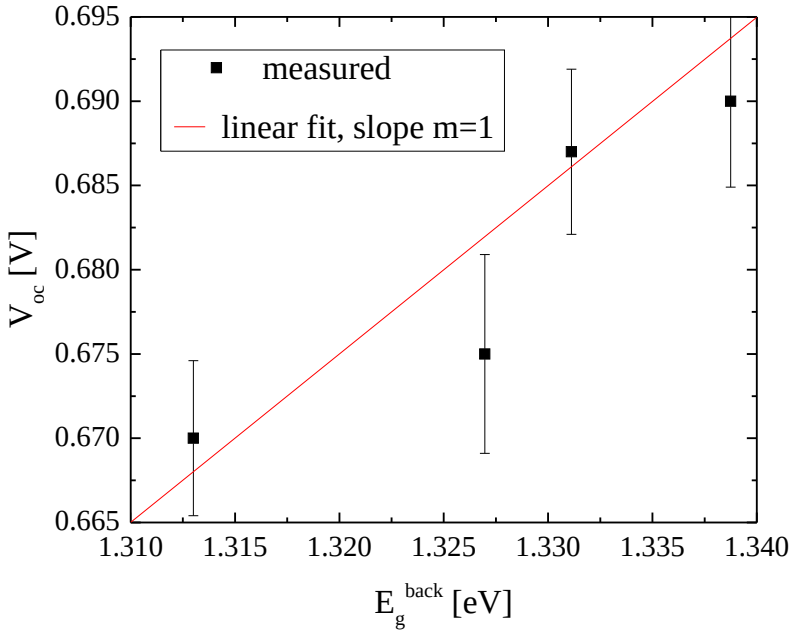


**Figure 6.5.:** Plot of the open circuit voltage $V_{oc}$ *vs.* the bang gap energy $E_{\mathrm{g}}^{\mathrm{back}}$ at the back-interface. The red line corresponds to a linear fit with a fixed slope $m = 1$.

has an influence on $L_{\mathrm{eff}}$ for comparably small values of $D/sL_{n,\mathrm{a}}$.

$$L_{\mathrm{eff}}^{L\gg d,\ sL\gg D} = D/sL_{n,\mathrm{a}} + \tanh(d/L_{n,\mathrm{a}}) \tag{6.3}$$

The assumption $L_{\mathrm{eff}} = D/s$ is valid for $D/s \gtrsim 10\ \mu$ m and $L_{n,\mathrm{a}} \gtrsim 5\ \mu$m. Typical values for the diffusion length in CIGS are smaller ($\approx 1.5-3\ \mu$m [152, 153]) but the necessary diffusion length becomes shorter for lower values of $D/s$. For a typical mobility of $\mu_e = 100$ cm$^2$/Vs this corresponds to back-interface recombination velocity of $s \lesssim 2.6 \cdot 10^3 cm/s$. Both the necessary recombination velocity and diffusion length are not necessarily met by our CIGS absorber layer. An experimental measure of the diffusion length for example by electron beam induced curent [152] would be useful in order to verify or not the applied model.

It might furthermore be interesting to use the applied formalism to very thin CIGS absorber layers and as a function of their thickness in order to modify the effective diffusion length $L_{eff}$ in eq. 2.25 and to control the ratio $d/L_{n,\mathrm{a}}$.

## 6.2. The front-interface

In this chapter the physical properties of the CIGS/buffer layer heterointerface are studied. We adress the question which influence the interface-near Ga composition

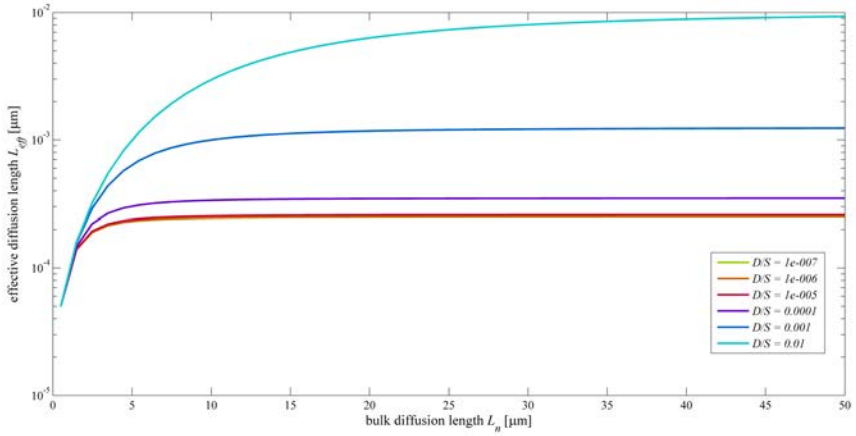


**Figure 6.6.:** Theoretical effective electron diffusion length in the CIGS absorber layer as a function of $D/s$ and the bulk electron diffusion length $L_{n,\mathrm{a}}$ according to eq. 2.25. A sample thickness of 2.5 $\mu$m was assumed. D/s is given in units of cm.

of the CIGS absorber layer and the choice of the buffer layer (CdS *vs.* Zn(S,O)) have on the energy band setup at the interface. Thereby we adress in particular the conduction band offset and its influence on temperature dependent IV characteristics. Often the influence of the Ga concentration in the whole absorber layer is studied [154, 155]. Since our goal is to study only the interface between the absorber and the buffer layer, in this set of experiments we varied the In and Ga deposition rates only during the $3^{rd}$ stage of our 3-stage co-evaporation process. This way, 7 absorber layers with different Ga contents $x_\mathrm{f} :=$ [Ga]/([Ga]+[In]) in the top 400 nm were obtained and then completed with a CdS and a Zn(S,O) buffer layer. Details about the buffer-layer deposition are given in sec. 3.2. Current-voltage measurements in the dark as well as under illumination were conducted at varied temperatures between 200 and 320 K. The extraction of dark saturation current activation energies as well as the comparison of IV-curve anomalies with curves from simulated devices were used to gain information on the energy band setup at the interface.

### 6.2.1. Band gap gradient

The GGI composition profiles as measured by GD-OES are shown in Fig. 6.7 together with the band gap energy $E_\mathrm{g}$ for the 7 samples with different front surface Ga compositions $x_f$. The band gap has been calculated from the GGI using eq. 1.3. The inlet table shows the integral CGI and GGI values as well as the surface band gap $E_\mathrm{g,f}$ and the minimum band gap $E_\mathrm{g,min}$ throughout the absorber layer extracted from the GD-OES measurement.

It can be seen that the systematic variation of the Ga and In deposition rates in the third stage of our 3-stage co-evaporation process led to a systematic variation of

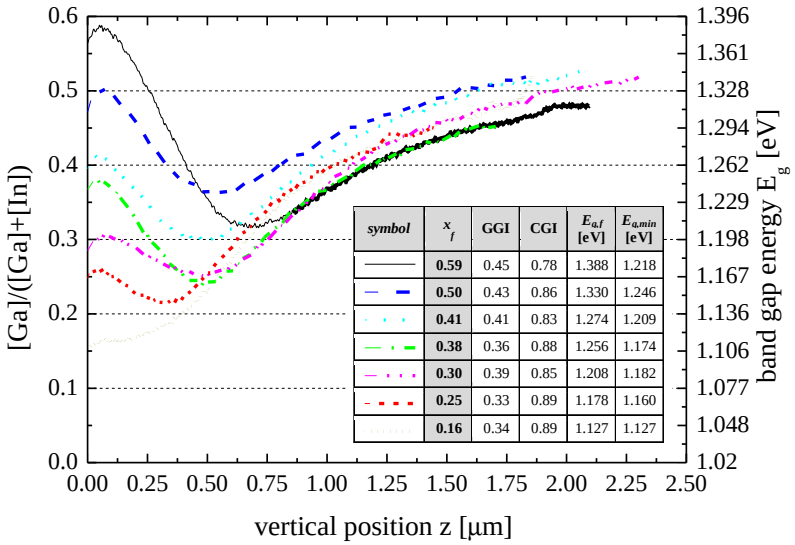


**Figure 6.7.:** In-depth profiles of the GGI compositional ratio measured by GD-OES. The main variation is confined to about the top 400 nm and due to a variation of the In and Ga deposition rates in the 3rd stage of our 3-stage co-evaporation process.

the GGI ratio $x_\mathrm{f}$ in the top 400 nm. The composition in the bulk and towards the back-side stay rather constant. The position $z_\mathrm{min}$ of the minimum GGI is almost identical for $0.30 \leq x_f \leq 0.5$ and is slighly shifted towards the surface for $x_f = 0.25$ and into the bulk for $x_\mathrm{f} = 0.59$. Due to the lack of statistical information, this shift can not be interpreted as a consequence of $x_f$. We attribute it rather to a statistical variation of the deposition rates for which we described possible reasons in sec. 3.1.1.1. A slight decrease of the (In,Ga) deposition for example would lead to less material deposition for a constant length of stage 3 and thus a shift of $z_\mathrm{min}$ towards the surface. The integral GGI varies slightly due to the front Ga gradient while all samples are overall Cu poor (CGI $< 1$), as expected for CIGS from a 3-stage process.

## 6.2.2. Solar cell characteristics

The solar cell parameters for the different Ga gradings finished with a CdS and a Zn(S,O) buffer layer are shown in Fig. 6.8.

Concerning device optimisation, the most important statement is that the optimal Ga concentration in the CIGS front region depends on the used buffer layer. For the CdS buffer layer, the best efficiency (15.0 %) was obtained with $x_\mathrm{f} = 0.41$ while with a Zn(S,O) buffer layer, this absorber layer led to a significantly lower efficiency of 13.8 %. The best efficiency for a Zn(S,O) buffer layer of 14.6 %, thus very close to the best sample with a CdS buffer layer, was obtained with a reduced Ga concentration of $x_\mathrm{f} = 0.3$ close to the hetero-interface. Four key observations regarding the cell

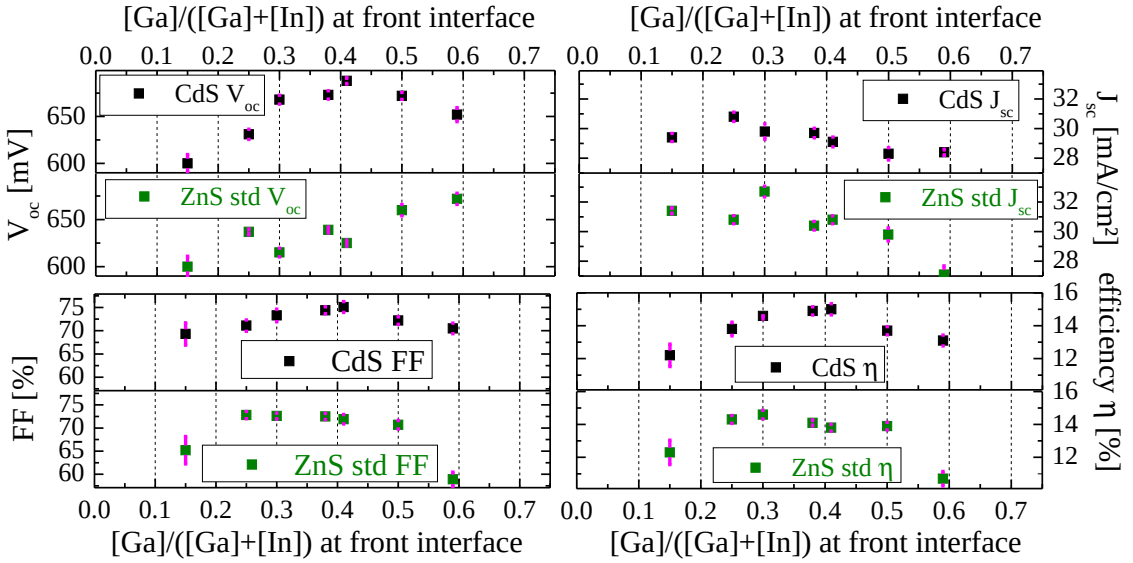


**Figure 6.8.:** Solar cell parameters as a function of the relative Ga concentration at the front interface for a CdS and a Zn(S,O) buffer layer. The optimum cell efficiency is obtained at different GGI ratios for a CdS (0.4) and a Zn(S,O) (0.3) buffer layer. The mean values of about 10 – 20 cells of each sample are indicated, error bars represent the standard deviation.

parameters are made:

1. The optimal efficiency is achieved at different Ga contents for the CdS (0.4) and the Zn(S,O) (0.3) buffer layer.

2. The FF reflects the tendency of $\eta$ and is bell-like shaped with a relative maximum at $x_\mathrm{f} = 0.3$ for the ZnS buffer layer and at $x_\mathrm{f} = 0.4$ for the CdS buffer layer.

3. For both buffer layers the short circuit current density Jsc decreases with increasing $x_\mathrm{f}$ for $x_\mathrm{f} \geq 0.3$ while for $x_\mathrm{f} \leq 0.3$ there seems to be a plateau for $J_\mathrm{sc}$.

4. For the CdS buffer layer, the $\mathrm{V}_{oc}$ dependence on $\mathrm{x}_f$ shows a bell shape with a maximum at $x_\mathrm{f} \approx 0.4$ while for the ZnS buffer layer $V_\mathrm{oc}$ increases steadily with increasing Ga concentration at the surface. This is even true for the sample with $x_\mathrm{f} = 0.59$ which has a drastically reduced FF.

In the following, the comparison between IV measurements in the dark and under illumination, temperature dependent IV characteristics as well as SCAPS simulations will be analysed in order to understand the four key observations mentioned above. Furthermore we will propose a valid energy band setup at the interface that can explain the experimental results.

## 6.2.3. Room temperature IV profiling

Room temperature IV curves in the dark as well as under STC have been measured. The results are shown in the following for CdS (sec. 6.2.3.1) and Zn(O,S) (sec. 6.2.3.2) buffer layers and first interpretations of the curves will be given. An advanced discussion follows in sec. 6.2.6.

### 6.2.3.1. CdS buffer layer

In Fig. 6.9 the IV characteristics in the dark and under illumination are compared for the different samples with CdS buffer layer. We see a cross over of the two IV curves for the samples with $0.16 \leq x_f \leq 0.38$, *i.e.* relatively low Ga surface concentrations. For the higher values $x_f > 0.38$ no such crossover is observed. For the high Ga surface concentrations $x_\mathrm{f} = 0.5$ (and to a lower extent for $x_f = 0.58$) a decreased parallel resistance in the dark can be observed.

The observed cross-over effect of the IV curves in the dark and under illumination is usually attributed to an electron barrier at the ZnO/CdS or at the CdS/CIGS interface which is reduced under illumination. This reduction can be due to for example a photo-doping of the buffer layer which reduces the potential drop over the buffer layer and the electron barrier [156] (as illustrated in Fig. 6.10a) or an occupation of surface-near acceptor states in the CIGS with holes photogenerated in the CdS buffer layer, reducing the negative space charge and barrier at the interface [157] (illustrated in Fig. 6.10b).

Independent of the reason for the barrier, it can explain the cross-over for $x_f \leq 0.38$. For the samples with higher Ga surface composition (and conduction band position) it might rather be the conduction band spike of the CIGS which represents the principal barrier to electron transport. Due to its non-sensitivity to illumination no cross-over is observed for these samples. Following this argumentation, we might interpret the $x_\mathrm{f}$ value for which the cross-over disappears, that is between $x_\mathrm{f} = 0.38$ and $x_\mathrm{f} = 0.41$ for the CdS buffer layer, as the case where the conduction band offset at the CdS/CIGS interface becomes zero.

In order to further investigate possible conduction band offsets and to extract the saturation current activation energies, temperature-dependent current-voltage measurements have been conducted in the temperature range from 200 to 320 K and will be discussed in sec. 6.2.5.

### 6.2.3.2. ZnS buffer layer

The IV characteristic in the dark and under illumination for the different absorber layers with ZnS buffer layer are shown in Fig. 6.11. No cross over of the two IV curves is observed for the samples with $x_f = 0.30$ and $x_\mathrm{f} = 0.38$, *i.e.* for a medium Ga surface concentration. For low concentrations $x_\mathrm{f} \leq 0.25$ a rather small crossover is observed while for high Ga surface concentrations of $x_f \geq 0.41$ the cross-over is very pronounced.

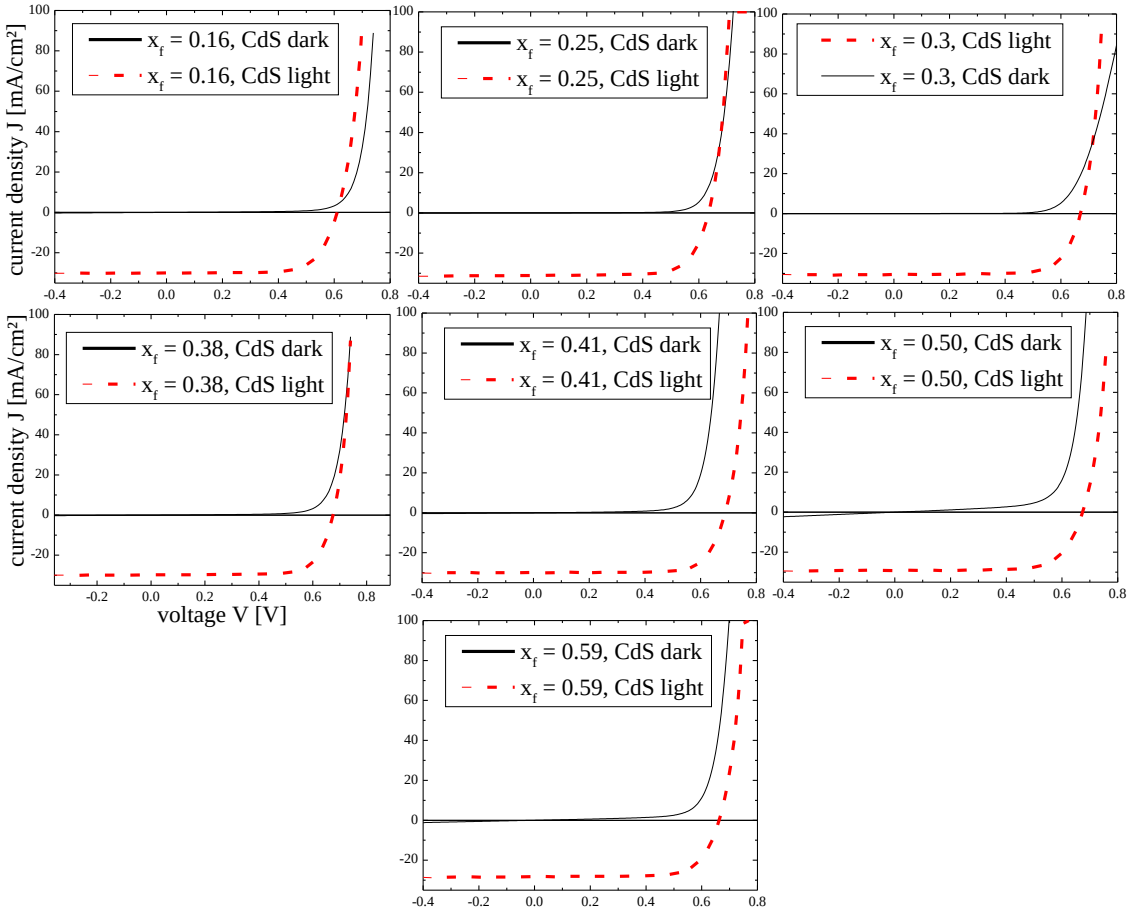


**Figure 6.9.:** Current voltage characteristics in the dark and under illumination of cells with a CdS buffer layer and absorber layers with different Ga surface compositions, as shown in Fig. 6.7. A crossover of the dark and light curves is only observed for small Ga surface compositions $x_\mathrm{f} \leq 0.38$.

Possible reasons for the cross-over effect reported in the literature have been mentioned in sec. 6.2.3.1. In general, the photodoping or the occupation of surface-near acceptor states in the CIGS by holes photogenerated in the buffer can be very different for CdS and Zn(S,O) buffer layers. Therefore, the reduction of a possible electron barrier by illumination can be completely different as well. The cross-over for low values of $x_f$ can be explained, as for the CdS buffer layer by a photo-induced reduction of an electron barrier. Interestingly, the $x_\mathrm{f}$ for which the cross-over disappears ($x_f = 0.30$) is lower compared to the CdS buffer layer. Following the interpretation where the cross-over disappearance corresponds to an alignment of the conduction bands in the buffer and absorber layer, this means that the conduction band lies at a lower energy in our Zn(S,O) buffer than in the CdS buffer layer. According to our argumentation before, for high $x_f \geq 0.41$ a negative conduction band offset (cliff) should prevail at the CIGS/Zn(O,S) interface. The reappereance of the cross-over

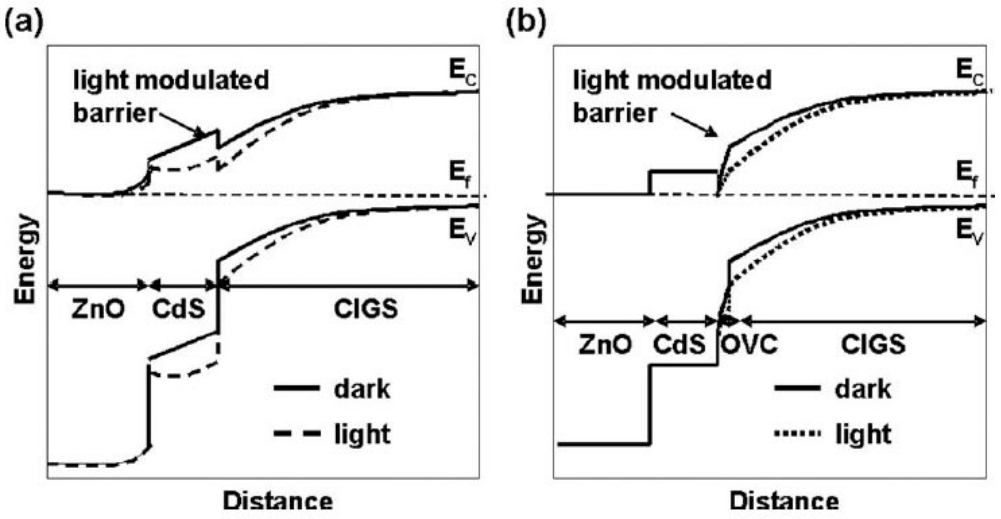


**Figure 6.10.:** Energy band diagrams showing possible barriers for the diode current in the dark and under illumination. a) Illumination dependent net carrier concentration in the CdS modulates the barrier height for the current transport at the CdS/CIGS interface. b) Light modulated charge occupation of deep acceptor states in the OVC changes the barrier height in the OVC layer whereas the position of the Fermi level at the CdS/CIGS interface stays constant [158].

effect for high $x_f$ thus cannot be explained by the photo-induced reduction of an electron barrier at the buffer layer. A possible cause might be the occupation of deep acceptor states in the surface near CIGS or OVC phase by photo-generated holes from the buffer layer which occurs in the case of a Zn(O,S) buffer layer but in the case of a CdS buffer layer [157].

### 6.2.4. Quantum efficiency

The internal quantum efficiency for most of the absorber layers with varied front gradient have been measured. We choose to analyse the internal quantum efficiency because the optical interferences caused by slightly different buffer and window layer thicknesses would influence the external quantum efficiency but in real applications the use of an anti-reflection coating (ARC) would avoid these interferences. In the case of the Zn(O,S) buffer layer, a 1h light-soaking at STC has been performed prior to the measurement. The results are shown in Fig. 6.12a for a CdS buffer layer and Fig. 6.12b for a Zn(O,S) buffer layer. The absorption gain in the region of 350 nm $< \lambda <$ 525 nm in the case of the high band-gap Zn(O,S) buffer layer can be directly seen. Slight variations of the IQE for the samples with the CdS buffer layer in this spectral region are due to the fact that the CdS buffer layer was fabricated in 2 different runs in which the thickness might have varied slightly.

The long wavelength edge which is mainly influenced by the minimum band gap

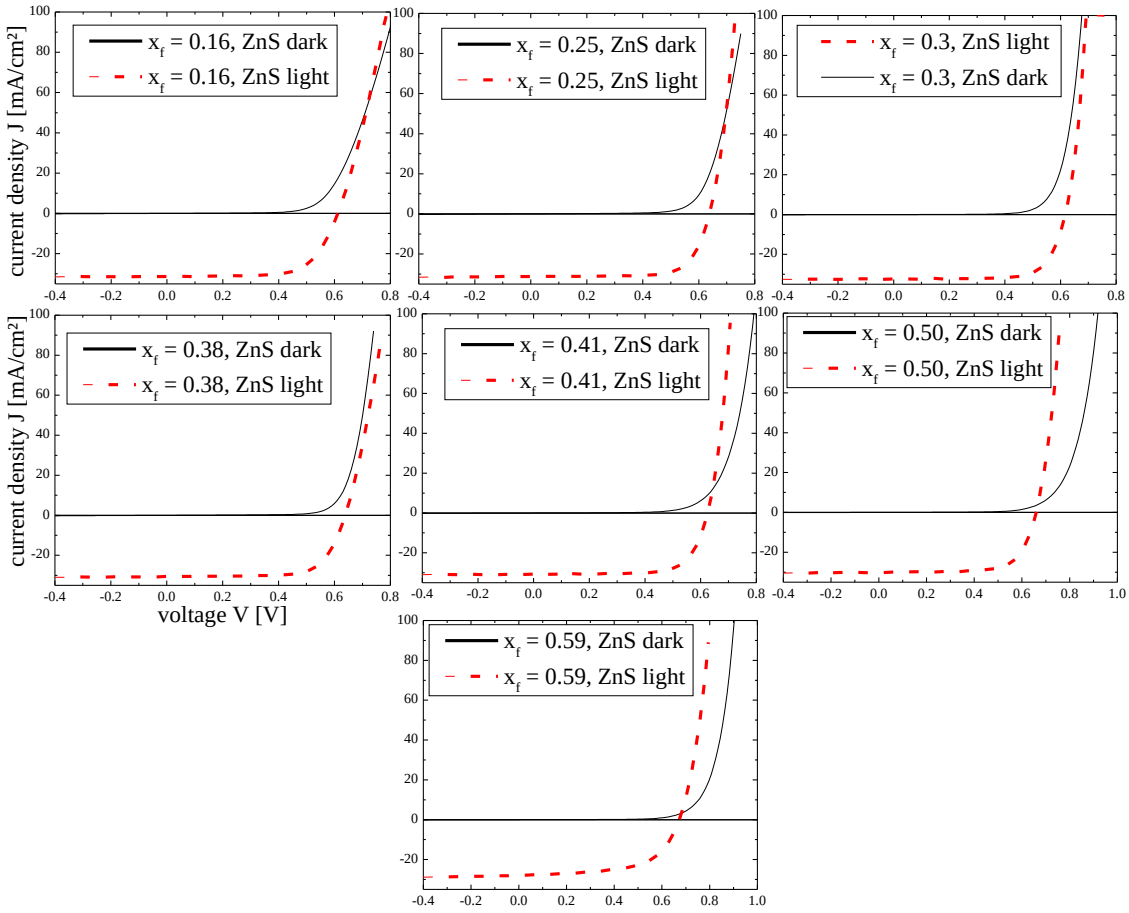


**Figure 6.11.:** Current voltage characteristics in the dark and under illumination of cells with a Zn(O,S) buffer layer and absorber layers with different Ga surface compositions, as shown in Fig. 6.7. A crossover of the dark and light curves is observed for all Ga surface compositions except $x_f = 0.30$ and $x_f = 0.38$.

energy throughout the absorber layer thickness, is not influenced by the choice of the buffer layer. It is correlated to the minimum band gap in the absorber layer (see Fig. 6.7).

### 6.2.5. Temperature dependent IV profiling

Temperature-dependent current-voltage analysis has been found to deliver important information about loss mechanisms in CIGS solar cells with various buffer layers. Pettersson *et al.* found that for a ZnMgO buffer layer, the dominating recombination mechanism depends on the buffer layer composition [159]. Several authors have used temperature-dependent IV measurements in order to assess the energy band setup [158, 160, 161]. In this work, temperature dependent IV-measurements have been conducted in the dark as well under illumination for all 7 absorber layers

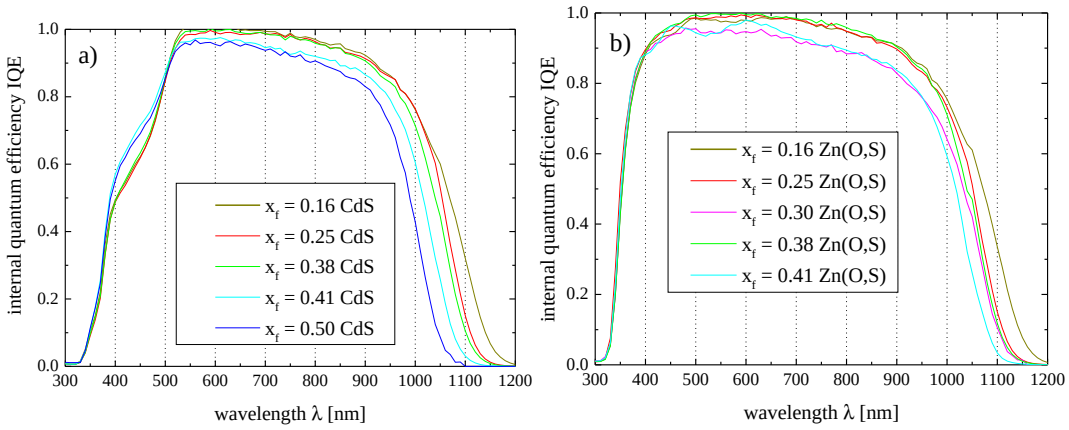


**Figure 6.12.:** Internal quantum efficiency for CIGS solar cells with a) a CdS buffer layer and b) a Zn(O,S) buffer layer and absorber layers with different Ga surface compositions $x_\mathrm{f}$.

finished both with the CdS and the Zn(S,O) buffer layer. Prior to the cool-down all samples were light-soaked during 1h under STC. The influence of light soaking has been studied in separate experiences and no influence for CdS buffer layers was observed while for Zn(O,S) buffer layers it increased the efficiency. Prior experiments showed that the effect of the lightsoaking can be considered as constant throughout the temperature dependent IV measurements which took about 2-3 h for each sample.

#### 6.2.5.1. CdS buffer layer under illumination

In order to assure to work under an illumination power density close to 100 mW/cm², the light intensity has been adjusted slightly before each measurement to a constant short circuit density $J_\mathrm{sc} = 30$ mA/cm². The resulting IV characteristics are shown in Fig. 6.13. The curves do not show any anomalies for moderate Ga surface compositions $0.3 \leq x_\mathrm{f} \leq 0.40$. For the extreme values of $x_\mathrm{f}$ two types of anomalies are observed:

1. For the very low temperatures of 200 and 220 K, a current-blocking behaviour (roll over) can be observed in the injection regime ($V > V_\mathrm{oc}$) for $x_\mathrm{f} = 0.16$ and $x_\mathrm{f} = 0.25$.
2. For the highest Ga front-side compositions $x_f = 0.50$ and especially $x_f = 0.59$, the photo-current is observed to decrease with increasing voltage in the range of $0 < V < V_\mathrm{oc}$ at low temperatures. Since this effect increases with decreasing temperature, this leads to a crossover of the IV curves.

The kink effect (anomaly 1) corresponds to a reduction of the injection current, since it occurs at $V > V_\mathrm{oc}$. In the literature this kind of behaviour has been attributed either to an energy barrier for holes at the back contact CIGS/Mo [162] or to a barrier for electrons at the front interface [163, 158]. Since in our case, the back-interface

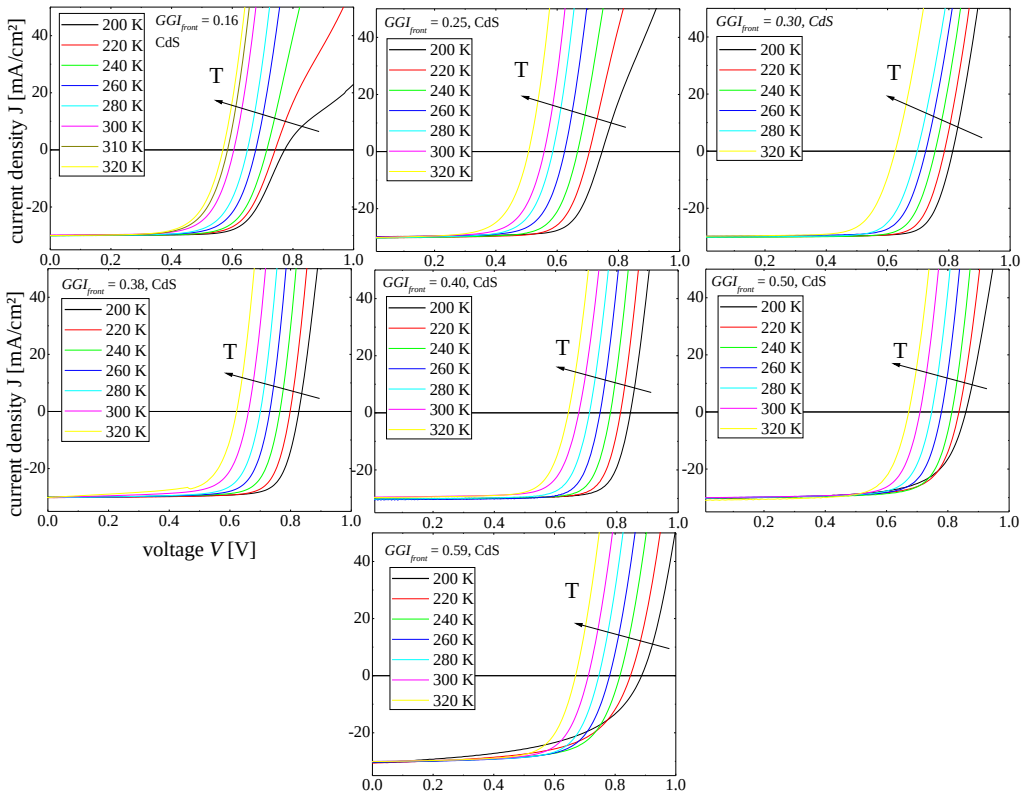


**Figure 6.13.:** Temperature dependend current-voltage characteristics under illumination of solar cells with a CdS buffer layer and different front-side Ga gradients as shown in Fig. 6.7. The light intensity has been re-ajusted for each measurement in order to work at a constant short circuit current density of $J_{sc} = 30$ mA/cm$^2$.

has not changed between the different samples we can attribute it to the front interface CIGS/CdS. The temperature and voltage dependent photocurrent (anomaly 2) has been observed by other groups as well for high Ga surface compositions. We agree with Chirila *et al.* [147] who attribute this behaviour to an electron barrier towards the front-interface that increases the recombination rate of minority electrons that are for relatively low voltages almost exclusively photo-generated. For lower temperatures, this barrier becomes more effective since electrons have less thermal energy to overcome it and the photo-current is reduced.

According to 2.43, a plot of the open circuit voltage against the temperature should lead to a straight line from which the activation energy $E_a$ (interception with the ordinate) and current density prefactor $J_{00}$ (from the slope) for the dominating recombination mechanism can be deduced. As can be seen in Fig. 6.14 this is the case for all samples with CdS buffer layer. The activation energies are shown in the respective figures. If we divide the samples roughly into three groups of small ($x_f \leq 0.3$), medium ($0.38 \leq x_f \leq 0.41$) and large $x_f$ ($0.5 \leq x_f$), we see that the activation energy increases with increasing Ga concentration at the surface.

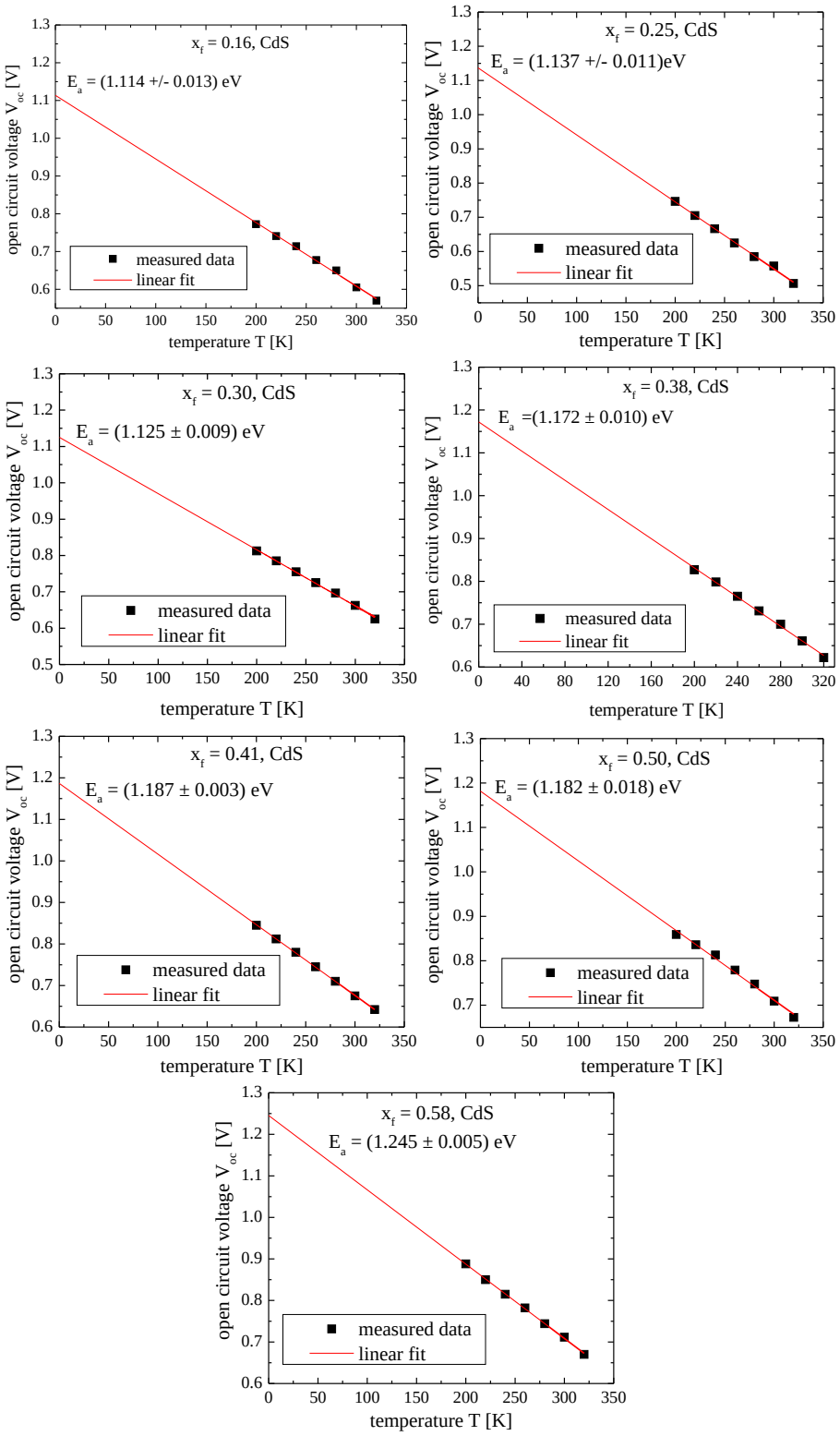


**Figure 6.14.:** Measured $V_{\mathrm{oc}}$ at different temperatures and linear fit for cells with different Ga surface compositions, as seen in Fig. 6.7. The interception with the ordinate corresponds to the activation energy $E_{\mathrm{a}}$ of the respective dominating recombination mechanism.

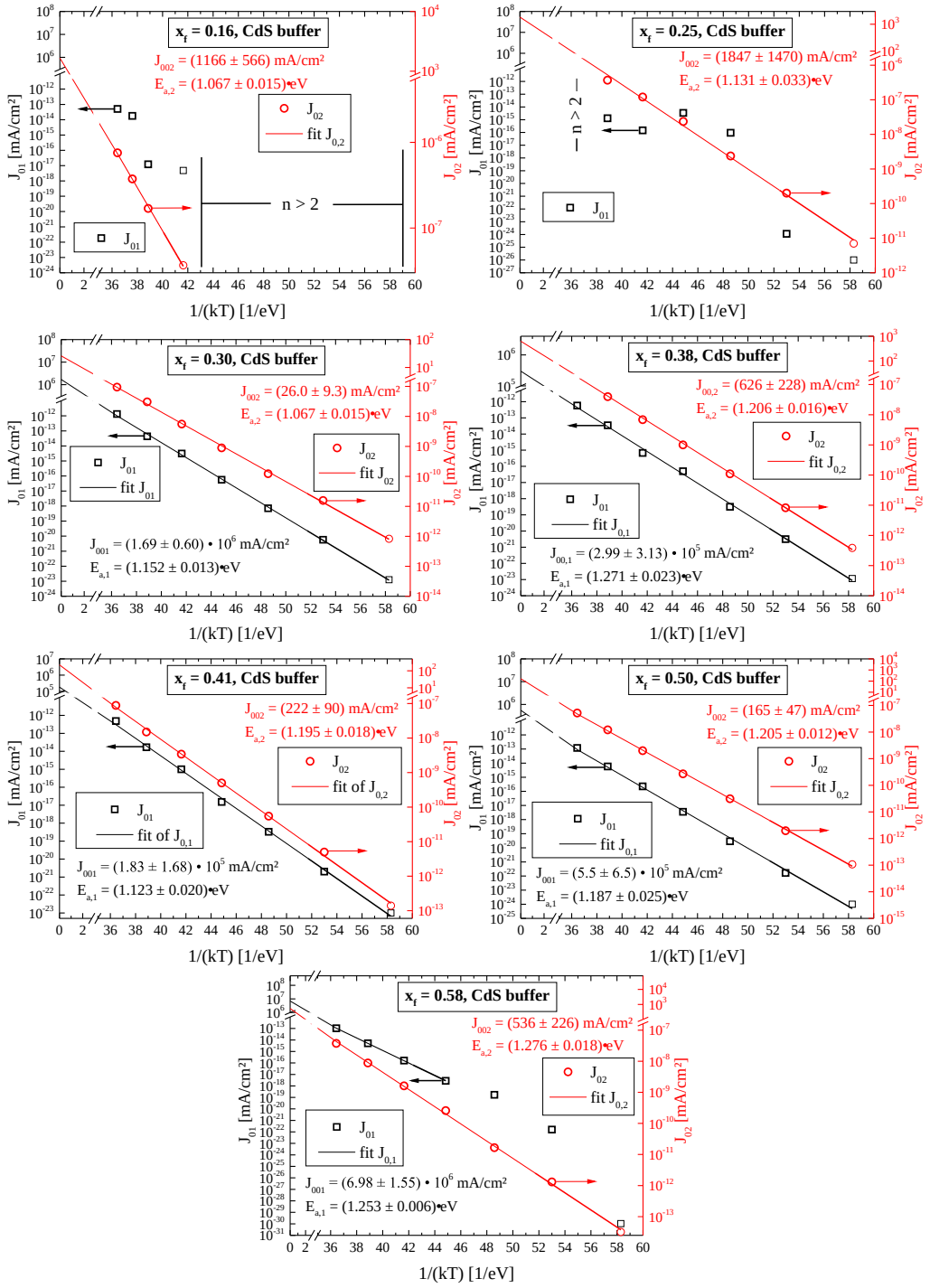


**Figure 6.15.:** Arrhenius plots of IV characteristics in the dark for samples with varied Ga surface composition (as shown in Fig. 6.7) and CdS buffer layer.

In the discussion the extracted activation energies will be compared to the band gap energies at different positions in more detail.

#### 6.2.5.2. CdS buffer layer in the dark

The IV curves in the dark for the 7 different absorber layers finshed with a CdS buffer layer have been fitted to a 2-diode model, as explained in sec. 2.4.2.

The extracted dark saturation current densities $J_{0,1}$ and $J_{0,2}$ are plotted in a semi-logarithmic plot against $\frac{1}{AkT}$ (Arrhenius plot) in Fig. 6.15. For the sample with the lowest Ga surface concentration $x_f = 0.16$ at low temperatures $T \leq 260$ K ($1/(kT) > 44.8$ eV$^{-1}$) and for $x_f = 0.25$ at $T = 320$ K ($1/(kT) = 36.4$ eV$^{-1}$) the ideality factor is higher than 2 and thus a 2-diode fit with fix ideality factors $A_1 = 1$ and $A_2 = 2$ was not possible. An ideality factor $A > 2$ exceeds the limit for SRH recombination of 2.0 and is attributed to a recombination mechanism saturating with increasing forward bias such as tunneling enhanced SCR or interface recombination [20]. The samples with a low conduction band position at the CIGS surface ($x_f = 0.16$ and $x_\mathrm{f} = 0.25$) have the highest spike in the conduction band at the CIGS/CdS interface and a tunneling through this energetic barrier can explain the observed ideality factors $A > 2$. While $J_{02}$ decreases exponentially with $1/(AkT)$ for all samples, for $J_{01}$ this is only the case for the samples with $x_\mathrm{f} = 0.30$, 0.38, 0.41 and 0.50. Together with the extracted activation energies, this will be discussed in sec. 6.2.6.

#### 6.2.5.3. ZnS buffer layer

For the majority of the samples with a Zn(S,O) buffer layer, the ideality factor extracted from dark current-voltage measurements was superior to 2 and the 2-diode model with fix ideality factors of 1 and 2 does not have any physical sense (see sec. 2.4.2). In order to interpret the dark IV curves, we fitted them to a 1-diode model with variable ideality factor. The resulting ideality factors are shown Tab. 6.1. Arrhenius plots of $J_0$ *vs.* $1/(AkT)$ in a semilogarithmic scale do not, as expected considering eq. 2.40 result in straight lines (see Fig. D.1).

The recombination mechanisms in the samples with $x_f = 0.25$ and $x_f = 0.30$ can be explained by a combination of radiative and Shockley-Read-Hall recombination (at the interface and/or in the bulk) since the ideality factor does not overcome 2. Higher values for $A$ as observed for all other samples can be explained by a recombination mechanism that is gradually saturated with increasing forward bias [20], for example by tunneling enhanced recombination in the SCR or at the interface. For the very low Ga surface concentration $x_\mathrm{f} = 0.16$ this is probably due to a high conduction band offset at the CIGS/Zn(O,S) interface. For $x_\mathrm{f} \geq 0.38$ it is not quite clear why the ideality factor is superiour to 2. One possible explanation might be SRH recombination at a large intrinsic field [20] caused by the strong front-surface grading for high $x_\mathrm{f}$ values.

| | Ga surface concentration $x_f$ | | | | | | |
|---|---|---|---|---|---|---|---|
| **T [K]** | 0.16 | 0.25 | 0.30 | 0.38 | 0.41 | 0.50 | 0.59 |
| **200** | 7.98 | | 1.81 | 5.7 | | 3.86 | |
| **220** | 5.91 | | 1.75 | 4.45 | 4.50 (227 K) | 3.58 | 4.75 |
| **240** | 5.33 | 1.61 | 1.71 | 3.6 | 4.50 | 3.48 | 4.50 |
| **260** | 3.42 | 1.93 | 1.57 | 2.95 | 3.50 | 2.63 | 3.50 |
| **280** | 2.54 | 1.50 | 1.60 | 2.55 | 3.50 | 3.16 | 3.44 |
| **300** | 1.89 | 1.65 | 1.6 | 2.4 | 2.86 | 3.13 | 2.75 |
| **320** | 2.00 | 1.51 | 1.56 | 1.92 | 2.20 | 2.80 | 2.75 |

**Table 6.1.:** Ideality factors for solar cells with varied Ga surface composition, according to Fig. 6.7 and Zn(O,S) buffer layers at different measurement temperatures. The ideality factor is superior to 2 for the majority of the measurements and in general shows a temperature dependence.

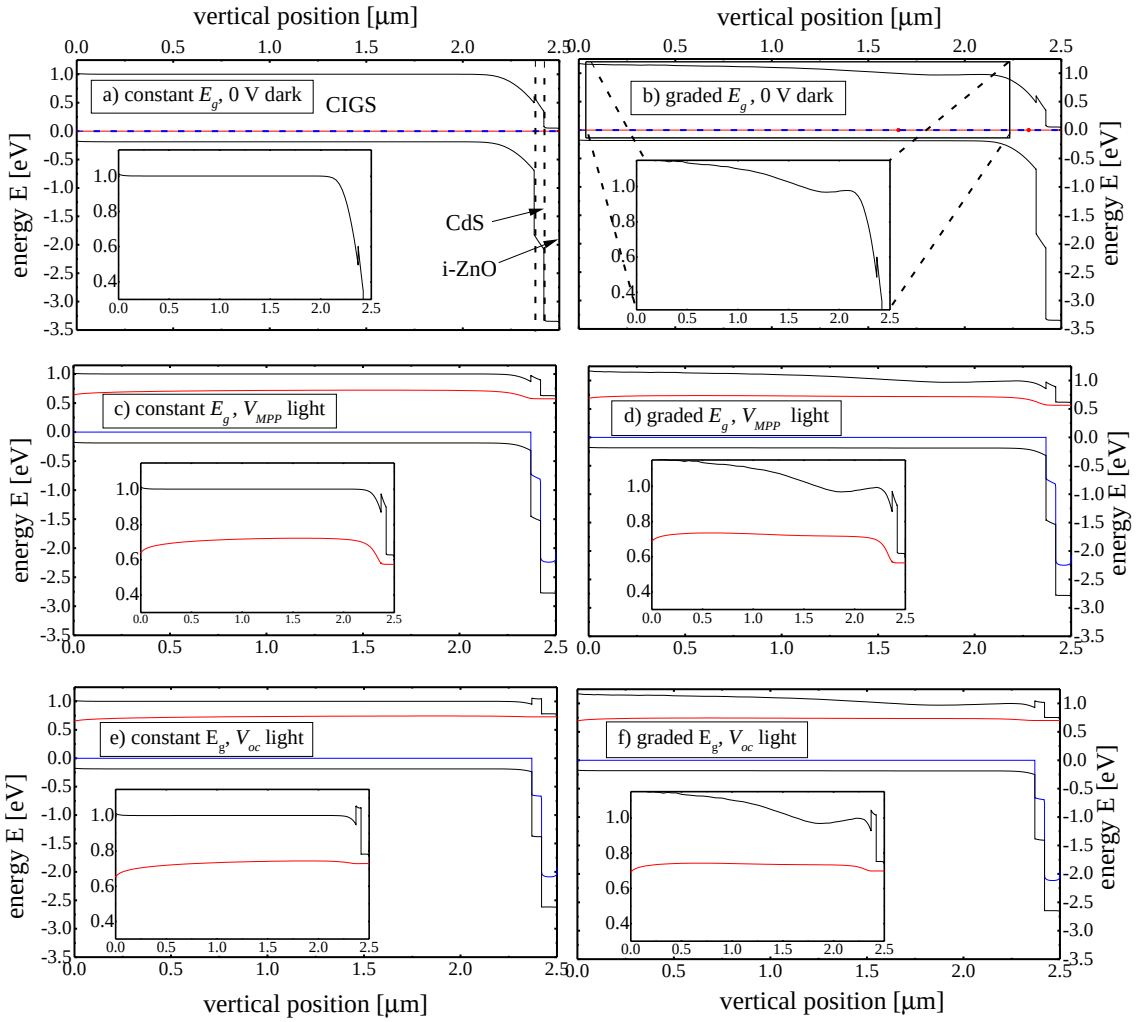


**Figure 6.16.:** Energy band diagram for a CIGS solar cell in the CIGS/CdS/i-ZnO/ZnO:Al structure as simulated by SCAPS for different voltages and with or without illumination under STC. In a, c and e the CIGS band gap is set to a constant level while in b, d and f the conduction band minimum and band gap is graded according to a Ga-profile measured by GD-OES.

### 6.2.6. Discussion

In order to illustrate the principal influence of a Ga gradient in the absorber layer on the energy band diagram, it has been simulated with SCAPS for a typical set of material properties (Appendix E). The results are shown in Fig. 6.16 for a non-graded absorber layer on the left and an absorber layer with a double Ga-gradient on the right with CdS buffer layer. We have assumed that as frequently reported in the literature only the conduction band energy changes with the Ga composition. In the inlets in Fig. 6.16 the bending of the conduction band can be observed. It is interesting to note that towards the CIGS/CdS interface, the increased Ga composition can lead to a barrier for the photo-generated electrons. This barrier is increased at the maximum power point $V = V_{\mathrm{MPP}}$ (d) and at $V = V_{\mathrm{oc}}$ (f) as compared to equilibrium conditions (b). For high Ga concentrations towards the surface this can lead to a voltage-dependent photocurrent. This is observed for the sample with $x_{\mathrm{f}} = 0.59$ in Fig. 6.13 for low temperatures.

Regarding the solar cell parameters extracted from STC IV measurements, shown in Fig. 6.8, the trend in efficiency $\eta$ (as a product of $FF$, $V_{\mathrm{oc}}$ and $J_{\mathrm{sc}}$) described in observation i) in sec. 6.2.2 can be attributed to a) the FF which shows exactly the same tendency as $\eta$ and b) the $V_{oc}$ which for the CdS buffer layer increases clearly between $x_{\mathrm{f}} = 0.25$ and $x_{\mathrm{f}} = 0.4$ but for the Zn(S,O) buffer layer seems to be rather constant or increase only slightly for $0.2 \leq x_{\mathrm{f}} \leq 0.4$. The decrease of $J_{\mathrm{sc}}$ with increasing $x_{\mathrm{f}}$ for $x_{\mathrm{f}} \geq 0.3$ (observation ii) can be explained by the increase of the absorber layers minimum band gap energy $E_{\mathrm{g,min}}$, as shown in Fig. 6.7, with $x_{\mathrm{f}}$. A corresponding shift of the long-wavelength absorption edge in external quantum efficiency measurements (Fig. 6.12) confirms this tendency. The dependence of $V_{\mathrm{oc}}$ on $x_{\mathrm{f}}$ (observation iii) could possibly be explained by the conduction band alignment between the absorber and the buffer layer. Platzer-Björkman *et al.* reported a decrease of the $V_{\mathrm{oc}}$ for a negative conduction band offset $E_{\mathrm{g}}^{\mathrm{Zn(O,S)}} - E_{\mathrm{g}}^{CIGS}$[164]. For the CdS buffer layer, the optimal conduction band alignment is supposed to be achieved for $x_f = 0.4$ corresponding to a surface band gap energy of $E_{\mathrm{g}}^{\mathrm{front}} = 1.27$ eV. For higher (lower) Ga interface compositions, a cliff (spike) at the CIGS/CdS interface leads to a successive decrease of the $V_{\mathrm{oc}}$. The fact that the $V_{\mathrm{oc}}$ increases continuously with $x_f$ until $x_{\mathrm{f}} = 0.59$ ($E_{\mathrm{g}}^{\mathrm{front}} = 1.39$ eV) is interpreted as a continuous decrease of the spike at the interface. This results in the conclusion that the position of the conduction band is at least 0.12 eV superiour for the Zn(O,S) buffer layer compared to the CdS buffer layer.

An overview of the anomalies observed in temperature-dependent IV characteristics is given in Tab. 6.2. For certain samples ($x_f = 0.41$ for the CdS buffer layer and $x_{\mathrm{f}} = 0.25$ and 0.30 for the Zn(O,S) buffer layer) no such anomalies were observed. Interestingly, this anomalie-free region coincides with the best cell efficiencies and fill factors (see Fig. 6.8) and in the case of a CdS buffer layer as well in the highest $V_{\mathrm{oc}}$.

The cross-over of the light and dark IV measurements as well as the roll-over of the IV

| $x_f$ | CdS buffer | Zn(O,S) buffer |
|---|---|---|
| 0.16 | $A > 2$, c.-o. IV, r.-o. IV | $A > 2$ low T, $A = f(T)$, c.-o. IV |
| 0.25 | $J_{001}$, $J_{002} = f(T)$, c.-o. IV, r.-o. IV | c.-o. IV |
| 0.30 | c.-o. IV | |
| 0.38 | c.-o. IV | $A > 2$ low T, $A = f(T)$ |
| 0.41 | | $A > 2$ low T, $A = f(T)$, c.-o. IV |
| 0.50 | $J_{ph} = f(V)$ low T | $A > 2$ low T, $A = f(T)$, c.-o. IV |
| 0.58 | $J_{001} = f(T)$, $J_{ph} = f(V)$ low T | $A > 2$ low T, $A = f(T)$, c.-o. IV |

**Table 6.2.:** Anomalies in current voltage measurements at varied temperatures for solar cells with varied Ga surface composition $x_f$ in the CIGS layer and CdS or Zn(O,S) buffer layer. A cross-over of the light and dark IV curves at ambient temperature is denoted as 'c.-o. IV', a rollover of the light IV curve at low temperatures as 'r.-o. IV'.

curve under illumination at low temperature (for the CdS buffer) can be explained by an illumination dependent conduction band offset at the window layer/buffer layer interface acting as a barrier against the electron injection from the window to the buffer layer. Under illumination, the buffer layer is photo-doped and the potential drop over the buffer and thus the electron barrier is reduced, as proposed *e.g.* in [20]. This leads to an increase of the diode current, explaining the cross over with the dark IV curve. At low temperatures, the thermal energy of the electrons in the conduction band is not sufficient to pass the barrier, leading to the current blocking behaviour at $V \approx V_{oc}$ observed in Fig. 6.13 for $x_f = 0.16$ and 0.25. The fact that this rollover under illumination is observed only for the very low $x_f$ values of 0.16 and 0.25 while the cross-over of dark and light IV curve (Fig. 6.9) occurs also for $x_f = 0.30$ and $x_f = 0.38$ supports the hypothesis of a photodoping of the buffer layer reducing the conduction band offset under illumination. For high $x_f$, the CIGS conduction band edge at the interface might become superior to the buffer layer band-gap and in the case of a photo-doped buffer layer, the electron barrier still forms between the buffer layer and the absorber layer. This explains that for high $x_f$ in Fig. 6.9 no cross over of the IV curves nor a roll-over of the light IV curve in Fig. 6.13 is observed.

The activation energies extracted from $V_{oc}$ vs. T plots are shown as a function of $x_f$ in Fig. 6.17. For comparison with the theory, we plotted as well the activation energy for interface recombination at the CIGS/buffer interface following [20] as described in sec. 2.3.3.4. Therefore the band gap energies of $E_{g,CdS} = 2.4$ eV for CdS and $E_{g,Zn(S,O)} = 3.6$ eV for Zn(S,O) and a valence band offset of 1.13 eV (CdS/CIGS, [165]) and 2.0 eV (Zn(S,O)/CIGS, [165]) were used. For the CIGS bandgap relation 1.3 was used with $E_g^{CIS} = 1.04$ eV and $E_g^{CGS} = 1.68$ eV. At $x_f \approx 0.4$ where the theoretical interface activation energy $E_{a,int}$ becomes constant corresponds to the transition from a type 1 to a type 2 interface, as illustrated in Fig. 6.17.

As can be seen the activation energy follows rather the minimum band gap energy

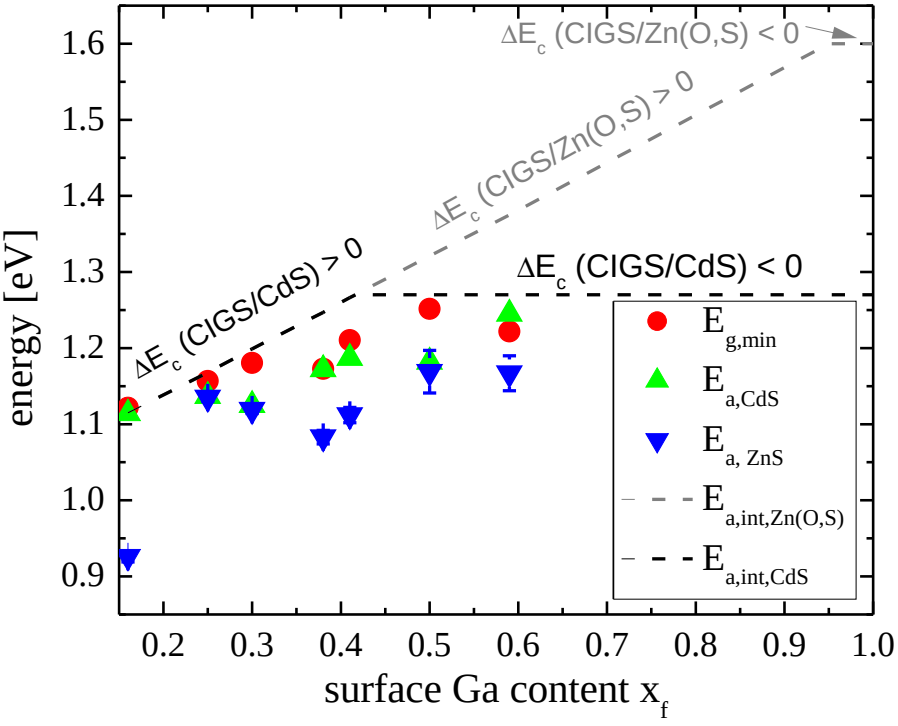


**Figure 6.17.:** Activation energies extracted from $V_{oc}$ *vs.* $T$ plots for the samples with CdS and Zn(S,O) buffer layers as a function of the Gallium surface concentration $x_f$. For comparison, the theoretical curves according to [20] as described in sec. 2.3.3.4 are shown as dashed lines. The assumed conduction band positions for the absorber and buffer layer are described in the text.

than the surface band gap energy. Therefore we consider the dominant recombination mechanism to be localised in the absorber layer rather than at the interface. Since the bulk band gap energy was kept constant (to a certain extent), the observed variations are interpreted nevertheless to result from interface recombination. It is interesting to note that for the CdS buffer layer, the activation energy follows the theoretical curve quite well in the range $0.3 \leq x_f \leq 0.5$ but with an offset. This might indicate that the applied theoretical models are valid for these $x_f$ values but not for the extreme values. The same can be observed for the Zn(O,S) buffer layer for $0.38 \leq x_f \leq 0.59$. This indicated that the assumed position of the conduction band minimum of the Zn(O,S) layer, which has been taken from the literature, might be too high. In order to prove the exact energy band alignment at the interface, we would need to conduct more direct methods such as X-ray photoelectron spectroscopy [166, 167, 164].

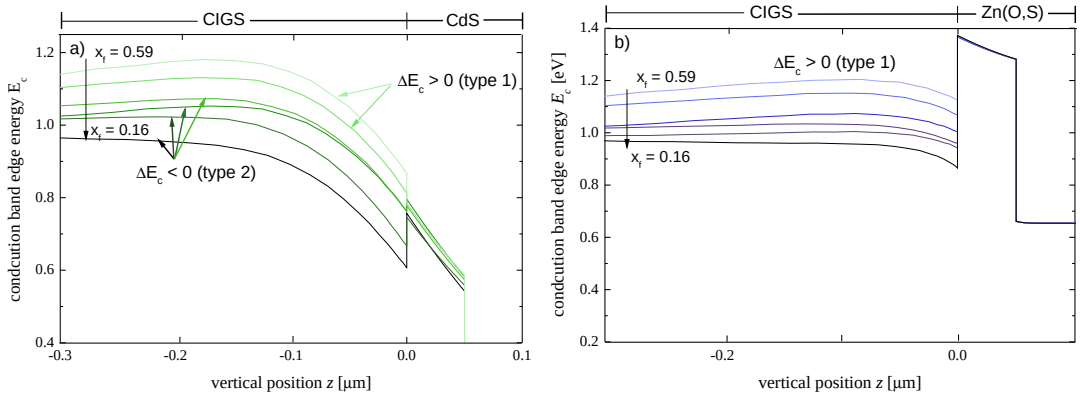


**Figure 6.18.:** Conduction band edge setup at the absorber layer / buffer layer interface for a) a CdS and b) a Zn(O,S) buffer layer at $V_{\mathrm{oc}}$. While for a CdS buffer layer, the band offset changes sign at a certain Ga front composition in the absorber layer, the CIGS/Zn(O,S) interface is of type 1 for all samples. Band diagrams are calculated with SCAPS, the parameter set is given in Appendix E. The assumed band offsets are detailed in the text.

## 6.2.7. Conclusion

While in the literature the Zn(O,S) buffer layer composition is often optimised in order to match with the CIGS absorber layer [164] we chose to vary rather the CIGS composition, in particular in the front-near region, and study its influence on the opto-electronic device properties with a CdS as well as Zn(O,S) buffer layer. We found that the optimal Ga concentration in the CIGS front region depends on the buffer layer: For the CdS buffer layer, the best efficiency of 15.0 % was obtained with $x_{\mathrm{f}} = 0.41$ while combined with a Zn(S,O) buffer layer, this absorber layer led to only 13.8 %. The best efficiency of 14.6 % for a Zn(S,O) buffer layer was obtained with a lower Ga concentration close to the hetero-interface of $x_{\mathrm{f}} = 0.30$. The results could have been explained by variations of the optical band gap and the conduction band offset at the hetero-interface.

The best performances were furthermore found to coincide with temperature dependent IV curves without any anomalies in the investigated temperature range 200 K $< T <$ 320 K and no cross over of the dark and illuminated IV curves at ambient temperature which we interpreted as absence of any electron barrier at the window/buffer layer interface.

The roll over of the IV curve at low temperatures is controversely discussed in the literature. Some groups suspect the CIGS / buffer layer heterointerface or the interface between CIGS and an ordered vacancy compound at the surface to be responsible for this phenomenon [163] while others suggest a barrier at the back contact to form a secondary diode and thus result in a roll over [158]. Since in our experiments the front interface is excessively changed but the back-interface is left unchanged, we can exclude the back interface as the origin of the roll over at low

temperatures and attribute it to the front interface.

## 6.3. Conclusion

In this chapter the deposition fluxes and the substrate temperature have been varied systematically in order to obtain a) a variation of the notch-deepness in the V-shape band gap profile and b) a varied conduction band offset at the CIGS/buffer layer interface. In order to vary the conduction band setup at the CIGS/buffer layer interface further, two different buffer layers, CdS and Zn(S,O), were deposited on identical absorber layer. The pure cell parameters $V_{\mathrm{oc}}$, $J_{\mathrm{sc}}$ and $FF$ were analysed for the process optimisation and it was found that the adaption of the absorber layer surface composition to the specific buffer layer increases the cell performance. While the solar cell parameters give only few information about possible energy band setups and the location of the dominant recombination mechanisms, temperature dependant IV measurements unveiled anomalies (light and dark IV crossover, kink in the injection regime) that can be attributed to electrostatic potential barriers and the conduction band offset at the front interface hindering carrier transport. Based on the experimental results, a energy band diagram has been proposed and its viability has been shown in 1D device simulations.

# General Conclusion and Perspectives

The aim of the present work was the comprehension and optimisation of the CIGS thin film deposition by co-evaporation at a freshly installed co-evaporation reactor. The study of the literature led to the decision to set up a 3-stage process and systematically study the material growth during the different process stages. Since the 3-stage process has already been studied and optimised for about 20 years, it has been tried to adapt and learn from the work in the literature as well as to adress actual research topics and open questions which have been detailed in sec. 4.1. In a second step, the influence of the material properties on the opto-electronic device parameters was adressed. Thereby the focus was put on the influence of the band gap gradient and the conduction band setup at the absorber/buffer layer interface.

As a prerequisite for the process control, the substrate temperature has been calibrated with an infrared camera. The calibration is confirmed by the observation of a solid/liquid phase transition of the $Cu_2Se$ surface layer at a temperature of 530 °C which is in agreement with the literature. The temperature values indicated in this thesis are thus absolute values which is not necessarily the case in work found in the literature.

While the presence of a $MoSe_2$ interfacial layer at the CIGS/Mo back interface is known to be important for an ohmic back-contact, it has been shown that the observed crystal orientation of this layer is influenced by the duration of a Se evaporation step at 480 °C prior to the evaporation of In, Ga and Se during the first stage. An observed orientation of $MoSe_2$ with the (002) plane parallel to the surface, *i.e.* the hexagonal c-axis normal to the surface, has been explained by an increased thickness of the $MoSe_2$ layer and seems to be necessary for the device optimisation, resulting in a lower series resistance and thus an increased fill factor and better homogenity.

The substrate temperature and the deposition rates of the CIGS constituents were identified as key process parameters. Therefore this thesis provides a systematic study of the influence of these parameters during the 3 stages of our process. While in the literature often only the final CIGS absorber layer is characterized, in this work we have investigated the material at different points and have shown the evolution throughout the process. We can conclude that the material recrystallises throughout the process and the morphology of the $(In,Ga)_2Se_3$ precursor has no essential influence on the final absorber layer. The crystal orientation and elemental in-depth distribution of the precursor layer in contrast are partly conserved and determine the final absorber layer properties. Our observation of a preferential $Cu(In,Ga)Se_2$ orientation with the (220)/(204) planes parallel to the surface if the $(In,Ga)_2Se_3$ pre-

cursor was grown with its (300) plane parallel to the surface confirm recent results from the literature [47].

In order to investigate the in-depth variations of material properties observed in CIGS from a 3-stage process, an innovative etching-technique has been proposed, which in principle can be applied to any thin-film material. This way, the Ga gradient has been linked to a gradient of the tetragonal lattice parameters. An affinity of grains with the (312) plane parallel to the surface to grow on top of grains with the (116) plane orientated parallel to the surface has been observed. Interestingly, the OVC phase is detected by Raman spectroscopy throughout the whole absorber layer thickness and not only close to the surface as usually observed in the literature.

Based on the literature and on our results, a reaction pathway for the 3-stage process is proposed. The separation of surface and bulk reactions allows for the quantitative explanation of the Ga gradient. In order to quantitatively understand the in-depth Ga gradient it would be interesting to develop a model for a numerical simulation approach with diffusion coefficients for the different atoms that depend on the temperature and composition. First work in this direction using a one dimensional Fickian model has been conducted very recently by Rodriguez *et al.* in [133].

In chapter 6 we have studied the correlation between the CIGS material properties and the opto-electronic cell properties. Thereby the focus was put on the in-depth band gap gradient induced by a compositional GGI variation as well as on the CIGS/buffer layer interface. We have seen that the Ga gradient optimisation depends on the used buffer layer and the optimal surface near Ga concentration is higher in case of a CdS buffer layer compared to a Zn(O,S) buffer layer. Temperature dependant IV measurements unveiled anomalies (light and dark IV crossover, kink in the injection regime) that can be attributed to electrostatic potential barriers and the conduction band offset at the front interface hindering carrier transport. Surprisingly and in constrast to the literature our interpretation leads to the hypothesis of a lower conduction-band offset for the CIGS/Zn(O,S) interface compared to the CIGS/CdS interface. In order to prove this hypothesis we would need to conduct a more direct method such as X-ray photoelectron spectroscopy at our samples in order to access the energy band setup at the interface.

While in this thesis the results are shown for series of samples which were characterised and analysed in-depth, for many samples only a basic characterisation (composition, IV and EQE) was conducted. A special focus was put on the systematic variation of the Ga gradient throughout the absorber layer as well as the optimisation of the substrate temperature in the different stages of the 3-stage process which have led to continuous improvements of the solar cell efficiency. The highest efficiency obtained throughout this thesis has been 16.7 %. For instance we have not used an anti-reflection coating but this will be applied in the near future. The IV characteristic and deduced cell parameters are shown in Fig. 6.19.

It is evident that there still is a performance gap to current state-of-the-art CIGS solar cells. Compared to the current world record cell the efficiency difference is 5 %

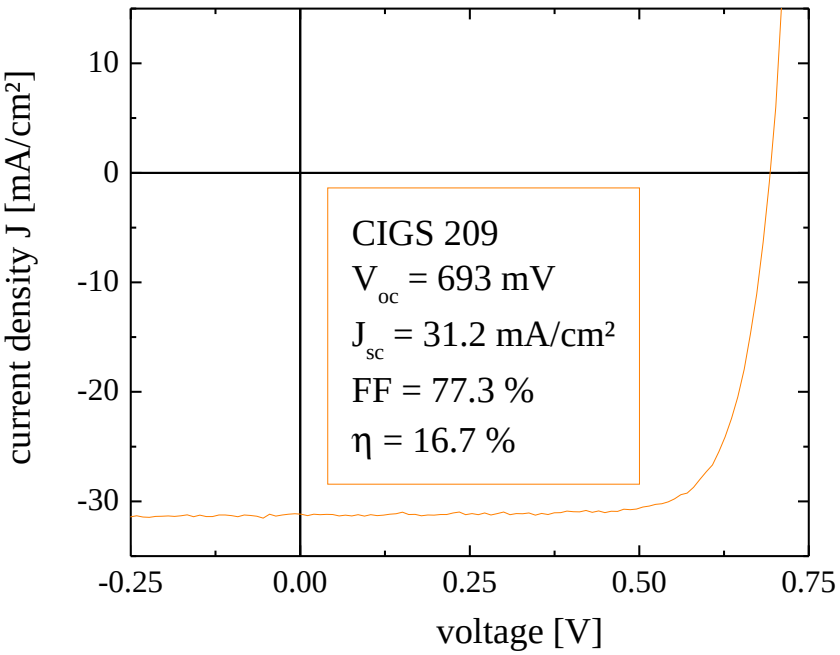


**Figure 6.19.:** Current-voltage characteristic of the solar cell with the highest efficiency obtained throughout this thesis. The cell has not been coated by an anti-reflection layer.

absolute. The deposition of an anti-reflection coating could make up for $1-2$ % absolute of this gap.

Throughout my work it was naturally not possible to adress the whole of process optimisation routes for CIGS solar cells. The deposition temperature and the in-depth Ga gradient have been identified as key elements for the optimisation and the concious decision has been made to focus on the comprehension and optimisation of these two elements during most of my thesis. Additional studies on the $MoSe_2$ interfacial layer at the back-interface and a systematic variation of the conduction band offset at the front interface have been conducted.

For the further comprehension and optimisation of solar cells based on co-evaporated $Cu(In,Ga)Se_2$ three approaches which could not have been adressed in this thesis are proposed:

1. The comprehension and optimisation of the front-interface chemistry. In this work the front interface has been studied rather from a physical point of view and the main parameter that was tried to vary was the conduction band minimum by changing the Ga surface composition. It might be interesting to finish the absorber layer under different conditions. It has been shown that the conditions of the CIGS co-evaporation process termination, which will influence the interface chemistry, have an influence on the solar cell performance. Positive effects of termination under a pure Se flux [168] and in absence of Ga (only Se and In) [76] have been reported for example.

2. Use of potassium as a dopant in the CIGS absorber layer. Recent work [24, 25] has shown that a post-deposition evaporation of KF and the resulting incorporation of small amounts of potassium into the absorber layer can lead to a Cu and Ga depletion in the surface near region which is beneficial for the cell performance. This treatment furthermore allows for the use of a thinner CdS buffer layer which would lead to an increased short circuit current density.
3. Use of an alternative buffer layer with a higher band gap as compared to the traditional CdS buffer layer. This strategy has been employed in this thesis but the short circuit current gain using a Zn(O,S) buffer layer was accompanied by a reduction of the open circuit voltage. But since points 1. and 2. change the absorber layer surface chemistry this might allow for a better match with alternative buffer layers.

In conclusion, this thesis has enabled to set up a three-stage co-evaporation process with an optimized Ga gradient and to understand the role of the substrate temperature and the deposition rates during the different process stages on the intermediate and final material properties. Thereby different open questions concerning the growth of CIGS thin films have been adressed. The in-depth Ga gradient as well as the conduction band setup at the absorber/buffer layer interface have been correlated with the solar cell properties at ambient and low temperatures. We are confident that the bulk material is at a sufficient quality to allow for higher efficiencies towards 20 % and have proposed three optimisation routes that are focussed on the front interface with the buffer layer.

# Bibliography


[1] BP, *Statistical Review of World Energy 2014 | About BP | BP Global*. BP global, 2014.

[2] J. L. Swain, F. Sverrisson, *et al.*, "Renewables 2014 global status report," 2014.

[3] *Summary for policymakers. In: Climate Change 2014: Impacts, Adaptation, and Vulnerability. Part A: Global and Sectoral Aspects. Contribution of Working Group II to the Fifth Assessment Report of the Intergovernmental Panel on Climate Change*. [Field, C.B., V.R. Barros, D.J. Dokken, K.J. Mach, M.D. Mastrandrea, T.E. Bilir, M. Chatterjee, K.L. Ebi, Y.O. Estrada, R.C. Genova, B. Girma, E.S. Kissel, A.N. Levy, S. MacCracken, P.R. Mastrandrea, and L.L. White (eds.)], Cambridge University Press, Cambridge, United Kingdom and New York, NY, USA, pp. 1-32.

[4] A. de La Tour, M. Glachant, and Y. Méniere, "Predicting the costs of photovoltaic solar modules in 2020 using experience curve models," *Energy*, vol. 62, pp. 341–348, Dec. 2013.

[5] K. E. Trenberth, J. T. Fasullo, and J. Kiehl, "Earth's global energy budget," *Bulletin of the American Meteorological Society*, vol. 90, pp. 311–323, Mar. 2009.

[6] B. Burger, "Electricity production from solar and wind in germany in 2014," Aug. 2014.

[7] K. Kroh, "Germany sets new record, generating 74 percent of power needs from renewable energy."

[8] IEA, *Solar Energy Perspectives*. OECD Publishing, 2011.

[9] M. A. Green, K. Emery, Y. Hishikawa, W. Warta, and E. D. Dunlop, "Solar cell efficiency tables (version 44)," *Progress in Photovoltaics: Research and Applications*, vol. 22, no. 7, pp. 701–710, 2014.

[10] B. Burger, K. Kiefer, C. Kost, S. Nold, S. Philipps, R. Preu, R. Schindler, T. Schlegl, G. Stryl-Hipp, G. Willeke, H. Wirth, I. Brucker, A. Häberle, V. Schacht, and W. Warmuth, "Photovoltaics report," July 2014.

[11] M. J. Shiao, "Thin film 2012-2016: Technologies, markets and strategies for survival - GTM research."

[12] "Manz AG - media & PR - PR-news - CIGS reaches efficiency of polycrystalline panels for the first time," Aug. 2014.

[13] T. Dullweber, G. Hanna, U. Rau, and H. W. Schock, "A new approach to high-efficiency solar cells by band gap grading in Cu(In,Ga)Se2 chalcopyrite

semiconductors," *Solar Energy Materials and Solar Cells*, vol. 67, pp. 145–150, Mar. 2001.

[14] T. Dullweber, U. Rau, M. Contreras, R. Noufi, and H. Schock, "Photogeneration and carrier recombination in graded gap Cu(In, Ga)Se2 solar cells," *IEEE Transactions on Electron Devices*, vol. 47, no. 12, pp. 2249–2254, 2000.

[15] V. Gremenok, V. Zalesski, A. Khodin, O. Ermakov, R. Chyhir, V. Emelyanov, and V. Syakersky, "Analysis of CIGS-based thin film solar cells with graded band gap," *physica status solidi (c)*, vol. 6, no. 5, pp. 1237–1240, 2009.

[16] O. Lundberg, M. Edoff, and L. Stolt, "The effect of Ga-grading in CIGS thin film solar cells," *Thin Solid Films*, vol. 480-481, pp. 520–525, 2005.

[17] H. Hahn, G. Frank, W. Klingler, A.-D. Meyer, and G. Storger, "Untersuchungen über ternare chalkogenide. v. uber einige ternare chalkogenide mit chalkopyritstruktur," *Zeitschrift für anorganische und allgemeine Chemie*, vol. 271, pp. 153–170, Feb. 1953.

[18] Shay, J. L., Wagner, S., and Kasper, H. M., "Efficient CuInSe2/CdS solar cells," *Appl. Phys. Lett.*, vol. 27, no. 2, p. 89.

[19] L. L. Kazmerski, F. R. White, and G. K. Morgan, "Thin-film CuInSe2/CdS heterojunction solar cells," *Applied Physics Letters*, vol. 29, pp. 268–270, Aug. 1976.

[20] R. Scheer and H.-W. Schock, "Thin film heterostructures," in *Chalcogenide Photovoltaics*, pp. 9–127, Weinheim, Germany: Wiley-VHC, 2011.

[21] ZSW, *ZSW sets 21.7 % CIGS cell record, http://www.pv-tech.org.* 2014.

[22] R. Mickelsen, W. S. Chen, Y. Hsiao, and V. Lowe, "Polycrystalline thin-film CuInSe2/CdZnS solar cells," *IEEE Transactions on Electron Devices*, vol. 31, pp. 542–546, May 1984.

[23] P. Jackson, D. Hariskos, E. Lotter, S. Paetel, R. Wuerz, R. Menner, W. Wischmann, and M. Powalla, "New world record efficiency for Cu(In,Ga)Se2 thin-film solar cells beyond 20%," *Progress in Photovoltaics: Research and Applications*, vol. 19, no. 7, pp. 894–897, 2011.

[24] A. Chirila, P. Reinhard, F. Pianezzi, P. Bloesch, A. R. Uhl, C. Fella, L. Kranz, D. Keller, C. Gretener, H. Hagendorfer, D. Jaeger, R. Erni, S. Nishiwaki, S. Buecheler, and A. N. Tiwari, "Potassium-induced surface modification of cu(in,ga)se2 thin films for high-efficiency solar cells," *Nature Materials*, vol. advance online publication, Nov. 2013.

[25] P. Jackson, D. Hariskos, R. Wuerz, W. Wischmann, and M. Powalla, "Compositional investigation of potassium doped Cu(In,Ga)Se2 solar cells with efficiencies up to 20.8%," *physica status solidi (RRL) - Rapid Research Letters*, pp. 219–222, 2014.

[26] J. Hedstrom, H. Ohlsen, M. Bodegard, A. Kylner, L. Stolt, D. Hariskos, M. Ruckh, and H. Schock, "ZnO/CdS/Cu(In,Ga)Se2 thin film solar cells with improved performance," in *, Conference Record of the Twenty Third IEEE Photovoltaic Specialists Conference, 1993*, pp. 364–371, May 1993.

[27] S.-H. Wei, S. B. Zhang, and A. Zunger, "Effects of na on the electrical and structural properties of CuInSe2," *Journal of Applied Physics*, vol. 85, pp. 7214–7218, May 1999.

[28] D. Rudmann, G. Bilger, M. Kaelin, F.-J. Haug, H. Zogg, and A. Tiwari, "Effects of NaF coevaporation on structural properties of Cu(In,Ga)Se2 thin films," *Thin Solid Films*, vol. 431-432, pp. 37–40, May 2003.

[29] D. Rudmann, D. Brémaud, A. F. da Cunha, G. Bilger, A. Strohm, M. Kaelin, H. Zogg, and A. N. Tiwari, "Sodium incorporation strategies for CIGS growth at different temperatures," *Thin Solid Films*, vol. 480-481, pp. 55–60, 2005.

[30] M. Bodeg Ard, K. Granath, and L. Stolt, "Growth of Cu(In,Ga)Se2 thin films by coevaporation using alkaline precursors," *Thin Solid Films*, vol. 361-362, pp. 9–16, 2000.

[31] M. Powalla, W. Witte, P. Jackson, S. Paetel, E. Lotter, R. Wuerz, F. Kessler, C. Tschamber, W. Hempel, D. Hariskos, R. Menner, A. Bauer, S. Spiering, E. Ahlswede, T. Friedlmeier, D. Blazquez-Sanchez, I. Klugius, and W. Wischmann, "CIGS cells and modules with high efficiency on glass and flexible substrates," *IEEE Journal of Photovoltaics*, vol. 4, pp. 440–446, Jan. 2014.

[32] D. Herrmann, F. Kessler, K. Herz, M. Powalla, A. Schulz, J. Schneider, and U. Schumacher, "High-performance barrier layers for flexible CIGS thin-film solar cells on metal foils," *MRS Online Proceedings Library*, vol. 763, 2003.

[33] J.-H. Yoon, T.-Y. Seong, and J.-h. Jeong, "Effect of a mo back contact on na diffusion in CIGS thin film solar cells," *Progress in Photovoltaics: Research and Applications*, vol. 21, pp. 58–63, Jan. 2013.

[34] T. Lepetit, D. Mangin, E. Gautron, M. Tomassini, S. Harel, L. Arzel, and N. Barreau, "Impact of DC-power during mo back contact sputtering on the alkali distribution in Cu(In,Ga)Se2-based thin film solar cells," *Thin Solid Films*, 2014.

[35] K.-J. Hsiao, J.-D. Liu, H.-H. Hsieh, and T.-S. Jiang, "Electrical impact of MoSe2 on CIGS thin-film solar cells," *Physical Chemistry Chemical Physics*, vol. 15, pp. 18174–18178, Oct. 2013.

[36] T. Wada, N. Kohara, S. Nishiwaki, and T. Negami, "Characterization of the Cu(In,Ga)Se2/Mo interface in CIGS solar cells," *Thin Solid Films*, vol. 387, pp. 118–122, May 2001.

[37] R. J. Matson, O. Jamjoum, A. D. Buonaquisti, P. E. Russell, L. L. Kazmerski, P. Sheldon, and R. K. Ahrenkiel, "Metal contacts to CuInSe2," *Solar Cells*, vol. 11, pp. 301–305, Apr. 1984.

[38] K. Momma and F. Izumi, "*VESTA 3* for three-dimensional visualization of crystal, volumetric and morphology data," *Journal of Applied Crystallography*, vol. 44, pp. 1272–1276, Dec. 2011.

[39] B. Grzeta-Plenkovic, S. Popovic, B. Celustka, and B. Santic, "Crystal data for AgGaxIn1-xSe2 and CuGaxIn1-xSe2," *Journal of Applied Crystallography*, vol. 13, no. 3, pp. 311–315, 1980.

[40] S. Siebentritt, M. Igalson, C. Persson, and S. Lany, "The electronic structure of chalcopyrites-bands, point defects and grain boundaries," *Progress in Photovoltaics: Research and Applications*, vol. 18, pp. 390–410, Sept. 2010.

[41] S.-H. Wei and S. B. Zhang, "Defect properties of CuInSe2 and CuGaSe2," *Journal of Physics and Chemistry of Solids*, vol. 66, pp. 1994–1999, Nov. 2005.

[42] R. Herberholz, U. Rau, H. W. Schock, T. Haalboom, T. Gödecke, F. Ernst, C. Beilharz, K. W. Benz, and D. Cahen, "Phase segregation, cu migration and junction formation in Cu(In, Ga)Se2," *The European Physical Journal - Applied Physics*, vol. 6, no. 02, pp. 131–139, 1999.

[43] S.-H. Wei and A. Zunger, "Band offsets and optical bowings of chalcopyrites and zn-based II-VI alloys," *Journal of Applied Physics*, vol. 78, pp. 3846–3856, Sept. 1995.

[44] S. Jung, S. Ahn, J. H. Yun, J. Gwak, D. Kim, and K. Yoon, "Effects of ga contents on properties of CIGS thin films and solar cells fabricated by co-evaporation technique," *Current Applied Physics*, vol. 10, no. 4, pp. 990–996, 2010.

[45] T. Schlenker, V. Laptev, H. W. Schock, and J. H. Werner, "Substrate influence on cu(in,ga)se2 film texture," *Thin Solid Films*, vol. 480-481, pp. 29–32, June 2005.

[46] S. Chaisitsak, A. Yamada, and M. Konagai, "Preferred orientation control of cu(in1-xGax)se2 (x =0.28) thin films and its influence on solar cell characteristics," *Japanese Journal of Applied Physics*, vol. 41, p. 507, Feb. 2002.

[47] T. Mise and T. Nakada, "Microstructural properties of (In,Ga)2Se3 precursor layers for efficient CIGS thin-film solar cells," *Solar Energy Materials and Solar Cells*, vol. 93, pp. 1000–1003, June 2009.

[48] M. Powalla, P. Jackson, W. Witte, D. Hariskos, S. Paetel, C. Tschamber, and W. Wischmann, "High-efficiency cu(in,ga)se2 cells and modules," *Solar Energy Materials and Solar Cells*, vol. 119, pp. 51–58, Dec. 2013.

[49] K. Sakurai, R. Scheer, S. Nakamura, Y. Kimura, T. Baba, C. A. Kaufmann, A. Neisser, S. Ishizuka, A. Yamada, K. Matsubara, K. Iwata, P. Fons, H. Nakanishi, and S. Niki, "Structural changes of CIGS during deposition investigated by spectroscopic light scattering: A study on ga concentration and se pressure," *Solar Energy Materials and Solar Cells*, vol. 90, pp. 3377–3384, Nov. 2006.

[50] T. Klinkert, M. Jubault, F. Donsanti, D. Lincot, and J.-F. Guillemoles, "Ga gradients in Cu(In,Ga)Se2: Formation, characterization, and consequences," *Journal of Renewable and Sustainable Energy*, vol. 6, p. 011403, Feb. 2014.

[51] H. Wang, Y. Zhang, X. L. Kou, Y. A. Cai, W. Liu, T. Yu, J. B. Pang, C. J. Li, and Y. Sun, "Effect of substrate temperature on the structural and electrical properties of CIGS films based on the one-stage co-evaporation process," *Semiconductor Science and Technology*, vol. 25, p. 055007, May 2010.

[52] W. N. Shafarman and J. Zhu, "Effect of substrate temperature and depostion profile on evaporated Cu(InGa)Se2 films and devices," *Thin Solid Films*, vol. 361-362, pp. 473–477, Feb. 2000.

[53] P. M. P. Salomé, A. Hultqvist, V. Fjällström, B. Vermang, M. Edoff, B. Aitken, K. Zhang, K. Fuller, and C. Kosik Williams, "The effect of high growth temperature on Cu(In,Ga)Se2 thin film solar cells," *Solar Energy Materials and Solar Cells*, vol. 123, pp. 166–170, 2014.

[54] M. Gloeckler, J. R. Sites, and W. K. Metzger, "Grain-boundary recombination in cu(in,ga)se2 solar cells," *Journal of Applied Physics*, vol. 98, p. 113704, Dec. 2005.

[55] D. Schmid, M. Ruckh, F. Grunwald, and H. W. Schock, "Chalcopyrite/defect chalcopyrite heterojunctions on the basis of CuInSe2," *Journal of Applied Physics*, vol. 73, pp. 2902–2909, Mar. 1993.

[56] M. Morkel, L. Weinhardt, B. Lohmüller, C. Heske, E. Umbach, W. Riedl, S. Zweigart, and F. Karg, "Flat conduction-band alignment at the CdS/CuInSe2 thin-film solar-cell heterojunction," *Applied Physics Letters*, vol. 79, pp. 4482–4484, Dec. 2001.

[57] M. Contreras, H. Wiesner, D. Niles, K. Ramanathan, R. Matson, J. Tuttle, J. Keane, and R. Noufi, "Defect chalcopyrite Cu(In1-xGax)3Se5 materials and high Ga-content Cu(In,Ga)Se2-based solar cells," in *, Conference Record of the Twenty Fifth IEEE Photovoltaic Specialists Conference, 1996*, pp. 809–812, May 1996.

[58] C.-S. Jiang, F. S. Hasoon, H. R. Moutinho, H. A. Al-Thani, M. J. Romero, and M. M. Al-Jassim, "Direct evidence of a buried homojunction in Cu(In,Ga)Se2 solar cells," *Applied Physics Letters*, vol. 82, pp. 127–129, Dec. 2002.

[59] T. Nakada and A. Kunioka, "Direct evidence of cd diffusion into Cu(In,Ga)Se2 thin films during chemical-bath deposition process of CdS films," *Applied Physics Letters*, vol. 74, pp. 2444–2446, Apr. 1999.

[60] K. Ramanathan, R. Bhattacharya, J. Granata, J. Webb, D. Niles, M. A. Contreras, H. Wiesner, F. S. Hasoon, and R. Noufi, "Advances in the CIS research at NREL," in *, Conference Record of the Twenty-Sixth IEEE Photovoltaic Specialists Conference, 1997*, pp. 319–322, Sept. 1997.

[61] T. Nakada, "Nano-structural investigations on Cd-doping into Cu(In,Ga)Se2 thin films by chemical bath deposition process," *Thin Solid Films*, vol. 361-362, pp. 346–352, 2000.

[62] T. Nakada and M. Mizutani, "Improved efficiency of Cu(In,Ga)Se2 thin film solar cells with chemically deposited ZnS buffer layers by air-annealing-formation of homojunction by solid phase diffusion," in *Conference Record of the Twenty-Eighth IEEE Photovoltaic Specialists Conference, 2000*, pp. 529–534, 2000.

[63] N. Naghavi, D. Abou-Ras, N. Allsop, N. Barreau, S. Bücheler, A. Ennaoui, C.-H. Fischer, C. Guillen, D. Hariskos, J. Herrero, R. Klenk, K. Kushiya,

D. Lincot, R. Menner, T. Nakada, C. Platzer-Björkman, S. Spiering, A. Tiwari, and T. Törndahl, "Buffer layers and transparent conducting oxides for chalcopyrite Cu(In,Ga)(S,Se)2 based thin film photovoltaics: present status and current developments," *Progress in Photovoltaics: Research and Applications*, vol. 18, no. 6, pp. 411–433, 2010.

[64] "Singulus technologies picks up EUR15 million CIGS order from hanergy: pv-magazine."

[65] A. Luque and S. Hegedus, *Handbook of Photovoltaic Science and Engineering*. 2003.

[66] R. Ortega Borges, D. Lincot, and J. Vedel, "Chemical bath deposition of zinc sulfide thin films," (Montreux, Switzerland), pp. 862–865, 1992.

[67] J. Kessler, M. Ruckh, D. Hariskos, U. Rühle, R. Menner, and H. W. Schock, "Interface engineering between CuInSe2 and ZnO," (Louisville), pp. 447–452, 1993.

[68] A. Ennaoui, M. Bär, J. Klaer, T. Kropp, R. Sáez-Araoz, and M. C. Lux-Steiner, "Highly-efficient Cd-free CuInS2 thin-film solar cells and mini-modules with Zn(S,O) buffer layers prepared by an alternative chemical bath process," *Progress in Photovoltaics: Research and Applications*, vol. 14, pp. 499–511, Sept. 2006.

[69] C. Persson, C. Platzer-Björkman, J. Malmström, T. Törndahl, and M. Edoff, "Strong valence-band offset bowing of ZnO1-xSx enhances p-type nitrogen doping of ZnO-like alloys," *Physical Review Letters*, vol. 97, p. 146403, Oct. 2006.

[70] "Optimization of rf-sputtered ZnO/ZnO:Al] for Cu(In,Ga)Se2 based devices, author = Kessler, J. and Norling, J. and Lundberg, O. and Wennerberg, J. and Stolt, Lars, month = may, year = 2000, pages = 775-778„" (Glasgow, UK).

[71] U. Rau and M. Schmidt, "Electronic properties of ZnO/CdS/Cu(In,Ga)Se2 solar cells - aspects of heterojunction formation," *Thin Solid Films*, vol. 387, pp. 141–146, May 2001.

[72] "Solar frontier press release, http://www.solar-frontier.com/eng/news/2014/c031367.html, 23.07.2014," July 2014.

[73] F. Karg, V. Probst, H. Harms, J. Rimmasch, W. Riedl, J. Kotschy, J. Holt, R. Treichler, O. Eibl, A. Mitwalsky, and A. Kiendl, "Novel rapid-thermal-processing for CIS thin-film solar cells," in *, Conference Record of the Twenty Third IEEE Photovoltaic Specialists Conference, 1993*, pp. 441–446, May 1993.

[74] R. A. Mickelsen and W. S. Chen, "High photocurrent polycrystalline thin-film CdS/CuInSe2 solar cella," *Applied Physics Letters*, vol. 36, pp. 371–373, Mar. 1980.

[75] J. R. Tuttle, M. A. Contreras, T. J. Gillespie, K. R. Ramanathan, A. L. Tennant, J. Keane, A. M. Gabor, and R. Noufi, "Accelerated publication 17.1%

efficient Cu(In,Ga)Se2-based thin-film solar cell," *Progress in Photovoltaics: Research and Applications*, vol. 3, pp. 235–238, Jan. 1995.

[76] I. Repins, M. A. Contreras, B. Egaas, C. DeHart, J. Scharf, C. L. Perkins, B. To, and R. Noufi, "19 · 9%-efficient ZnO/CdS/CuInGaSe2 solar cell with 81 · 2% fill factor," *Progress in Photovoltaics: Research and Applications*, vol. 16, no. 3, pp. 235–239, 2008.

[77] G. Brown, P. Stone, J. Woodruff, B. Cardozo, and D. Jackrel, "Device characteristics of a 17.1% efficient solar cell deposited by a non-vacuum printing method on flexible foil," in *2012 38th IEEE Photovoltaic Specialists Conference (PVSC)*, pp. 003230–003233, June 2012.

[78] V. Bermudez, "Current status at NEXCIS, towards industry," (Berlin), 2014.

[79] D. Lincot, J. F. Guillemoles, S. Taunier, D. Guimard, J. Sicx-Kurdi, A. Chaumont, O. Roussel, O. Ramdani, C. Hubert, J. P. Fauvarque, N. Bodereau, L. Parissi, P. Panheleux, P. Fanouillere, N. Naghavi, P. P. Grand, M. Benfarah, P. Mogensen, and O. Kerrec, "Chalcopyrite thin film solar cells by electrodeposition," *Solar Energy*, vol. 77, pp. 725–737, Dec. 2004.

[80] S. Shirakata, Y. Kannaka, H. Hasegawa, T. Kariya, and S. Isomura, "Properties of cu(in,ga)se2 thin films prepared by chemical spray pyrolysis," *Japanese Journal of Applied Physics*, vol. 38, p. 4997, Sept. 1999.

[81] D. B. Mitzi, M. Yuan, W. Liu, A. J. Kellock, S. J. Chey, V. Deline, and A. G. Schrott, "A high-efficiency solution-deposited thin-film photovoltaic device," *Advanced Materials*, vol. 20, pp. 3657–3662, Oct. 2008.

[82] K. R. Murali, "Preparation and characterization of chemically deposited CuInSe2 films," *Thin Solid Films*, vol. 167, pp. L19–L22, Dec. 1988.

[83] V. K. Kapur, A. Bansal, P. Le, and O. I. Asensio, "Non-vacuum processing of CuIn1-xGaxSe2 solar cells on rigid and flexible substrates using nanoparticle precursor inks," *Thin Solid Films*, vol. 431-432, pp. 53–57, May 2003.

[84] P. D. Paulson, R. W. Birkmire, and W. N. Shafarman, "Optical characterization of CuIn1-xGaxSe2 alloy thin films by spectroscopic ellipsometry," *Journal of Applied Physics*, vol. 94, pp. 879–888, July 2003.

[85] W. W. Gärtner, "Depletion-layer photoeffects in semiconductors," *Physical Review*, vol. 116, pp. 84–87, Oct. 1959.

[86] P. Würfel, *Physics of Solar Cells: From Principles to New Concepts*. Weinheim, Germany: Wiley-VCH Verlag GmbH & Co. KGaA, 2005.

[87] S. S. Hegedus and W. N. Shafarman, "Thin-film solar cells: device measurements and analysis," *Progress in Photovoltaics: Research and Applications*, vol. 12, no. 2-3, pp. 155–176, 2004.

[88] W. Shockley and H. J. Queisser, "Detailed balance limit of efficiency of p-n junction solar cells," *Journal of Applied Physics*, vol. 32, pp. 510–519, May 1961.

[89] M. Paire, *Highly efficient solar cells in low dimensionality based on*

*Cu(In,Ga)Se2 chalcopyrite materials*. PhD thesis, Pierre et Marie Curie, Paris, 2012.

[90] K. A. Bulashevich and S. Y. Karpov, "Is auger recombination responsible for the efficiency rollover in III-nitride light-emitting diodes?," *physica status solidi (c)*, vol. 5, pp. 2066–2069, May 2008.

[91] M. Gloeckler, A. Fahrenbruch, and J. Sites, "Numerical modeling of CIGS and CdTe solar cells: setting the baseline," in *Proceedings of 3rd World Conference on Photovoltaic Energy Conversion, 2003*, vol. 1, pp. 491–494 Vol.1, May 2003.

[92] B. Ohnesorge, R. Weigand, G. Bacher, A. Forchel, W. Riedl, and F. H. Karg, "Minority-carrier lifetime and efficiency of Cu(In,Ga)Se2 solar cells," *Applied Physics Letters*, vol. 73, pp. 1224–1226, Aug. 1998.

[93] I. Repins, W. Metzger, C. Perkins, J. Li, and M. Contreras, "Correlation between measured minority-carrier lifetime and device performance," *IEEE Transactions on Electron Devices*, vol. 57, pp. 2957–2963, Nov. 2010.

[94] C.-T. Sah, R. Noyce, and W. Shockley, "Carrier generation and recombination in p-n junctions and p-n junction characteristics," *Proceedings of the IRE*, vol. 45, pp. 1228–1243, Sept. 1957.

[95] T. Dullweber, O. Lundberg, J. Malmström, M. Bodegård, L. Stolt, U. Rau, H. W. Schock, and J. H. Werner, "Back surface band gap gradings in Cu(In,Ga)Se2 solar cells Cu(In,Ga)Se2," *Thin Solid Films*, vol. 387, pp. 11–13, May 2001.

[96] J. H. Werner, S. Kolodinski, U. Rau, J. K. Arch, and E. Bauser, "Silicon solar cell of 16.8 $\mu$m thickness and 14.7% efficiency," *Applied Physics Letters*, vol. 62, pp. 2998–3000, June 1993.

[97] H. J. Hovel, *Semiconductors and Semimetals*. New York: Academic Press, 11 ed., 1975.

[98] H. Wilhelm, H.-W. Schock, and R. Scheer, "Interface recombination in heterojunction solar cells: Influence of buffer layer thickness," *Journal of Applied Physics*, vol. 109, p. 084514, Apr. 2011.

[99] J. Kessler, C. Chityuttakan, J. Lu, J. Schöldström, and L. Stolt, "Cu(In,Ga)Se2 thin films grown with a Cu-poor/rich/poor sequence: growth model and structural considerations," *Progress in Photovoltaics: Research and Applications*, vol. 11, no. 5, pp. 319–331, 2003.

[100] J. Schöldström, J. Kessler, and M. Edoff, "Two-stage growth of smooth cu(in,ga)se2 films using end-point detection," *Thin Solid Films*, vol. 480-481, pp. 61–66, June 2005.

[101] J. Kessler, J. Scholdstrom, and L. Stolt, "Rapid cu(in,ga)se2 growth using end point detection," in *Conference Record of the Twenty-Eighth IEEE Photovoltaic Specialists Conference, 2000*, pp. 509–512, 2000.

[102] M. Nishitani, T. Negami, and T. Wada, "Composition monitoring method in CuInSe2 thin film preparation," *Thin Solid Films*, vol. 258, pp. 313–316, Mar. 1995.

[103] T. Satoh, S. Hayashi, S. Nishiwaki, S.-i. Shimakawa, Y. Hashimoto, T. Negami, and T. Uenoyama, "Fabrication of cu(in,ga)se2 by in-line evaporation (composition monitoring method using heat radiation)," *Solar Energy Materials and Solar Cells*, vol. 67, pp. 203–207, Mar. 2001.

[104] I. L. Repins, D. Fisher, W. K. Batchelor, L. Woods, and M. E. Beck, "A non-contact low-cost sensor for improved repeatability in co-evaporated CIGS," *Progress in Photovoltaics: Research and Applications*, vol. 13, no. 4, pp. 311–323, 2005.

[105] J. Schöldström, U. Zimmermann, and M. Edoff, "Determination of the optical constants for cu(in,ga)se2 and CuxSe in the IR region," *Journal of Physics D: Applied Physics*, vol. 45, p. 115101, Mar. 2012.

[106] R. Caballero, C. A. Kaufmann, V. Efimova, T. Rissom, V. Hoffmann, and H. W. Schock, "Investigation of cu(in,ga)se2 thin-film formation during the multi-stage co-evaporation process," *Progress in Photovoltaics: Research and Applications*, vol. 21, no. 1, pp. 30–46, 2013.

[107] S. Niki, P. J. Fons, A. Yamada, Y. Lacroix, H. Shibata, H. Oyanagi, M. Nishitani, T. Negami, and T. Wada, "Effects of the surface cu2-xSe phase on the growth and properties of CuInSe2 films," *Applied Physics Letters*, vol. 74, pp. 1630–1632, Mar. 1999.

[108] S. Ishizuka, A. Yamada, P. Fons, and S. Niki, "Texture and morphology variations in (In,Ga)2Se3 and Cu(In,Ga)Se2 thin films grown with various Se source conditions," *Progress in Photovoltaics: Research and Applications*, vol. 21, pp. 544–553, June 2013.

[109] N. Kohara, S. Nishiwaki, Y. Hashimoto, T. Negami, and T. Wada, "Electrical properties of the cu(in,ga)se2/ MoSe2/mo structure," *Solar Energy Materials and Solar Cells*, vol. 67, pp. 209–215, Mar. 2001.

[110] L. Assmann, J. C. Bernède, A. Drici, C. Amory, E. Halgand, and M. Morsli, "Study of the mo thin films and mo/CIGS interface properties," *Applied Surface Science*, vol. 246, pp. 159–166, June 2005.

[111] D. Abou-Ras, G. Kostorz, D. Bremaud, M. Kälin, F. Kurdesau, A. Tiwari, and M. Döbeli, "Formation and characterisation of MoSe2 for cu(in,ga)se2 based solar cells," *Thin Solid Films*, vol. 480-481, pp. 433–438, 2005.

[112] M. K. Agarwal and L. T. Talele, "Growth conditions and structural characterization of molybdenum sulphoselenide single crystals: (MoSxSe2-x, 0<x<2)," *Materials Research Bulletin*, vol. 20, pp. 329–336, Mar. 1985.

[113] J.-H. Yoon, J.-H. Kim, W. M. Kim, J.-K. Park, Y.-J. Baik, T.-Y. Seong, and J.-h. Jeong, "Electrical properties of CIGS/mo junctions as a function of MoSe2 orientation and na doping," *Progress in Photovoltaics: Research and Applications*, vol. 22, pp. 90–96, Jan. 2014.

[114] S. Nishiwaki, N. Kohara, T. Negami, and T. Wada, "MoSe 2 layer formation at Cu(In,Ga)Se2/Mo interfaces in high efficiency Cu(In1- xGa x)Se 2 solar cells," *Japanese Journal of Applied Physics*, vol. 37, p. L71, Jan. 1998.

[115] M. Lammer, R. Kniese, and M. Powalla, "In-line deposited Cu(In,Ga)Se2 solar cells: influence of deposition temperature and Na co-evaporation on carrier collection," *Thin Solid Films*, vol. 451–452, pp. 175–178, Mar. 2004.

[116] D. Y. Lee, B. T. Ahn, K. H. Yoon, and J. S. Song, "Effect of first-stage temperature on Cu(In,Ga)Se2 solar cells using the evaporation of binary selenide compounds," *Solar Energy Materials and Solar Cells*, vol. 75, pp. 73–79, Jan. 2003.

[117] L. Zhang, Q. He, W.-L. Jiang, F.-F. Liu, C.-J. Li, and Y. Sun, "Effects of substrate temperature on the structural and electrical properties of cu(in,ga)se2 thin films," *Solar Energy Materials and Solar Cells*, vol. 93, pp. 114–118, Jan. 2009.

[118] W. Witte, D. Abou-Ras, K. Albe, G. H. Bauer, F. Bertram, C. Boit, R. Brüggemann, J. Christen, J. Dietrich, A. Eicke, D. Hariskos, M. Maiberg, R. Mainz, M. Meessen, M. Müller, O. Neumann, T. Orgis, S. Paetel, J. Pohl, H. Rodriguez-Alvarez, R. Scheer, H.-W. Schock, T. Unold, A. Weber, and M. Powalla, "Gallium gradients in Cu(In,Ga)Se2 thin-film solar cells," *Progress in Photovoltaics: Research and Applications*, pp. n/a–n/a, Mar. 2014.

[119] C. Kaufmann, R. Caballero, T. Unold, R. Hesse, R. Klenk, S. Schorr, M. Nichterwitz, and H.-W. Schock, "Depth profiling of cu(in,ga)se2 thin films grown at low temperatures," *Solar Energy Materials and Solar Cells*, vol. 93, no. 6-7, pp. 859–863, 2009.

[120] H. Rodriguez-Alvarez, R. Mainz, R. Caballero, D. Abou-Ras, M. Klaus, S. Gledhill, A. Weber, C. Kaufmann, and H.-W. Schock, "Real-time study of ga diffusion processes during the formation of cu(in,ga)se2: The role of cu and na content," *Solar Energy Materials and Solar Cells*, vol. 116, pp. 102–109, Sept. 2013.

[121] S. M. Schleussner, T. Törndahl, M. Linnarsson, U. Zimmermann, T. Wätjen, and M. Edoff, "Development of gallium gradients in three-stage cu(in,ga)se2 co-evaporation processes," *Progress in Photovoltaics: Research and Applications*, vol. 20, no. 3, pp. 284–293, 2012.

[122] H. Mönig, C. A. Kaufmann, C.-H. Fischer, A. Grimm, R. Caballero, B. Johnson, A. Eicke, M. C. Lux-Steiner, and I. Lauermann, "Gallium gradients in chalcopyrite thin films: Depth profile analyses of films grown at different temperatures," *Journal of Applied Physics*, vol. 110, p. 093509, Nov. 2011.

[123] K. Zhang, C.-l. Yang, L. Yin, Z. Liu, Q.-m. Song, H.-l. Luo, Z.-y. Xiong, M.-m. Xu, and X.-d. Xiao, "Fabricating highly efficient cu(in,ga)se2 solar cells at low glass-substrate temperature by active gallium grading control," *Solar Energy Materials and Solar Cells*, vol. 120, Part A, pp. 253–258, Jan. 2014.

[124] B. Fleutot, D. Lincot, M. Jubault, Z. J. Li Kao, N. Naghavi, J.-F. Guillemoles, and F. Donsanti, "GaSe formation at the Cu(In,Ga)Se2/Mo interface-a novel approach for flexible solar cells by easy mechanical lift-off," *Advanced Materials Interfaces*, vol. 1, pp. n/a–n/a, July 2014.

[125] T. J. Wieting, A. Grisel, and F. Lévy, "Interlayer bonding and localized charge in MoSe2 and a-MoTe2," *Physica B+C*, vol. 99, pp. 337–342, Jan. 1980.

[126] A. M. Gabor, J. R. Tuttle, D. S. Albin, M. A. Contreras, R. Noufi, and A. M. Hermann, "High-efficiency CuInxGa1-xSe2 solar cells made from (Inx,Ga1-x)2Se3 precursor films," *Applied Physics Letters*, vol. 65, pp. 198–200, July 1994.

[127] W. P. Davey, "Precision measurements of the lattice constants of twelve common metals," *Physical Review*, vol. 25, no. 6, pp. 753–761, 1925.

[128] A. Tonejc, S. Popovic, and B. Grzeta-Plenkovic, "Phases, lattice parameters and thermal expansion of (ga $_{x}$ in $_{1-x}$ ) $_{2}$ se $_{3}$, between room temperature and melting point," *Journal of Applied Crystallography*, vol. 13, pp. 24–30, Feb. 1980.

[129] D. Abou-Ras, R. Caballero, C. A. Kaufmann, M. Nichterwitz, K. Sakurai, S. Schorr, T. Unold, and H. W. Schock, "Impact of the ga concentration on the microstructure of CuIn1-xGaxSe2," *physica status solidi (RRL) – Rapid Research Letters*, vol. 2, pp. 135–137, June 2008.

[130] T. Wada, N. Kohara, T. Negami, and M. Nishitani, "Growth of CuInSe2 crystals in cu-rich cu-in-se thin films," *Journal of Materials Research*, vol. 12, no. 06, pp. 1456–1462, 1997.

[131] T. Painchaud, *Mécanismes de croissance des couches minces de Cu(In,Ga)Se2 co-évaporées : vers des synthèses rapides et à basse température*. PhD thesis, Université de Nantes, 2010.

[132] S. Schleussner, *ZrN Back-Contact Reflectors and Ga Gradients in Cu(In,Ga)Se2 solar cells*. PhD thesis, Uppsala Universitet, Uppsala, 2011.

[133] H. Rodriguez-Alvarez, R. Mainz, and S. Sadewasser, "A one-dimensional fickian model to predict the ga depth profiles in three-stage cu(in,ga)se2," *Journal of Applied Physics*, vol. 115, p. 204913, May 2014.

[134] R. Klenk, T. Walter, H.-W. Schock, and D. Cahen, "A model for the successful growth of polycrystalline films of CuInSe2 by multisource physical vacuum evaporation," *Advanced Materials*, vol. 5, pp. 114–119, Feb. 1993.

[135] A. M. Gabor, J. R. Tuttle, D. S. Albin, R. Matson, A. Franz, D. W. Niles, M. A. Contreras, A. M. Hermann, and R. Noufi, "A microstructural comparison of Cu(In,Ga)Se2 thin films grown from CuxSe and (In,Ga)2Se3 precursors," in *Symposium H - Polycrystalline Thin Films - Structure, Texture, Properties and Applications*, vol. 343 of *MRS Online Proceedings Library*, Jan. 1994.

[136] P. Jackson, R. Würz, U. Rau, J. Mattheis, M. Kurth, T. Schlötzer, G. Bilger, and J. H. Werner, "High quality baseline for high efficiency, cu(in1-x,gax)se2 solar cells," *Progress in Photovoltaics: Research and Applications*, vol. 15, no. 6, pp. 507–519, 2007.

[137] R. Caballero, V. Izquierdo-Roca, X. Fontane, C. Kaufmann, J. Alvarez-García, A. Eicke, L. Calvo-Barrio, A. Perez-Rodríguez, H. Schock, and J. Morante,

"Cu deficiency in multi-stage co-evaporated Cu(In,Ga)Se2 for solar cells applications: Microstructure and Ga in-depth alloying," *Acta Materialia*, vol. 58, pp. 3468–3476, May 2010.

[138] R. W. Birkmire and B. E. McCandless, "Specular CuInSe2 films for solar cells," *Applied Physics Letters*, vol. 53, pp. 140–141, July 1988.

[139] B. Canava, J. Guillemoles, J. Vigneron, D. Lincot, and A. Etcheberry, "Chemical elaboration of well defined cu(in,ga)se2 surfaces after aqueous oxidation etching," *Journal of Physics and Chemistry of Solids*, vol. 64, pp. 1791–1796, Sept. 2003.

[140] W. Li, S. Cohen, K. Gartsman, R. Caballero, P. van Huth, R. Popovitz-Biro, and D. Cahen, "Chemical compositional non-uniformity and its effects on CIGS solar cell performance at the nm-scale," *Solar Energy Materials and Solar Cells*, vol. 98, pp. 78–82, Mar. 2012.

[141] N. Kohara, T. Negami, M. Nishitani, and T. Wada, "Preparation of device-quality cu(in, ga)se2 thin films deposited by coevaporation with composition monitor," *Japanese Journal of Applied Physics*, vol. 34, no. Part 2, No. 9A, pp. L1141–L1144, 1995.

[142] W. Witte, R. Kniese, and M. Powalla, "Raman investigations of Cu(In,Ga)Se2 thin films with various copper contents," *Thin Solid Films*, pp. 867–869, July 2008.

[143] S. Marsillac, "Experimental evidence of the low-temperature formation of gamma-in2se3 thin films obtained by a solid-state reaction," *Thin Solid Films*, pp. 14–20, Feb. 1996.

[144] L. Calvo-Barrio, A. Perez-Rodiguez, J. Alvarez-Garcia, A. Romano-Rodriguez, B. Barcones, J. Morante, K. Siemer, I. Luck, R. Klenk, and R. Scheer, "Combined in-depth scanning auger microscopy and raman scattering characterisation of CuInS2 polycrystalline films," *Vacuum*, vol. 63, no. 1-2, pp. 315–321, 2001.

[145] E. J. Friedrich, R. Fernandez-Ruiz, J. M. Merino, and M. Leon, "X-ray diffraction data and rietveld refinement of CuGaxIn1-xSe2 (x=0.15 and 0.50)," *Powder Diffraction*, vol. 25, no. 03, pp. 253–257, 2010.

[146] A. Rockett, "The effect of na in polycrystalline and epitaxial single-crystal CuIn1-xGaxSe2," *Thin Solid Films*, vol. 480-481, pp. 2–7, 2005.

[147] A. Chirila, S. Buecheler, F. Pianezzi, P. Bloesch, C. Gretener, A. R. Uhl, C. Fella, L. Kranz, J. Perrenoud, S. Seyrling, R. Verma, S. Nishiwaki, Y. E. Romanyuk, G. Bilger, and A. N. Tiwari, "Highly efficient cu(in,ga)se2 solar cells grown on flexible polymer films," *Nature Materials*, vol. 10, pp. 857–861, Nov. 2011.

[148] M. Gloeckler and J. R. Sites, "Band-gap grading in cu(in,ga)se2 solar cells," *Journal of Physics and Chemistry of Solids*, pp. 1891 – 1894, 2005.

[149] J. Song, S. S. Li, C. Huang, O. Crisalle, and T. Anderson, "Device modeling

and simulation of the performance of cu(in1-x,gax)se2 solar cells," *Solid-State Electronics*, vol. 48, pp. 73–79, Jan. 2004.

[150] A. Morales-Acevedo, "Effective absorption coefficient for graded band-gap semiconductors and the expected photocurrent density in solar cells," *Solar Energy Materials and Solar Cells*, vol. 93, pp. 41–44, Jan. 2009.

[151] A. Delamarre, L. Lombez, and J.-F. Guillemoles, "Contactless mapping of saturation currents of solar cells by photoluminescence," *Applied Physics Letters*, vol. 100, p. 131108, Mar. 2012.

[152] M. Nichterwitz, R. Caballero, C. A. Kaufmann, H.-W. Schock, and T. Unold, "Generation-dependent charge carrier transport in cu(in,ga)se2/CdS/ZnO thin-film solar-cells," *Journal of Applied Physics*, vol. 113, pp. 044515–044515–16, Jan. 2013.

[153] C. Champness, "Estimation of diffusion lengths in CuInSe2-based cells using the photocurrent-capacitance method," in *Conference Record of the Twenty-Ninth IEEE Photovoltaic Specialists Conference, 2002*, pp. 732–735, May 2002.

[154] A. Hultqvist, C. Platzer-Björkman, E. Coronel, and M. Edoff, "Experimental investigation of cu(in1-x,gax)se2/zn(o1-z,sz) solar cell performance," *Solar Energy Materials and Solar Cells*, vol. 95, no. 2, pp. 497–503, 2011.

[155] S. Sharbati and J. R. Sites, "Impact of the band offset for zn(o,s)/p-cu(in,ga)se2 solar cells," *IEEE Journal of Photovoltaics*, vol. 4, pp. 697 – 702, Mar. 2014.

[156] I. L. Eisgruber, J. E. Granata, J. R. Sites, J. Hou, and J. Kessler, "Blue-photon modification of nonstandard diode barrier in CuInSe2 solar cells," *Solar Energy Materials and Solar Cells*, vol. 53, pp. 367–377, June 1998.

[157] A. Niemegeers, M. Burgelman, R. Herberholz, U. Rau, D. Hariskos, and H.-W. Schock, "Model for electronic transport in cu(in,ga)se2 solar cells," *Progress in Photovoltaics: Research and Applications*, vol. 6, pp. 407–421, Nov. 1998.

[158] T. Eisenbarth, T. Unold, R. Caballero, C. A. Kaufmann, and H.-W. Schock, "Interpretation of admittance, capacitance-voltage, and current-voltage signatures in cu(in,ga)se2 thin film solar cells," *Journal of Applied Physics*, vol. 107, p. 034509, Feb. 2010.

[159] J. Pettersson, C. Platzer-Björkman, and M. Edoff, "Temperature-dependent current-voltage and lightsoaking measurements on cu(in,ga)se2 solar cells with ALD-zn1-xMgxO buffer layers," *Progress in Photovoltaics: Research and Applications*, vol. 17, pp. 460–469, Nov. 2009.

[160] T. Eisenbarth, R. Caballero, M. Nichterwitz, C. A. Kaufmann, H.-W. Schock, and T. Unold, "Characterization of metastabilities in cu(in,ga)se2 thin-film solar cells by capacitance and current-voltage spectroscopy," *Journal of Applied Physics*, vol. 110, p. 094506, Nov. 2011.

[161] I. Riedel, J. Ohland, J. Neerken, J. Keller, and J. Parisi, "Photodoping and band offsets in CIGS solar cells with varied buffer layers," (Valencia, Spain), Sept. 2010.

[162] G. Koishiyev, J. Sites, S. S. Kulkarni, and N. Dhere, "Determination of back contact barrier height in cu(in,ga)(se,s)2 and CdTe solar cells," in *33rd IEEE Photovoltaic Specialists Conference, 2008. PVSC 2008*, pp. 1–3, May 2008.

[163] M. Topic, F. Smole, and J. Furlan, "Examination of blocking current-voltage behaviour through defect chalcopyrite layer in ZnO/CdS/cu(in,ga)se2/mo solar cell," *Solar Energy Materials and Solar Cells*, vol. 49, pp. 311–317, Dec. 1997.

[164] C. Platzer-Björkman, T. Törndahl, D. Abou-Ras, J. Malmström, J. Kessler, and L. Stolt, "Zn(o,s) buffer layers by atomic layer deposition in cu(in,ga)se2 based thin film solar cells: Band alignment and sulfur gradient," *Journal of Applied Physics*, vol. 100, p. 044506, Aug. 2006.

[165] L. Weinhardt, O. Fuchs, D. Gross, G. Storch, E. Umbach, N. G. Dhere, A. A. Kadam, S. S. Kulkarni, and C. Heske, "Band alignment at the CdS/cu(in,ga)s2 interface in thin-film solar cells," *Applied Physics Letters*, vol. 86, p. 062109, Feb. 2005.

[166] T. Nakada, M. Hongo, and E. Hayashi, "Band offset of high efficiency CBD-ZnS/CIGS thin film solar cells," *Thin Solid Films*, vol. 431-432, pp. 242–248, May 2003.

[167] L. Larina, D. Shin, J. H. Kim, and B. T. Ahn, "Alignment of energy levels at the ZnS/cu(in,ga)se2 interface," *Energy & Environmental Science*, vol. 4, pp. 3487–3493, Aug. 2011.

[168] C. Platzer-Björkman, P. Zabierowski, J. Pettersson, T. Törndahl, and M. Edoff, "Improved fill factor and open circuit voltage by crystalline selenium at the cu(in,ga)se2/buffer layer interface in thin film solar cells," *Progress in Photovoltaics: Research and Applications*, vol. 18, pp. 249–256, June 2010.

[169] J. W. Edwards, R. Speiser, and H. L. Johnston, "High temperature structure and thermal expansion of some metals as determined by x-ray diffraction data. i. platinum, tantalum, niobium, and molybdenum," *Journal of Applied Physics*, vol. 22, pp. 424–428, Apr. 1951.

[170] P. B. James and M. T. Lavik, "The crystal structure of MoSe2," *Acta Crystallographica*, vol. 16, pp. 1183–1183, Nov. 1963.

# Appendix

# A. Material characterisation

## A.1. X-ray fluorescence

For this work, the commercialy available Fischerscope X-ray XDV-SDD has been used. It consists of an energy-dispersive x-ray spectrometer, a micro-focus x-ray tube with tungsten anode and beryllium window and a peltier-cooled Si-drift x-ray detector. The setup has been calibrated on a Cu(In,Ga)$Se_2$ calibration standard with known composition and thickness and permits the quantitative determination of the constituents atomic concentrations.

## A.2. X-ray diffraction

In this work, X-ray diffraction is used to identify the crystallographic structure of a sample. The elastic scattering of x-ray photons by atomic planes leads to constructive interference of the scattered light under certain angles $\theta$ given by Bragg's law in A.1. From the known wavelength $\lambda$ of the x-ray radiation and the measured angle $\Theta$ of diffracted light, the interplanar distance $d$ can be estimated.

$$2d\sin(\theta) = n\lambda \tag{A.1}$$

The distance $d$ depends on the crystallographic structure of a sample and can be used to identify the crystal structure, lattice parameter and orientation of a crystal. In the classic, so-called Bragg-Brentano setup, the angle between the sample surface and the detected beam is set to follow the angle between the surface and the incident beam. This way only planes parallel to the sample surface can be detected. For the CIGS unit cell, five principal lattice planes are shown in Fig. A.1. The distance $d_{h,k,l}$ between two adjacent lattice planes of orientation (h,k,l) in a tetragonal lattice as for example the chalcopyrite CIGS structure is given by A.2.

$$\frac{1}{d_{h,k,l}^2} = \frac{h^2+k^2}{a^2} + \frac{l^2}{c^2} \tag{A.2}$$

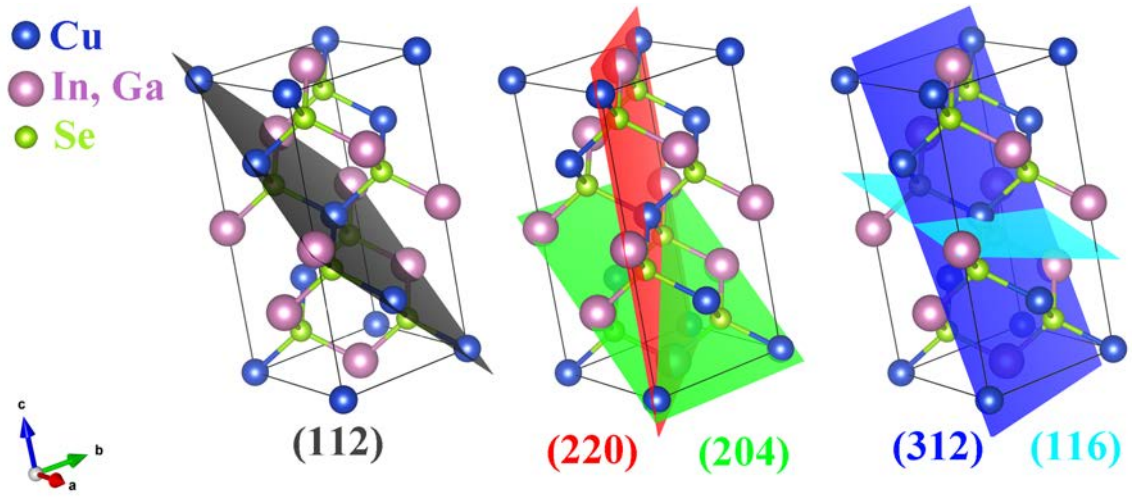


**Figure A.1.:** Principal lattice planes in the CIGS chalcopyrite unit cell. Visualisation with vesta[38].

In this work XRD is used for the identification of CIGS, $(In,Ga)_2Se_3$ and Mo with reference diffraction diagrams taken from the literature. In Tab. A.1, the publication, database ID, material composition, crystal system, space group and lattice parameters are listed.

| material | ref. | database | system | $a$ [Å] | $c$ [Å] | group |
|---|---|---|---|---|---|---|
| $Cu(In_{0.7},Ga_{0.3})Se_2$ | [39] | ICDD 00-035-1102 | tetragonal | 5.736 | 11.448 | $I\bar{4}2d$ |
| $\gamma-(In_{0.75},Ga_{0.25})_2Se_3$ | [128] | ICSD 634424 | hexagonal | 7.010 | 19.080 | $P622$ |
| Mo | [169] | ICDD 01-089-5156 | cubic | 3.147 | | $Im\bar{3}m$ |
| $MoSe_2$ | [170] | ICDD 00-017-0887 | hexagonal | 3.288 | 12.931 | $P63$ |

**Table A.1.:** Reference data used for the material identification and orientation thoughout this work.

## A.3. Scanning electron microscopy

The presented SEM-images were made with a Zeiss Merlin VP COMPACT equipped with a field-emission-gun (SEM-FEG) allowing for a maximum amplification of x300$k$ and a resolution (at optimum voltage) of about 1 nm. The electron acceleration voltage is in the range of 10-15 kV and the work distance between 5 and 10 nm. The microscope is coupled to an energy-dispersive spectrometer (EDS or EDX) allowing a semi-quantitative elemental analysis with a resolution in the order of $1\mu m^3$.

## A.4. Raman spectroscopy

The spectra shown in this work were measured by a HORIBA Jobin-Yvon HR800 with a laser excitation at $\lambda = 532$ nm.

For CIGS, this excitation wavelength is very surface sensitive which is illustrated by the following simple calculation: The fraction $f_{85}$ of the measured Raman signal which has been scattered in the top 85 nm can be calculated using the Beer–Lambert law. The intensity of light scattered at a certain distance $x$ perpendicular to the surface and traversing the sample on the way back to the surface (which is necessary to be measured by the detector) is given by A.3 with the absorption coefficient $\alpha$, incident intensity $I_0$ and a scattering constant $c$.

$$I_s(x) = I_0 \cdot c \cdot exp(-2 \cdot \alpha \cdot x) \tag{A.3}$$

The fraction $f_{85}$ of measured intensity of light scattered in the top 85 nm is then given by A.4.

$$f_{85} = \frac{\int_0^{85nm} I_s(x)dx}{\int_0^{\infty} I_s(x)dx} = 1 - exp(-2 \cdot \alpha \cdot 85 \text{ nm}) \tag{A.4}$$

A typical CIGS absorption coefficient $\alpha = 1.35 \cdot 10^5$ cm$^{-1}$ for light with a wavelength of 532 nm [91] leads to $f_{85} = 0.90$ thus 90% of the measured Raman intensity is scattered in the top 85 nm.

## A.5. Glow discharge optical emission spectroscopy, quantified by ICP

Glow discharge optical emission spectroscopy (GD-OES) is a spectroscopic method for the quantitative analysis of solid state materials. The sample is used as the cathod in a plasma and successively decomposed by argon atoms. The removed atoms diffuse into the plasma. Excited by collision processes, they emit light at specific wavelengths. The spectrometric analysis of the emitted light allows for the quantification of the material composition.

For the quantification, the integral composition of the investigated sample is measured by inductively coupled plasma mass spectrometry where the sample is completely diluted and the solution is then analysed quantitatively by mass spectrometry.

# B. Solar cell characterisation

## B.1. Current-voltage characterisation

The presented current-voltage curves were measured in the 3-point setup using a Keithley source-measure-unit. The sample temperature is set to 25 °C and for the measurements under illumination, a class AAA solar simulator of the AM1.5g solar spectrum with a total power density of 1000 $W/m^2$ is used. For each sample, 36 solar cells are defined by mechanical scribing of the CIGS/CdS/ZnO stack to a size of 0.1 $cm^2$ for each cell. The front contact is established directly with a gold pin on the ZnO:Al layer.

## B.2. As a function of temperature

In the case of current-voltage measurements as a function of temperature, the sample was placed into a cryostat. The measurements were conducted by successively decreasing the temperature. After the substrate temperature first reached the set-point, we waited for 5 min for the temperature to stabilize.

## B.3. External quantum efficiency

In our setup a halogen lamp at 1000 W was used as light source and a monochromator for the wavelength separation. The monochromatic light is separated into two beams. One past is focused on the sample surface while the other part is collected by a reference detector in order to estimate the incident photon flux $\Phi_0$. This calibration is realised by a silicon detector for 300 nm $\leq \lambda <$ 1050 and a germanium detector for 1050 nm $\leq \lambda \leq$ 1300 nm.

# C. Material characterization of absorber layers used in the devices studied in chapter 6

| **front Ga content $x_f$** | **0.16** | **0.25** | **0.30** | **0.38** | **0.41** | **0.50** | **0.59** |
|---|---|---|---|---|---|---|---|
| **Cu [at. %]** | 20.8 | 20.7 | 20.6 | 20.8 | 20.7 | 20.5 | 20.5 |
| **In [at. %]** | 17.7 | 17.8 | 16.4 | 16.4 | 15.5 | 13.9 | 13.5 |
| **Ga [at. %]** | 7.5 | 7.7 | 8.71 | 8.3 | 9.2 | 9.9 | 10.2 |
| **Se [at. %]** | 53.9 | 53.9 | 54.3 | 54.5 | 54.6 | 55.8 | 55.9 |
| **GGI** | 0.30 | 0.30 | 0.35 | 0.34 | 0.37 | 0.42 | 0.43 |
| **CGI** | 0.84 | 0.81 | 0.82 | 0.84 | 0.84 | 0.86 | 0.87 |
| **2[Se]/([Cu]+3[In]+3[Ga])** | 1.12 | 1.11 | 1.13 | 1.15 | 1.15 | 1.22 | 1.22 |

**Table C.1.:** Elemental composition and certain fractions of absorber layers with varying front Ga composition $x_f$ as described in sec. 6.2 measured by X-ray fluorescence.

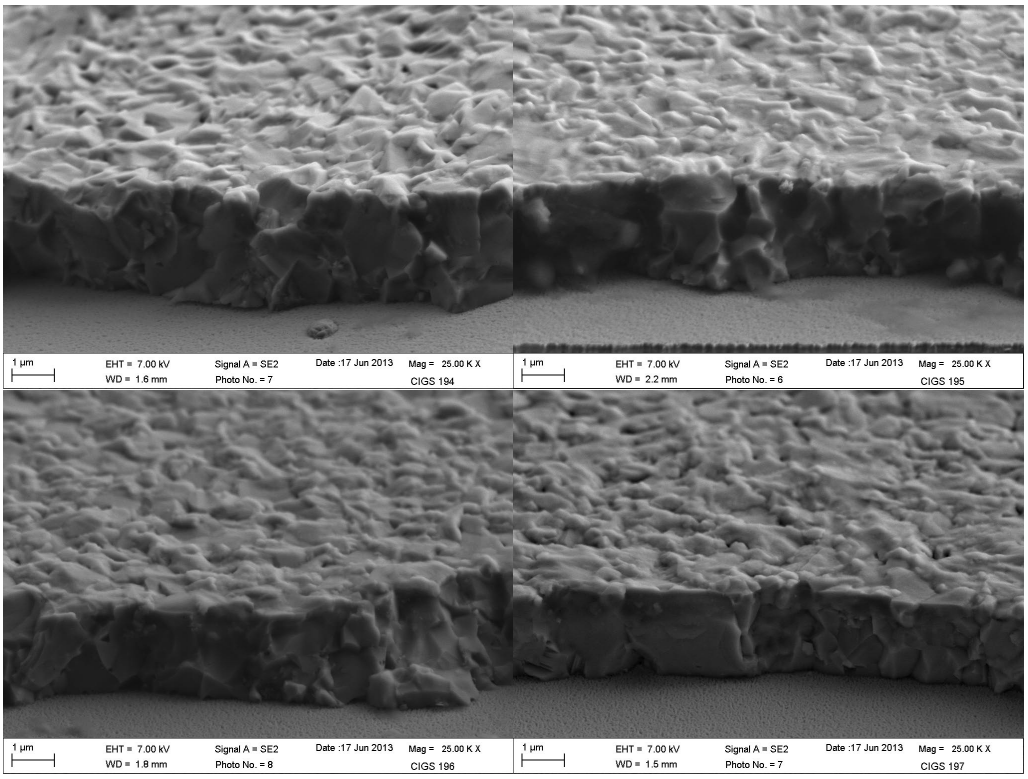


**Figure C.1.:** SEM images of absorber layers with varying front Ga composition $x_f$ as described in sec. 6.2. Top left: $x_f = 0.30$, top right: $x_f = 0.41$, bottom left: $x_f = 0.50$, bottom right: $x_f = 0.59$.

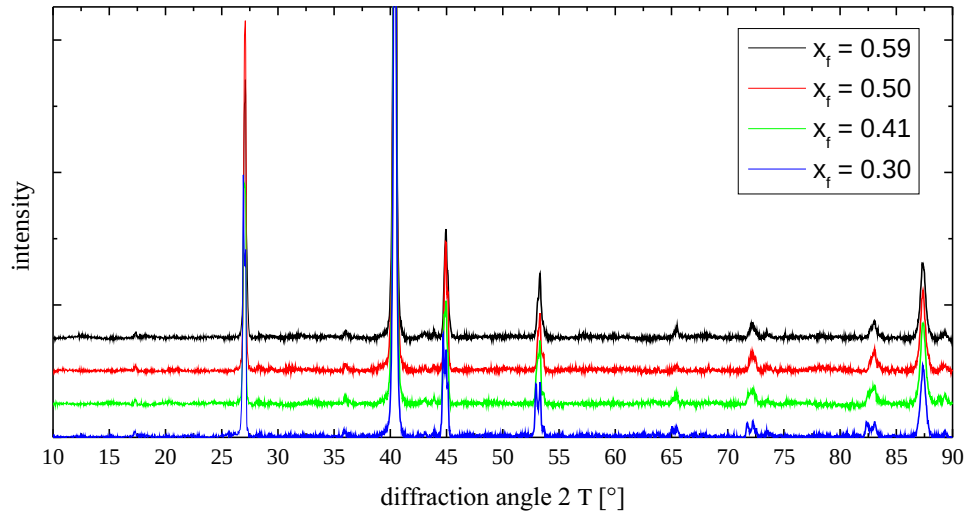


**Figure C.2.:** X-ray diffractograms for absorber layers with varying front Ga composition $x_f$ as described in sec. 6.2.

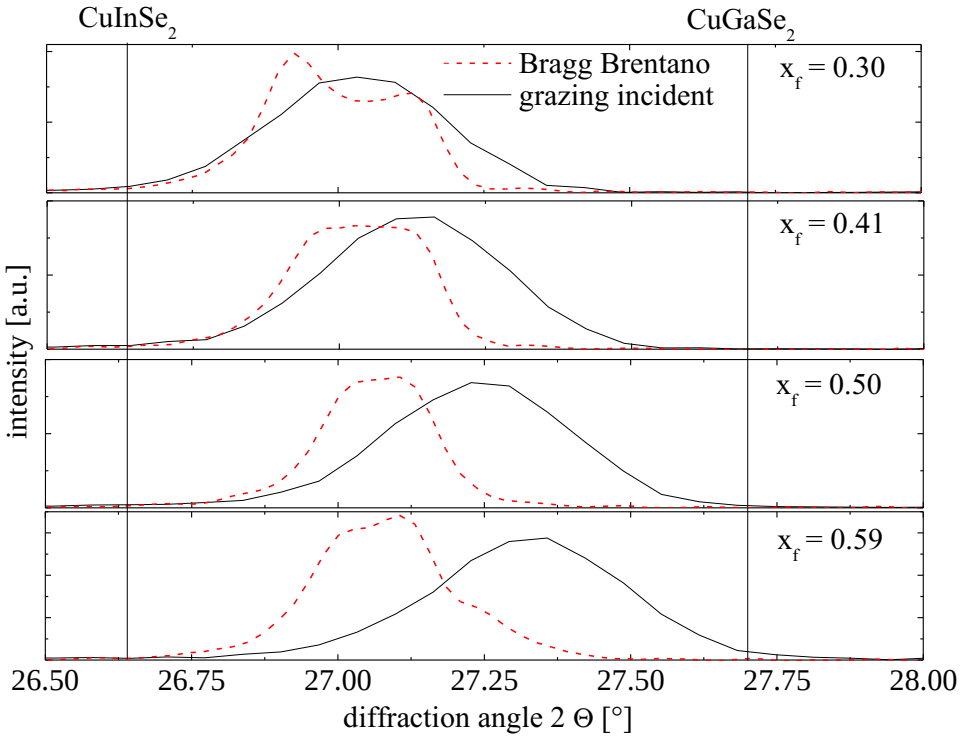


**Figure C.3.:** X-ray diffraction diagrams in the Bragg-Brentano as well as in the surface sensitive grazing-incidence setup of the (112) lattice planes for absorber layers with varying front Ga composition $x_f$ as described in sec. 6.2.

# D. Arrhenius plots for varied Ga surface composition $x_f$ and ZnS buffer layer

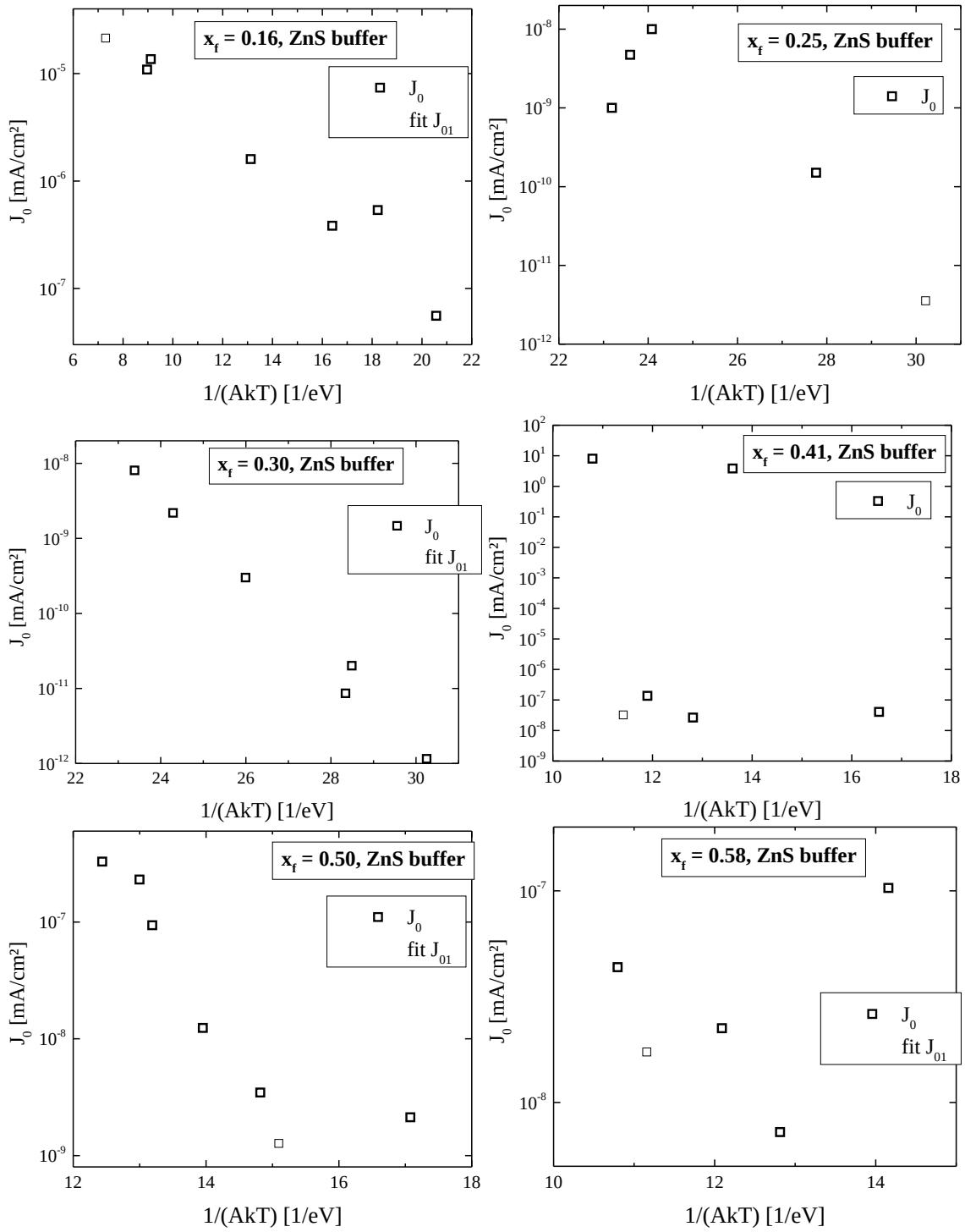


**Figure D.1.:** Arrhenius plots of IV characteristics in the dark for samples with varied Ga surface composition shown in Fig. 6.7 and CdS buffer layer.

# E. Simulation parameters

| | | CIS | CGS | CdS | i-ZnO | ZnO:Al |
|---|---|---|---|---|---|---|
| | $E_g$ [eV] | 1.0 | 1.7 | 2.425 | 3.4 | 3.3 |
| | $\chi_{el}$ [eV] | 4.57 | 3.87 | 4.275 | 4.54 | 4.45 |
| | $N_A$ [$cm^{-3}$] | $10^{16}$ | | 0 | 0 | 0 |
| | $N_D$ [$cm^{-3}$] | 0 | | $10^{16}$ | $5 \cdot 10^{17}$ | $10^{17}$ |
| | $\epsilon/\epsilon_0$ | 13.6 | | 10 | 10 | 9 |
| | $N_c$ [$cm^{-3}$] | $2.2 \cdot 10^{18}$ | | $2.2 \cdot 10^{18}$ | $4 \cdot 10^{18}$ | $2.2 \cdot 10^{18}$ |
| | $N_v$ [$cm^{-3}$] | $1.8 \cdot 10^{19}$ | | $1.8 \cdot 10^{19}$ | $9 \cdot 10^{18}$ | $1.8 \cdot 10^{19}$ |
| | $v_{th,n}$ [cm/s] | $10^7$ | | $10^7$ | $10^7$ | $10^7$ |
| | $v_{th,p}$ [cm/s] | $10^7$ | | $10^7$ | $10^7$ | $10^7$ |
| | $\mu_n$ [$cm^2$/ Vs] | 1 | | 100 | 50 | 100 |
| | $\mu_p$ [$cm^2$/ Vs] | 15 | | 25 | 20 | 25 |
| defect | distrib. | single | | single | none | single |
| | charge | neutral | | neutral | | neutral |
| | $N_{t,total}$ [$cm^{-3}$] | $5 \cdot 10^{12}$ | | $5 \cdot 10^{17}$ | | $10^{16}$ |
| | $E_t - E_v$ [eV] | 0.6 | | 1.2 | | 1.65 |
| | $\sigma_n$ [$cm^2$] | $10^{-14}$ | | $5 \cdot 10^{-11}$ | | $10^{-12}$ |
| | $\sigma_p$ [$cm^2$] | $10^{-17}$ | | $5 \cdot 10^{-11}$ | | $10^{-12}$ |

**Table E.1.:** Material parameters taken into account for the SCAPS simulation.

# Nomenclature

| | |
|---|---|
| $\alpha_i$ | Absorption coefficient of material $i$ |
| $\epsilon$ | Dielectric function |
| $\eta_c$ | Collection function |
| $\lambda$ | Wavelength |
| $\nu$ | Frequency of an electromagnetic (light) wave |
| $\Phi_{0,i}$ | Incident photon flux at the surface of layer $i$ |
| $\Phi_{AM1.5G}$ | Global solar spectra with an airmass coefficient of 1.5 |
| $\rho$ | Charge density |
| $\varphi$ | Electrostatic potential |
| $A_i$ | Diode ideality factor for recombination mechanism $i$ |
| $E_{Fn}$ | Quasi Fermi level for electrons |
| $E_{Fp}$ | Quasi Fermi level for holes |
| $E_{g,i}$ | Band gap energy of material $i$ |
| $F$ | Electric field component |
| $G$ | Generation rate of electron-hole pairs |
| $G_n$ | Electron generation rate |
| $G_p$ | Hole generation rate |
| $J_n$ | Electron current density |
| $J_p$ | Hole current density |
| $J_{0,i}$ | Dark saturation current density of recombination mechanism $i$ |
| $J_{ph,ideal}$ | Ideal photo current assuming perfect carrier collection |
| $J_{ph}$ | Photocurrent |
| $L_{n,a}$ | Diffusion length of electrons in the absorber layer |
| $n$ | Elektron density |
| $N_A^-$ | Ionised acceptor density |
| $N_D^+$ | Ionised donor density |
| $p$ | Hole density |
| $q$ | Elemental charge |
| $R_p$ | parallel resistance |
| $R_s$ | series resistance |

$t_{CIGS}$ Thickness of the CIGS absorber layer
$U_n$ Electron recombination rate
$U_p$ Hole generation rate
$w$ Space charge region width
CBD chemical bath deposition
CGI atomic concentration ratio [Cu]/([Ga]+[In])
EDX energy dispersive x-ray spectroscopy
EQE external quantum efficiency
GDOES Glow discharge optical emission spectroscopy
ICDD Internation Center for Diffraction Data
ICSD Inorganic Crystal Structure Database
Mtoe Million tons oil equivalent
NREL National Renewable Energy Laboratory (USA)
ODC ordered defect compound
OVC ordered vacancy compound
PDT Post deposition treatment
PV photovoltaic
RF radio frequency
SCR Space charge region
SEM scanning electron microscopy
SRH Shockley-Read-Hall
XRD x-ray diffraction
XRF X-ray fluorescence
ZSW Zentrum für Sonnenenergie- und Wasserstoff-Forschung, Center for solar and hydrogen research, Stuttgart, Germany